

College of Instrumentation & Electrical Engineering, Jilin University

Academic Practice “Six in One” Training Project

English Proceedings

2017 (Second Half)

CONTENTS

Design of Intelligent Express System Based on Digital Road Information.....	
.....Zhang Shang; Liu Zhijie; Lu Manyu	1
Design of Methane Detection and Wireless Transmission System Based on MSP430	
.....GAO Peng; QIN Wei-ying; LI Xiang	9
Design of Multi-wavelength Human Muscle Lactic Acid Measuring Instrument	
.....Cai Jing; Xu Zitong; Hu Shiran; Zhu Xiaoxu	15
Research on Android-based wearable body temperature measuring equipment	
.....Cai Jing; Liu Huaqing; Liu Weifeng; Sun Mengyan	19
Design of head mounted gaze tracking control system based on embedded system	
.....Yuan Jinfeng; Chen Guanyu; Sun Pengyong	25
Design of mobile intelligent patrol instrument based on Cloud Computing	
.....YUAN Ya-qi; GAOYu-miao; DAI Xin-ping	31
High Stability DFB Driver Utilized in Near Infrared Gas Detection	
.....Deng Weifen; Wang Qianqian; Jiang Rongqiu	37
A Design of Indoor Intelligent Ventilation and Purification System Consisted of Fans	
.....Zhu Yurong; Ma Jingxuan; Gu Yujing	45
Design and study on resistance type semiconductor gas sensor characteristics test system based on LabVIEW	
.....ZHANG Jun-hong; WANG Qiao; ZHANG Shu-hui	51
Study on the Measurement of Cerebral Blood Flow Parameters Based on PDD – NIRS	
LIU Guang-da; WANG Yu-lin; QIN Qi, ZHANG Lan-xi; QIAN Cheng-hui; SHANG Xiao-hu; ZHA	
.....Yu-tong; CAI Jing	55
The design and implementation of intelligent trash can based on Stm32.....	
.....Xu Quan; Wang Mingcong; Xia Renqiu	63
Soft switch plasma loudspeaker based on PWM pulse-width modulation	
.....WU Zi-Bo; WANG Yu-Ge; TIAN Hao; YU Sheng-Bao	71
Time - Frequency Characteristic Analysis for Electromagnetic Detection of Motion Noise	
.....Pang Yidi; Zhang Xiaoshuang; Qian Zeli; Zhu Kaiguang	79
Design of Three Dimensional Magnetic Compensation System Based on PID Algorithm	
.....Jiao Bin; Suo Peng; Wang Zhaoxun	85
A design of non-contact ECG machine based on capacitive coupling	
.....LING Zhen-bao; FAN Tian-jiao; ZHOU yu-cheng; YU Si-jia	89

Research on Sign Language Translation System Based on Kinect.....	
.....Liu HuaiBin; Xia Tao; Shao JingYa	93
Study on High Power LED Electrical Parameter Model	
..... WANG Zhao-feng; CAO Jia-rui; LI Gang; HE Zong-ze	99
Design of Bluetooth Car Lock Based on Fingerprint Recognition.....	
.....Fang Zizheng; Liu Shuai; Zhang Zhichao	105
The study of light intensity traceable photovoltaic power generation lighting system	
..... Xia Tiancheng; Yang Yuanyuan; Huang Sibao	111
Research of brain-computer interface based on multi-feature integration and BP neural network	
..... Liu Guangda; Wang Can; Li Mingjia; Sun Ruichen; Cai Jing; Gong Xiaoyu	115
Research on gesture recognition based on Probabilistic Neural Network	
..... Wei Qingli; Xiao-Wei; Liang Weiqiang; Sun Zhenchao; Zhang-Li	119
Design of small-sized full tensor magnetic gradiometer	
.....ZHANG WEN-YE; WEN YAN-LING; ZHU WEN-HAO	123

Design of Intelligent Express System Based on Digital Road Information

Zhang Shang; Liu Zhijie; Lu Manyu

(*jilin university instrument science and engineering institute, changchun, 130012*)

Abstract—This paper designs an intelligent express system based on digital road information in view of the low efficiency of manual distribution and delivery. Digitized road information intelligent express delivery system includes car system, road system and management station system. Car system includes automatic travel subsystem, communication subsystem, automatic delivery subsystem. Automatic travel subsystem is automatically driven by the STM32 microcontroller of judging the ultrasonic module feedback data and controlling L298 DC motor to drive the car; and in the communication subsystem, the YS-NEC infrared decoding module is responsible for reading the road information and traffic lights, and the SIM900A Module is responsible for the car and the management station under the machine communication; automatic delivery subsystem with a password lock module and a LCD5110 LCD display achieves human-computer interaction and controls the door. The road system includes a node information communication module, a traffic light communication module and a turn signal communication module. The node information communication module transmits the road information with the YS-NEC infrared coding transmission module; the traffic light communication module sends the traffic light state to the car through the YS-NEC infrared coding transmission module; the turning signal communication module uses the infrared tube to provide the turning signal. The management station system includes the host computer module and the lower computer module. The host computer of LabVIEW display interface is mainly responsible for monitoring the operation of the car, the lower machine module of STM32 MCU controls SIM900A for the car to send the delivery location and receipt password information. Digital road information intelligent expresses delivery system to achieve the delivery of the unmanned and automated, and solve the problem of low efficiency of express delivery effectively.

Keywords—intelligent express system digital road information.

I INTRODUCTION

DATA shows that the general commodity processing and manufacturing time will not exceed 10%, and more than 90% of the time are in condition of warehousing, transportation, packaging and distribution logistics, including that the logistics industry is also true. Therefore, to improve logistics efficiency and reduce logistics costs, which has been from the seller's market into the buyer's market, profits gradually diluted logistics industry has become particularly important [1].

Intelligent courier system is a delivery system, which can be in the customer after the order, instead of the original way of human transport vehicles, and it has intelligent, fast, managed way directly by the seller to transport.

Intelligent express system is a direction of smart logistics system, for the form of logistics and transport has important significance in future [2]. Intelligent logistics system is in the intelligent transportation system and related information technology on the basis

of e-commerce mode of operation of the modern logistics service system. It through the intelligent transportation system and related information technology to solve the logistics operations real-time information collection, and in an integrated environment for the collection of information analysis and processing. Through the information transmission in the various logistics links, logistics service providers and customers to provide detailed information and advisory services system. Thus, intelligent courier system is the product of network systems and e-commerce, his appearance is a new type of logistics industry [3].

Based on the above practical considerations, this study is expected to use the basic principles of electronic aspects, by simulating the way of transport and customer picking, and the use of signal and system, analog electronic circuits, microcontroller theory and application of disciplinary knowledge of electronic signal digital processing. And finally through the comprehensive calculation and analysis to be more scientific and reliable experimental results. In addition, this study aims to complete the basic smart car on the

basis of innovative use in the logistics and transportation industry, and can control the car's trajectory and determine the correctness of the fetters [4]. Which greatly improved the efficiency of the logistics industry, making the logistics industry to enhance the intelligence. The intelligent express system is relatively simple and portable, suitable for real-time use in life, which also contributes to the modernization of electronic technology applications [5].

II OVERALL DESIGN OF SYSTEM

Intelligent courier system is divided into three parts:

(1) car system: divided into automatic travel subsystem, communication subsystem and automatic delivery subsystem. Wherein the automatic sub-system comprises a driving module, a distance measuring module and a power supply module; the communication subsystem comprises a car information and communication module; the automatic delivery subsystem includes a customer human-computer interaction module, a trolley delivery management module and a gate control module.

(2) road system: including node information communication module, traffic light communication module and turn signal communication module.

(3) management station system: including express management station module.

There are distance measurement module, drive module, human-computer interaction module, car delivery management module and information and communication module in car. The distance measurement module sends the distance measurement value to the car management module to determine whether it is greater than the safety distance, thereby controlling the drive module. Car system in the human-computer interaction to complete the information input and verification, car control door switch, the user to confirm the information after the update. The communication between the car and the road system is achieved through a digital road node. The communication between the car and the management station system is realized by using SIM900A module in the form of sending and receiving text messages. The relationship between the system modules that the system block diagram shown in Figure 1.

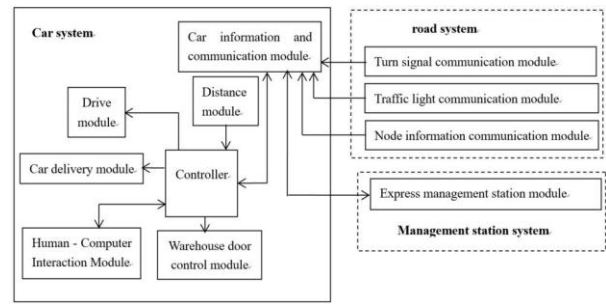


Fig. 1 System Block Diagram

III DESIGN OF CAR SYSTEM

The car system adopts the STM32F407 single-chip microcomputer as the main control, controlling the running of the car, managing the ultrasonic distance measuring module, the communication between the car and the node, the infrared tube module, the driving module, SIM900A module and the automatic delivery module, so that the module can work in coordination and stable operation and complete the delivery process [6].

Car master control system flow chart shown in Figure 2.

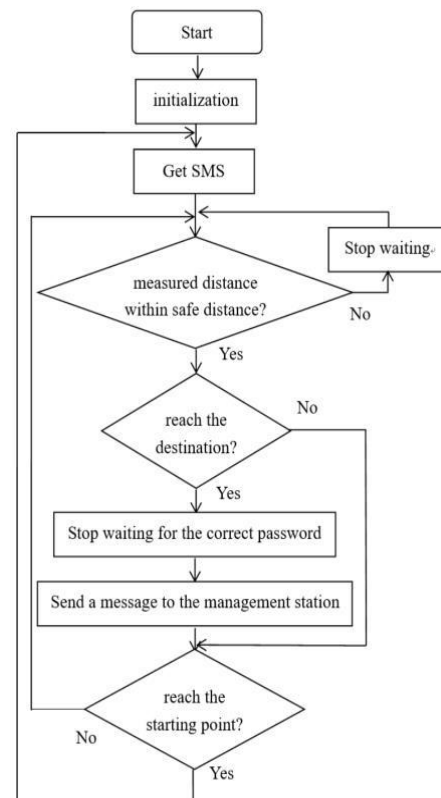


Fig. 2 Car master control system flow chart

3.1 Automatic travel subsystem

3.1.1 Drive module

Driver module is mainly composed of L298N drive module and DC motor, is responsible for driving the car's DC motor, so that the car to walk correctly. The drive modules IN1 to IN4 are connected to F0 to F3 of

the main control unit. The ENA and ENB of the drive module are connected to the 5V supply. The GND of the driver module is connected to the GND of master microcontroller [7]. L298N drive module circuit shown in Figure 3.

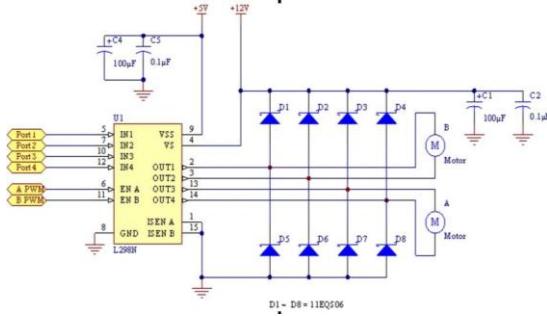


Fig. 3 L298N drive module circuit diagram

3.1.2 Distance module

The distance module is used to determine the safety of the front when the car is running. The US-100 ultrasonic module is connected to the USART6 of the master microcontroller. The RXD of the ultrasonic module is connected to the TXD of the master microcontroller. The TXD of the ultrasonic module is connected to the RXD of the master microcontroller. Ultrasonic module serial port configuration: baud rate 9600 bit / s, 1 start bit, 1 stop bit, 8 data bit, no parity, no flow control. This module comes with the distance measurement results of temperature compensation function, which can effectively suppress the interference of different temperature environment on the distance measurement results, in order to achieve accurate ranging.

Ultrasonic module measured the distance before the obstacle is greater than the set safe distance, the car parking waiting, until the front can be safe driving after the car to continue driving. Ultrasonic distance measurement program flow chart shown in Figure 4.

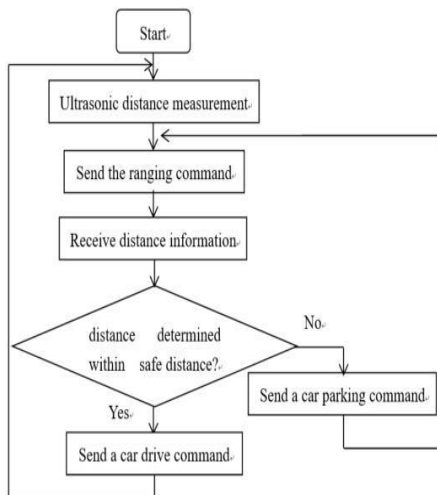


Fig. 4 Ultrasonic distance measurement program flow chart

3.1.3 Power module

Power supply module with 12V lithium battery polymer power supply, battery capacity 4400mAh.

This battery can be multiple charge and discharge, stable performance, large capacity, small size, to meet the needs of various parts of electricity to ensure the stability of work.

3.2 Communication subsystem

Car information and communication module by the YS-NEC infrared decoding receiver module and SIM900A module. The infrared decoding receiver module on the express car gets the road information, and the current road information is transmitted to the car master for the master to judge the current road condition and determine the running status. When the car arrives at the intersection, and receives the digital road node information, the courier car using the SIM900A module to the management station to transmit the current car position information and the upcoming location information for the management station to supervise the car.

3.2.1 Infrared decoding receiving module

Infrared decoding receiver module and the car management system master microcontroller USART5 connected. The RXD of the infrared decoding receiving module is connected with the TXD of the master microcontroller. The TXD of the infrared decoding receiving module is connected with the RXD of the master microcontroller. Infrared decoding receiver module Serial configuration: baud rate 4800 bit / s, 1 start bit, 1 stop bit, 8 data bit, no parity, no flow control. The infrared decoding receiving module obtains the current road node information and the traffic light signal by receiving the coding information.

Infrared decoding receiver module program flow chart shown in Figure 5.

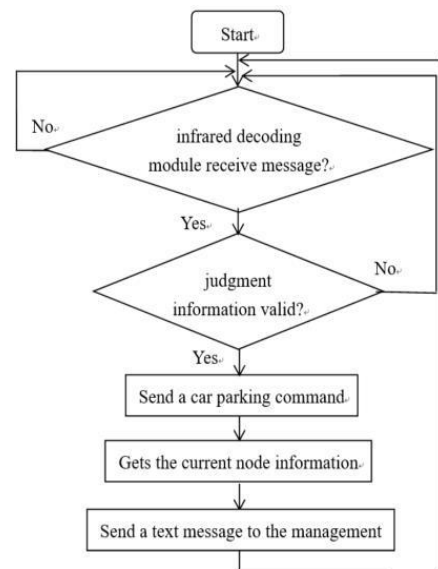


Fig. 5 Infrared decoding receiver module program flow chart

3.2.2 SIM900A module

The communication between the cart and the management station is mainly done by the SIM900A

module, which is controlled by the AT command. SIM900A module and car management system master microcontroller USART3 connected. The RXD of the SIM900A module is connected to the TXD of the master microcontroller. The TXD of the SIM900A module is connected to the RXD of the master microcontroller. SIM900A module serial port configuration: baud rate 9600 bit / s, 1 start bit , 1 stop bit , 8 data bit , no parity, no flow control.

The car gets the short message from the management station before departure, analyzes the destination and sends the shipment. SIM900A module program flow chart shown in Figure 6.



Fig. 6 SIM900A module program flow chart

3.3 Automatic delivery subsystem

3.3.1 Client man - machine interaction module

The client man-machine interaction module consists of 4*4 determinant keyboard and LCD5110 screen. The 4*4 determinant keyboard is used for the customer to enter the password and switch box. LCD5110 display with the customer access to the relevant information [8]. LCD5110 screen's SCE, RES, DC, SDIN, SCLK connects the main control of the microcontroller's D0, D1, D15, D14, D12. LCD5110 screen has only four I / O lines which can be driven, less occupied I/O , high communication speed, the working voltage of 3.3V. Client man-machine interaction module program flow chart shown in Figure 7.

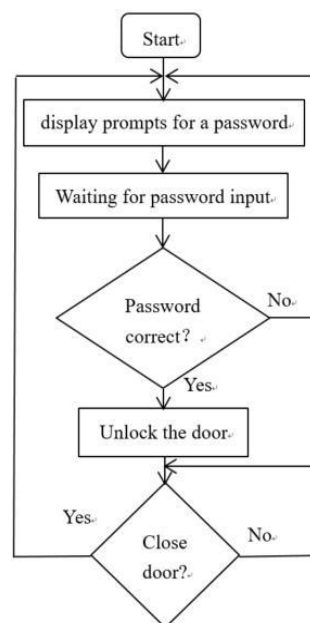


Fig. 7 Client man - machine interaction module program flow chart

3.3.2 Car delivery management module

Car delivery management module when the user enters the correct password, open the door, so that users remove the courier, the user through the keyboard to confirm receipt is completed, the car closed the door, car delivery management module to the traffic management system to send instructions to the next delivery task [9].

3.3.3 Warehouse door control module

The door control module consists of an electromagnet, which uses micro-through-type electromagnet, the use of 12v voltage power supply, stroke 4mm, when the power inhalation, power release, as an analog lock. The warehouse is simulated by the carton [10].

IV DESIGN OF ROAD SYSTEM

The road system includes a node information communication module, a traffic light communication module and a turn signal communication module. The YS-NEC Infrared Encoding Module sends the node information correctly, and the traffic lights signal and the infrared control module are sent at each intersection. The YS-NEC Infrared Encoding Module sends the node information correctly. The YZ-NEC Infrared Encoding Module sends the node information correctly. Using intersection to send the function of the turn signal.

YS-NEC infrared coding module and each 51 single-chip serial port connected. The infrared code module RXD and 51 single-chip TXD connected; infrared coding module TXD and 51 single-chip RXD connected. YS-NEC infrared coding module serial port

configuration: baud rate 4800 bit / s, 1 start bit , 1 stop bit , 8 data bit , no parity, no flow control. The infrared coding module transmits the current road node information and the traffic light signal. The infrared signal is transmitted to the tube emission module.

4.1 Node information communication module

The node information transmission function consists of 51 MCU and YS-NEC infrared coding transmission module. The digital road information node is set up on the road (such as the intersection) of the road, and the operation of the node information transmitting module is controlled by the 51 single-chip microcomputer, and the current road node information is transmitted by the YS-NEC infrared coding transmission module. Using 51 single-chip control YS-NEC infrared coding transmitter module, loop send node information. 51 single-chip transmission to the YS-NEC infrared coding transmission module "A1, F1,00,00,01" code to send YS-NEC infrared coding transmitter module node 1 information, in this way the transmission of node information.

4.2 Traffic light communication module

In the need for traffic management road junction with YS-NEC infrared emission module, used to transmit the current traffic lights state, tell the car is currently safe driving.

The use of 51 single-chip timer function, when the timing time to arrive, in turn change the traffic signal status, to achieve the function of analog traffic lights. 51 single-chip to the YS-NEC infrared coding transmission module to transmit "A1, F1,00,00,09" code to make YS-NEC infrared coding transmitter module to send a red light signal, 51 single-chip to the YS-NEC infrared encoding transmitter module transmission "A1, The F1, 00, 00, 0a "code causes the YS-NEC Infrared Encoding Transmitter module to send a green light signal to transmit the traffic light signal in this way. Traffic light communication module program flow chart shown in Figure 8.

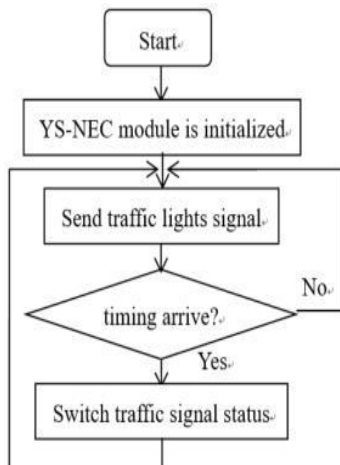


Fig. 8 Traffic light communication module program flow chart

4.3 Turn signal communication module

The corner signal communication module consists of 51 single-chip and infrared tube-emitting module. The car need to turn the place at the intersection by the 51 single-chip control of infrared tube on the conduction, you can send a turning signal for the car.

V DESIGN OF MANAGEMENT STATION SYSTEM

Express management station module can be divided into the next crew and the host computer module. Express management station system by the host computer, SIM900A module and STM32F103 under the machine composition. The host computer is responsible for realizing the man-machine interaction between the management station and the express car. The use of serial port to achieve the lower computer and the host computer between the communication, the microcontroller TXD and PC-side RXD connected to the microcontroller RXD and PC-side TXD connected. Serial configuration: baud rate 9600 bit / s, 1 start bit, 1 stop bit, 8 data bit, no parity, no flow control. The host computer receives the current position of the car using the "0xx1xx" protocol to receive ('0' followed by the car has reached the node, '1' behind the car is about to go to the node). The host computer transmits the destination information to the car using the "2xx3xx" protocol ('2' followed by the first destination node, followed by the second destination node). The SIM900A module is responsible for the communication between the express management station and the express car. STM32F103 lower machine control courier management station operation, responsible for the management of the host computer and SIM900A module, so that the module stable operation, coordination work, to achieve the function of express delivery station. Express management station system block diagram shown in Figure 9.

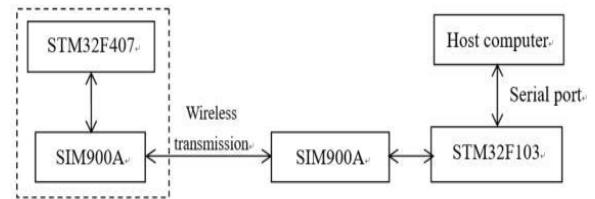


Fig. 9 Express management station system block diagram

5.1 Lower machine module

Lower machine STM32F103 single-chip control management station operation, management of the host computer and SIM900A module. To achieve access to information on the host computer and control SIM900A module to send text messages function, including the host computer information, including express courier express destination information and recipient phone number information. The MCU

controls the SIM900A module to send the SMS containing the destination information of the express mail, and obtains the SMS information received by the SIM900A module, confirms the current position of the express car and is about to go to the location, and transmits the location information to the host computer for the supervisor to view the supervisor. STM32F103 single-chip program flow chart shown in Figure 10.

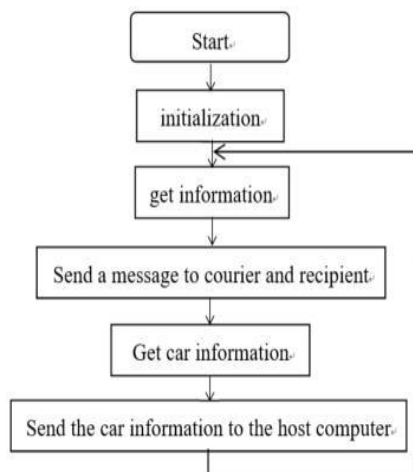


Fig. 10 STM32F103 single-chip program flow chart

5.2 Host computer module

Express management station host computer interface shown in Figure 11. The controls used in this host interface include numeric input controls, numeric display controls, switch button controls, circular light controls, square indicator controls, button controls, text boxes, string input controls, string display controls, and VISA resource name controls and so on. The functions used in this host interface are: string constant function, comparison function, VISA read and VISA shutdown. This interface can be set up, including: terminator, XON / XOFF characters, baud rate, data bits, parity bits, stop bits and flow control. In order to achieve the function of serial detection of serial information, the serial port write and read the cycle scan control. LED analog junction is used to display the running status of the car, this function from the structure of the formula node function.

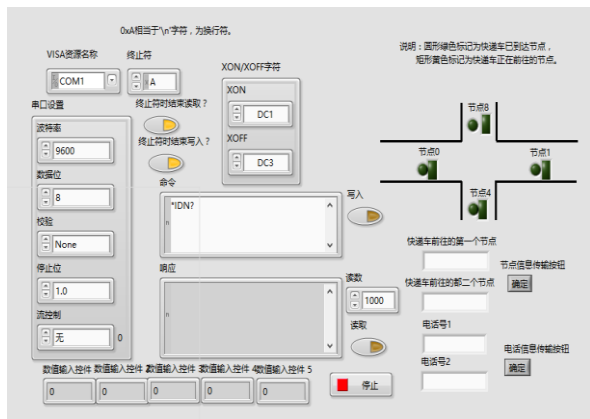


Fig. 11 Express management station host computer interface

Host computer rear panel serial interface procedures shown in Figure 12. This serial program based on LabVIEW own routines, the function of the expansion, to achieve the general function of the serial interface. The content that can be set for this interface includes the terminator, XON / XOFF character, baud rate, data bit, parity bit, stop bit and stream control.

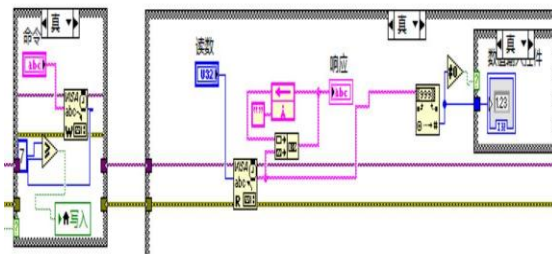


Fig. 12 Host computer rear panel serial access procedures

The host computer rear panel simulation road information program shown in Figure 13. This simulation road information program can use the LED lights to simulate the current car position, the use of formula nodes to program, make full use of LabVIEW and C language their own characteristics.

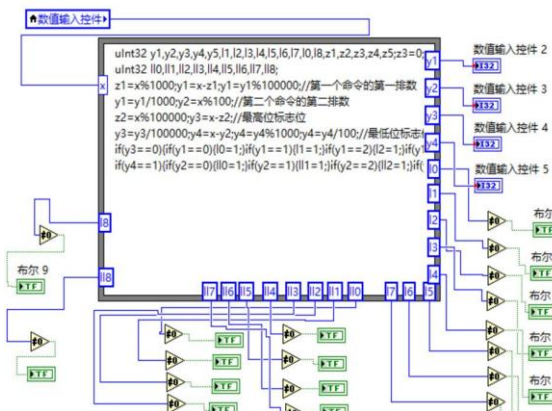


Fig. 13 The host computer rear panel simulates the road information program

VI EXPERIMENT AND ANALYSIS

Using the hardware and software design makes an experiment in the simulation on the road, exploring the route planning and the realization of the entire system.

As the car once distributed two parcels, so this experiment set the destination of the node 0 and node 1, the car starts from the node 4 (warehouse). The simulation road diagram is shown in Figure 14.

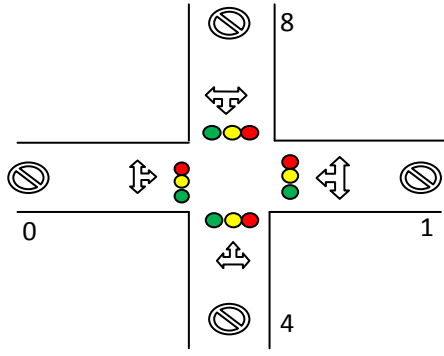


Fig. 14 The simulation road diagram

First in the host computer to enter the destination location node 0 and node 1, the recipient 1: 188 **** 2434, the recipient 2: 171 **** 4465. The management station will send the location to the main control of the car microcontroller and notify the recipient A and B including location and password. A receives short message: Please go to node 0 to receive express parcel 1, password 1590. B receives the short message: Please go to node 1 to receive express parcel 2, the password is 2486. The host computer displays the running road interface as shown in Figure 15. And the car starts, when the car receives the node 4, the car stops and sends SMS to inform car current position to the management station, the management station of the host computer interface on behalf of node 4 green light (as shown in Figure 15 above). When the ultrasonic measurement of the car in front of obstacles are less than the safe distance, the car parks to wait. When the car travels to the crossroads, the red light signal sends the infrared coding module, and the signal is "A1, F1, 00, 00, 09". The car receives the parking signal and waits for the green signal. When the car receives the turn signal and turn left to node 0. When the car arrives at node 0, the car waits for the recipient 1 to enter the password which was sent by the message before opening. When the pickup is completed, the car closes the door and sends a message to the management station. The management station of the host computer on behalf of node 0 green light (as shown in Figure 15 above). And then the car turns 180 degrees straight after the trip to the node 1, and arrives at the node 1 when the car waits for the recipient 2 before entering the password to send the password. When the pickup is completed, the car closes the door and sends a message to the management station. The management station of the host computer on behalf of node 1 green light (as shown in Figure 15 below). After the completion of the two parcels delivery, the car returns to the warehouse node 4, the management station of the host computer on behalf of node 4 green light (as shown in Figure 15 below), and the car waits for the next delivery task.



Fig. 15 The host computer displays the running road interface

The results of the experiment can be seen, the car travels according to the planning of the route node 4 → node 0 → node 1 → node 4, and the car waits for the opening of the pickup and feedback to the management station at the destination, the host computer interface can also update the car status. And the corresponding green light signal to show it. The last car can return to the warehouse, waiting for the next task execution. The intelligent express delivery system based on digital road information realizes the functions of route planning, driving, communication, mailing distribution and system management under simulated road conditions and meeting the design requirements.

VII CONCLUSION

This paper designs intelligent express delivery system based on digital road information, including car system, road system and management station system. Car system includes automatic travel subsystem, communication subsystem and automatic delivery subsystem. The automatic travel subsystem includes the STM32 microcontroller by judging the ultrasonic module feedback data and controls L298 drive DC motor to drive the car; the YS-NEC infrared decoding module is responsible for reading the road information and traffic lights and the SIM900A Module is responsible for the car communication to the management station; the automatic delivery subsystem with a password lock module and LCD5110 display achieves human-computer interaction and controls the door. The road system includes a node information communication module, a traffic light communication module and a turn signal communication module. The node information communication module transmits the road information with the YS-NEC infrared coding transmission module; the traffic light communication module sends the traffic light state to the car through the YS-NEC infrared coding transmission module; the turning signal communication module uses the infrared tube to provide the turning signal. The management station system includes the host computer module and

the lower computer module. One of the host computer of LabVIEW interface is mainly responsible for monitoring the operation of the car, and the lower machine module of STM32 MCU controls SIM900A of the car to send the delivery location and receipt password information. Digital road information intelligent expresses delivery system to achieve the delivery of the unmanned and automated, and this system effectively solves the problem of low efficiency of express delivery.

References

- [1] Dian-Jun Fang, the Innovation and Development of Logistics Center Automation Solution - Logistics Center Automation Solution Innovation and Development [J]. Journal of Logistics Technology and Applications, 2014, 19 (9): 78-82.
- [2] Wei ZHANG, Ying CHEN, Li-na HAN, Yun XU , et al. Design of Intelligent Car System [J]. Laboratory Research and Exploration, 2011, 30 (9): 53-57.
- [3] Huiqiu Fen, Ning Lu, Shuaifeng Huang. Design of multi-functional intelligent car [J]. Occupation, 2011 (3): 107-107.
- [4] Liang, Guo Liwei Tan, Yongyong Li, et al. Development of new intelligent car based on single chip microcomputer [J]. Silicon Valley, 2010 (2): 18-18.
- [5] Huan Xu. Research on Motion Control System of Intelligent Car [D]. Central South University, 2009.
- [6] Wen-chao ZHENG, Jian SHU, Yu SONG, et al. Intelligent Express System Based on STM32 [J]. New Technology & New Products, 2017 (13): 10-11.
- [7] Xiao-yu SHI. Study and Design of Intelligent Express System Based on STM32 [J]. Electronic Technology and Software Engineering, 2014 (1): 132-133.
- [8] Kun QIAN, Lingyun XUE, Ying XU, et al. Tengfei DONG. Design and implementation of identity authentication in intelligent courier receipt system [J]. Industrial Instrumentation & Automation Devices, 2015 (1): 122-124.
- [9] De Kan, Xiong Luo, Daifu Ouyang, etc. Intelligent Express Pick-up System [J]. Communications World, 2016 (12): 225-226.
- [10] Jiejie XIE, Songlin LAI, Yunfeng LAI. Design of an intelligent express delivery box system based on S3C6410 [J]. Microcomputer and Application, 2015, 34 (7): 92-94.

Design of Methane Detection and Wireless Transmission System Based on MSP430

GAO Peng; QIN Wei-ying; LI Xiang

(Jilin University Instrument science and engineering institute, Changchun, 130012)

Abstract— A methane gas detection wireless transmission system based on MSP430F149 is designed. This system used nRF24L01 as the wireless transmission module. It can realize the real-time data acquisition of the methane concentration in the environment, wireless transmission and communication with the host computer. The accuracy of measurement is improved by least square fitting, fuzzy revising, sensitivity correction and digital filtering. Using LabVIEW to build a convenient man-machine interface, can be real-time monitoring of underground data. The results compared with optical fiber data show that the system measurement accuracy is about 6%. When the sampling time is 5ms, the data packet loss rate is only 0.7%. The system is high in accuracy and low in power consumption. It provides a feasible scheme for realizing digital and networked underground measurement and control and visual integrated management.

key words— methane concentration detection; wireless transmission fiber transmission MSP430 LabVIEW

I INTRODUCTION

METHANE is a common gas in the exploitation of coal, oil and natural gas. In the process of mining these energy sources, mine safety accidents associated with methane gas occur from time to time. Hence, it is of great significance to do the research aimed at methane detection.

At present, there are two main types of methane detection in our country. One is to take the gas inspection tour, with gas detector handheld, the professionals should designate the security of the mine regularly, and take notes[2]. This approach mainly has the following problems: firstly, personal safety is not guaranteed. Secondly, the recorded data uneasy to form a network leading to query historical data troublesome. Thirdly, because of long time interval while querying, it is not easy to deal with it in time if dangerous accident happened as real-time data is not available. The other is methane monitoring system, due to the complexity of environment in coal mines, the monitoring system is usually connected to the ground center by fiber or cable to record data. The main problems are as follows: firstly, the maintenance of wire transmission is complicated and expensive. Secondly, lines that have been constructed cannot be altered according to the change of the construction environment. Thirdly, it is prone to form blind spots

caused by the limitation of layout design.

Based on existing problems, the real-time methane concentration measured by MQ-4 for a single node is transmitted through nRF24L01—a wireless data transfer method—in this system. Comparing wireless transmission data with optical fiber transmission data, this paper attempts to analyze the theoretical feasibility of wireless multi node network system by measuring the rate of packet loss, delay interval, and effective transmission distance.

II SYSTEM HARDWARE DESIGN

A Overview of System Hardware Design

Hardware of this system mainly includes sensor module, A/D conversion module, microprocessor, wireless RF module and LCD module. Data of the analog voltage signal produced by the MQ-4 sensor is digitized by the sending end microcontroller. On the one hand, it is sent to the upper computer through the optical fiber after the photoelectric conversion carried out by the optical fiber transceiver. On the other hand, the data is sent to the receiver MCU through the nRF24L01 wireless module, then sent to host computer by using serial communication. This system realizes fast and real-time detection of methane gas under low power consumption, the schematic diagram is shown in Figure 1.

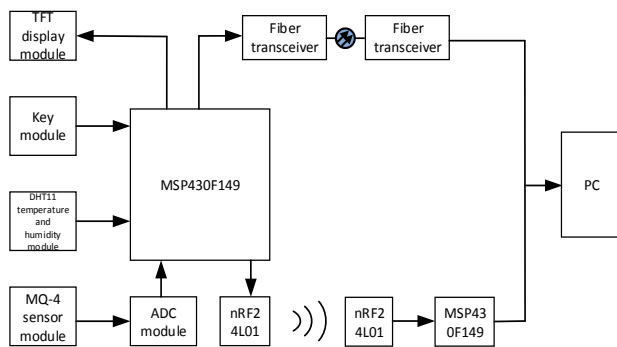


Figure1 System principle block diagram

B Overview of Microprocessor

Adopting the TI's ultralow-power and 16-bit RISC MSP430F149 as the core of system control, of which low-power mode is very suitable for wireless node design. The microprocessor mainly coordinates the operation of the whole system, specifically dealing with the information collected by MQ-4 sensors, conveyed by fiber, and transmitted and received via RF module.

C Overview of Gas Sensors

Concentration of methane in target gas is detected by MQ-4 sensor. MQ-4 has the characteristics of high sensitivity to methane, short response time and stable time response, especially suitable for maintenance free occasions. Furthermore, due to the driving circuit is simple, we can build a simple amplifier circuit to amplify the output voltage signal of the sensor, so that the input can be limited within the voltage range permitted by the AD.

D Overview of Wireless Transmission

The nRF24L01 module is a RF transceiver that operates within the 2.4GHz-2.5GHz ISM band, of which the working mode, communication channel, output power and transmitting speed of the wireless module can be controlled by program. The data communication process between nRF24L01 and MCU is at low speed while high between the wireless transmitter and receiver, which can help reduce the average consumption current of the communication. Thus, this utility model, undoubtedly, is suitable for the design of low power consumption and energy saving.

E Overview of Fiber Optic Transmission

Industrial RS232 optical fiber transceiver has the characteristics of automatic detection of serial data, discrimination control, data transmission direction, zero delay automatic forwarding, good

anti-interference and so forth. The signal should be converted into an optical signal before transmitted by optical fiber at the signal acquisition end, while the reverse process at the receiving end, that is to say, it is necessary to convert the optical signals into electrical signals to be processed by the host computer monitoring system. The fiber optic transceiver commonly used is mainly aimed at building Ethernet networking, as well as realizing the conversion between the Ethernet electrical signal and the Ethernet optical signal which is in accordance with the optical fiber transmission. The industrial RS232 optical fiber transceiver, without protocol conversion, can communicate with the MCU much more freely.

III. THE ANALYSIS OF ERRORS

The error sources of measurement system mainly come from the following aspects: signal interference, environment temperature, humidity and the influence of ADC analog to digital conversion.

--First, signal interference: The coal mine environment is complex, the electromagnetic interference has great influence on the monitoring system and equipment. Electromagnetic interference has 3 basic elements: interference source, receiver sensitive to interference energy, and interference coupling channel. The most common, effective and economical method of suppression is shielding, grounding method is adopted in this system to restrain electromagnetic interference to some extent.

--Second, influence of environmental temperature and humidity: The measurement data of methane sensor can be compensated and corrected while temperature and humidity of the environment in this system measured by DHT11.

--Third, AD conversion: The existence of detection fluctuations, sampling delay, limited resolution, and conversion measurement errors of MSP430F149 built-in 12 bits ADC will produce a non-adjustment error.

IV SYSTEM DATA PROCESSING

A Sensitivity Correction

The sensitivity of the MQ-4 will decrease with the increase of the use time, thus affecting the

measurement accuracy. Therefore, sensitivity correction is needed to reduce the error. Generally, hardware circuit will be used in sensitivity compensation, but the system works in the bad underground environment, using hardware circuit can reduce system stability and add new interference, so we use software methods to modify the sensitivity[5].

A quantitative methane gas is injected into the closed gas chamber and the gas concentration value C is not changed. As time goes on, the measured series of concentration changes as sensor sensitivity decreases. When the gas concentration is C_i , the corresponding sensitivity is S_i . Fitting the relation curve between C_i and S_i , the correction coefficient K is obtained. So the sensitivity of the MQ-4 sensor can be corrected.

If use microcontroller to programming, we must correct the series of values exist in FLASH, so that data will not be lost when power loss, it is very troublesome. If LabVIEW is used to process the received data, the programming work of the lower computer can be greatly reduced.

Joining a check in LabVIEW is very convenient. When the value of S_i is relatively small, it is believed that the data transmitted at this time is not real, which can be used as the self check of the system. The alarm staff will replace the sensor, so that the staff can maintain the system.

B Temperature and Humidity Compensation

MQ-4 is greatly affected by temperature and humidity. The temperature and humidity of the sensor can be compensated by measuring the environment in which the sensor is located, so as to improve the accuracy and accuracy of the measurement system. Through the fuzzy inference to get the correction coefficient for data correction.

When the concentration of CH_4 is collected, the environment temperature of the measuring system is 10-40 °C, and the environmental humidity is 40%-60%RH. Take 25 °C and 50%RH as standard environmental test conditions. Take the temperature(T), humidity(H) and correction factor α as the fields in the fuzzy set. The domain quantization is located at 5 levels. And the fuzzy subsets are {VS, S, N, B, VB}, which represent small, small, normal, large and large. The kernel of fuzzy control is fuzzy rule. At present, it is mainly based on experience to formulate the corresponding rules. Since there is no relevant

empirical formula, the comparative method is adopted in this system, that is, comparing to design the relative levels of the fuzzy sets. The membership function is shown in Figure 2, and the fuzzy inference rules are shown in Table 1.

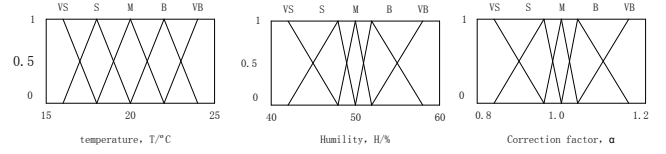


Figure 2 The membership function

Table 1 the fuzzy inference rules

α		H				
		VS	S	N	B	VB
T	VS	VB	VB	B	B	N
	S	VB	VB	B	N	S
	N	B	B	N	S	S
	B	B	N	S	VS	VS
	VB	N	S	S	VS	VS

C Software Filtering

In the measuring process, the interference of the instrument and the environment will cause random error, which affects the measurement accuracy.

In order to eliminate the random error effectively, we can proceed from two aspects.

--First, applying digital filter to the lower computer: The digital filter, which is convenient and flexible in use, has the advantages of high reliability, no impedance matching, non consistency, etc. Since the concentration of methane is not transient, the measured result fluctuates over a certain value over a given period of time. The random error can be filtered by means of filtered extreme value mean filter with low-pass characteristics. The mathematical expression of mean filter is: $\bar{x} = \frac{1}{N} \sum_{i=1}^N x_i$. Take the average value of AD in 10 times as the standard value of the sampling.

--Second, using limiting filtering in LabVIEW: If the data from the two rounds are different, the data of the second time is considered wrong, and the first value is used as the agreed value instead of the second one. This method can not only eliminate the singular data effectively, but also avoid the false alarm generated by the initial action.

D Least square fitting

Since there is no known empirical formula for MQ-4,

it is necessary to measure multiple sets of data, and the fitting curves of the output voltage and the concentration are obtained. The most common fitting method is the least square method.

The fitting formula of least square method is: $y(x) = ax + b$, a is the slope of the fitted line, and b is the offset of the fitted line. There are known m data, respectively $(x_i, y_i), (i = 1, 2, 3, \dots, m)$. Application of least square method, is to enable:

$$\begin{cases} \frac{\partial S}{\partial a} = 2 \sum_{i=1}^m (ax_i + b - y_i)x_i = 0 \\ \frac{\partial S}{\partial b} = 2 \sum_{i=1}^m (ax_i + b - y_i) = 0 \end{cases}$$

Regard a and b as independent variable, S as dependent variable. According to the necessary condition of the extreme value of multivariate function, the value of a and b can be found, and the fitting formula is determined[10]. By means of MATLAB, the least squares polynomial fitting can be performed by using the polyfit and polyval polynomial fitting instructions.

V SYSTEM SOFTWARE DESIGN

The lower computer program is written in IAR Embedded Workbench software. The system software can realize the function design of A/D acquisition, data processing, wireless communication and optical fiber communication. The program flow chart of the sending end is shown in Figure 3. The receiver program flow chart is shown in figure 4.

Fig. 3 flow chart of transmitter

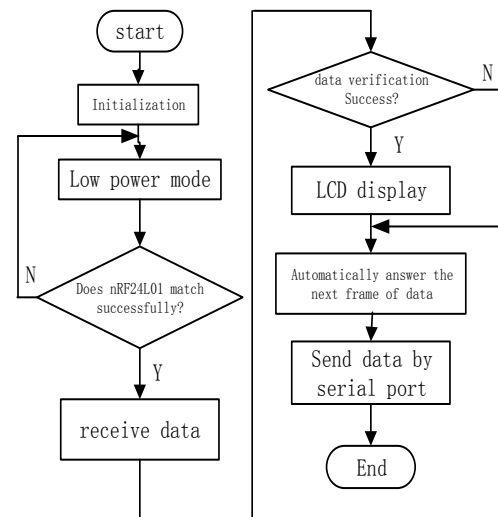
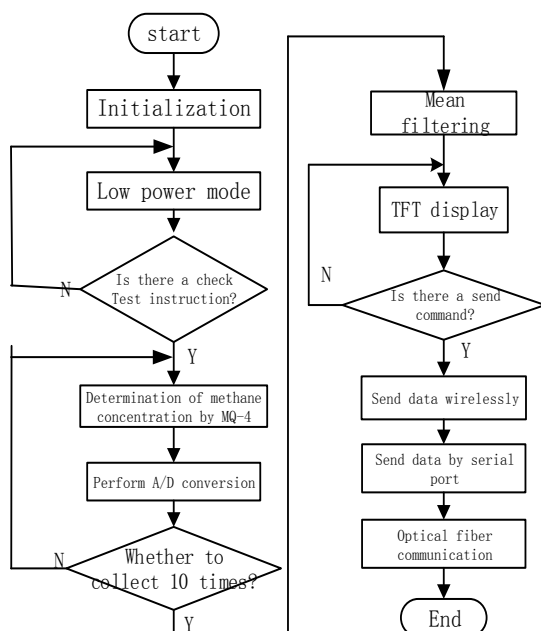


Fig. 4 Flowchart of receiver



The upper computer software uses LabVIEW to design, and uses the VISA function serial port to receive data from the receiving end microcontroller and optical fiber. It can display the trend curve and data of the concentration change in real-time. And the threshold setting function, concentration, overload alarm function. Putting these functions on the host computer is not only convenient for query and adjustment, but also can reduce the workload of the lower computer programming. When the program exits, you can automatically generate documents of date format, with data in time format, and build a data network which is easy to query.

VI SYSTEM TEST

A Communication Distance Test

The communication distance of Nrf24L01 will affect the node density and layout ^[11]. The underground environment is complex, and the effective communication distance of wireless will be greatly reduced, so the communication distance of Nrf24L01 must be tested. The main factors that affect the transmission distance of Nrf24L01 module include data transmission rate, power amplification, chip, external chip and barrier. The system uses Nrf24L01 without power chip and external antenna to test, the data transmission rate is 1Mbps, and the effective transmission distance is tested in open space and room respectively. 1000 data are sent, and the communication distance is tested by studying the packet loss rate. The results show that in a wireless communication environment with open environment, the transmission distance of a block is farther than that of an obstacle. In the open space, the more appropriate transmission distance is 30m, and when there is an obstacle, the appropriate transmission distance is 15m. In actual measurement, can be selected and arranged node distance wireless module according to the need, can use the wireless module with power chip and external antenna in weak signal areas, in order to meet the general requirements of the system and control the cost under the condition of objective.

B Communication Effect Test

In order to reduce the influence of communication distance measurement, wireless communication distance is below 0.1M, the data transmission rate of 1Mbps data transmission, a number of 1000 was conducted to test the effect of optical fiber communication and wireless communication data packet number for wireless communication. Test results show that, compared with optical fiber transmission, wireless transmission data will have some delay and packet loss, and the larger the sampling period, the smaller the delay and the rate of data packet loss will be reduced.

C Sensor Test

At different concentrations of methane gas, the concentration of methane was measured with sensor nodes and standard instruments, respectively. The results show that the error of the measurement system is about 6%, and the concentration of methane in the gas can be measured accurately, as shown in table 2.

Table 2 measurement data of sensors

	MQ-4	Standard	Error (%)
Frequency	measuring gas concentration (%)	instrument for detecting gas concentration (%)	
1	0.35%	0.34%	2.9%
2	0.54%	0.51%	5.9%
3	0.61%	0.62%	1.6%
4	0.71%	0.73%	2.7%
5	1.17%	1.21%	3.3%

VII EPILOGUE

For cable system maintenance limitations of high cost and complicated installation, the system uses nRF24L01 wireless data transmission, not only can collect real-time data information, and when constructing a multi node wireless network is more convenient for the energy saving design of low power consumption. At the same time, it is convenient to adjust the arrangement of the nodes and eliminate the blind areas according to the needs of the topography. Using the system to measure the methane data, the system measurement accuracy is about 6%, to meet the actual demand. This design method also has certain reference significance for other gas detection.

Reference

- [1] Li Xianggui. Design and Realization of infrared methane detector based on MSP430 of Taiyuan University of Technology.
- [2] Pan Jiayu. Design of downhole methane concentration detection system based on wireless sensor networks [D]. Shenyang University of Technology, 2016.
- [3] Zhang Hailan. Research on intelligent control technology of underground mining air pressure system [D]. Nanjing University of Science and Technology, 2013.

- [4] Yu Chunsheng. Combustible gas with the wireless transceiver [D]. detection device design of Yanshan University, 2010.
- [5] Liao Zhiqiang, Chen Dongchun, Liu Shuiwen. Research on electromagnetic interference sources and anti jamming technology in coal mine [J]. automation of industry and mining, 2012, (07): 25-28.
- [6] Yang Rendi, Zhang Yanli. Design of intelligent methane concentration detector [J]. automation of industry and mining, 2009, (11): 69-72.
- [7] GaoFeng, Qu Jianling. A new method for temperature and humidity compensation in gas measurement [J]. instrument technique and sensor, 2000, (08): 9-10+26.
- [8] Cheng Yi Ji. Intelligent instrument [M]. Beijing: China Machine Press, 2009:116-117
- [9] Xie Yuedong. Design of indoor formaldehyde detector based on MSP430 [D]. Taiyuan University of Technology, 2012.
- [10] beam. AI mathematical modeling [M]. Beijing: Metallurgical Industry Press, 2004:79-81
- [11] Li Xuntao. Design of wireless monitoring network for toxic gases [D]. HeFei University of Technology, 2010.

Design of Multi-wavelength Human Muscle Lactic Acid Measuring Instrument

Cai Jing; Xu Zitong; Hu Shiran; Zhu Xiaoxu

(jilin university instrument science and engineering institute, changchun, 130021)

Abstract—Blood lactic acid concentration is important in the evaluation of the exercise intensity and human physiological function. Blood oxygen saturation is one of the important intermediate variables, in order to measure blood lactic acid concentration for a long time continuously, we propose a design based on the separation of ac/dc.[1] By measuring the transmitted pulse wave, the signal is processed by the separation of ac/dc, and the relationship between blood oxygen and lactic acid is based on the function relationship, so as to realize the measurement of non-invasive lactic acid concentration for a long time.

keywords—lactic acid blood oxygen multi wavelength

I INTRODUCTION

IN 1927, the research of Kerridge and Furusawa indicated that the fatigue of muscle contractions produced lactic acid, and the pH of the muscle cells decreased to 6.2-6.3, and the concentration of lactate and pH in the blood decreased synchronously. In a few minutes after the end of mass movement, the lactic acid concentration of the muscles can reach 16 to 18mmol/kg and the muscles are fatigued. The report says increased levels of lactic acid can lead to "acid poisoning" and "muscle fatigue." [2]

Knowing the level of lactate in the body can help us reschedule training programs more scientifically, in case of unnecessary athletic injury.

To sum up, the multi-wavelength human muscle lactic acid measuring instrument is of necessary research significance, it can help the targeted groups to constantly monitor their lactic acid concentration in the body, reducing their health risks.

So we need to know our lactate levels. For normal people, acknowledging the amount of lactate in the body can allow us to control the time and intensity of exercise. For people with paralysis and for athletes, it can help develop a training program.

II BASIC THEORY

A The Principle Of Transmitted Blood Oxygen Saturation Measurement

When the the arterial blood vessels pulsate, the absorption of the blood of the arteries will change accordingly, which is called the pulsating component or the amount of communication. The absorption of

light by other tissues such as skin, muscle, bone and venous blood is constant, known as direct flow. [3]

If you ignore the attenuation caused by scattering and reflection, according to the Lamber—Beer's law, when the arteries don't beat, assume that a monochromatic light whose wavelength is λ , and the

intensity is I_0 , vertically illuminate the human body, the transmitted light intensity through the body is:

$$I_{DC} = I_0 \cdot e^{-\varepsilon_0 C_0 L} \cdot e^{-\varepsilon_{HbO_2} C_{HbO_2} L} \cdot e^{-\varepsilon_{Hb} C_{Hb} L} \quad (1)$$

The total absorptivity of the non-pulsating components and the venous blood in the tissues, the concentration of light absorption material, and the length of the light path are expressed as ε_0 , C_0 and L respectively. The main components of the arterial blood is reduced hemoglobin (Hb) and oxygenated hemoglobin (HbO₂). In (1), ε_{HbO_2} , C_{HbO_2} are respectively absorption coefficient and the concentration of HbO₂, while ε_{Hb} and C_{Hb} are respectively absorption coefficient and the concentration of Hb. When the arterial blood vessels are pulsing, assume that the length of the arterial blood path is increased from L to $L + \Delta L$, and the corresponding transmission intensity is changed from

I_{DC} to $I_{DC} - I_{AC}$, then equation (1) can be written as:

$$I_{DC} - I_{AC} = I_{DC} \cdot e^{-(\varepsilon_{HbO_2} C_{HbO_2} + \varepsilon_{Hb} C_{Hb}) \Delta L} \quad (2)$$

Deform the equation (2) and take the logarithm of e:

$$\ln[(I_{DC} - I_{AC}) / I_{DC}] = -(\varepsilon_{HbO_2} C_{HbO_2} + \varepsilon_{Hb} C_{Hb}) \Delta L \quad (3)$$

Consider that the percentage of the alternating component in transmitted light is much less than 1, so:

$$\ln[(I_{DC} - I_{AC}) / I_{DC}] \approx I_{AC} / I_{DC}$$

Deform the equation (3), so:

$$I_{AC} / I_{DC} = -(\varepsilon_{HbO_2} C_{HbO_2} + \varepsilon_{Hb} C_{Hb}) \Delta L \quad (4)$$

Because the length of the light path is unknown, two beams of different wavelengths are used as the time-sharing incident light. The wavelengths of the two beams are λ_1 and λ_2 respectively.

$$D_{\lambda_1} = I_{AC}^{\lambda_1} / I_{DC}^{\lambda_1}, D_{\lambda_2} = I_{AC}^{\lambda_2} / I_{DC}^{\lambda_2}, \text{ so:}$$

$$\frac{D_{\lambda_1}}{D_{\lambda_2}} = \frac{I_{AC}^{\lambda_1} / I_{DC}^{\lambda_1}}{I_{AC}^{\lambda_2} / I_{DC}^{\lambda_2}} = \frac{\varepsilon_{HbO_2}^{\lambda_1} C_{HbO_2} + \varepsilon_{Hb}^{\lambda_1} C_{Hb}}{\varepsilon_{HbO_2}^{\lambda_2} C_{HbO_2} + \varepsilon_{Hb}^{\lambda_2} C_{Hb}} \quad (5)$$

Take equation (5) into the blood oxygen saturation formula $SpO_2 = C_{HbO_2} / (C_{HbO_2} + C_{Hb})$ and deform it as:

$$SpO_2 = \frac{\varepsilon_{Hb}^{\lambda_2} \cdot (D_{\lambda_1} / D_{\lambda_2}) - \varepsilon_{Hb}^{\lambda_1}}{(\varepsilon_{HbO_2}^{\lambda_1} - \varepsilon_{Hb}^{\lambda_1}) - (\varepsilon_{HbO_2}^{\lambda_2} - \varepsilon_{Hb}^{\lambda_2}) \cdot (D_{\lambda_1} / D_{\lambda_2})} \quad (6)$$

When the wavelength λ_2 is selected at the intersection on the absorption coefficient curve of oxygenated hemoglobin (HbO₂) and the reduced hemoglobin (Hb), $\varepsilon_{HbO_2}^{\lambda_2} = \varepsilon_{Hb}^{\lambda_2}$. The upper deformation is:

$$SpO_2 = \frac{\varepsilon_{Hb}^{\lambda_1}}{(\varepsilon_{Hb}^{\lambda_1} - \varepsilon_{HbO_2}^{\lambda_1})} - \frac{\varepsilon_{Hb}^{\lambda_2}}{(\varepsilon_{Hb}^{\lambda_2} - \varepsilon_{HbO_2}^{\lambda_2})} \cdot \frac{D_{\lambda_1}}{D_{\lambda_2}} \quad (7)$$

In the equation (7), $\varepsilon_{Hb}^{\lambda_1}$, $\varepsilon_{HbO_2}^{\lambda_1}$ and $\varepsilon_{Hb}^{\lambda_2}$ are constant,

$A = \frac{\varepsilon_{Hb}^{\lambda_1}}{(\varepsilon_{Hb}^{\lambda_1} - \varepsilon_{HbO_2}^{\lambda_1})}$, $B = \frac{\varepsilon_{Hb}^{\lambda_2}}{(\varepsilon_{Hb}^{\lambda_2} - \varepsilon_{HbO_2}^{\lambda_2})}$, so the equation is:

$$SpO_2 = A - B \cdot \frac{I_{AC}^{\lambda_1} / I_{DC}^{\lambda_1}}{I_{AC}^{\lambda_2} / I_{DC}^{\lambda_2}} \quad (8)$$

A and B can be determined in the experiment.

B Ac - Dc separation technology

Receiving part receives the photoelectric pulse wave signal for ac/dc mixed signals, as shown in Fig.1., the communication component accounts for a small part of the mixed signal amplitude, in order to effectively measure the received ac component and dc component, we need separate the signals.

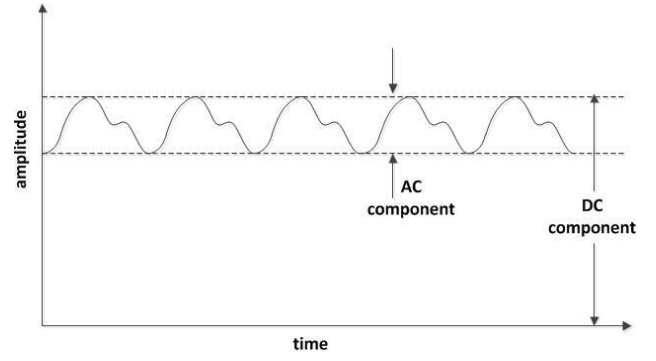


Fig.1 Pulse wave ac/dc mixed signal

Normal human pulse signal mainly concentrated in the vicinity of 1 Hz. In order to keep the instrument's versatility, select 0.5 Hz ~ 20 Hz for measuring range. Design a 20 Hz active second-order low-pass filter and 0.5 Hz active second-order high-pass filter and use A/D to collect the signal processed by the low-pass filter. The signal approximately is dc, after passing the high-pass filter, the remaining ac signal will be amplified and then sampled by the A/D, so we can get the ac/dc signal separation. The block diagram is shown below.

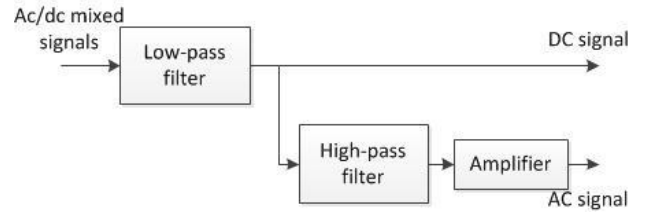


Fig.2 Block diagram of ac/dc signal separation

Select LM324 to form filters and amplifiers and set low-pass filter parameters: $R = 1.6K\Omega$, $C = 5\mu F$, as shown in Fig.3.. The transfer function of the second-order low-pass filter is:

$$A(s) = \frac{A_{vf}}{1 + (3 - A_{vf})sCR + (sCR)^2},$$

$$A_{vf} = 1 + R_2 / R_1 = 2$$

If $R_1 = R_2 = R$, $C_1 = C_2 = C$, The cutoff frequency is

$$f_c = 1 / 2\pi RC \approx 20Hz.$$

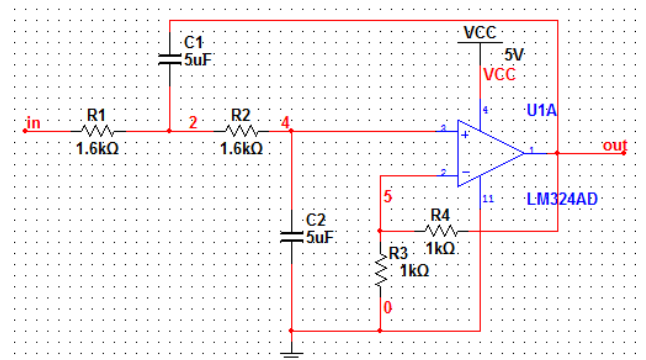


Fig.3 Active second-order low-pass filter

Set the high-pass filter parameters: $R = 30K\Omega$, $C = 10\mu F$, as shown in Fig.4.. The transfer function of the second-order high-pass filter is:

$$A(s) = \frac{A_v s^2}{s^2 + \omega_c / Q + \omega_c^2},$$

$$A_v = 1 + R_2 / R_1 = 2$$

If $R_1 = R_2 = R$, $C_1 = C_2 = C$, The cutoff frequency is

$$f_c = 1 / 2\pi RC \approx 0.5Hz.$$

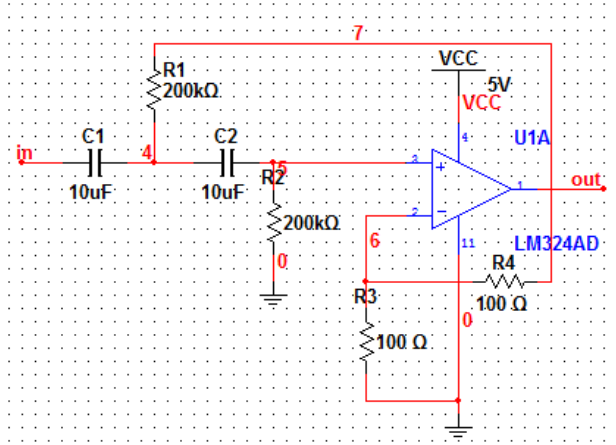


Fig.4 Active second-order high-pass filter

By amplifying the ac signal with the amplifier, the ac/dc signal can be collected by AD to realize the separation of mixed signals.

III IMPLEMENTATION OF THE SYSTEM

A The hardware design

The overall block diagram of the system is shown in figure 5, which consists of photoelectric probe, signal processing module and data acquisition module. The photoelectric probe includes 660nm, 940nm led, triode and photoelectric receiving tube; The signal processing part includes the high-pass filter and the low-pass filter, the amplifier; The data acquisition part includes A/D conversion, bluetooth communication and the microprocessor.

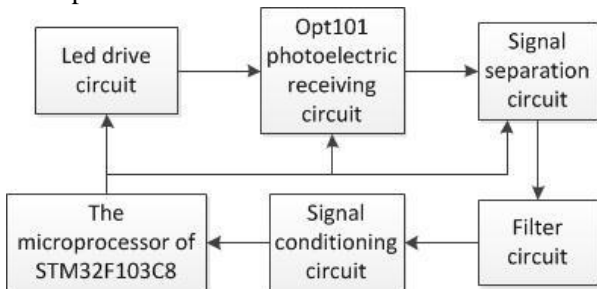


Fig.5 Block diagram of the system

B The system algorithm and the software design

By controlling the two wavelength cycles, the corresponding voltage amplitude of the two

wavelengths of light are measured and the corresponding parameters are obtained. Android phones can receive the parameters of lactic acid and blood oxygen real time with bluetooth.

IV RESULTS

Through the test results of the interviewees, the least squares fitting data was carried out through MATLAB software, and finally the relationship of lactic acid and blood oxygen was obtained as:

$$\text{Lactic acid value} = 8 \times 10^{55} \times \text{blood oxygen value}^{-28} - 0.85 \quad (9)$$

V EPILOGUE

The lactic acid measurement system based on the separation of ac/dc uses transmitted pulse wave and the method of separation of ac/dc measurement of blood oxygen saturation. The corresponding relation with the concentration of lactic acid can be obtained by the experimental method. And we can acknowledge the amount of the lactic acid concentration of the person.

Thus, the concentration of lactic acid and blood oxygen can be measured without painful tests, which greatly reduces the harm to human beings and improves safety and portability.

References

- [1] Ying Qin, Jing Zhang, Jing Cai, Qiang Dai. Design of the Reflective Blood Oxygen Saturation Measurement System Based on the Separation of AC and DC [J]. Chinese Journal of Sensors and Actuators, 2015, 28 (06) : 933-937. [2017-08-02].
- [2] Guoqiang Xiao. Reinterprets the role of lactic acid in muscle fatigue [J]. China Sport Science, 2007, (9) : 92-96. [2017-09-29]. DOI: 10.16469 / j.css 2007.09.011
- [3] Guodong Xu, Fang Liu, Hui Gong, Xinfu Ge, Qingming Luo. the Relationship between Skeletal Muscle Tissue Blood Oxygen and Blood Lactate Concentration during Exercise [J]. Aerospace Medicine and Medical Engineering, 2003, (01) : 41-43. [2017-08-02]. DOI:10.16289 / j.c.nki. 1002-0837.2003.01.010
- [4] Xinzhong Yan Jing Yang, Lue Guo. The Human Body Blood Oxygen Saturation Monitoring Method Research [J]. Journal of Medical Equipment, 2005, (12) : 4-7. [2017-08-02].

- [5] Hongjian Zhou, Guiyan Cai. Measurement algorithm and application of noninvasive oxygen saturation in three wavelengths [J]. Journal of Chinese Biomedical Engineering, 2007, (05) : 68-683 + 689. [2017-08-02].
- [6] Zhengjian Lin. The Development of Three Wavelengths of Blood Oxygen Saturation Measuring Instrument [D]. University of electronic science and technology, 2005.
- [7] Xiuzhang Wang, Shengquan Chen. Research on the Detection Method of Pulse Blood Oxygen Saturation. Chinese journal of medical physics.

Research on Android-based wearable body temperature measuring equipment

Cai Jing; Liu Huaqing; Liu Weifeng; Sun Mengyan

(College of Instrument Science and Electrical Engineering, Jilin University, Changchun 130021, China)

Abstract—Body temperature is a familiar Physiological indicators, being in a fever is the behavior to fight against the disease. Babys are weak and with complicate conditions. It is important to measure and observe the variety of temperature. However, the traditional measurements have low speed, low accuracy and disability to monitor. If body temperature curve can be displayed, it would contribute to observe the babies' condition. In order to solve the disadvantages of traditional temperature measurement, including slow measurement, disability of monitoring and other issues. Try to use a high small size and high sensitivity temperature sensor to collect temperature, a microprocessor for data processing, and bluetooth device for transmission, Android mobile platform with software to achieve the temperature data display, curve drawing and fever alarm.

Key words—Body temperature monitoring Wearable medical equipment Android developing

I INTRODUCTION

REGULAR measurement of human body temperature changes is a common medical examination, at present, the body temperature detection equipment is basically divided into contact and non-contact categories. Mercury thermometers and alcohol thermometers are typical contact devices. They measures according to the principle of thermal expansion, but the measurement speed is slow, and it is inconvenient to hold. Infrared thermometer is a typical non-contact device, it measures fast, but lacks stability[1]. The traditional temperature measurement methods can not complete the automatic continuous measurement, so these devices have some shortcomings in medical field. Wearable body temperature monitoring equipment solves the above problems. It uses high sensitivity, small size of the temperature sensor, Bluetooth data transmission module and Android platform to display and alarm. It ensures the high precision measurement of body temperature, and can also achieve the baby temperature real-time monitoring, draw the body temperature curve and achieve the alarm function.

II HARDWARE SYSTEM DESIGN

A System Overall Design

The overall design is divided into five parts, The

overall system block diagram is shown in Figure 1. First LMT70 temperature sensor collects temperature signal, get analog output, then uses an analog-to-digital converter to convert the output signal. The microprocessor performs data processing, sends the integrated data to the Bluetooth transmission module, eventually the data sent to andriod mobile devices. We compile an andriod software to display the body temperature, draw the temperature curve and achieve the alarm function[2].

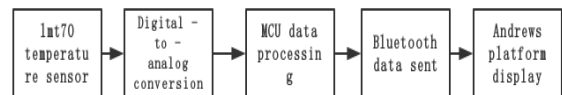


Fig .1 System block diagram

B Sensor Selection

In order to meet high accuracy requirements, we use Texas Instruments' LMT70. Its internal principle is shown in Figure 2. The LMT70 is an ultra-small, high-precision, low-power complementary metal-oxide-semiconductor (CMOS) analog temperature sensor with output enable pins.

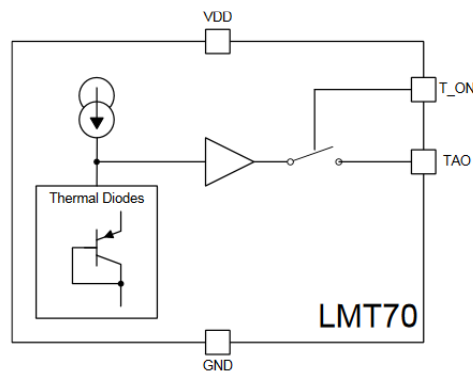


Fig. 2 LMT70 internal schematic diagram

The sensor has a precision of $0.1\text{ }^{\circ}\text{C}$ and is even up to $0.05\text{ }^{\circ}\text{C}$ in the human body temperature range. Its pin assignment is simple: VCC, GND, T-ON, TAO.

C Microprocessors and analog - to - digital converters

According to the low power requirements of the system, we need to choose low-power analog-to-digital converters and low-power microprocessors. MSP430 series of microprocessors is very suitable, and the internal 12-bit A / D just meets the conversion requirements. If we use MSP430 internal AD (reference voltage 3.3V):

$$1\text{LSB} = 3.3 / 4096 \approx 0.805\text{ mV}.$$

If we use MSP430 internal AD (reference voltage 2.5V):

$$1\text{LSB} = 2.5 / 4096 \approx 0.611\text{ mV}.$$

If we use MSP430 internal AD (reference voltage 1.5V):

$$1\text{LSB} = 1.5 / 4096 \approx 0.366\text{ mV}.$$

Considering the choice of 1.5V reference voltage, it can meet the conversion requirements, to achieve the required accuracy of the system.

D Bluetooth Wireless Module

The transmission temperature requires the use of the Bluetooth protocol module. In order to achieve low power consumption. We use the Bluetooth 4.0 chip CC2541. The schematic diagram of the chip is shown in Figure 3. The chip's power consumption is more than three times smaller than that of a conventional bluetooth 2.0 chip, and support sleep and wake up, transmission power has also greatly improved. The circuit diagram is shown in Figure 3.

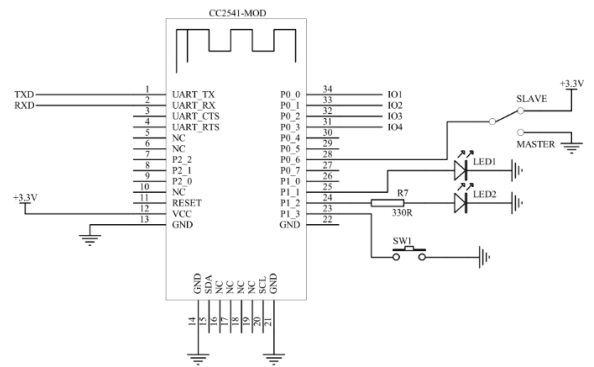


Fig.3 Schematic diagram of the CC2541 module

Use the module before the AT mode settings, then we can receive and send data to achieve the remote transmission of data.

III MICROPROCESSOR SOFTWARE DESIGN

A Overall microprocessor software design

The overall design flow of the software is shown in Fig.4. [3]Microprocessor with the sensor, Bluetooth module associated. First, the entire system is initialized, control the sensor for temperature acquisition, use the internal 12-bit ADC for analog-to-digital conversion, after the conversion, through the microprocessor serial port, communicate with the Bluetooth module, send the processed data to the Bluetooth module. Android equipment is in accordance with the communication protocol to receive body temperature data, for database storage, temperature playback and curve drawing, and determine whether the temperature exceeds the limit for alarm.

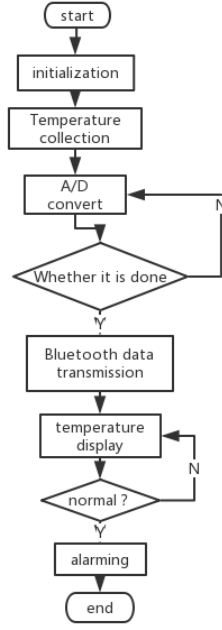


Fig.4 Software flow chart

B Temperature data processing conversion

Through the sensor to measure the temperature, we can get a voltage output, and then through the MSP430 internal ADC conversion, we can get the voltage quantization gradient value. To obtain a true voltage, the voltage quantization gradient value needs to be converted, use formula (1) :

$$V_S = \frac{V_{ref}}{2^{12}} \times N_{adc} \quad (1)$$

The V_{ref} is a 1.5V reference voltage and the N_{adc} can be read from register ADC12MEM0 in MSP430. According to the official output characteristics of the sensor can be seen; the sensor has a super-linear characteristics, and the output temperature have strong anti-interference. We can use the three times fits in the human body temperature range.

Three times fits require the use of a three-dimensional function of the dollar. The official handbook gives three times the required four coefficients, as shown in Table 1. Three times fit in the human body temperature range fitting accuracy is the highest, as shown in Figure 5, but the drawback is that the amount of computation is large and takes more time.

$$T_M = a (V_{TAO})^3 + b (V_{TAO})^2 + c(V_{TAO}) + d \quad (2)$$

TABLE 1 Three - time fitting parameters

	Best fit for -10°C to 110°C
a	-1.809628E-09
b	-3.325395E-06
c	-1.814103E-01
d	2.055894E+02

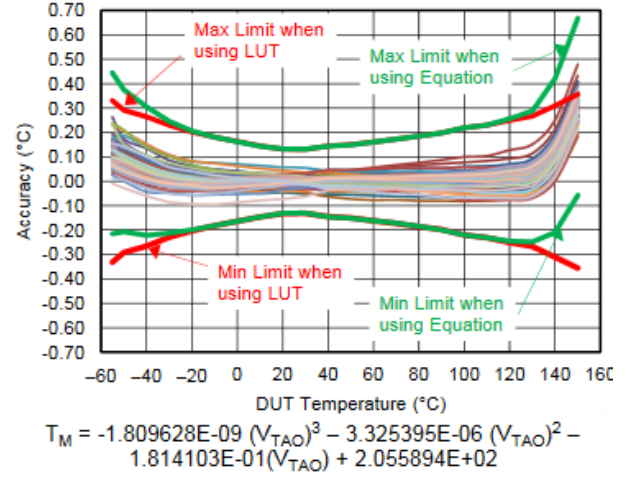


Fig.5 Three-fit renderings

C Calibration of temperature values

In accordance with the fitting method of the temperature, compared with the standard $\pm 0.1^\circ\text{C}$ mercury thermometer, there is a constant deviation. So it needs to be constant voltage compensation. This is mainly due to the connection of the hardware circuit caused by the deviation, has been calculated, the measured temperature is 1.4°C lower than the actual temperature, this requires a voltage reduction of 7mV.

D Mean Filtering Algorithm

ADC as part of the digital circuit, ADC open and turn off the time, there will be data leakage collection and disorder, resulting in the measured voltage quantization value is too large or too small, therefore, it is necessary to perform a median filtering algorithm for the voltage data over a period of time. In the program, defines a 900-bit long integer array, after the array has collected over 900 sets of voltage data, sort it by bubbling. The voltage values in the array are arranged from low to high, and first remove 300 sets of minimum, then remove the 300 maximum, take the middle 300 groups to find the average. In this way, the resulting voltage value tends to be stabilized by extreme values and the effect of noise is small.

$$N_{aver} = \sum_{i=a}^b X_i \quad (3)$$

As shown in Equation 3, sort the data first, and set

a=300,b=600 to get results.

IV ANDROID DEVICE SOFTWARE DESIGN

Android software block diagram is shown in Figure 6. The smart body temperature stickers is attached to the android phone as the host computer, the user observes the body temperature data through the Android program and receives the alarm by phone.

The Android software program is an important part of the intelligent body temperature system. Ontology temperature design and installation procedures in the eclipse software environment using java language programming. Using SDK tools and real machine debugging.

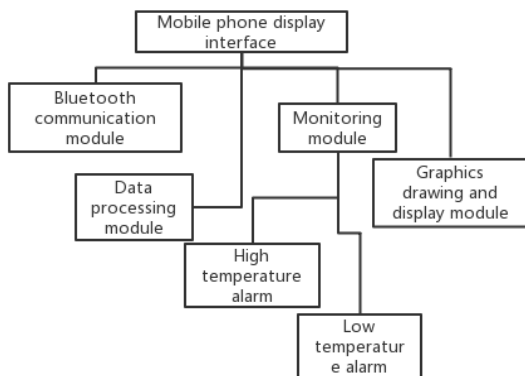


Fig. 6 Andriod software structure diagram

Android software program design need to consider the integration of the entire system functions. So the Android program contains the Bluetooth communication module, data processing module, monitoring module and graphics rendering and display module four main modules. The Bluetooth communication module is responsible for searching for the Bluetooth device of the microprocessor and establishing a Bluetooth data communication link between the phone and the microprocessor. When the hardware is found in the Bluetooth device and the connection is established, the mobile station sends the start bit "a" to the microprocessor and receives the end bit "b" and the body temperature data returned by the microprocessor.

Data processing module will first use the Android mobile phone system storage to establish sql database, The data received by the Bluetooth communication module is then processed, the end bit is identified and

the valid temperature data is written to the database.

The monitoring module is responsible for judging the latest temperature data received by Bluetooth communication, if the received data beyond the body temperature range, it will be issued for abnormal temperature alarm.

The graphic drawing and display module will collect the temperature data stored in the database, use the body temperature data as the vertical axis, add the time axis as the horizontal axis drawn into a line graph, show changes in body temperature clearly.

V IMPLEMENTATION AND ANALYSIS

A Hardware equipment temperature test

Hardware in kind as shown in Figure 7. On the basis of the above theory, completed the production of hardware equipment and improve the optimization, in the premise of measuring the temperature function, ensured a low power consumption and small size of the design concept, while making the measurement mode more convenient and fast.

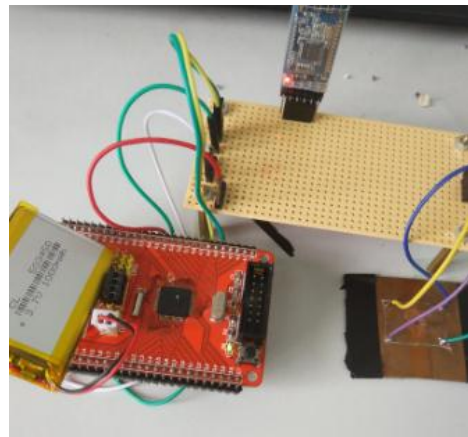


Fig.7 The picture of hardware

In order to test the work of the hardware system, do the following experiment: Heating test (the results shown in Table 2), Cooling test (the results shown in Table 3), Transmission distance test (the results shown in Table 4).

Use a heating device to heat the ± 0.1 °C mercury thermometer and the body temperature patch, observing the difference between the current temperature and the measured temperature and the output voltage.

TABLE2 Heating measurement results

temperature °C	Voltage V	Measure temperatur°C
30.0	950.2	30.0
31.0	944.7	31.0
32.0	939.5	32.0
33.0	934.4	33.0
34.0	929.3	33.9
35.0	924.1	35.0
36.0	918.9	36.0
37.0	913.7	37.0
38.0	903.4	37.9
39.0	898.1	39.0
40.0	898.1	40.0

TABLE3 Cooling measurement results

temperature °C	Voltage V	Measure temperatu°C
40.0	898.1	40.0
39.0	898.1	39.0
38.0	903.3	38.0
37.0	913.7	37.0
36.0	918.9	36.0
35.0	924.0	35.1
34.0	929.2	34.0
33.0	934.4	33.0
32.0	939.5	32.0
31.0	944.7	31.0
30.0	950.2	30.0

TABLE 4 Distance test table

voltage V	distance m
3.3	6.2
5.0	9.8

B Android platform display

Through the Bluetooth connection to the microprocessor, open the Android software, the Android software display interface shown in Figure 8. Where "状态" indicates the Bluetooth connection status of the handset and the microprocessor, "温度" shows the current real body temperature value, and the temperature value is refreshed every ten seconds. When abnormal temperature is detected, the program will control the phone vibration alarm.[4]

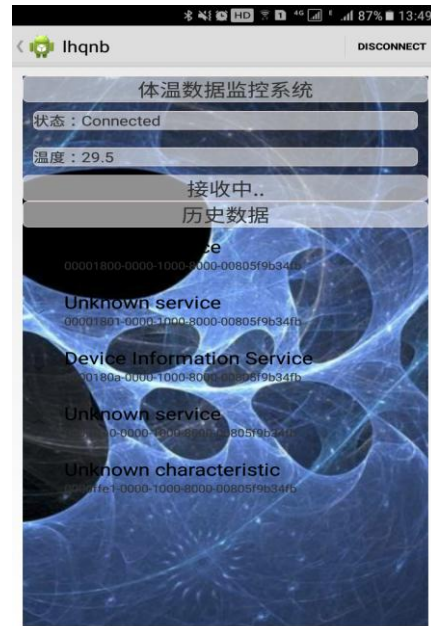


Fig.8 Andriod program interface

Click "历史记录" on the Android program interface to display the temperature chart of the body temperature data in the database, as shown in Figure 9. The latest body temperature data will be refreshed on the left, where the ordinate is ten times the value of the body temperature and the abscissa is the time of the corresponding handset system when the temperature is written to the database.

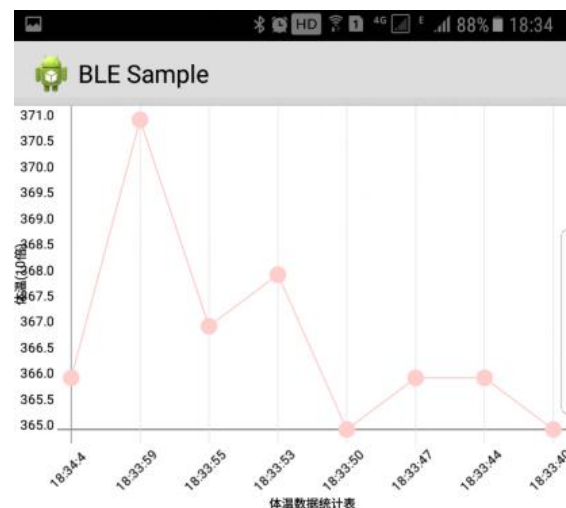


Fig.9 Andriod interface icon

VI CONCLUSION

By designing the hardware of the wearable body temperature stickers, with Andrews platform-assisted measurement. We achieve the baby body temperature measurement which is high-precision real-time monitoring. Equipment meets the accuracy

requirements, low power requirements, volume requirements and convenience requirements.

Traditional methods measure body temperature, we need someone to keep in real time, the child and the guardian can not get a good rest. Wearable body temperature testing equipment for both saves a lot of labor, and provides a more detailed, accurate temperature data. This is a great help to medical care, condition detection, state judgment.

At present, most of the domestic hospital temperature measurement methods still remain in the mercury thermometer stage, The body temperature was monitored by manual measurement and recording of data, the temperature information we can get is very limited, and it do not have the potential to form an automated monitoring system. Similar temperature monitoring products have appeared abroad, but its use is far from universal and the price is very expensive. Therefore, developing wearable temperature monitoring equipment and putting it into the market will be of great help to the medical field and people's life.

References

- [1] Zhang Yongliang, Yong Haiyu, Zhang Fuyu et al. Research and application of high precision digital temperature device instead of mercury thermometer [J]. Mechanical Research and Application, 2017, (01): 124-126.
- [2] Deng Chi. Wearable electronic thermometer research and hardware and software design [D]. China University of Science and Technology, 2016.
- [3] Ttao Yi-yang. Study on Service Design of Wear-type Temperature Monitoring Equipment [D]. Zhejiang University, 2015.
- [4] Comparison of body temperature in rats by non-contact infrared thermometer and glass thermometer [J]. Chinese Journal of Medical Science, 2010, (13): 213-214.

Design of head mounted gaze tracking control system based on embedded system

Yuan Jinfeng; Chen Guanyu; Sun Pengyong

(Jilin university instrument science and engineering institute, changchun, 130021)

Abstract—The existing eye tracking products rely on computer processing, the cost is expensive and most of them only realize virtual reality interaction. In response to this phenomenon, a head mounted eye tracking control system based on embedded system is designed. It takes actual moving object as control object and human eye as control source. Then it uses image processing algorithm and coordinate mapping model to realize the eye tracking technology. Through the optimization and synthesis of centroid detection and ellipse fitting algorithm, the accuracy of locating the pupil center of the system is less than 1.4 degree. By using the least square method to coordinate the line of sight space, this system can finally control moving parts to the specified points. Experimental results show that, the fixed point error of the controlled object is less than 5cm when the human eye is within 2 m of the controlled object, the system response time is less than 0.3 s, fully meet the user's daily operational requirements.

keywords—Eye tracking; pupil location; least square method; space coordinate transformation; embedded

I INTRODUCTION

WITH the development of computer vision technology, the use of gaze tracking technology to transmit information through human eyes has become a hot research topic both at home and abroad. Gaze tracking is a technique that uses the mechanical, electronic, optical and other detection methods to obtain the current "gaze direction" of the user[1-2]. Abroad, EyeTrackShop is committed to the development of gaze tracking technology. Google uses eye tracking technology to ensure that users can see the ads they put on the line. At the Freescale Technology Forum, Freescale Carle CEO shows people the advanced technology of "track where to look"[3]. As a Tobii official authorized agent, Beijing Jin FA Polytron Technologies Inc launched a series of eye movement instruments. Products at this stage are always in the forefront of high-tech products, and failed to popularize people's daily life. On the one hand, the processing of the vision information relies on the computer, and has not yet completely independent, limiting the user's mobile space. On the other hand, product functionality has always been limited to human computer interaction, such as cursor movement[4], reading, turning pages, typing, games, etc., but most of the physical control of life has rarely been tapped.

In this paper, we mainly study the vision tracking technology, and use the embedded processor and infrared camera to design a headed eye tracking

control system. In order to verify the feasibility of the intelligent car or home robot motion control system, using the 50 cm² square moving platform as the operation target, we realized this function by simulation, successfully making the vision tracking system independent, which expands the application scope of the entity and improves the performance to price ratio.

II DESIGN OF SYSTEM HARDWARE

A Design of head on line of sight tracking device

The hardware circuit mainly includes the Freescale K60 minimum system, Mt9v032 camera, TFT display screen, keyboard, Bluetooth and infrared light circuit. Mt9v032 digital image sensor is qualified with global shutter, high dynamic performance and the advantages of automatic exposure, suitable for car, wearing system such as in a place of great unrest, and effectively capture the high-speed moving objects. To the Kinetis K60 series MCU, the lowest operating voltage is up to 1.71V, using the ARM Cortex-M4 kernel, the performance can reach 1.25 Dhrystone MIPS/MHz, the maxed working frequency 180 MHz and low power consumption characteristics is suitable for replacing computer image processing on the portable system.

Through the system the camera is put in front of the left eye, the installation of infrared light is used to emitting tube light to the human eye. Through the 8 bit data bus and DMA mode, the human eye grayscale data K60 collected is quickly stored in the RAM. Each

time the field interrupt signal is given, K60 will implement image array processing. The keyboard circuit selects access to the initialization state or working state. HC-05 Bluetooth is connected to MCU by serial communication. The display screen is used to display the pupil location image so that the user can correct it himself. The hardware circuit diagram of the system is shown in figure 1.

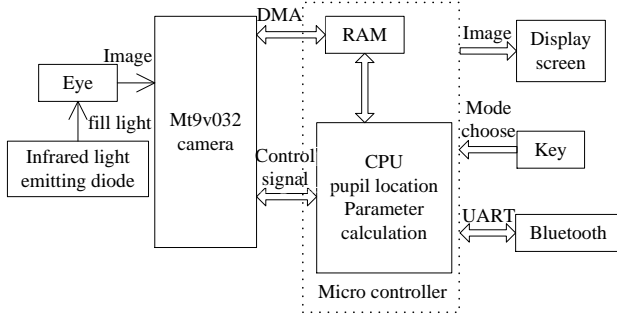


Fig. 1 Magnetization as a function of applied field.

B Design of controlled motion platform

The motion platform is designed to measure the feasibility and accuracy of the head mounted eye tracking system, the most important is the platform and eye tracking system to achieve the agreement of receiving instructions and run according to the requirement. The platform design mainly includes: STM32 controller, Bluetooth, L298N motor drive circuit, infrared tube detection circuit. The use of DC deceleration encoding moto can achieve the precise movement of the slide rail. Each cell of the platform is 1 cm, and the intersection of the X axis and the Y axis is the fixation point of the sight. The hardware object and the actual operation are shown in Figure 2.

III DESIGN OF SIGHT TRACKING ALGORITHM

A Accurate positioning of human eye and pupil

1 Human eye image preprocessing

In order to improve the efficiency of the algorithm and make the system have fast response ability, the narrow vision infrared camera is chosen to be 3 cm away from the human eye, and only the gray information of the eye image is collected. The gray value is 0~255. 8 infrared diodes are used to make light compensation around the camera, which is easy to separate the pupil and the corner of the eye. Median filtering is used to denoise the image.

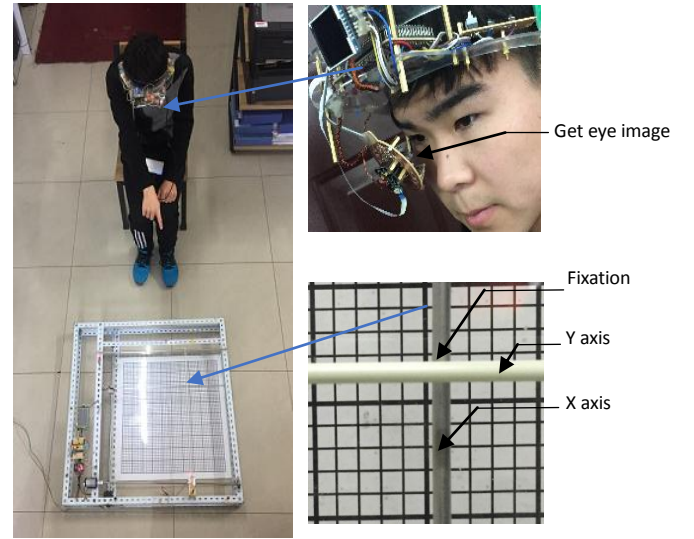


Fig. 2 Operation chart of gaze tracking system

2 Adaptive threshold for image binaryzation

The Otsu method is an adaptive threshold determining method, which can segment images more clearly in different light environments. In order to avoid the disadvantages of embedded processor algorithm efficiency, only to get the pixel gray image in the value of the successive traversal value, can make the traversal times dropped, this is a kind of improved Otsu method. In order to improve the efficiency further, the linear gray level transformation of the image is carried out to enlarge the difference between the gray values, and then the threshold is determined by the improved Otsu method. Let i be the roll of image pixels, where the column is j , a pixel value is $image[i][j]$, after linear gray level transformation the value is $imageI[i][j]$, enhancement ratio is A , there are:

$$imageI[i][j] = \begin{cases} A \times image[i][j], & image[i][j] < \frac{255}{A} \\ 255, & image[i][j] \geq \frac{255}{A} \end{cases} \quad (1)$$

After verification, $A=3\sim5$ is more appropriate. This method can remove most of the larger gray values, and can further reduce the maximum number of traversal times between the class variance methods. According to the enhancement factor A , the efficiency of the algorithm will be increased by 3~5 times.

3 Removal of small areas of two valued images

The eyelashes and corners are close to the pupil, there are still a few stray areas in the image, and in the system dynamic test, the spurious region cannot be eliminated by binaryzation. Comparing shows that the pupil is the largest area of the image. In the computer software, MATLAB or OpenCV with retention of library function is easy to solve this problem, the embedded processor baremetal procedures generally

do not have this function, so a general algorithm for embedded image processing is designed to remove the small black area surrounding the pupil, retain the largest pupil area. The thought is:

- (1) Filling the independent white dots in the image. If the center pixel is 255, and the number of '0' pixels in the neighborhood is over 4, the central pixel is changed to 0, otherwise 255.
- (2) Doing image scanning roll by roll, the information of each line of each '0' pixel is included in the array a [i, cols, cole], where i is the number of rows, cols is the start column of the segment pixel, cole is the end column of the segment pixel.
- (3) Using a [i, cols, cole] to judge whether the adjacent two rows of pixels are connected in the binaryzation image. Set the first row of pixel segments with information a [i, cols1, cole1], and the second row of pixel segments with information a [i+1, cols2, cole2]. If $cols1 < cole2 + 2$ or $cols2 < cole1 - 2$, the adjacent two row pixel segments are of the same class. Rank it in the array a [i, cols, Cole, n], and n is the class of that segment pixel.
- (4) Using a[i, cols, Cole, n], determine whether the two segments separated from the same line are of the same class. If the two segment pixels are connected by the following row of pixel segments, the two segment pixels are of the same class.
- (5) After the above steps are processed, each black area in the image is divided into different classes, the number of pixels of each class is calculated, the region corresponding to the largest class is retained, and the rest pixels are white.

The algorithm is universal and can be ported to other 32 bit embedded processors. The effect diagram obtained by the improved Otsu method is shown in Figure 3, where the black pupil in the (d) diagram represents the extracted pupil. The results show that the removal of small area algorithm has a good effect.

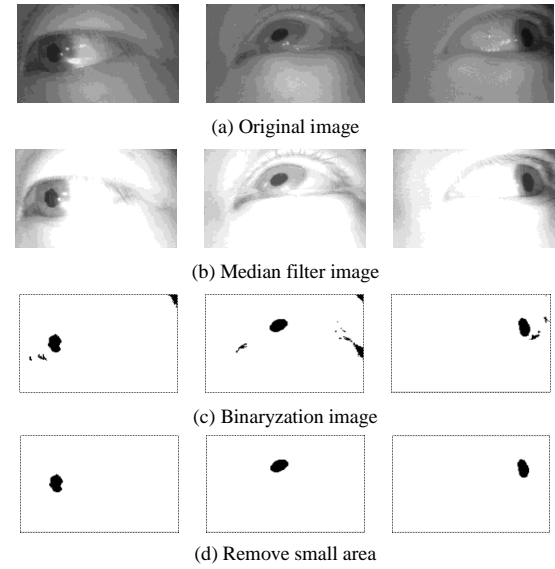


Fig. 3 Improved Otsu method image

4 Positioning pupil

After removing the small area only pupil area is approximately elliptic, the accurate algorithm determining the regional center is Hough transform [7-9] and ellipse fitting algorithm[10] at present, but a large amount of data need to be processed. Taking into account the embedded processor speed, the centroid detection algorithm to determine the geometric center of the ellipse, has great advantages in time. Let the pupil center be (x, y), the abscissa of the pixels in the pupil is x_i , the ordinate is y_j , and the number of pupil pixels is N, then there is:

$$x = \frac{\sum_{i=0}^N x_i}{N}, y = \frac{\sum_{j=0}^N y_j}{N} \quad (2)$$

The effect of locating the pupil after the center of the pupil is shown in Figure 4. The center of the cross in the picture is the center of the pupil.

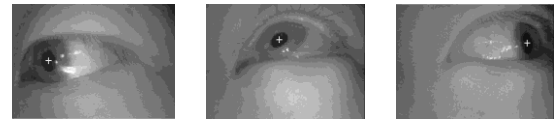


Fig. 4 Final pupil location image

B Line of sight coordinate and platform coordinate mapping

The method of mapping includes ellipse normal direction method [11], pupil corneal reflection method [11-12] and two-dimensional space coordinate fitting [13-14]. The normal direction of ellipse method needs high resolution image to increase the amount of data; Contrasting pupil cornea reflection method and two-dimensional space coordinate fitting, we select two-dimensional space coordinate fitting method of which data processing quantity is small and the efficiency of the algorithm is high.

The eyes is a sphere, and the platform on the ground is plane, the platform and the eyes have complex spatial relationship. By observing the horizontal movement of the line of sight on the platform, it is found that the pupil not only moves laterally, but also moves vertically. After collecting 50 pairs of coordinate (X_n, Y_n) and (x_n, y_n) , through the equal precision linear parameter least square algorithm, it is found that the following coordinate relation exists between the line of sight coordinate and the platform space coordinate:

$$X = a_0x + b_0y + c_0, Y = a_1x + b_1y + c_1 \quad (3)$$

The solution is to initialize the system before each user uses it to determine the coefficients of formula (3). The characteristics points selected in the service platform is the 9 black mark in the graph (5), and the error equation (4) is established.

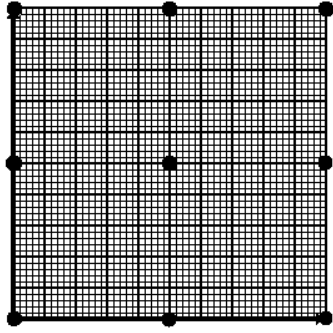


Fig. 4 Initial alignment point of moving platform

$$\left. \begin{aligned} v_1 &= X_1 - (a_{01}x_1 + b_{01}y_1 + c_{01}) \\ v_2 &= X_2 - (a_{02}x_2 + b_{02}y_2 + c_{02}) \\ &\vdots \\ v_n &= X_n - (a_{0n}x_n + b_{0n}y_n + c_{0n}) \end{aligned} \right\} \quad (4)$$

The least squares condition is the formula (5):

$$\sum_{i=1}^n v_i^2 = v_1^2 + v_2^2 + \dots + v_n^2 = \min \quad (5)$$

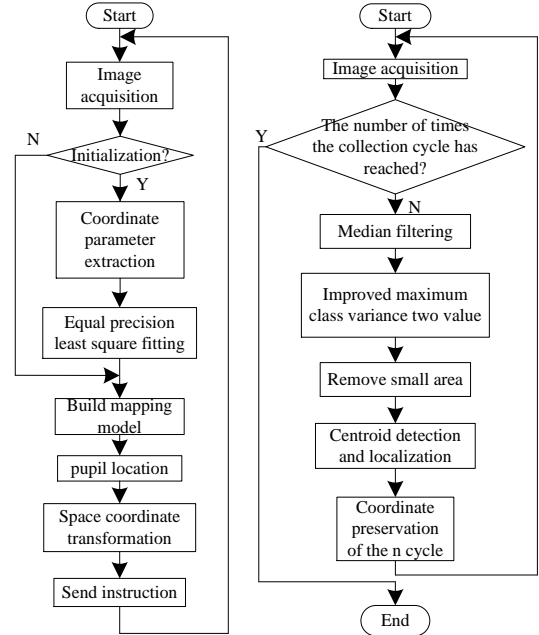
By solving the corresponding normal equation, we can obtain the best estimate of the coefficients of formula (3), and then establish the coordinate space mapping model.

IV SYSTEM SOFTWARE DESIGN

When user wear the system, select the initialization mode, observe the nine point of the field, through the K60 controller to deal with the eye region image data, and record the pupil coordinate parameter calculation. Select the working mode, the system based on the line of sight gaze direction of the controlled object to send control commands, and then the processing of the mark image was displayed on the screen to facilitate user

calibration. The system software flow chart is shown in Figure 6, in which (a) is the overall process design of the system, and (b) is the sub process design of the initialization process.

The motion platform operation process: Bluetooth receive real-time data, STM32 controller decode the data, get the gaze coordinates on the motion platform, thereby driving motor make the slider guide screw to the calibration point, and closed-loop control with encoder, to achieve the purpose of accuracy control.



(a) Overall flow chart

(b) Initialization process flowchart

Fig. 6 System software flow chart

V TEST AND ANALYSIS

The frequency of K60 controller is 100 MHz. The tests are based on platform motion accuracy and system response time. The system response time is the time needed for the user to change the view when the platform starts to move. The simulation time is timed by the MDK software, which can test the speed of the algorithm.

When testing, the distance D of the same user's eyes to the platform is 2 m, random gaze any point of the platform. Figure 7 dots are the specified point of view, cross points are platform movement. Then it can see that from the table 1 the error of fixed-point radius Δr are within 5 cm, which corresponds to the angle error of pupil localization, mathematical approximation can be calculated by formula (6):

$$D \times \sin \theta = \Delta r \quad (6)$$

It solved that $\theta=1.4^\circ$.

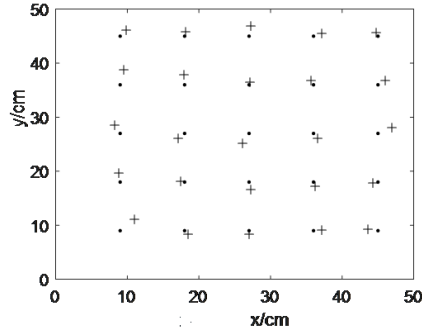


Fig. 7 Line of sight tracking control results

Table.1 Quantitative results for the same user at the same distance

Test times	1	2	3	4	5	6
Error radius /cm	3.64	2.82	4.58	3.79	2.21	4.06
response time /s	0.263	0.247	0.256	0.288	0.275	0.251
Test times	7	8	9	10	11	12
Error radius /cm	4.02	3.35	4.43	2.98	3.26	4.67
response time /s	0.289	0.268	0.274	0.272	0.264	0.290
Test times	13	14	15	16	17	18
Error radius /cm	2.12	1.38	3.45	2.56	4.72	3.16
response time /s	2.14	2.51	2.66	2.43	2.78	2.88

Plot the error data of the test into figure 8. The average error radius is 3.3 cm, and the variance is 0.61. It can be intuitively seen that the maximum error is not more than 4.8 cm, and the minimum is 1.1 cm.

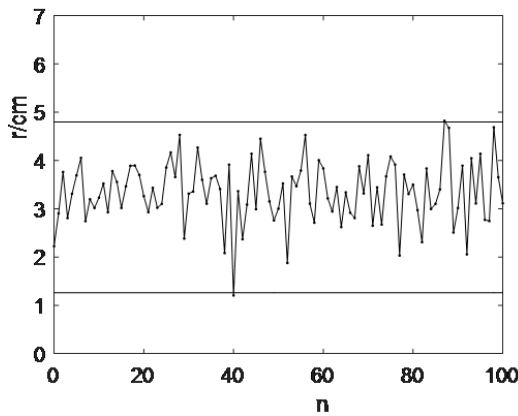


Fig. 8 Multiple same distance test results

When the user gazes at 5 different points on the platform with each increase of 10 cm, get the curve of error and distance, as shown in Figure 9, the black spot is a fixed distance error value of each point, the black curve is the average value of the error. It can be seen that the location error is linearly related to the distance, and the principle is given by formula (6).

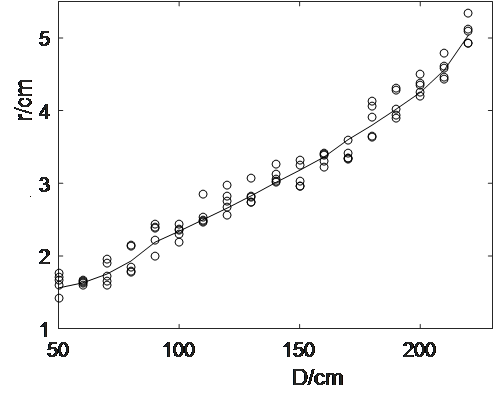


Fig. 9 Line of sight tracking control results

After analysis, the main reason for the error is the relative displacement between the camera and the eye, the operator's slight head movement, and the pixel resolution is not high enough. In addition, the error of the closed-loop control of the moving platform and the cumulative error in the continuous operation will affect each fixed-point effect.

VI CONCLUSION

The designed head based eye gaze tracking system can make the gaze tracking technology separate from the computer hardware platform, reduce the system cost, and realize the controllable operation of realistic objects. In the process of human eye image processing, through the optimization and synthesis of a variety of image processing algorithms, the line of sight parameters are obtained accurately. By using the least square method to transform the line of sight space coordinates, the moving parts of the platform can be accurately moved to the eye point of view, and the vision tracking system can be independent and mobile. That system has a certain application potential in the disabled and control home robot, application of eye tracking technology to broaden the field, has a good market prospect.

References

- [1]Zhang Chuang, Chi Jiannan, et al. Study of line of sight estimation method in Los system [A]. Chinese science, 2011, 41 (5): 580-591.
- [2] Tamara van Gog. Eye tracking as a tool to study and enhance multimedia learning [J]. Learning and Instruction, 2010, 20 (2):95-99.
- [3] Li Xingyu. Freescale, Carle, i.MX6 application processor, power machine vision application, [Z]. microcontroller and

embedded system application, 2015, 2:82-83.

- [4] Zhu Qiwen, Yan LONCIN. [A]. eye mouse design of electronic devices, eye tracking based on 2016, 39 (2): 235-240.
- [5] Wang Xuan, Zhang Fan, Cheng Jing. Segmentation of gray scale images based on improved Otsu method [A]. microcomputer information, 2010, 26 (12): 206-207.
- [6] Huang Lili, Yang Fan, et al. Method of pupil localization based on improved Otsu method [A]. computer engineering and application, 2013, 49 (23): 137-140.
- [7] Zhang Lin, Wang Baoqiang. An improved iris location algorithm based on Hough transform [A]. application of electronic technology, 2014, 40 (4): 66-69.
- [8] Chen Li, Wan Peng, he Tao, et al. Sub-pixel ellipse detection based on Hough transform [J]. Journal of Hubei University of Technology, 2005 (5): 132-134.
- [9] Yang, su. Research on Key Techniques of shape detection based on local analysis Hough transform [D]. Qinhuangdao: Yanshan University, 2009.
- [10] Chen Jian, Zheng Shaohua, et al. A method of pupil detection combining ellipse fitting and parameter transfer [A]. proceedings of the Institute of instrumentation, 2014,35 (8): 1890-1899.
- [11] Zhang Chuang, Chi Jiannan. A new eye gaze tracking method based on pupil corneal reflex technique [A]. proceedings of the Chinese society of computers, 2010, 33 (7): 1272-1285.
- [12] Cao Ye. Wearable gaze tracking system of [A]. computer and digital engineering, 2016, 44 (6): 1085-1088.
- [13] Shin Y G, Choi K A, Kim S T, et al. A novel 2D mapping-based remote eye gaze tracking method using two IR light sources[C]//Proc of IEEE International Conference on Consumer Electronics. 2015: 190-191.
- [14] Hansen D W, Ji Q. In the eye of the beholder: A survey of models for eyes and gaze[J]. IEEE Trans on Pattern Analysis and Machine Intelligence, 2010, 32(3): 478-500.

Design of mobile intelligent patrol instrument based on Cloud Computing

YUAN Ya-qi; GAO Yu-miao; DAI Xin-ping

(College of Instruction & Electrical Engineer Jilin University, Changchun, Jilin, 130061, China)

Abstract—The data collected in traditional routing inspection project mainly depended on manual recording. This method had many problems, such as tedious operation, low efficiency and poor real-time performance. In order to improve the performance of the system, a routing inspection system based on cloud computing was designed. The system combined the embedded system, Android platform and cloud computing platform based on the Cloud computing and ‘Internet plus’ mode. It made the inspection data can be viewed and corrected online in the background server. Experimental results show that, the data collected by sensors can be wirelessly transmitted by Socket protocol, and the real-time monitoring and analysis of data can be carried out in the background server. Compared with traditional routing inspection method, this system has higher efficiency and real-time performance, makes the inspection method more convenient and automatic.

Key words—routing inspection cloud computing cloud computing platform embedded system

I INTRODUCTION

THE most commonly used method of inspection is the manual inspection. The safety condition of the inspection equipment should be inspected periodically which is manual or irregular manual recording[1]. However, there are some shortcomings in the traditional inspection management methods, such as not timely inspection, insufficient data, omission of data, data inconvenience, and so on. Late again, the workers need to manually input the result into the computer, and work out the report to meet the different needs, more in need of additional manpower and time to organize data, these are to some extent, restrict the improvement of the quality inspection work.

With the development of mobile devices, ubiquitous Internet, Internet cloud computing technology, it is possible to provide the future inspection with paperless mode[2] and data recording intellectualization. With Internet communication technology, the data can be transmitted in real time, which can solve the problems caused by the limitation of the cable transmission mode and the poor interactivity of the real-time information of the traditional patrol inspection[3]. The use of mobile terminal devices, which can overcome the difficulty of carrying out the equipment caused by the poor geographical environment. If mobile terminals such as

mobile phones, tablets and on-board devices are applied to the inspection, it will ensure the reliability of data transmission and make the interface more concise and friendly[4-5]. The application of cloud computing technology enables the database to provide flexible and efficient analytical computing power[6], which can efficiently manage massive data. Combining mobile terminal, cloud computing technology and inspection work can create a new mode of inspection.

II THE DEVELOPMENT OF CLOUD COMPUTING TECHNOLOGY

With the change of global Internet data traffic in recent decades, explosive growth of data from 100GB/day in 1992 to 35000GB/s in 2017 has emerged as the emergence of cloud computing. Back in 1961, John McCarthy had said that turn a computer network into a public facility, it was the beginning of the first concept of cloud computing. Until 2006, when Google CEO Eric Schmidt put forward the concept of cloud computing, cloud computing is only known to people, and rapid development both at home and abroad. Because of its parallel computing, dynamic easy extension, virtualization resources and characteristics of fault tolerance, it is favored by people. So companies such as Yahoo, Intel, Amazon and HP have announced cloud computing research, pushing ahead the plan of cloud computing. Domestic

companies such as Tencent and Alibaba have also made good profits in the enterprise management due to cloud computing research results.

III CLOUD INSPECTION TECHNOLOGY

Cloud computing and mobile terminal equipment are introduced into traditional inspection work, realizing the dynamic interaction of online or offline and dynamic view of data, which can greatly improve the traditional cumbersome manual inspection, opening a new type of efficient checking mode. The "cloud" side carries on the statistics and analysis of the data, processing the data in parallel, thus effectively ensuring the stable operation of the inspection equipment.

IV SYSTEM ARCHITECTURE

A Systematic review

The cloud-based intelligence patrol has a unique advantage on data acquisition, transmission and storage. The data collection module adopts the embedded system, the mobile terminal adopts the mobile phone of the Android system as the carrier of its software, and the cloud computing center is constructed with the framework of SOA. The mobile terminal can locate the location of the inspector in position, check the personnel in place, and the inspector will transmit the data collected by the sensor to the mobile terminal in a wireless way, so that the inspector can quickly and intuitively observe the collected data and interact with the cloud platform through the network communication protocol, realizing real-time data viewing, statistics and analysis. The realization of the real-time data interaction between the mobile terminal and the background reduce the requirement of the storage space of the inspection instrument itself, reduce the human consumption, and realize the intelligence of the inspection work.

B Cloud platform system design

1 Database design

To ensure that the system run smoothly, it is need to design database to input the tasks of patrol, scope of work and authority of the staff. In addition to them anagement of the tasks and the personnel information, database also need to save the data, a large amount of

data is helpful for later analysis and evaluation.

The background database needs to analysis the basic parameters of the inspection equipment, the specific orientation and whether the inspection work is completed. Therefore, the data model which can support the inspection business is designed, including: employee information sheet, employee level sheet, task releasinglist, task management table, data information management form, etc.

(1) Employee information sheet

It mainly includes ID, employee name, gender, age, telephone and related remarks.

(2) Employee level sheet

It includes the first level ID, the second level ID, the first level name, and the second level name.

(3) Task releasing list

It mainly includes task time, task name, task content and number of tasks.

(4) Task management table

It mainly includes the task release time, task name, task content, number of tasks, task completion, inspector's name and inspector level.

(5) Data information management table

It mainly includes task name, temperature parameters, humidity parameters, air pressure parameters, altitude parameters, longitude parameters and latitude parameters.

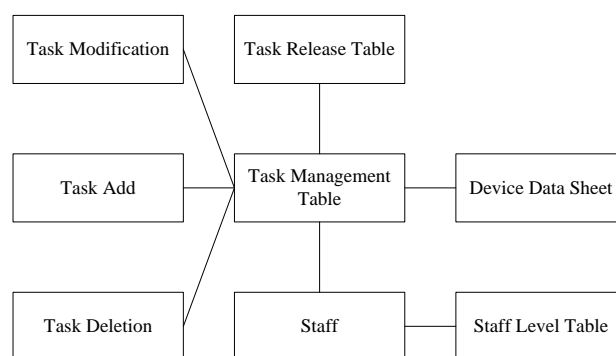


Fig. 1 Relationships between major tables

2 Winform interface design

The Winform interface is designed by VS2010, each module designed in the main interface can switch through the button key, there are "staff information", "task query" and "task release" and other interface options.

(1) Login module design

The module mainly verify whether the person who logged in is relevant, and judge whether the person who logged on the system is employee based on the

user name and password.

(2) Data receiving module design

The Socket protocol is used to connect by the IP address and port matching pairs, monitoring the client to determine whether a client request send data, and if a client sends data, it receives the data. If not, continue monitor.

(3) Data view module design

In this module, you can see the specific tasks, task time, and parameters collected. It can add, delete, and modify data.

(4) Task view module design

In this module, you can see specific tasks, task time, task content, people performing tasks, and related levels. Tasks can be modified, deleted, and added.

(5) Employee information module design

At this interface, you can see the corresponding managers and employees, as well as their gender, age and date of birth and other information. The functional modules of the Winform interface are shown in figure 2.

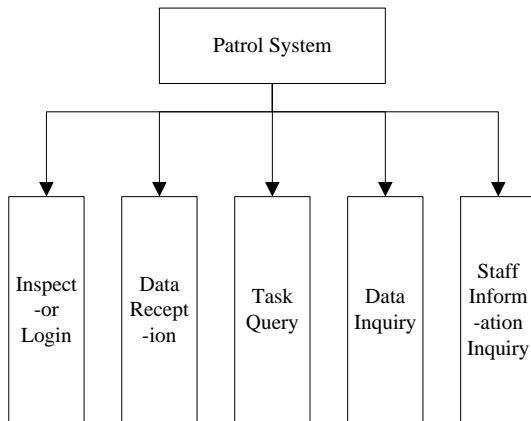


Fig. 2 Function module structure

C Data acquisition terminal design

The data acquisition terminal is embedded system, the core is ARM processor, and the peripheral circuit includes power module, sensor module, local storage module, communication module and human-computer interaction module (LCD display). Sensor module for raw data collection, using the BMP180 pressure sensor and DHT11 temperature and humidity sensor, BMP180 pressure sensor has the advantages of small volume and low power consumption, and put it in the handheld device can reduce the weight of the equipment and power consumption, increase equipment life. DHT11 temperature and humidity sensor accuracy, humidity is $\pm 5\%RH$, temperature ± 2 degrees, the accuracy meets

the measurement requirements. The central processor of the sensor drive control and complete transmission and the local data stored in local memory, the main function is for temporary storage of the collected information, the communication module is also known as the input and output interface unit, Using WIFI/4G/Bluetooth and other means of communication to achieve data acquisition side communication, the collected data is transmitted to the cloud computing platform.

D Construction of mobile intelligent Android platform

Mobile handheld terminal is the important man-machine interaction and data observation equipment of the whole patrol system. In order to meet the requirements of portability, versatility and scalability, a handheld mobile terminal based on Android system is adopted in this system. The functional flow of the mobile terminal is shown in figure 3.

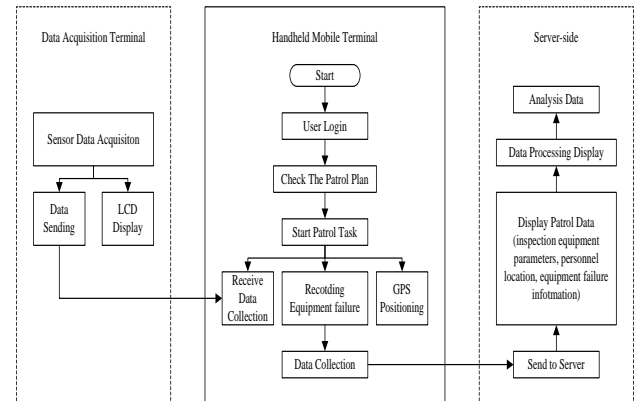


Fig.3 Function flow chat of mobile terminal

The mobile inspection system needs to provide the function of convenient inspection, record and upload function for inspection workers, providing a convenient query, management and real-time supervision function for inspection management personnel, the introduction of the design of specific modules.

1 Map location module

The main function of this module is to display the location points on the map, and to draw the patrol track line of the patrol personnel.

First, locate the longitude and latitude of the location by locating SDK, which is equivalent to the X, Y axis, and the SDK of the map provides Mapview, BaiduMap, and other API, for map manipulation and layer rendering. The map finds the corresponding points

according to the corresponding coordinates, and draws an icon on the map layer, that is, the location.

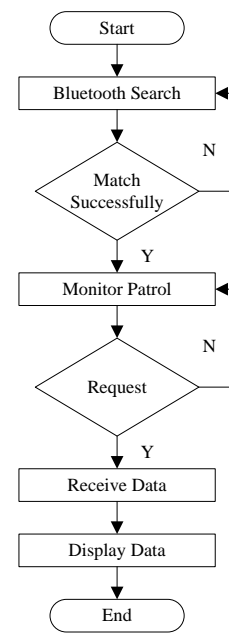
Using GPS positioning, when the patrol personnel began to patrol, click start button, on the layer, according to the trajectory of walking trajectory drawn. The patrol track is visually displayed on the map, and the patrol personnel are convenient to see the running track.

2 Data transmission module

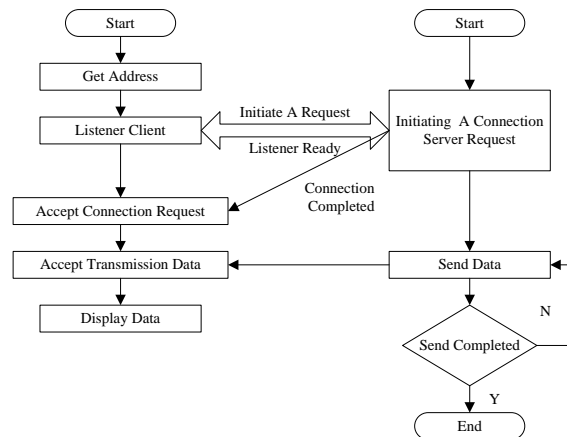
The main function of this module for receiving inspection instrument through the handheld mobile terminal data acquisition, and data analysis, the corresponding data uploaded to the server, then the server count and analyse data.

Data transmission: The communication of Bluetooth is done by the client and the server Socket, Bluetooth client is BluetoothSocket, Bluetooth server is BluetoothServerSocket, the two class can complete the corresponding data transmission. Then, the corresponding thread is used to monitor whether the data is transmitted. When the data is sent, the data of the patrol instrument is sent to the data receiving interface by means of SendMessage (). Program flow chart, shown in Figure 4a.

To realize the data transmission between the mobile terminal and the server: first ,server initializes Socket, then bind with the port, and monitor the port, waiting for client connection, if the client initializes a Socket (connect), If success, it represents a link has been established. The client sends the data request, the server accepts the request and processes it, and finally closes the connection. The upload data flow diagram is shown in Figure 4b.



(a) Collect data flow chart of patrol instrument



(b) Upload data flow chart of mobile terminal

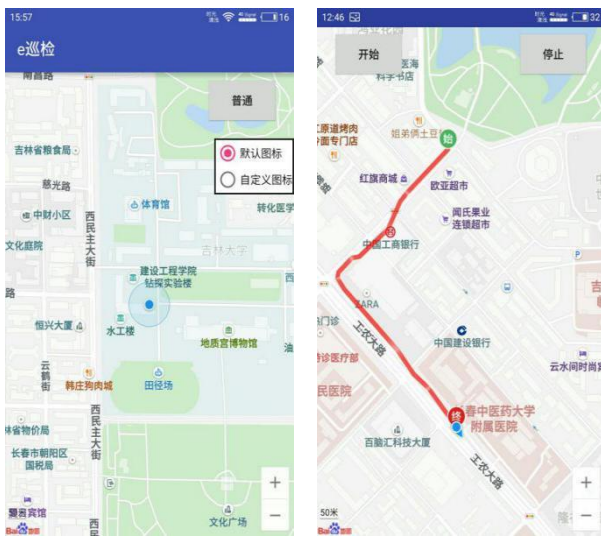
Fig. 4 Data acquisition and uploading process

V SYSTEM OVERALL TEST

During the test, the Bluetooth on the handheld mobile terminal is opened and matched with the Bluetooth module of the data acquisition, data collected by the sensor module of the data acquisition terminal is transmitted to the mobile phone interface, and can map positioning and trajectory description, as shown in figure 5.



(a) Data sending and receiving chart



(b) location map (c) trajectory drawing

Fig. 5 Handheld mobile terminal functional test

The data sent by the mobile terminal carries out data transmission with the Socket connection of the computer terminal (IP address matching, port number matching), and the data received by the computer terminal is shown in figure 6.

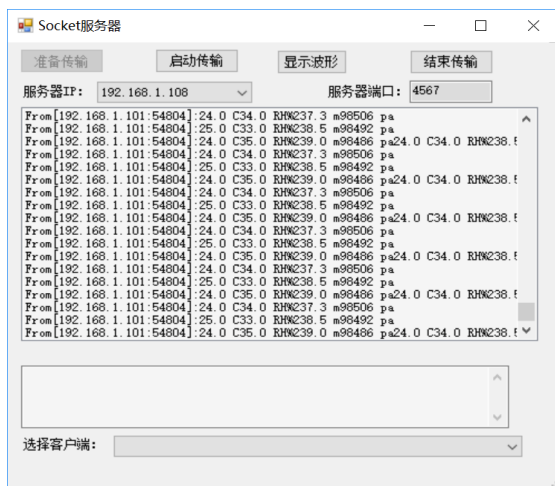


Fig. 6 Data upload diagram

The data after the transfer is stored in the SQL Server database and can be queried through the Winform interface, as shown in figure 7.

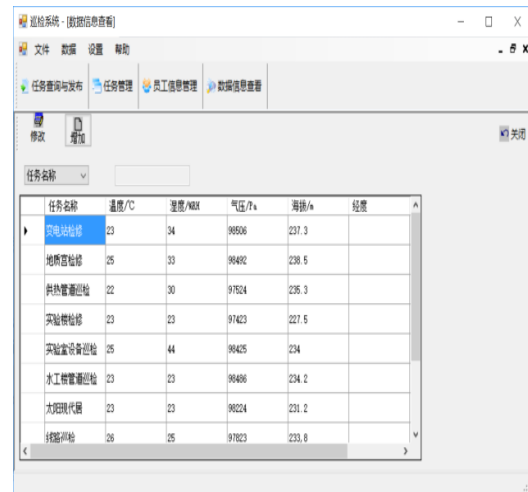


Fig. 7 Data query interface

IV CONCLUSION

Based on the "Internet plus", introduce the cloud computing to the daily inspection work, design and development of intelligent patrol instrument based on Cloud Computing, realize time online view and analysis data of remote device, improve the shortcomings of the traditional inspection, It is very helpful to realize modern intelligent patrol and has very far-reaching practical value.

References

- [1] Li GuoWei. Research in Power Plant Based on Intelligent Inspection System[J]. Science & Technology Information (Academic Research)2008,(27):520. [2017-09-02].
- [2] CHEN Cong. Research on Electronic Communication Equipment Inspection System Supported by RFID[D]. Jilin University, 2011.
- [3] Wang KeJun. The Design and Implementation of Mobile Intelligent Inspection System on Wind Turbine Generator[D]. Beijing Jiaotong University, 2015.
- [4] Meng Chen Xi. Design and Implementation of Mobile Inspection System[D]. University of Electronic Science and Technology of China, 2015.

- [5] Kang Ying Hua,Gao Zhen Yan.De-sign of all Directional Intelligent Power Patrol System[J].Transactions of China Electrotechnic-al Society,2008,(08):8-10. [2017-09-02].
- [6] Zheng Hai Rong,Gao Jing.Cloud Computing T-echnology and Its Application[J]. Communicati-ons Technology, 2013,46(04):96-98+102.[2017-09-02].

High Stability DFB Driver Utilized in Near Infrared Gas Detection

Deng Weifen; Wang Qianqian; Jiang Rongqiu

(*jilin university instrument science and engineering institute, changchun, 130021*)

Abstract—In order to meet the requirements of infrared gas detection for high performance laser drive power supply, this paper adopted PID control algorithm, a High Stability DFB Driver had been designed and manufactured. In terms of hardware, mainly include signal generation module, voltage-controlling current source module, circuit protection module. The system has the function of output current protection. In the signal generation module, the sine wave is generated by DDS and then generate square waves through a comparator. At the same time, DA conversion technique is adopted to realize the output of DC wave, triangular wave and saw-tooth wave. Meanwhile, in respect of control scheme, the current high stability was effectively ensured by the use of PID control algorithm and veep negative feedback[1]. With this driver, performed driving test on a DFB laser with a center wavelength at 1563.09 nm. The results show that the diver has the function of the output waveform type, amplitude and frequency can be changed by digital control, the current amplitude ranged from 0 to 1A and the frequency range from 1Hz to 1MHz. The frequency resolution was 1Hz. The linearity of the system is 99.93% and the long term output current stability is reached 0.0197%.

Keywords—Mid infrared gas detection; DFB laser driving power; PID control algorithm; High Stability; High linearity

I INTRODUCTION

INFRARED gas analysis is based on Lambert-Beer's law of absorption of gas concentration analysis method, DFB laser with its strong monochrome and high common mode rejection ratio of the detection method to become an irreplaceable light source. In the gas concentration detection, the use of DFB laser based on the wavelength modulation detection method can make the detection sensitivity than the direct absorption method to improve the 2 to 3 orders of magnitude [4]. DFB lasers rely on the direct injection of carriers for work [2], the stability of the output wavelength directly affected by the drive current stability [3], the tiny current changes will have a great impact on the output optical power, the most Intuitive is to cause fluctuations in the wavelength of light, which will reduce the life of the laser. In addition, the effect of different driving power supply for the laser is different, the saw-tooth wave is used to tune the laser wavelength, the sine wave is used to modulate the amplitude of the laser.

At present, the development of foreign semiconductor laser driver power supply performance

parameters, security protection, user interface optimization and so have an absolute advantage to the United States Wavelength MPL-2500 as an example [6], the constant power stability of less than 0.02% , Short-term stability of the current is less than 30ppm, long-term stability of the current is less than 75ppm, but not portable and economical. In recent years, domestic enterprises have also begun to get involved in the field of laser drive, and actively develop related products, but compared with foreign advanced products in the control of current accuracy and long-term response stability is still a large gap [5].

Based on the research status at home and abroad, In this paper, a variety of waveforms are generated by DA conversion technology according to the requirements of project indicators. A high stability drive power for driving DFB lasers is designed by using PID control technology and digital control technology. The linearity of the control system is tested experimentally and stability.

II DRIVE POWER SUPPLY DESIGN

The system block diagram of the high stability DFB laser drive power supply for infrared gas detection is

shown in Figure 1, which mainly includes the core controller module, the signal generation module, the voltage control constant current source module, the circuit protection module and so on.

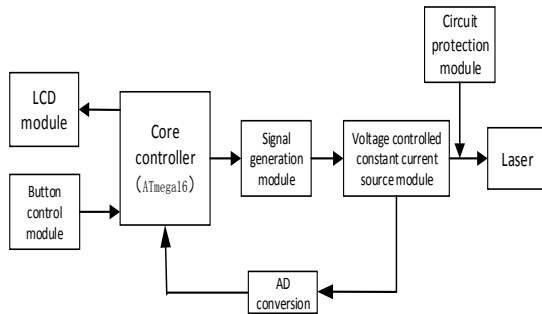


Fig.1 Diagram of DFB laser driving system

The system uses ATmega16 as the core of the laser drive power control, used to control high-resolution direct digital frequency synthesizer (DDS) and drive high-precision 16-bit digital analog converter (DAC), to produce a variety of high-precision CNC Adjustable analog voltage. The signal generation module consists of DDS module, DAC module, multiplier module and voltage amplification module, which can generate periodic, amplitude adjustable sine wave, square wave, triangular wave, saw-tooth wave, DC wave five high-precision signal, used to drive constant current source module. The voltage-controlled constant current source takes the high-power MOSFET as the core, uses the deep negative feedback, collects the current signal of the injected laser, converts the current signal into the voltage signal back to the input end. The system uses PID control technology, effectively improve the output current accuracy and stability. Circuit protection module consists of electrostatic protection circuit, soft start circuit, current limiting circuit, sound and light alarm circuit, can effectively protect the laser. Peripheral auxiliary circuit with LCD display, beer button input, security alarm and so on.

A Signal Generation Module Design

Signal block diagram of the signal generation module shown in Figure 2.

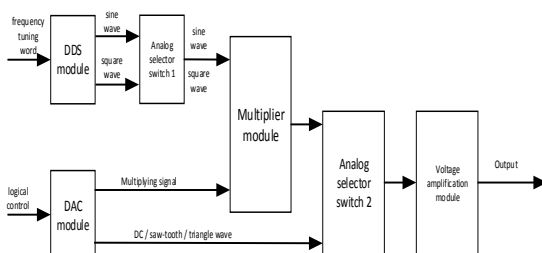


Fig.2 Principle diagram of signal generation module

ADAM51 chip developed by the United States AD as the core components of the DDS module, the output frequency up to 72Mhz, by the ATmega16 control its frequency adjustable high-precision stable sinusoidal signal, and then through a voltage comparator to get the same amplitude, The frequency of the square wave signal. The DAC module uses a high-resolution 16-bit LTC1655 chip that uses the ADR130 to provide its reference voltage. As the DDS output signal amplitude is fixed to 1V, the use of LTC1655 0 to 1V change the DC multiplication signal, through the multiplier AD835 to achieve the output signal 0 to 1V NC adjustable. At the same time, using the DA conversion technology to control the LTC1655 to produce the corresponding set of triangular / saw-tooth / DC signal, analog select switch 2 output high stability and high precision frequency, amplitude are numerically adjustable signal. As the output signal maximum amplitude of 1V, in order to achieve the design of the system indicators, the use of low-noise high-speed operational amplifier LT1226 amplitude of the front-end signal amplification, which has 1GHz operating bandwidth, 400V /ms conversion rate to achieve the post-level Drive circuit signal requirements.

B Design of Constant Voltage Source Module for Voltage Control

The voltage-controlled constant current source module uses a deep negative feedback architecture and a PID algorithm to form a closed-loop control system that allows the input signal to be constant regardless of the DC voltage or the AC voltage. The current is regulated by the input voltage amplitude. The sense current divides the load current into a voltage signal as a feedback signal, regulates the gate-source voltage V_{gs} of the MOSFET, causes the MOSFET to operate in the active linear region and enables the output current to be between 0 and 1A Tune. Through the depth of the operational amplifier negative feedback link, the current flowing through the laser can be stabilized in the order of 10^{-3} [1], improve the stability of the circuit, signal to noise ratio and reduce the nonlinear distortion. At the same time, in order to stabilize the current output, through the current-sense resistor to collect analog voltage signal, through the AD conversion, transfer to the single chip, through the PID algorithm, control the current high stability output.

Voltage control constant current module schematic diagram shown in Figure 3.

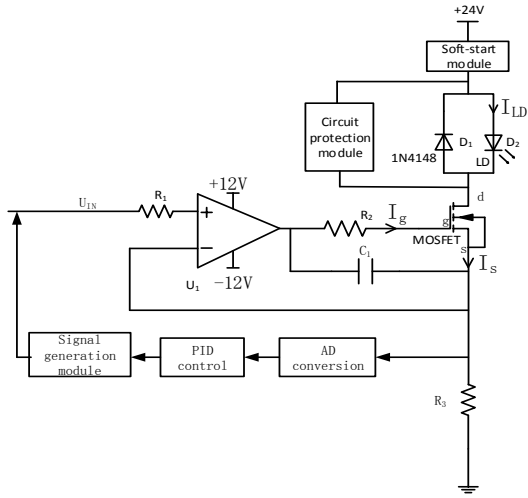


Fig.3 Schematic diagram of voltage-controlling current source module

In this system, Op Amp chip AD8513 is chosen as the proportional amplifying part of the feedback loop that provide fast and extremely high stability under capacitive loads, which ensures high stability current output requirements. The resistance R_3 takes samples of the current of the DFB laser (D_2) branch, which converts the current signal into a voltage signal and is fed back to the negative input of the operational amplifier U_1 . By adjusting the voltage difference of integration capacitor C_1 to control the gate-source voltage of MOSFET, which could change the current value that flows through the DFB laser, nonlinear feedback loop adjustment for linear MOSFET tube. The R_2 can effectively reduce the driving current inactivation caused by parasitic capacitance and parasitic inductance in the circuit, and greatly reduce the time of rising / falling edge of the driving signal. The D_1 provides leakage current pathway for the reverse voltage, while the diode's fast turn-on limits the reverse bias of the DFB laser to less than 0.6V. I_s was defined as the current flowing through the sampling resistance R_3 . According to the principle of "virtual short circuit" and "virtual open circuit" of operational amplifier, there are

$$I_s = \frac{U_{IN}}{R_3} \quad (1)$$

$$I_{LD} = I_s + I_g \approx I_s \quad (2)$$

In the negative feedback regulation, the AD converter is used to collect the voltage signal of the laser branch

and reduce the output broadband. But for the low-frequency triangular wave, saw-tooth wave, and direct wave, adopting double loop to improve the stability of the drive current and for the high-frequency sine wave and square wave, the stability of the output current is improved by using analog linear negative feedback and single closed loop mode. Thus, the AD conversion has no influence on the output of the high-frequency sine wave and square wave signals.

C Circuit Protection Module

The injection current affects the stability of the output wavelength of the laser directly. When it is larger than the maximum allowable current, the laser will break down and can not work properly. Therefore, current limiting protection is added into the circuit, when the injection current is greater than the set value, the system will automatically cut off the current injected into the laser, and the acousto-optic warning circuit give an alarm. In addition, the driving circuit will produce a large impact current when it closes or opens, which poses a great harm to the performance of the laser. Therefore, a delay soft start circuit is designed to prevent the momentary surge impact caused by the switching moment of the power supply. At the same time, when the system works, there is a lot of static electricity in the inductance, capacitance and inductance of the circuit. Excessive static electrostatic value could cause laser damage, so the ESD protection circuit is designed in the system to protect the laser.

III THE CONTROLLING ALGORITHM

This system adopts PID algorithm. The output current is sampled by current resistance, after the voltage signal is converted into a voltage signal, the signal is converted into digital quantity by AD and sent into the MCU. Because the MCU can only deal with discrete signals, the bilinear transformation is used to make the control system more accurate and stable. By dividing the difference between the collected current value and the set value (That is error value), and according to different error value segments, corresponding voltage compensation is applied to speed up dynamic response, reduce overshoot, and improve system stability. The block diagram of the PID control system is shown in figure 4.

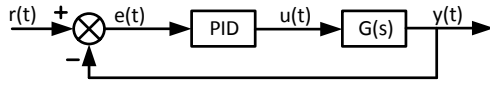


Fig.4 diagram of PID closed-loop control system

The discretized equations of the PID controller are represented as

$$u(k) = K_p[e(k) + \frac{1}{T_i} \sum_{i=0}^k e(i)T + T_d \frac{e(k) - e(k-1)}{T}] \quad (3)$$

Among them, $e(i) = y(i) - r(i)$. The control process is affected by K_p , T_i and T_d together. In the system, the optimal parameters are determined by setting the system to ensure the stability of the system. The value and proportion relationship between K_p , T_i and T_d directly affect the performance of the system. In order to obtain the best parameters, the critical proportion method is adopted to optimize the K_p , T_i and T_d . The empirical formula of parameter setting is shown in table 1.

Table I EMPIRICAL FORMULA OF CRITICAL PROPORTION

Controller type	TURNING METHOD		
	Proportional	Integral	Differential
	ity $\delta/\%$	time T_i	time T_d
P	$2\delta_p$	∞	0
PI	$2.2\delta_p$	$0.833T_p$	0
PID	$1.7\delta_p$	$0.50T_p$	$0.125T_p$

Firstly, set the T_i to the maximum, T_d to 0, and the delta to the appropriate value. Then, start the system to the system stability, and gradually reduce the degree of proportionality to appear equal amplitude oscillation, and record the critical degree of proportionality and the critical oscillation period. Finally, according to the critical proportion method, adjust the empirical formula of the parameter calculate the parameters.

IV TEST OF DRIVE POWER PERFORMANCE

A Driving Waveform

Control the type, amplitude and frequency of the driving power output signal through the buttons and detect the output signal through digital oscilloscope GDS-2002E. The result shows that the system can produce five kinds of wave-forms, including sine wave, square wave, triangle wave, saw-tooth wave and direct

current wave, and the output current, frequency and amplitude are adjustable numerically. The output frequency of sine wave and square wave range 1Hz to 1MHz, and the resolution is 1Hz. The output frequency of triangular wave, saw-tooth wave and DC wave range 1Hz to 100Hz, and the resolution is 1Hz. The voltage range of all output signals ranges from 0 to 5V with a resolution of 0.1V. The output current of six high precision multifunctional digital instrument measuring driving power, results show that the steady current range from 0 to 1A. Measure the output current of the driving power supply with a high precision multi-function digital instrument DM3068 produced by Beijing RIGOL Technology Co. Ltd. . The result shows that the constant current range is from 0 to 1A. Taking the saw-tooth amplitude of output signal as 2.0V and frequency 5KHz as an example, the driving test of DFB laser is carried out. The driving waveform is shown in Figure 5.

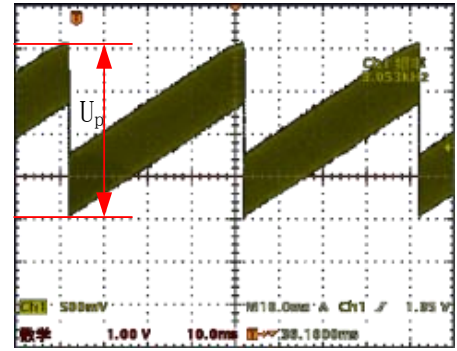


Fig.5 diagram of driving signal waveform

The results show that the peak value of the actual output voltage is 1.95V, and the frequency is 5.053kHz, which meets the requirements of the design accuracy .

B Experiment of Tuning PID Parameters With Critical Proportion Degree Method

Adjust the parameters of the current controller through critical proportion method, that is, get the values of delta δ_p and T_p by test, and then get the parameters by empirical formula. The output current was experimentally tested by using the P regulator. Set T_i to be the largest, T_d is 0, and gradually reduce K_p . Constant amplitude oscillation occurs at $K_p=73$. This

moment, $T_p=5.0s$, so, $\delta_p = \frac{1}{K_p} = 0.0137$. By the

setting formula of Table 1, $\delta=0.0233$, $T_i=2.5s$,

$T_d=0.625s$. The current control task 1s runs once, so

the PID algorithm has a sampling period of 1s. From above, $K_p=1/\delta=42.92$, $K_i=K_p*T/T_i=17.17$, $K_d=K_p*T=45.625$.

C Test for Linearity of Drive Current

The linearity of the driving power supply is the percentage of the maximum deviation measured by the system and the theoretical full-scale output. The principle of a voltage controlled constant current source is that the output current varies with the input voltage. By changing the input voltage of the voltage controlled constant current source, which change ranged from 0 to 5V, with 0.2V as step size, the output current is measured by DM3068 . The result is shown in Figure 6.

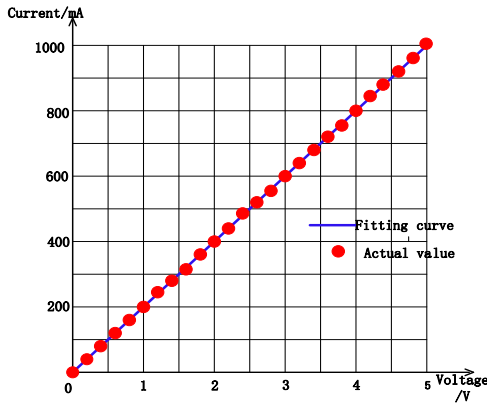


Fig.6 The relationcurve of laser driving voltage-current

A value is taken every 0.2V in the experiment. From the actual and theoretical curve, the results show that the set value has a good effect and linear output current. The output current maximum deviation value is 0.092mA and the linearity is 99.93%. the good performance of the system. It proves that the system has good stability.

D Current Stability Test

Drive power output current stability formula is

$$p = \frac{\text{averagevalue} - \text{calibration value}}{\text{averagevalue}} . \text{Select the model for the}$$

TED200C laser temperature controller produced by United States Thorlabs to control the laser operating temperature stability of 39 °C, and test the stability of DFB lasers. Preset target current of 400mA, the laser for 8 hours, every 10 minutes using DM3068 test a current, the test results shown in Figure 7.

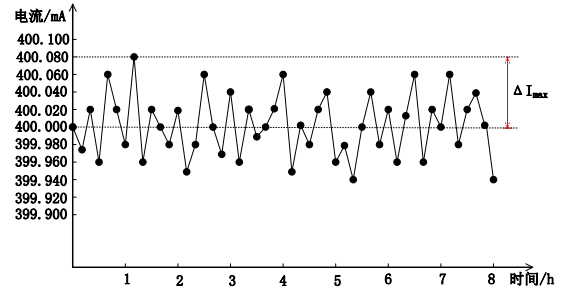


Fig.7 The test of stability of driving current

The results show that the output current of the driving power is stable at 400mA, the maximum deviation of the output current is 0.08mA, the output average is 400.079mA, the current stability reaches 0.0197%, and the system stability is good.

E Relationship Between Lasing Wavelength and Driving Current of Laser

When the carrier is injected, the DFB semiconductor laser begins to operate. The ambient temperature and injection current have a direct influence on the stability of the output wavelength. As the temperature and current values change, the output wavelength fluctuates and the lasing spectrum changes. In this experiment, the lasing spectrum of an infrared distributed feedback laser with a near-infrared emission wavelength of about 1563.09nm is measured. The change of laser output center wavelength is detected by changing the drive current and the operating temperature. The laser temperature controller is used to control the change of the laser operating temperature from 39 to 43, which was manufactured by Thorlabs, USA, and the model is TED200C. Set the operating current between 40mA and 70mA, and the spectrum of laser is measured by a FTIR spectrometer. The excitation spectrum changes are shown in figure 8.

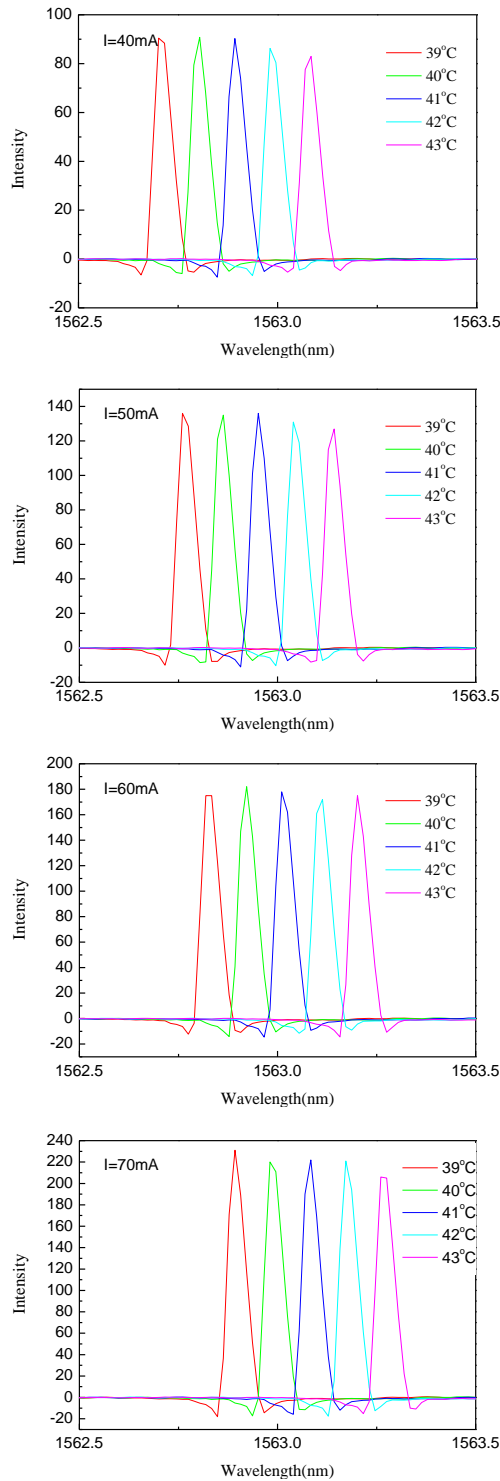


Fig.8 Relationship between DFB lasing spectrum and driving current

By analyzing the lasing spectrum shown in Fig. 8, the relationship between the output center wavelength and the temperature and the operating current is shown in Figure 9.

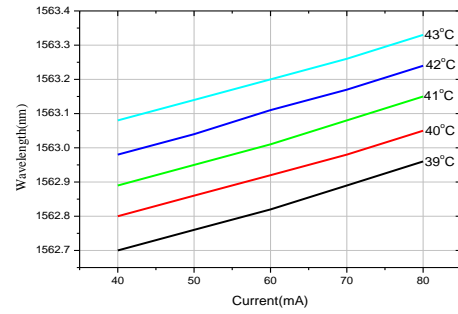


Fig.9. The influence of temperature and driving current on the centerwavelength of laser

As can be seen from the figure above, when the operating temperature of the laser is constant, the output peak wavelength of the laser is in stable linear relationship with the operating current. When the operating current of the laser is constant, changing the operating temperature of the laser can effectively tune the center wavelength of the DFB laser.

F DFB Laser Emission Spectroscopy Repeatability Test

In the gas concentration test, in order to ensure the accuracy of the system and improve the reliability of the system, the DFB laser output stable luminescence spectrum is required. In this experiment, the TED200C laser temperature controller is used to set the operating temperature of the laser to be 39 °C, and the same DFB laser is used to drive the concentration of carbon monoxide gas. Set the working current of 60mA, the laser output of the continuous spectrum of three consecutive measurements, measurement time interval of 1 hour, the measurement results shown in Figure 10.

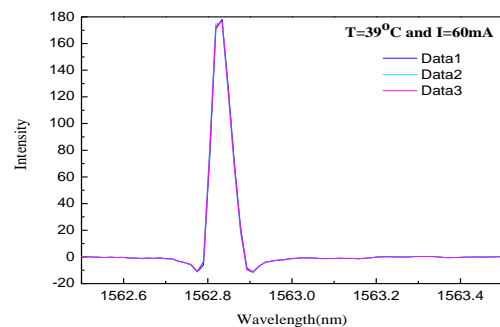


Fig.10 Stability test curve of luminescence spectrum of DFB laser

From the experimental results, it can be seen that the measured output lines of the three lasers are almost completely coincident, indicating that the driving signal of the laser is stable.

V CONCLUDING REMARKS

A high stability DFB laser drive power is designed and developed, and the performance of the DFB laser is tested. The results show that the system can output a variety of waveforms, and the output current, frequency and amplitude are numerically adjustable. The waveform signal is stable. Using the principle of deep negative feedback, control the voltage output stable current, the use of PID control algorithm, stable current output, driven by the current linearity and stability of the test curve can be seen that Linearity of 99.93%, stability of 0.0197%, the drive current without burr, laser work is stable, but compared to foreign products still have a certain gap. At present, this paper adopts simple linear negative feedback, which can re-refer to the simulation integration link to improve the stability of the current, but the corresponding output signal bandwidth will be reduced, fail to meet the corresponding requirements. Using the drive power to drive the DFB laser for CO gas detection, the laser output spectrum is stable, showing that the system has good accuracy and stability, can be applied to DFB laser based infrared gas detection system.

References

- [1] Chen Chen, Huang Jianqiang, Lv Mo, Wang Dingyi. High narrow pulse drive power for infrared quantum cascadelaser[J]. Journal of Jinlin of University Engineering and Technology Edition, 2011, 41(6): 1739-1740. (in Chinese)
- [2] Zhan Juntong, Fu Qiang, Duan Jin, Zhang Su, Gao Zerui, Jiang Huilin. Stability improvement of DFB laser driving power using digital position PID algorithm[J]. Infrared and Laser Engineering, 2015, 44(6): 1757-1761. (in Chinese)
- [3] Qu Tianrun, Xue Tianliang. Development of Driver for Semiconductor Laser Diode Based on Negative Feedback of Current and Digital PID Algorithm[J]. Laser Journal, 2015, 36(8): 105-108. (in Chinese)
- [4] Wang Xiaoyu. Design of DFB Laser Driving Based on FPGA[D]. Jilin University, 2013
- [5] Wang Yu. The design of DFB laser Drive and Temperature Controller[D]. Jilin University, 2015
- [6] Yu Wangzu. Development of driver for semiconductor laser diode[D]. Harbin institute of technology, 2015
- [7] Chui Yuqi, Xie Jiantong, Huang Linshu, Chen Chen. High-precision Drive Power Supply for Nano-second and narrow pulsed QCL[J]. Laser Journal, 2015, 36(9): 30-32. (in Chinese)
- [8] Hu Yemin. Design of DFB Laser Driver Based on DSP[J]. Laser Journal, 2015, 36(1): 82-84. (in Chinese)
- [9] Dang Jingmin, Zha Bing, Gao Zongli, Chen Chen, Wang Dingyi. Nanosecond driver for multiple pulse-modulated Infrared quantum cascade lasers[J]. Optics and Precision Engineering, 2013, 21(09): 2209-2216.
- [10] Wang Chunmin, Yi Hui. Continuous and discrete Engineering[M]. Beijing: Beijing University of Posts and Telecommunications Press, 2015: 266-267

A Design of Indoor Intelligent Ventilation and Purification System Consisted of Fans

Zhu Yurong; Ma Jingxuan; Gu Yujing

(College of Instrument Science and Electrical Engineering, Jilin University changchun130000)

Abstract—Aiming at the constant pursuit of modern home intelligence, the rapid development of intelligent home industry and the status of complex living conditions in modern social environment, this paper introduces an intelligent ventilation system with multi-fan control system principally. Expect the use of multi-fan control technology, it also combines the duct ventilation technology to enhance the ability of indoor and outdoor ventilation, and optimize the performance of intelligent multi-fan purification system. By the use of Bluetooth communication technology, a mobile APP can control the fan speed which strengthens the intelligence and controllability of the system. The additional air purification device that uses the filter Photocatalyst can effectively accomplish the purification for the room.

Key words—Bluetooth Multi-fan Complex living conditions Mobile APP Purification

I INTRODUCTION

WITH the rapid development of computer technology, network technology, control technology and artificial intelligence, an Intelligent society has become the new trend in the 21st century. Under the circumstances, smart home has also grown rapidly [1]. Besides, the urbanization process in China is accelerated and the buildings are going up. So, indoor ventilation naturally becomes a serious problem. At the same time, although the use of air-conditioning satisfies the requirement of “warm winter and cool summer”, it will cause air pollution and the waste of resources, and have a chronic hazard to human health. Therefore, creating an intelligent, energy-saving and pollution-free home system is extremely urgent.

It's not common to see ventilation cooling system consisted of multi fans. But they have long been used in car radiators. In the traditional single fan radiator of the automobile engine, due to the uneven distribution of the cooling water flow, the temperature difference exists in each part of the radiator flat tube. But the cooling air flow distribution of fan conveying does not match with the flat tube radiator temperature distribution. And the local temperature of the radiator is so high that the accumulated heat caused by stress concentrates produces pipe cracking and heat sink deformation. Through the improvement of the traditional single fan radiator, the arrangement of multi

fans can be adopted to make the temperature distribution of each part of the radiator more even and reduce the partial heat accumulation phenomenon of the radiator [2]~[3]. Multi fan ventilation system not only can be used in the automotive radiator, but also in the smart home by after transforming it to replace the air-conditioning which has high power consumption and high pollution.

Smart home is based on the residential platform. The comprehensive utilization of automatic control technology and network communication technology will create an efficient, safe, convenient and environmental living environment. This indoor intelligent ventilation and purification system consisted of fans can collect the indoor temperature, humidity and concentration of pollutants, and have an intelligent algorithm to control fans' speed automatically and make the indoor temperature under the standard value set. Bluetooth communication can also be used to control the speed of fans with a mobile phone. In order to increase the ventilation between indoor and outdoor surroundings and strengthen the ventilation effect, the system combines the loop ventilation technology by setting the air inlet and outlet in the pipe mouth. The air purification equipment such as filters are also added, which can purify the indoor air and reduce the harmful substances to the human body.

II SYSTEM FRAMEWORK

This system mainly is made up of fans control module, a Bluetooth communication module and an air purification module. Multi fans control module is responsible for automatic ventilation and cooling, so that the indoor temperature and the air flow rate varies within a certain range. Bluetooth communication module is responsible for connecting the mobile phone and each fan, and users can control the speed of fans through the mobile phone. The air purifying module is responsible for eliminating the harmful substances indoors. Three modules are mutually independent, but there are inseparable links among them. When the user controls fans via Bluetooth communication, the automatic control function of multi fans is limited. The running of air purification module depends on the result of the pollutant concentration detector in fans control module. The mobile phone can control the air purification module indirectly by controlling the switch of the ultraviolet device. The overall framework of the system is shown in figure 1.

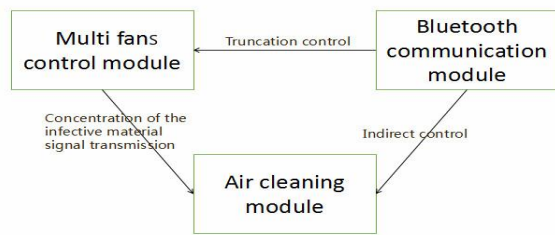


Fig. 1 System framework

III DESIGN OF MULTI FANS CONTROL MODULE

A Fans Automation

At the age of electronic information, controllers of temperature are used in all walks of life, which has function of watching temperature to ensure that industrial instruments, measuring tools and agricultural cultivation could have a normal operation. The main characteristic of them is watching the temperature around in real time and controlling the fans to change the temperature. Their widespread application and popularization has brought the convenience to people's daily life[4]~[6]. The fans automation device in our system also uses the concept of temperature controller.

This module uses STM32F103ZET6 as MCU, with L298N module, blue-teeth module, and formaldehyde sensor, temperature and humidity sensor, to realize the intellectualization and automation for the speed of fans controlling. The fans control modes are consisted of the auto-control and manual-control. The sketch graph of auto-control structure is figure 2. First set in advance manually of indoor temperature, harmful gas concentration, and set sensitivity. When these modules are working, the MCU calculates the unattended ventilation loop, detects the concentration of harmful substances and determines whether the filter cleaning device is opened. The manual control structure is shown in figure 3. The fans controller and the communication software are connected by the Bluetooth. The software can be operated by the user to change the fans' speed and open of the air purification device.

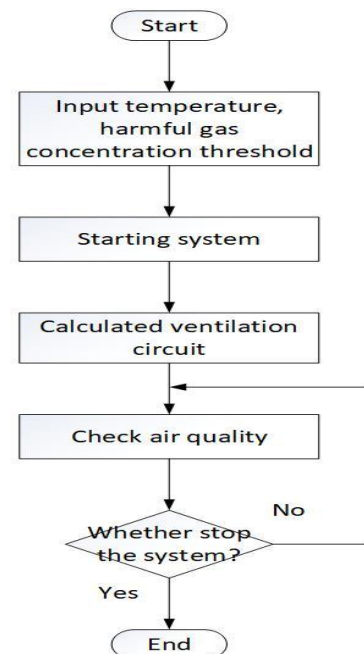


Fig. 2 Automatic control structure diagram

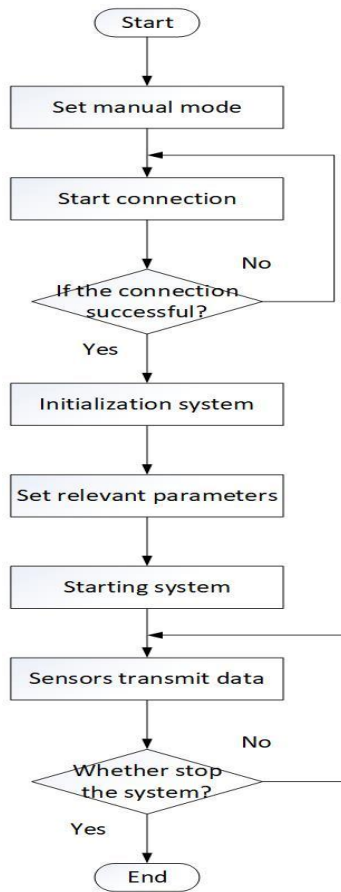


Fig. 3 Manual control structure diagram

The system is mainly applied to the home life. Aiming at indoor ventilation and cooling in different rooms, ventilation mode can be divided into the following categories.

1. Single room and single check value are abnormal: The fan in the corresponding room operates.
2. Multi rooms and single detection value are abnormal: Check the temperature, humidity and formaldehyde value. If they are normal, choose the indoor-outdoor cycle. If not, choose the indoor self-purification cycle.
3. Multi rooms and multi detection values are abnormal: On the basis of 2, introduce an algorithm $P=KT+AH+BF$. Among them, P is fan speed; T is indoor temperature; H is indoor humidity; F is indoor formaldehyde concentration; K , A and B are coefficients, which vary with the ventilation strategy (cooling priority, pollution removal priority, or equilibrium model).

B Duct Ventilation

China's existing construction area has reached 42 billion square meters. With the development of social economy, people's material conditions have been improved and they have higher demands for living quality. Thus the air-conditioning system has gotten more and more applications. The rationality of air conditioning ventilation system plays an important role to improve the effective utilization rate of energy in the whole society and reduce the energy waste[7]~[8]. The application of loop ventilation in this system is very important. The design combined with loop makes the air between indoor and outdoor exchange and promote the indoor ventilation.

The design of loops in the system is based on the model of two rooms with one hall. The ventilating ducts are set up on the roof and the fans are installed at the joint between ducts and the air intakes to accelerate air circulation.

IV DESIGN OF BLUETOOTH COMMUNICATION MODULE

Bluetooth technology is an open global specification for wireless data and digital communication. It belongs to short distance wireless connection communication technology. It bases on a low cost wireless connection for close quarters and could build a wireless link for fixed and mobile device [9]~[11]. In order to achieve Bluetooth control, the first step is to set Bluetooth access, get Bluetooth adapter object and start it. Then found Bluetooth device and establish connection. After getting the device address, exchange data with each other and establish a data communication thread. The schematic diagram for Blue connection of this system is shown in figure 4. By Bluetooth software based on Android, the user's mobile phone is linked with the fans' controller to control the speed of fans and the air cleaner.

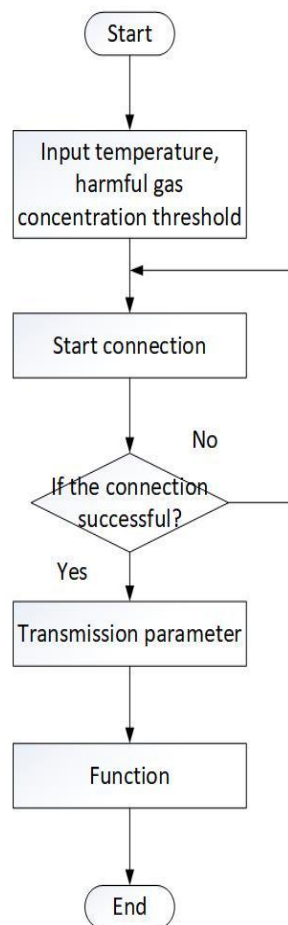
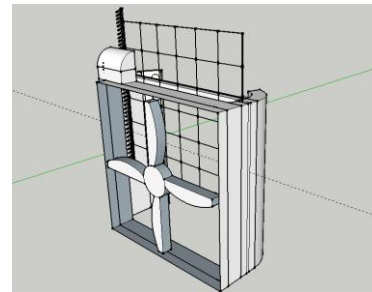


Fig. 4 Bluetooth connectivity diagram

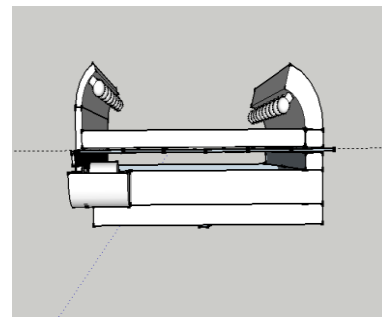
V DESIGN OF AIR PURIFICATION MODULE

The air purification module of this system utilizes a filter screen photo-catalyst technology which is widely used. Photo-catalyst is a general term for optical semiconductor materials with photocatalytic functions represented by titanium dioxide. It is the most ideal material for doing with the indoor environmental pollution in the world[12]~[14]. Photo-catalyst technology is also called cold catalyst technology. Its working principle is to plate nanoscale catalyst(TiO_2) on the particular carrier, and make a filter net. By the effect of fans, the catalyst reacts with the harmful gas in the light of the ultraviolet radiation of the specific wavelength. The virus protein is solidified and the activity of the virus is inhibited. Thus the air is purified. At the same time, titanium dioxide has good light activity in the near ultraviolet region. It also has stable chemical property, high hardness, low price and is harmless to human. Therefore, photo-catalyst technology will have an ideal effect if applied to air purification[15].

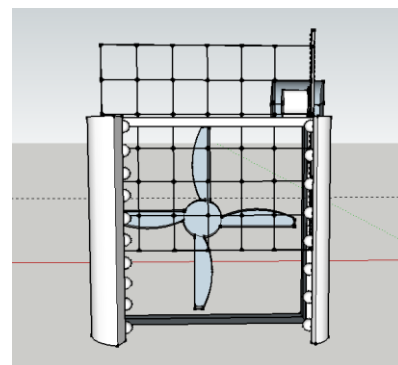
The air purification module is installed behind of the fan. It utilize multi fans to circulate air and make nano-level catalyst to react with harmful substances in the air. Thus the concentration of these substances could be reduced and the air could be purified. The diagram of the air purifier is shown in figure 5.



(a)Side view



(b)Top view



(c)Main view

Fig. 5. Air purification unit diagram

VI SUMMARY

In view of the low performance, poor flexibility and single function of the existing electric fans, a kind of intelligent fan cleaning ventilation system based on single chip microcomputer is designed. The system can detect the surrounding environment, automatically adjust the fan speed according to the changes of temperature, humidity and concentration of harmful substances, and also can be intelligently controlled by the user. Compared with the traditional fan, this system combines the pipeline ventilation technology,

Bluetooth technology, and photocatalytic purification technology. It is so energy saving, flexible and powerful that has a broad market prospect.

References

- [1] Minling Zhu, Ning LI. Development status and future analysis of smart home[J]. Television technology. 2015,(04):82-85.
- [2] Huang Weilong, Zhang Guangde, Guo Jianzhong, Zhao Huiyong, Chen Qingchu, Zhou Ze, Wang Likun. Performance Research of multi fan radiator for vehicle engine [J]. Journal of Wuhan University of Science and Technology, 2017,(01):65-69.
- [3] Zhang Yi, Lu Guodong, Yu Xiaoli, Shi Haimin, Zhang Wenfeng, Xia Lifeng. Many commercial vehicle cooling fan module, [J]. Automotive Engineering, 2014,(05):552-555.
- [4] Xu Zhigang, Huang Tao. [J]. electronic design project of intelligent fan based on single chip microcomputer, 2016,(11):154-156.
- [5] Liu Jinshan. Design of intelligent speed regulator for electric fans based on MCS-51. [J]. electronic quality, 2004, (10): 71-72.
- [6] Xie Zhiping. Intelligent temperature control fan based on single chip microcomputer [J]. new technology and products in China, 2011, (02): 152-153.
- [7] Sun Yang. Energy saving and economic evaluation method of air conditioning ventilation duct reconstruction in existing buildings [D]. Harbin Institute of Technology, 2010.
- [8] Wang Biao. Research on the resistance performance of air conditioning ventilation duct [D]. Harbin Institute of Technology, 2009.
- [9] Luo Jian. Research and implementation of Bluetooth communication system based on Android platform [D]. North China Electric Power University, 2013.
- [10] Wang Wei. Design and implementation of audio applications for Bluetooth devices based on Android platform [D]. Beijing University of Posts and Telecommunications, 2009.
- [11] Ding Fei, Zhang Xiliang, Zhang Shiqing. Wireless communication technology based on ZigBee and its application [J]. communication technology in Jiangsu, 2006, (05): 24-27.
- [12] Zhu Yan. Application of new biological photocatalyst technology in life and industry fields [J]. Tianjin paper industry, 2015, (03): 9-13.
- [13] Yang Weili. Market attention of photocatalyst technology [J]. environment, 2006, (01): 66-67
- [14] Zhang Bo, Wang Ming Lian, Wang Yue, Xing Rongqi. Application of photocatalysis technology in disinfection [J]. Chinese Journal of disinfection, 2009, (03): 314-315.
- [15] Weng Tong Sheng. Research and design of photocatalytic air purifier [J]. Canada, 2013, (24): 120-121.

Design and study on resistance type semiconductor gas sensor characteristics test system based on LabVIEW

ZHANG Jun-hong; WANG Qiao; ZHANG Shu-hui

(College of Instrument Science and electrical engineering, Jilin University, Changchun 130012, China)

Abstract—In view of the low efficiency of traditional gas sensor measurement system, a resistance type semiconductor gas sensor measurement system with data acquisition, analysis, display and storage is designed. This system includes three parts: host computer, hardware circuit and component experiment box. The host computer is written by LabVIEW software, and it has the function of displaying the parameters and response characteristic curve of the gas sensor. In the aspect of hardware circuit, the automatic switch circuit of matching resistance is designed to adapt to the larger resistance range of the gas sensor, and the related sensors are used to monitor the working environment of the gas sensor in real time. The experimental box is made of transparent organic glass, and also has an exhaust device and an air injection device, so that the measurement is simple and convenient. The system test results show that the system can complete the gas sensor measurement, real-time temperature monitoring, data acquisition and report generation, and realize the efficient test of gas sensors.

Key words—Gas sensor Test system LabVIEW

I INTRODUCTION

In recent years, gas sensors have been widely used in many fields, such as fire alarm, environmental detection, chemical engineering, biological medicine, industrial production and so on. With the development of gas sensors, a test system which can detect and calibrate gas sensors is urgently needed. So far, this system is mainly divided into the following two kinds: First one is that colleges and universities designed according to teaching or research needs; the other is the company customized according to user needs, and because of the limit of user's demand, the enterprise will not produce in batches. Therefore, the development of this system in our country is still at a low level, which cannot meet the actual measurement needs [1]. In this paper, a resistance type semiconductor gas sensor measurement system based on LabVIEW is designed. The system adopts the principle of resistance partial pressure method, and indirectly calculates the resistance value of the sensor, then, the data is sent to the computer via the RS232 serial bus. At last, LabVIEW will analyze and process the data. In LabVIEW, the limited amplitude filtering and Butterworth filtering are adopted to improve the accuracy. At the same time, the human-computer interaction interface is friendly, which makes the user more convenient to use. In addition, there are temperature and humidity detection devices used to

monitor the sensor's work environment. The system can not only detect resistance type semiconductor gas sensors but also study resistance type semiconductor gas sensitive materials.

II SYSTEM OVERALL DESIGN

A Sensors and Experimental Methods

The resistance type semiconductor gas sensor utilizes the oxidation and reduction reaction of gas on the surface of semiconductor. This reaction changes the resistance of the sensor. The measuring methods of gas sensors are mainly divided into constant current method, constant voltage method and resistance partial pressure method. Constant current method adds constant current source to the sensor circuit, and indirectly calculates the resistance value of the gas sensor by measuring the voltage at the two ends of the gas sensor. Constant pressure method is to measure the gas sensor at both ends with constant measuring voltage, and then calculate the resistance value of the gas sensor by measuring the current flowing through the sensor. It is difficult to measure the constant voltage or measure the constant current amplitude because of the large range of resistance change of the gas sensor [7]. Therefore, the design adopts resistance partial pressure method, as shown in Fig.1, the A and B are the two poles of the gas sensing element, and the V_F is the heating voltage of the gas sensing element. The 5V is usually sampled and the sampling resistor

RL is connected in series in the test circuit. Sensor resistance is:

$$R_s = \frac{V_c - V_0}{V_0} R_L \quad (1)$$

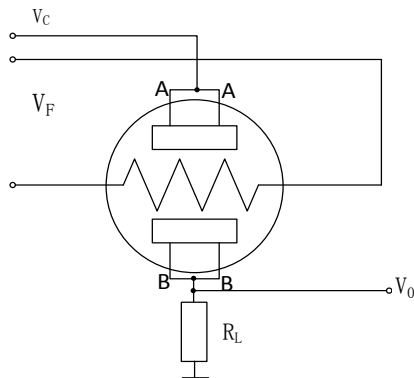


Fig.1 Measuring principle of resistance partial pressure method

According to the design plan, the operating temperature of the sensor needs 300 centigrade, and the resistance of the gas sensor is uncertain. Therefore, a heating circuit and a resistor automatic matching circuit are required. In practical test, the test voltage and heating voltage need to be stable 5V, so we designed the voltage regulator module. The voltage follower and low-pass filter also adopted to reduce random noise and high frequency noise.

B System Composition

The measuring circuit of this system adopts STM32F103C8 series chip as the core controller, and uses the ADC module of STM32, automatic switch circuit for matched resistance and signal conditioning circuit to realize the data acquisition of the gas sensor signal. At the same time, temperature and humidity sensors are used to monitor the working environment of the gas sensor. By using RS-232 bus communication, the host computer analyzes and processes the data sent out, and draws the response characteristic curve of the gas sensor, and saves the processed data. Among them, data conditioning, data acquisition, data communication and control are the key parts. The overall block diagram of the system is shown in Fig.2:

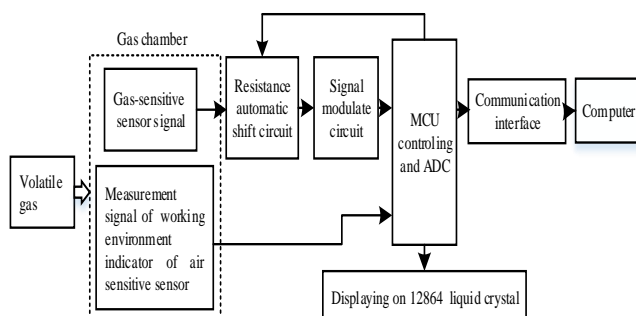


Fig.2 Block diagram of the sensor measurement system

C System Hardware Design

The hardware design of the system mainly includes measurement circuit design and component experiment box design. The design is mainly composed of voltage stabilizing source, matched resistance automatic switching part, signal conditioning part and serial communication part. The main function of the hardware circuit is to adjust, collect and detect the output signal of the gas sensor, and communicate with the host computer.

The regulator module uses the AMS1117 chip produced by AMS Company, which is used to generate stable 3.3V system voltage and 5V test voltage. The signal conditioning circuit includes a low-pass filter and a voltage follower, wherein the voltage follower is used as an impedance converter, and a low-pass filter can filter the system high-frequency noise. This circuit used the chip AD8571, which is a single supply, rail to rail zero drift, single channel amplifier produced by analog devices company.

The automatic switch circuit of matching resistance is composed of six controllable switches and a voltage dividing network, the switch adopts the relay switch, which has less internal resistance and can reduce the influence on the resistance value.

The driving circuit of the relay is mainly composed of PNP transistor and diode. The automatic resistance switch circuit is composed of six gears, and the resistance value of the sampling resistors includes 10, 100, 1k, 10k, 100k, 1M. In order to minimize the deviation of the measured resistance value, the shift critical value of each gear is x times of the matched resistance of the lower range gear, which is 1/x times of the matched resistance in the higher range gear. For the convenience of measurement, the maximum multiple of the measured resistance and the matched resistance in the first gear is 10, and the maximum multiple of the other gear is 5. When the measured resistance exceeds the range, the connected switch will automatically switch to a higher range gear; otherwise the switch will automatically switch to a lower range gear. The function of the automatic switch circuit which enlarges measuring range and measuring accuracy is to change the measuring voltage to less than 3.3V so that it can be collected by AD.

The component experimental box contains built-in testing elements, temperature and humidity sensors, gas injection and exhaust devices, which can simulate the working environment of the gas sensor very well. The measurement of the gas sensor is carried out in the experimental chamber. The configured gas is injected into the sealed experimental chamber, where the gas sensor is placed in. The collected data is sent to the host computer in real time.

D System Software Design

The upper computer of this system adopts LabVIEW graphical programming language as the programming tool, and the slave computer is programmed with C language.

The main function modules of the host computer include serial port setting, acquisition time display, real-time drawing, data table display, data storage and query. The host computer refreshes the data every 0.5s. The data processing module consists of Butterworth filter which can filter out various interference data and limiting filter which can effectively overcome the disturbances caused by accidental factors, which improves the accuracy of measurement effectively. As the data throughput of the acquisition system is relatively large, data storage needs to meet the characteristics of large capacity, high speed, reliability, real-time and easy to extract. Based on the above requirements, the system uses a spreadsheet file reading method. The front panel design of the upper computer is shown in Fig.3:

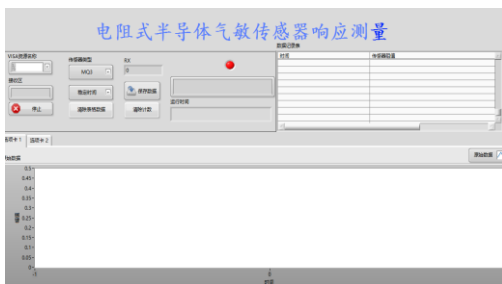


Fig.3 Design of computer display

The data processing software is modulus, and its structure is shown in Fig.4:

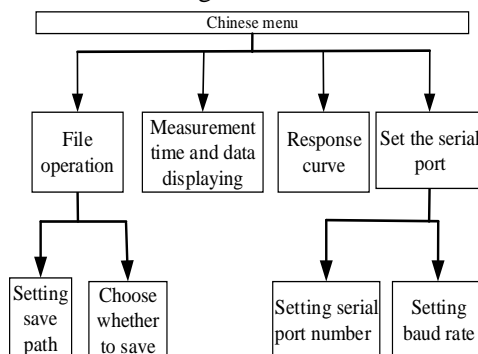


Fig.4 Diagram of data processing

The functions of the lower computer mainly include acquisition of sensing signals, automatic range switching, signal mean processing and serial communication. The lower computer collects the data collected every four times for average processing, and then sends the processed results to the upper computer, which effectively reduces the influence of system interference on the signal and improves the accuracy of the acquisition system. Fig.5 is a flow chart for completing a data acquisition.

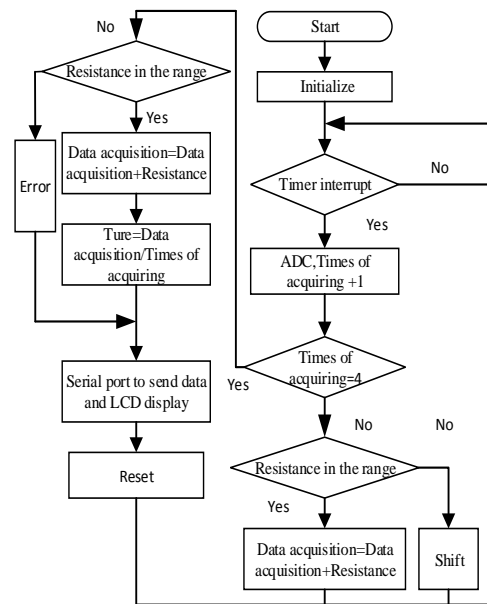


Fig.5 Software flow chart of lower computer

III RESULT ANALYSES

The sensor used in the experiment is MQ3 gas sensor. The volume of the experimental chamber is 1L, and the anhydrous ethanol is injected into the component experimental box through a micro sampler to observe the response curve of the gas sensor.

A Measurement of Initial Settling Time

When the gas sensor is heated, gas sensor resistance firstly decreased sharply and after a period of time called the initial stable time the resistance reaches a steady state which is called "initial steady state". The results of initial stability time measurements are shown in Fig.6:

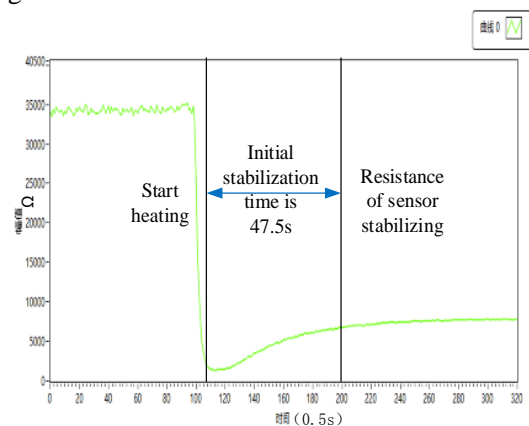


Fig.6 Initial stabilization time measurement

B Measurement of Response Recovery Time

The ambient temperature was 28.1 and the absolute amount of ethanol injected was 0.4μL. The measurement results are shown in Fig.7. The response time is 25.3s, and the recovery time is 38.7s.

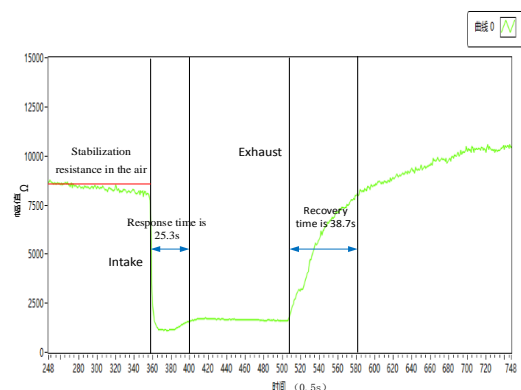


Fig.7 Response time of measurement of sensor

C Response of the Same Gas Sensor at Different Gas Concentrations

Different volumes of absolute ethanol were injected into the experimental box to observe the response parameters of the gas sensor.

Table 1 shows the response time and recovery time of gas sensors in ethanol gas at different concentrations.

Table 1 CHARACTERISTIC PARAMETERS OF GAS SENSOR IN ETHANOL GAS AT DIFFERENT CONCENTRATION

Absolute Ethanol(μL)	0.2	0.4	0.6	0.8	1
Response Time (s)	25.5	25.3	25	21.5	17.5
Recover Time (s)	49.5	38.7	49.5	30	49.5

The response time decreases with the increase of gas concentration, and the recovery time does not decrease with the increase of gas concentration.

IV CONCLUSION

The system has been experimentally verified to quickly and easily measure the response characteristics of resistive semiconductor gas sensor. It has the characteristics of high precision, stable and reliable performance and user convenient and flexible operation, great convenience to our life and production, has a certain practicality. Real-time measurement system using LabVIEW programming system display panel, you can collect data at the same time analysis and display data, draw the gas sensor response curve. Reliable hardware design and friendly software design interface make testing easier and more efficient. The gas sensor test system 0.5s refreshes the data once, and the measurement accuracy is better than 1%. It can meet the measurement requirements and has high cost performance. But the system still has a lot of room for improvement, the accuracy of the system needs to be

further improved. The mode of gas intake can be changed into automatic gas intake to reduce the harm of volatile gases to the human body.

Reference

- [1] Qi Changyu, Han Genliang, Xu Wude, Yang Xuhui, Ma Hongwei, Shang Liping. A gas sensor testing system based on Virtual Technology[J]. *Automatic instrument*. 2017, 38(5):81-84.
- [2] Qiao Jiping, Lv Yuxiang, Hu Hailin, Zhang Zhaoxia. Design and research of electrochemical gas sensor characteristic testing system based on LabVIEW[J]. *Instrument technology and sensors*. 2013, 12:90-96.
- [3] Lu Pin, Qiu Wei, Yue Chengjun, Kang Da, Zhang Shaocheng. Research progress of resistance type semiconductor formaldehyde sensors[J/OL]. *Sensors and Microsystems*. 2016, (12):1-6.
- [4] Lu KaiLin. Time response of gas sensors based on STM32 acquisition platform[D]. Anhui, Anhui University Of Science And Technology. 2015.
- [5] Xu Jiaqiang, Han Jianjun, Sun Yuan, Xie Bing. Research progress of sensitive mechanism of semiconductor gas sensors[J]. *Sensors and Microsystems*. 2006, (11):5-8.
- [6] An Wen, Wei Guangfen, Yang Chunying. Characteristic parameter analysis of gas sensor[J]. *Journal of Sensor Technology*. 2012, 25(4):438-443.
- [7] Ma Hongwei, Chen Xiaotong, Qi Changyu, Zhang Hongxia, Li Gongnong, Han Genliang. Circuit design of gas sensor static test system[J]. *Gansu Journal of Science*. 2010, 22(04): 124-128.
- [8] Zhu Zhipeng, Li Yinhua. Research on gas sensor characteristic test system [J]. *Chemical automation and instrument*. 2015, 43(5):508-512.
- [9] Song Ling, Shi Yunbo, Xiu Debin, Hu Min, Wang Liquan. MSP430 based gas sensor batch testing system [J]. *Electronic measurement technology*. 2009, 32(10):77-80.
- [10] Yang Yong, Bai Zikui, Xie Changsheng. Research progress of metal oxide gas sensor stability [J]. *Sensors and Microsystems*. 2007, (02):1-3+7.

Study on the Measurement of Cerebral Blood Flow Parameters Based on PDD – NIRS

LIU Guang-da; WANG Yu-lin; QIN Qi, ZHANG Lan-xi; QIAN Cheng-hui; SHANG Xiao-hu; ZHA Yu-tong; CAI Jing

(*jilin university instrument science and engineering institute, changchun, 130021*)

Abstract—Cerebral blood flow and cerebral blood flow parameters has been the focus of clinical medical research. They can be used to assess the human cerebrovascular parameters, prevention of cerebral infarction and cerebral hemorrhage and many other physiological diseases. The current clinical measurement of cerebral blood flow parameters mainly through the thermal dilution method and indicator dilution method. But the thermal dilution method and indicator dilution method requires catheter insertion and timing blood collection, which will cause some damage to the body. In this paper, a new, noninvasive and rapid method for measuring cerebral blood flow is proposed based on Fick's law and Lambert's law. The method based on PDD-NIRS technology, the use of indocyanine green as an indicator, through the introduction of brain and arterial ICG calculated CBF. In order to verify the correctness of the model, adult rabbit was used as the experimental object. The ICG pigment was injected rapidly in rabbits, at the same time the CBF was measured by PDD-NIRS method, also the CBF value was calculated. The experimental results demonstrate the correctness of the measurement method.

Key words—PPD-NIRS cerebral blood flow Noninvasive detection indocyanine green

I. INTRODUCTION

THE brain, as the central nervous system of human activity, has always been one of the key research directions in the field of life sciences. With the Human Brain Program and the Human Genome Project, brain function research and brain status monitoring have become an important research topic for current. And in the course of the normal operation of the brain, blood supply plays a vital role. The blood flow required by the human brain accounts for about 15% to 20% of the total blood output of the heart. At the same time monitoring the human brain blood flow parameters can be clinical cardiovascular and cerebrovascular disease monitoring and recovery of postoperative recovery to provide important help.

At present, the field of clinical medicine mainly through the thermal dilution method and indicator dilution method for cerebral blood flow testing, but with complex operation, high damage shortcomings. In addition, positron emission tomography (PET) and functional magnetic resonance imaging (fMRI) can also detect changes in blood flow to specific brain regions, but are expensive and radioactive. As a result, they are not suitable for rapid detection of CBF.

As early as 1977, the scientist Jobsis discovered the infrared light on human tissue good transmission. It is the first time to verify the near infrared spectroscopy to detect the feasibility of blood oxygen.

In 1988, Kuber et al proposed a new method of measuring the local blood flow by using near infrared spectroscopy. They used ICG as an indicator to verify the feasibility of its measurement. However, the measurement method requires catheter insertion, complicated operation and easy infection.

In 1992, Farrell et al. established a photon scattering mathematical model with near-infrared light characteristics based on the theory of light scattering. This provides a good correction for NIRS measurements.

In 1999, Jordan A. Guenette et al. used ICG as an indicator to measure the blood flow of human respiratory muscle based on near-infrared spectroscopy, and achieved good results [1]. Before and after 2012, Liu Guangda et al. measured cardiac output and circulating blood volume based on the method of PDD and NIRS, using ICG as an indicator. This verify the feasibility of ICG as an indicator on human blood flow measurement [2]. In 2016, Zhayu Tong et al. proposed a human brain blood flow measurement model based on NIRS-ICG technique, and used this model to

measure the cerebral hemodynamic parameters of pigs, the results are realistic[4].

This paper, based on predecessors' work, proposed a non-invasive measurement on the human body CBF. This method used the light scattering theory to correct the results, making use of Fick's Law and Revised Lambert's Law.

II CBF MEASUREMENT PRINCIPLE

CBF measurements were performed according to Fick's law. Fick's law indicates that the amount of dQ/dt in the biological tissue unit is equal to the difference between the material reaching the biological tissue and leaving the biological tissue flow. In this formula, the flow is calculated from the product of blood flow and substance concentration in the tissue.

$$\frac{dQ}{dt} = F \cdot (C_a - C_v) \quad (1)$$

Time integration of formula one:

$$\frac{F}{W} = \frac{C}{\int_0^t C_a - C_v dt} \quad (2)$$

In the above formula, F is defined as the blood flow in the unit brain tissue, C is the concentration of the tracer in the biological tissue, W is the quality of the biological tissue. C_a and C_v respectively represent the concentrations of arterial and venous tracers in the tissues. Fick's law further states that when the integration time t is less than the minimum propagation time of the blood through the organ, the tracer does not appear in the venous outflow. Therefore, the use of ICG as a measure of human brain blood flow tracer can be expressed as follows:

$$CBF = \frac{K \cdot \Delta C[ICG]_{\text{brain}}}{\int_0^t \Delta C[ICG]_{\text{ear}} dt} \quad (3)$$

Where MW_{ICG} is the relative molecular weight of ICG, D_t is the density of brain tissue (g/ml). That is, K is a normalized constant for relative molecular mass and brain tissue density, representing relative blood flow per 100 g of tissue. Where $C[ICG]_{\text{brain}}$ indicates the concentration change of ICG in brain tissue at minimum propagation time, That is, the concentration of tracer in the brain tissue, to characterize the flow of material from the brain tissue, That is measured with

frontal lobe probe data. $C[ICG]_{\text{ear}}$ indicates that ICG from the arterial blood into the brain tissue concentration changes, that is, the material into the brain tissue flow, That is measured with ear probe data.

2.1 $\Delta C[ICG]_{\text{brain}}$ Measurement methods

$\Delta C[ICG]_{\text{brain}}$ measurements were performed using NIRS near-infrared spectroscopy based on Langbobier's law. NIRS near-infrared spectroscopy is the introduction of clinical medicine in recent years, emerging technologies. Infrared light penetration is strong and can penetrate the body deep tissue. By analysis of the infrared light signal extraction, we can understand the human body tissue and blood flow.

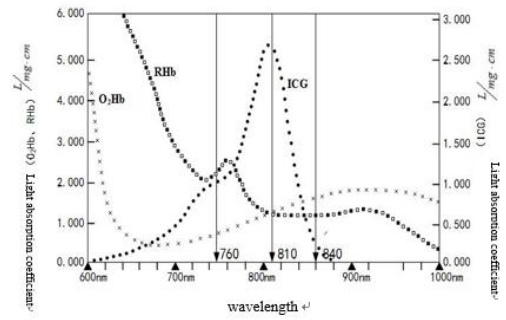


Fig.1 Absorption of HbR, HbO₂ and ICG

Figure 1 shows the absorbance curve of HbO₂ (oxygenated hemoglobin, HbO₂), HbR (reduced hemoglobin, HbR) and ICG for different wavelengths of infrared light. From the above-mentioned absorption spectrum characteristic curve, it was found that the absorption coefficient of HbO₂ and HbR was the same at 810 nm, and the absorbance of ICG reached a peak. And the absorbance characteristics of the absorption chromophores on both sides of 810nm were separated. Therefore, in the $C[ICG]_{\text{brain}}$ measurement process, we selected 760/810/840 three-wavelength light source for measurement.

Correction - Lambert's Law points out the relationship between the incident light intensity and the intensity of the emitted light after passing through the inhomogeneous medium. It quantitatively depicts the attenuation of the light intensity after the photon passes through the uniform medium and the situation which is absorbed by the medium.

$$OD^\lambda = \lg \frac{I_0}{I} = \mu_a^\lambda \cdot L + G$$

$$L \approx L(\lambda) = \frac{\partial OD}{\partial \mu_a} = DPF(\lambda) \cdot r \quad (4)$$

Where the absorption coefficient is the product of the chromospheric absorption coefficient and the chromophore concentration C , G is the optical attenuation coefficient, and L is the differential optical path. Further deduction shows that when the medium contains different light-absorbing material, The absorption coefficient is a linear superposition of the absorption coefficients of each substance.

$$\mu_a^\lambda = \mu_{a1}^\lambda + \mu_{a2}^\lambda + L + \mu_{an}^\lambda = \sum_{i=1}^n \mu_{ai}^\lambda \quad (5)$$

When the photons pass through the human brain tissue, the main absorption chromophore are HbO₂, HbR and ICG, μ_{ai}^λ indicate the absorption coefficient of the three, and we can get the following equations:

$$\Delta OD^{\lambda 1} = (\mu_{a1}^{\lambda 1} + \mu_{a2}^{\lambda 1} + \mu_{a3}^{\lambda 1}) \cdot L \quad (6)$$

$$\Delta OD^{\lambda 2} = (\mu_{a1}^{\lambda 2} + \mu_{a2}^{\lambda 2} + \mu_{a3}^{\lambda 2}) \cdot L \quad (7)$$

$$\Delta OD^{\lambda 3} = (\mu_{a1}^{\lambda 3} + \mu_{a2}^{\lambda 3} + \mu_{a3}^{\lambda 3}) \cdot L \quad (8)$$

$$\mu_{ai}^{\lambda i} = \alpha_i^{\lambda i} \cdot C_i \quad (9)$$

The solution of equations are as follows:

$$\begin{aligned} \Delta C[ICG_{\text{brain}}] = & \alpha_{\text{HbR}}^{\lambda 1} (\alpha_{\text{HbO}_2}^{\lambda 2} \cdot \Delta OD^{\lambda 3} - \alpha_{\text{HbO}_2}^{\lambda 3} \cdot \Delta OD^{\lambda 1}) \\ & - \alpha_{\text{HbO}_2}^{\lambda 1} (\alpha_{\text{HbR}}^{\lambda 2} \cdot \Delta OD^{\lambda 3} - \alpha_{\text{HbR}}^{\lambda 3} \cdot \Delta OD^{\lambda 2}) \\ & + \Delta OD^{\lambda 1} (\alpha_{\text{HbR}}^{\lambda 2} \cdot \alpha_{\text{HbO}_2}^{\lambda 3} - \alpha_{\text{HbR}}^{\lambda 3} \cdot \alpha_{\text{HbO}_2}^{\lambda 2}) \\ & \frac{L[\alpha_{\text{HbR}}^{\lambda 1} (\alpha_{\text{ICG}}^{\lambda 3} \cdot \alpha_{\text{HbO}_2}^{\lambda 2} - \alpha_{\text{ICG}}^{\lambda 2} \cdot \alpha_{\text{HbO}_2}^{\lambda 3})]}{L[\alpha_{\text{HbR}}^{\lambda 1} (\alpha_{\text{ICG}}^{\lambda 3} \cdot \alpha_{\text{HbO}_2}^{\lambda 2} - \alpha_{\text{ICG}}^{\lambda 2} \cdot \alpha_{\text{HbO}_2}^{\lambda 3})]} \\ & - \alpha_{\text{HbO}_2}^{\lambda 1} (\alpha_{\text{HbR}}^{\lambda 2} \cdot \alpha_{\text{ICG}}^{\lambda 3} - \alpha_{\text{HbR}}^{\lambda 3} \cdot \alpha_{\text{ICG}}^{\lambda 2}) \\ & - \alpha_{\text{ICG}}^{\lambda 1} (\alpha_{\text{HbR}}^{\lambda 2} \cdot \alpha_{\text{HbO}_2}^{\lambda 3} - \alpha_{\text{HbR}}^{\lambda 3} \cdot \alpha_{\text{HbO}_2}^{\lambda 2}) \end{aligned} \quad (10)$$

2.2 $\Delta C[ICG_{\text{ear}}]$ Measurement methods

$\Delta C[ICG_{\text{ear}}]$ measured by the method of the PDD. The pulse colorimetric is a method of measuring the concentration of a pigment by applying a periodic change in pulse pulsation time. When the photon passes through the earlobe, the path of the optical path changes due to the change in the thickness of the arterial pulse vessel. The size of the transmitted light

intensity will fluctuate with the pulse rate of cyclical changes. At this point the absorbance changes:

$$\Delta A = \log\left(\frac{I_0}{I - \Delta I}\right) - \log\left(\frac{I_0}{I}\right) = \log\left(\frac{I}{I - \Delta I}\right) \approx \frac{\Delta I}{I} \quad (11)$$

The main absorbable substances in the arteries are HbO₂, HbR, ICG. And arterial oxygen saturation is generally close to 99%, so the HbR content is very low and almost negligible. The following formula represents HbO₂ as Hb, ignoring the effect of HbR on light intensity. According to the correction of Langbobier's law, and the definition of pulsation is:

$$\begin{aligned} \varphi_A &= \frac{\Delta OD^{\lambda 1}}{\Delta OD^{\lambda 2}} = \frac{AC^{\lambda 1} / DC^{\lambda 1}}{AC^{\lambda 2} / DC^{\lambda 2}} \\ &= \frac{(\alpha_{\text{Hb}}^{\lambda 1} C_{\text{Hb}} + \alpha_{\text{ICG}}^{\lambda 1} C_{\text{ICG}}) \Delta D \cdot DPF(\lambda) + G}{(\alpha_{\text{Hb}}^{\lambda 2} C_{\text{Hb}} + \alpha_{\text{ICG}}^{\lambda 2} C_{\text{ICG}}) \Delta D \cdot DPF(\lambda) + G} \end{aligned} \quad (12)$$

Where DC is the direct light flow in the transmitted light intensity, mainly for the human skin, bone and other organizations on the absorption of light intensity, AC is the amount of pulse wave in the human body, which is related to the concentration of the absorption chromophore in the tissue.

Solution of formula (12) can be obtained:

$$\begin{aligned} C_{\text{ICG}} &= \frac{(\alpha_{\text{Hb}}^{\lambda 1} - \varphi_A \cdot \alpha_{\text{Hb}}^{\lambda 2}) \cdot C_{\text{Hb}}}{\varphi_A \cdot \alpha_{\text{ICG}}^{\lambda 2} - \alpha_{\text{ICG}}^{\lambda 1}} + \\ & \frac{1 - \varphi_A}{\varphi_A \cdot \alpha_{\text{ICG}}^{\lambda 2} - \alpha_{\text{ICG}}^{\lambda 1}} \frac{G}{\Delta D \cdot DPF(\lambda)} \end{aligned} \quad (13)$$

In formula (13), ΔD is the relative change in blood vessel thickness during pulse beat. When the thickness of the blood vessels of the human body occurs, the light scattering angle in the human body changes. As a result, the results can be amended to improve the measurement accuracy.

In this paper, the theory of light diffusion is introduced to correct the results: the biological tissue belongs to the light of the strong scatterer. When the photon enters the human tissue, the approximate diffuse reflection of the light in the biological tissue is described by the Boltzmann irradiance propagation formula:

$$\frac{1}{C} \cdot \frac{\partial}{\partial t} \cdot \varphi(r, t) - D \cdot \nabla^2 \cdot \varphi(r, t) + u_a \cdot \varphi(r, t) = s(r, t) \quad (14)$$

Where C is the propagation velocity of the photons in

the biological tissue, $\varphi(r,t)$ Represents the photon flow rate, $s(r,t)$ Represents the light source, D Represents the diffuse reflection coefficient. The specific conditions of the above equation solution [5-6] is available:

$$OD = \lg \frac{I_0}{I} = \frac{r\sqrt{3}u_a \cdot u_s'}{\ln 10} + 2\log r - \log \frac{\sqrt{3}}{2\pi} [1 + \frac{2}{3}A] - \log \sqrt{\frac{u_a}{u_s'}} \quad (15)$$

Where the optical density is related to the absorption coefficient, the scattering coefficient and the distance from the light source. The Full differential of formula is available:

$$\Delta OD^\lambda = \frac{1}{2\ln 10} \left[\sqrt{3}r \left(\sqrt{\frac{u_s'(\lambda)}{u_a(\lambda)}} - \frac{1}{u_a(\lambda)} \right) \cdot \Delta u_a + \sqrt{3}r \cdot \left(\sqrt{\frac{u_a(\lambda)}{u_s'(\lambda)}} + u_s'(\lambda) \cdot \Delta u_s' \right) \right] \quad (16)$$

The amount of change in optical density can be measured by a photodetector. At the same time, Through the above formula (5) we can get the following formula:

$$\Delta \mu_a^\lambda = \alpha_{HbO_2}^\lambda \Delta C(HbO_2) + \alpha_{Hb}^\lambda \Delta C(Hb) + \alpha_{ICG}^\lambda \Delta C(ICG) \quad (17)$$

The experimental results of ΔOD^λ and $\Delta \mu_a^\lambda$ into

(16) can be obtained $\Delta \mu_s'$. Simultaneously:

$$\mu_s' = \mu_s (1-g) \quad (18)$$

$$g = \frac{\int P(\theta) \cos \theta d\cos \theta}{\int P(\theta) d\cos \theta} \quad (19)$$

μ_s' as a constant, is the scattering coefficient only associated with the wavelength. g is the weighted average of the cosine of the scattering angle when the photon is scattered. The current real-time scattering angle can be obtained by differentiating the formula (19). And when the human arterial blood vessels beat, There is a function of the relationship between the thickness and the scattering angle. Using the method of segmented interpolation of equidistant nodes, The relative amount of periodic changes in the vessel wall can be obtained. And the accuracy of the thickness measurement is positively correlated with the number of segments N and the number of interpolation

polynomials. Using the above method and calculation formula, $\Delta C[ICG_{brain}]$ can be measured by the arterial blood into the brain tissue concentration.

III CEREBRAL BLOOD FLOW DETECTION SYSTEM

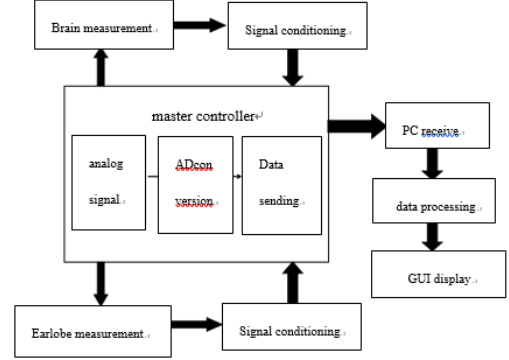


Fig.2 CBF measurement system block diagram

The system of the brain forehead and earlobe measurement module include 760nm, 810nm, 840nm LED and photodetector. The photodetector signal is processed by the signal conditioning module and is sent to the AD conversion. Then data was sent to the host computer through Bluetooth to calculate. Finally, the brain flow curve was drawn in the GUI interface.

IV EXPERIMENTAL METHODS AND ANALYSIS

In order to confirm the feasibility of this method. The method was verified by adult suffocation test and rabbit animal experiment. Because the cerebral blood flow measurement process involves scattering and absorption of HbO₂ and HbR on infrared light, the sensitivity of headware circuit is tested by adult suffocation test.

Suffocation test selected one healthy male, Then the amount of HbO₂ and HbR in the brain tissue was calculated when the male was normal and suffocated. At the same time, CBF measurement experiment selected rabbit as the experimental object, because the blood circulation systems of rabbits are similar to human. (This experiment has been reviewed by the Jilin University Ethics Committee):

We need choose a healthy male, whose age is 20 years old. The measuring device is fixed in the front frontal lobe of the measured person. Experiments require the measured staff to keep calm and maintain normal breathing. Half a minute later, he began to

suffocate as required. Then after the end of breath, the data was calculated by the host computer.



Fig.3 Suffrage experiment

Figure 4 is the software GUI interface, it can display the changes of the measured pulse wave.

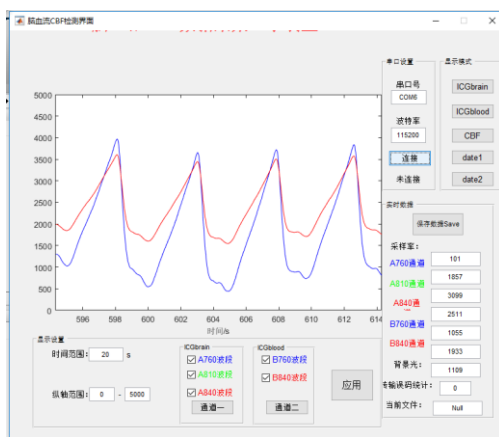


Fig. 4 GUI interface diagram

Figure 5 for the human pulse wave sign

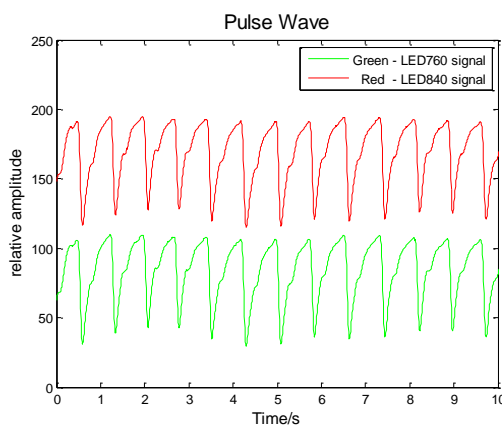


Fig.5 Human pulse wave chart

Figure 6 is a graph of the body's suffocation test. The red curve represents the amount of change in HbR concentration, and the blue curve represents the HbO₂ concentration change. As is depicted in the image, the concentration of HbR and HbO₂ did not change much during normal respiration. However, after time reach to 60s, HbR increased rapidly and HbO₂ decreased sharply. The result verifies that the sensitivity of the

hardware system meets the expected requirements. It can also explain the feasibility of blood flow algorithm indirectly.

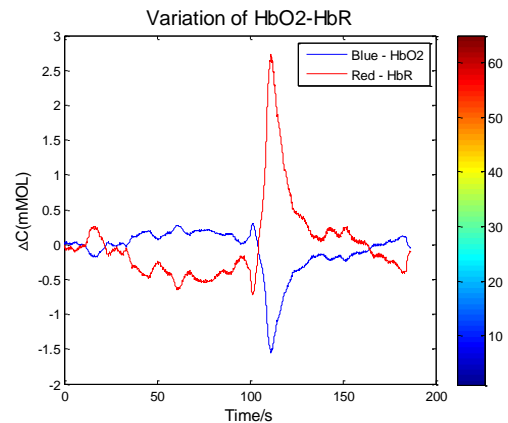


Fig.6 Cerebral oxygen fluctuation of suffocation

4.1 Animal experiments

The healthy rabbits were selected as the experimental subjects with the weight of 1.5kg-2kg. As is shown in Figure 7. The rabbit was placed on the bench with a supine position fixed. After intravenous injection of ketamine 6mg / Kg and 0.2mg / Kg stable basal anesthetic, The staff fixed the experimental device in the rabbit forehead and earlobe. Then the ICG was dissolved in sterile distilled water at a ratio of 1:10 and mixed thoroughly. According to white rabbits weight 0.5ml / Kg dispensing, at the same time, prepare 10ml of saline.

After the fixation of the device was completed, the brain blood flow measurement system was started. The ICG was injected into the white rabbits intravenously within 8s, then the saline was injected. The cerebral blood flow measurement system starts to measure and collect data since injecting ICG. Each experiment time is 2 minutes. After the end of the experiment by the lower computer to send all the data sent to the PC to processing.



Fig.7 Rabbit Experiment

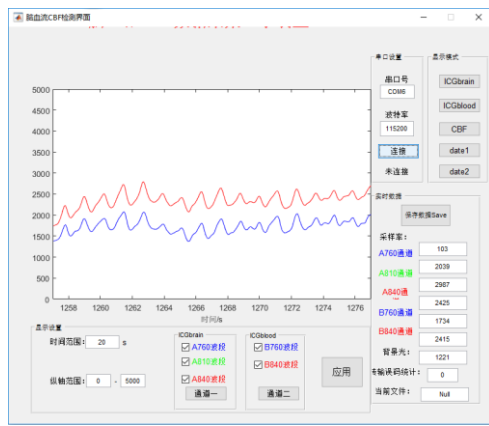


Fig.8 Rabbits raw pulse wave data

Figure 9 for the wavelength of 760nm and 840nm pulse rate ratio.

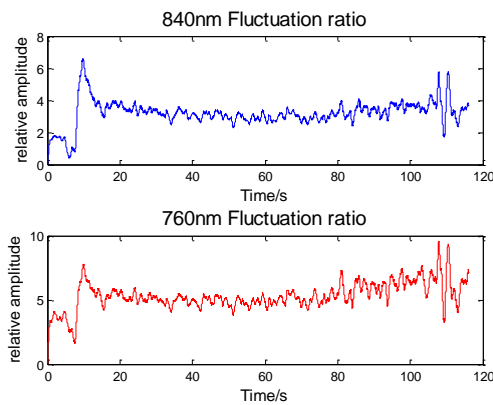


Fig.9 Pulse volume ratio chart

Figure 10 for the arterial ICG introduction curve. ICG concentration in the rapid arrival of the peak after injection, resulting in sharp decline in light intensity, the highest point of the curve represents the ICG in the white rabbit arterial lead to the largest ICG rapid metabolism, the rapid decline in concentration. ΔT in the figure 10 for the ICG concentration peak time required to rise time, about 8s or so. Figure 11 shows the concentration of brain tissue changes in the concentration of brain tissue in 16s or so reached a peak of about 21.26ml / g / min.

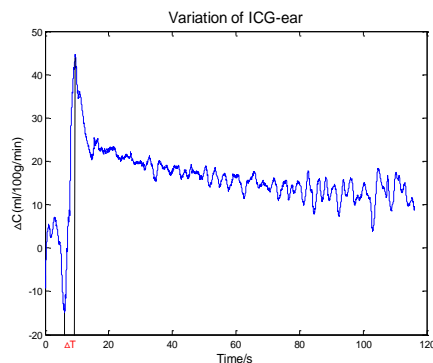


Fig.10 chart of Arterial ICG introduction

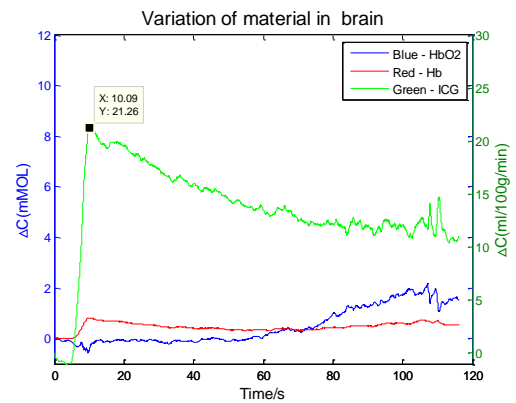


Fig.11 chart of brain tissue ICG introduction

The above data were obtained in (3), and the cerebral blood flow (CBF) of the white rabbits in resting state was 191.92 ml / 100 g min, which resulted in the noninvasive detection of cerebral blood flow in rabbits. The feasibility and correctness.

4.2 Experimental comparison

Ultrasound detection of white rabbits in a professional pet hospital, as shown in Figure 12, the use of ultrasound Doppler principle can measure blood flow velocity n (cm / s) and vascular diameter L (cm). Which can be estimated blood volume rate VC , and then push the cerebral blood flow. Take the healthy white rabbit as the experimental sample, remove the neck after the rabbit hair, ultrasonic probe to measure the rabbit's internal carotid artery, the internal carotid artery around the lateral back, but the trunk into the brain, the supply of brain blood. The total blood flow provided by the internal carotid artery estimates the value of cerebral blood flow. The internal carotid artery provides blood flow:

$$Q = n \cdot S$$

Where n is the blood flow velocity, S is the blood vessel area, and the above calculation results for the total intracranial total blood flow, in order to obtain unit cerebral blood flow, should be counted to every 100g brain tissue blood flow, rabbit brain weight. About 100g-150g, the average weight of 120g to calculate the unit of cerebral blood flow, find the internal carotid artery position, and every 10 minutes to measure the data.

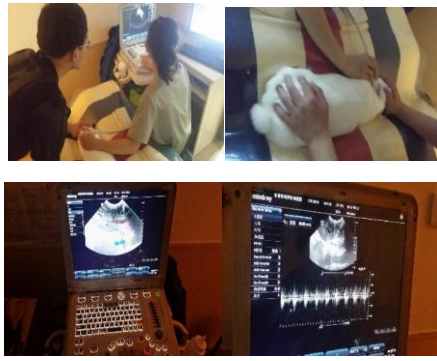


Fig.12 Animal ultrasound experiment

Table 1 Ultrasonic measurement of CBF data

Blood flow rate n(cm/s)	Blood vessel diameter L(cm)	Blood flow Q (ml/min)	Unit blood flow CBF(ml/100g · min)
25.26	0.46	251.87	209.89
25.21	0.45	240.56	200.47
25.78	0.45	246.00	205.00
26.58	0.45	253.64	211.36
26.02	0.45	248.29	206.91

Table.2 data of NIRS-DDG measurement CBF

The number of measurements	1	2	3	4	5
CBF(ml/100g · min)	199.92	195.03	200.56	203.82	201.31
Ultrasound results (ml/100g · min)	207.89	200.47	205.00	211.36	206.91
Experiment relative error (%)	3.83	2.71	2.17	3.57	2.71

Table.3 Comparison of multiple sets of experimental samples

Different experimental samples	Ultrasound results (ml/100g · min)	NIRS method to measure the results (ml/100g · min)	Experiment relative error (%)
Sample one	212.35	209.56	1.31
Sample two	207.56	202.32	2.52
Sample three	215.23	210.36	2.26
Sample four	235.32	228.32	2.97
Sample no	204.19	198.87	2.60

Analysis of experimental results: the internal carotid artery tissue not only for the experimental object to provide intracranial blood supply, but also for the neck and other parts of the blood, so the use of Doppler

ultrasound detection of a certain constant system error, in the subsequent data processing can be eliminated by algorithm. It can be seen that the relative error of CBF measured by PDD-NIRS method is in the range of 2% -4%, so the feasibility of PDD-NIRS method for measuring cerebral blood flow CBF can be successfully verified.

V CONCLUSION

Using NIRS, ICG method to measure cerebral blood flow, to overcome the traditional method of measuring a long time, measuring damage and easy to cause infection and other shortcomings. The method achieved a noninvasive rapid cerebral blood flow test, compared with the clinical test, the average error to meet the clinical diagnostic requirements. Based on the PDD-NIRS cerebral blood flow measurement method for the clinical diagnosis of cardiovascular and cerebrovascular diseases and clinical brain blood flow monitoring provides a useful reference means and methods. With the advancement of science and technology, the application of optical means to detect the human body will not only be limited to near infrared spectroscopy stage. The three-wavelength measurement method used in this paper proves the correctness of the NIRS-PDD measurement method. In the future, the near-infrared full spectrum will be used to measure the human body in order to obtain more detailed information and higher measurement accuracy degree.

References

- [1] GUENTTE JORDAN A, Henderson William R. Blood flow index using near-infrared spectroscopy [J]. AJP: Regulatory, Integrative and Comparative Physiology (Online), 2011, 300(4): 984-992.
- [2] LIU G D, ZHOU R D, ZHA Y T, et al.. Study on indicator densitometry determination method of hemodynamic parameters. [J]. Spectroscopy and Spectral Analysis. 2016, 36(03): 662-666. (in Chinese)
- [3] ZHA Y T, LIU G D, WANG Y X, et al.. Noninvasive Cerebral Blood Flow measurement base on NIRS-ICG. [J]

- Spectroscopy and Spectral Analysis. 2017, 37(04): 1069-1073.(in Chinese)
- [4] Roberts I G,Fallon P et al.. Measurement of cerebral blood flow during cardiopulmonary bypass with near-infrared spectroscopy.[J]. The Journal of thoracic and cardiovascular surgery,1998,115(1):94-102
- [5] HOU X L, TENG Z C, DING H S,et al..Detecting Cerebral Hypoxia-Ischemia of Newborn Piglets Using Spatially-Resolved Near-Infrared Spectroscopy.[J]. Spectroscopy and Spectral Analysis. 2008, 28(10): 2263-2267.(in Chinese).
- [6] Farrell T J, Patterson M S. A diffusion theory model of spatially resolve,steady-state diffuse reflectance for the noninvasive determination of tissue optical properties in vivo.[J]Medical Physics, 1992, 19(4): 879-888.
- [7] LUO Q M, DENG H, GONG H,et al..Near-infrared spectroscopy for the measurement of cerebral blood flow.[J]J Infrared Millim W.1999,18(02):44-50.(in Chinese)
- [8] LIU G D, JIN S L, LI F, et al..A method for detecting hepatic reserving function base on photoelectric pulse dye densitometry analysis.[J] Journal of Optoelectronics. Laser2012,23(06):1216-1220.(inChinese)
- [9] Guenette Jordan A,Vogiatzis Ioannis et al.. Human respiratory muscle blood flow measured by near-infrared spectroscopy and indocyanine green.[J]. Journal of Applied Physiology,2008,104(4):1202-10.
- [10] Habazettl Helmut,Athanasopoulos Dimitris,Kuebler Wo-lfgang M.et al..Near-infrared spectroscopy and indocyanine green derived blood flow index for noninvasive measurement of muscle perfusion during exercise.[J].Journal of Applied Physiology, 2010, 108(4):962-7
- [11] Boushel R,Langberg H,Olesen J.et al.. Regional blood flow during exercise in humans measured by near-infrared spectroscopy and indocyanine green.[J]. Journal of Applied Physiology,2000,89(5):1868-1878
- [12] LIU G D, CAO Z Y, ZHOU G. et al..A anti-disturbance cerebral oxygen analyzer base on near-infrared spectra[J] Optics and Precision Engineering.2016,24(08):1846-1853.
- [13] LIU M.Design of cerebral oxygenation monitor for the newborns.[D]TianjinUniversity,2005.27(4):591-593.
- [14] FANG H, XU J X.A new technique for cerebral blood flow measurement- One atmosphere C T[J].Journal of General Hospital of Air Force,1990,6(03):44-45.
- [15] YE J L,JIANG Y, LUO S,et al..Development of Cardiac Output Monitoring System Based on Thermodilution Method[J]Chinese Journal of Medical Instrumentation, 2014,38(05):337-340.
- [16] LIU C Y.Research of a cerebral dynamic parameter detecting system using Near-infrared spectroscopy. [D]. Harbin Institute of Technology.2013.
- [17] LI L C, LI K Y, QIN Z.Development of new-type near-infrared brain blood oxygen monitor.[J] Laser and Infrared | Laser Infr.2006,36(08):661-664.
- [18] ZHAO J.Non-invasive Measurements of the Optical Properties in Newborn Infant Brain.[D]Tsinghua University.2005.
- [19] TIAN F H, DING H S, WANG G Z,et al..The Use of Near Infra-red Spectroscopy for Monitoring Perfusion and Oxygen of Skin.[J]Spectroscopy and Spectral Analysis, 2002,22(02):209-212.
- [20] DENG Q K.Principle of modern medical instrument design.[M]Bei Jing:Science press,2005

The design and implementation of intelligent trash can based on Stm32

Xu Quan; Wang Mingcong; Xia Renqiu

(*jilin university instrument science and engineering institute, changchun, 130021*)

Abstract—This article introduces a design of smart trash bins, whose core is stm32, utilizing SolidWorks and AutoCAD to design and analyze the mechanical structure respectively. With the assistance of delicate mechanical structure and proper layout, the functions of the sensor get maximized and the system design tasks are completed eventually. When the system starts to work normally, various sensors are combined to detect and transfer the data to the controller. The controller can automatically control the switch cover, identify and classify the types of garbage via related algorithms.

keywords— intelligent trash can; Automatic switch cover; Automatic classification

I INTRODUCTION

WITH the increasing population all over the world, the production of garbage is growing gradually. Under this circumstance, environmental problems are becoming prominent increasingly. Facing the garbage flooding situation, the world's sight has transferred to focus on how to take scientific and effective means to achieve the re-use of resources instead of the control and destruction of the waste. It's reported that people have implemented garbage classification policy in Europe, the United States, Japan and other developed countries for many years [1]-[2], whereas the garbage classification mainly rely on manual sorting whose process is so cumbersome that cost a lot of manpower and resources.

The author is devoted to design a smart sort trash can which uses single-chip as the core [3]. Immediately people close to the trash, the infrared sensor gets signal and send a switch signal to the micro-controller. So that achieve the purpose that single-chip control stepper motor drive circuit and the function of open automatically through Mechanical transmission device. Under this circumstance, it facilitates the direct delivery of garbage which is beneficial to human health by reducing the direct contact with the trash and avoiding contamination of the trash cover the breeding of bacteria. When garbage is thrown into the barrel, the metal sensor works to detect whether the garbage is metal or not which decide the garbage sorted into the metal or non-metal area. In this paper, the intelligent trash must be convenient and practical, in which the metal sensor for non-contact detection of garbage also avoid the sensor pollution and damage, The trash can

with low price and simple structure, also simplifies the garbage classification process and achieve the effective recycling of garbage which has broad prospect of application.

II OVERALL SYSTEM AND MECHANICAL STRUCTURE

A Introduction to System Functions

In this paper, the intelligent classification trash can has two main functions which contains automatic flip and detection classification. The general design block diagram of the smart category trash is shown in Figure 1 below. The prototype is composed of the detection module, the classification module and the control module. The procedure of the research of the prototype is divided into mechanical structure design, control part hardware circuit design and software program design stage. The prototype uses a screw drive mechanism, central rotation mechanism, infrared sensor [4], metal proximity switch, stepper motor drive circuit which are connected with the micro-controller. The micro-controller will work by the sensor signal processing analysis to which control the stepper motor drive the corresponding Mechanism movement and then achieve automatic opening and closing of the trash. Finally it completes the automatic classification of garbage detection function by controlling the rotation of the steering gear [5].

B Overall Block Diagram of System

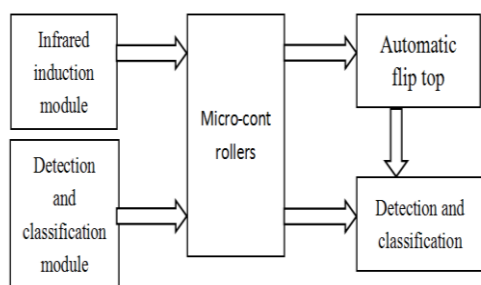


Fig. 1 The overall design diagram of system

C Introduction to System Mechanical Structure

In addition to the basic external frame, the mechanical structure of the prototype contains mainly prototype clamshell mechanism and prototype classification mechanism, the prototype flip mechanism selection screw drive mechanism, and then the stepper motor rotary motion into a lid of the opening and closing movement through the screw and stepper motor shaft connection; Garbage detection classification focus on the detection, the prototype classification agencies use the central rotation mechanism through the baffle rotation. The overall design of the mechanical mechanism shown in Fig. 2. below.

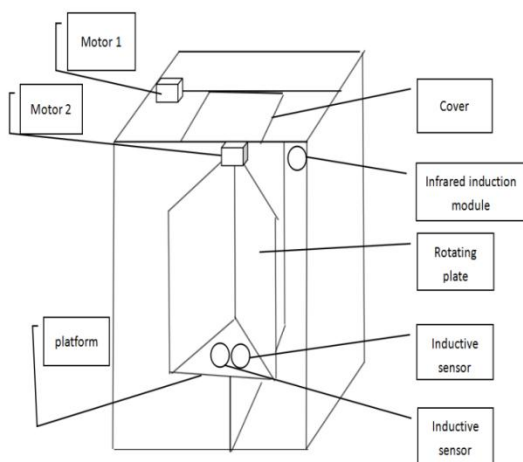


Fig. 2 Mechanical structure design drawing of intelligent trash can

D Design of Trash Automatic Clipping Mechanism

When someone approached the trash, the infrared sensor get the signal and send a switch signal to the micro-controller. Through the stepper motor drive circuit controlled by micro-controller, the stepper motor rotates so that achieve the action of the open and close of the lip. The prototype uses the screw drive mechanism to turn the stepping motor's output into the barrel opening and closing movement through the screw drive mechanism connected with the shaft.

What's more, there is a variety of mechanical transmission mechanism (device) can be used to achieve the movement of the lip's opening and closing

by stepping into the stepper motor rotation, such as winding mechanism, belt drive, hydraulic (air pressure) lifting system and so on.[6,7]. The winding mechanism is simple, while the system reliability is insufficient. The belt drive mechanism is low, in the process of switching cover, the lid and the trash cans easy to produce contact wear and deformation; Hydraulic or pneumatic lift system movement is smooth, while whose complex structure and practicality could not be satisfied. All in all, taking all factors into account such as durability, practicality, reliability etc. We select the screw drive mechanism to achieve the lid's opening and closing. Screw drive mechanism works smoothly with high precision which can achieve a more accurate opening and closing angle, so that avoid the contact wear and deformation between the barrel and the trash cans, thereby playing a role in improving product durability.

E Design of Automatic Classification Organization

After the trash can complete the automatic flip action [8]-[10], the garbage fell to the detection platform. Through the metal sensor detection, the single-chip control stepper motor rotation according to the signal which is sent to the micro-controller so that control the movement of the steering gear control mechanical structure which aims to achieve the garbage detection classification that the metal garbage and non-metallic garbage were pushed into the metal waste and non-metallic trash can. Aiming at the automatic classification mechanism of the trash can, this paper puts forward two kinds of design schemes which is called 'rail moving mechanism' and 'center rotation mechanism' respectively.

(1) Rail moving mechanism. This mechanism which is similar to the feeding car makes use of stepper motor drive box on the track to move back and forth. According to the sensor's test results, the mechanism moves to the corresponding trash top and open the bottom of the box to put the garbage into the corresponding bucket so that achieve the function of garbage detection classification.

(2) Center rotation mechanism. This structure utilizes the stepping stepper motor whose output certain rotation angle is accurate. Single-chip controls step stepper motor rotation direction and rotation angle according to the signal sent by the metal sensor. Under this circumstance, the structure could easily put different garbage into different barrels, thus realize the function of detection and classification.

Taking all the advantages and disadvantages of the two kinds of mechanical structures into consideration, the rail moving mechanism has the advantages of strong expansion and accurate operation which is easy to meet the requirements of the

classification of waste of different materials after the latter period while whose space and response is difficult to meet the design requirements of the prototype. The center rotation mechanism has the advantages of high classification efficiency and simple structure which can meet the requirements of the installation space of the prototype box under the existing conditions. The design of the rotating baffle is basically in accordance with the requirement of garbage detection classification. Eventually, we choose the central rotation mechanism as a prototype classification mechanism.

III DESIGN OF SYSTEM HARDWARE

A The Power Section

Power supply is the key components to ensure that

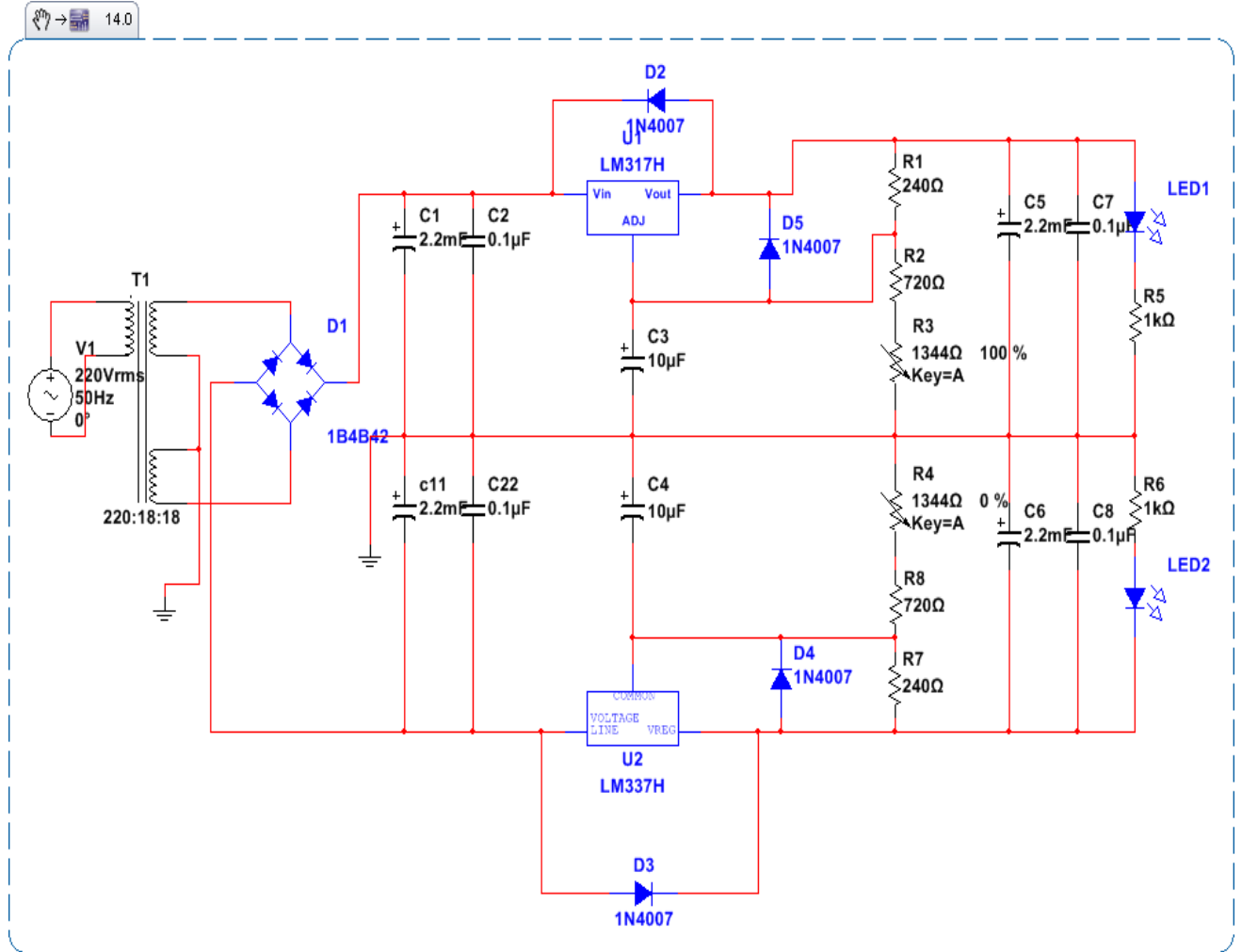


Fig. 3 The circuit of power

B Infrared Sensor(HC-SR501)

HC-SR501 small human body sensor module is automatic control products based on infrared technology, which is of high sensitivity, reliability, ultra-small size. Widely used in various types of automatic induction electrical equipment, it has a fully automatic sensing features (automatic induction: when people into its induction range is output high, people

the intelligent classification of trash can be stable and reliable. It directly affects the performance of the prototype. As the stepper motor's operating voltage, metal sensor's operating voltage, and the work voltage of the micro-controller is inconsistent, the design of the power supply module will be 220V AC voltage into 12V voltage output [11], while the original design power supply module replaced with potentiometer, to enhance the accuracy and adjustable of the power module, in addition to taking the power ripple interference into account, we add 0.1uF and 10uF filter circuit, the final power module can produce stable voltage which can be adjusted continuously from 5.00V to 12.00V. To meet the power supply of stepper motor, metal sensors, micro-controllers and other control circuit.

leave the sensor range is automatically delayed high, the output will be low). There are two ways to trigger, respectively, repeatable trigger mode and non-repeatable trigger mode.

Repeatable trigger mode: that is, after the induction output high level, in the delay period, if someone in its induction range, the output will remain high until the person left, after that the level will be low (the sensor

module detects that each activity of the human body automatically deferred a delay time period, and the last active time is the starting point of the delay time).

Non-repeatable trigger mode: that is, after the sensor output high, the delay time is over, the output will automatically change from high to low.

In this smart sort trash can, Infrared sensor module is the core of the auto flip module. This module has a large cone angle, which means very wide range of sensing. We take it installed in the trash on the top of the way, on the one hand due to induction cone angle, to prevent the situation that passers do not want to throw garbage while the garbage is automatically open the cover; on the other hand, to those who want to throw garbage from all over. Sensing range for the trash as the center, the radius of about 1mile round, close to the living habits, more humane.

C Metal Sensor (FY-3040N)

FY-3040N inductive proximity switch sensor, which is customized for the distance of 40mm long detection, the metal material sensor, with short circuit, surge, reverse polarity protection, whose oscillator can produce an alternating magnetic field, when the rubbish is metal, which produces eddy current inside the rubbish, resulting in shock attenuation, and even stop vibration, oscillator oscillation and vibration changes by the post-amplifier circuit processing and conversion into the switch signal, sent to the micro-controller, which is combined with program in the next step action.

D L298N Motor Drive Chip

The L298N motor driver chip is a high voltage and current motor driver chip, which is packaged in 15 feet. whose main features are: high voltage, the maximum working voltage can get to 46V. It's output current, instantaneous peak current up to 3A, whose continuous operating current of 2A with rated power 25W. A high-voltage and high-current full-bridge driver with two H-bridges can be used to drive inductive loads

such as DC motors and stepper motors and relay coils. It is controlled by standard logic level signals and has two enable control terminals. Without the impact of the input signal to allow or prohibit the device work has a logic power input, so that the internal logic circuit part of the low voltage operation; can also be an external detection resistor, the amount of feedback to the control circuit. Using the L298N motor driver chip drive motor, the chip can drive a two-phase stepper motor or four-phase stepper motor, can also drive two DC motors.

In this intelligent sorting trash, the first automatic clamshell part of the opening and cover because of the rotation of the angle is the same, if the use of DC motor, the motor will appear uncontrollable situation. For example, due to the impact of the gravity of the lid, the DC motor will increase the speed of the lid, and the closure will increase the speed. Over time, the angle error will be more and more. And the use of stepper motor to do, the rotation angle can be more accurately controlled, so open the lid and cover the angle must also be the same, in order to avoid the impact of the gravity of the lid, so there will not be a DC motor Angle error.

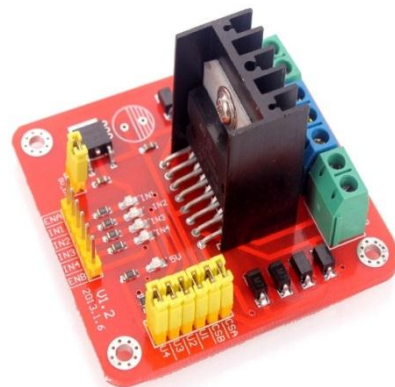


Fig. 4 L298N motor drive chip

E The Overall Circuit Diagram

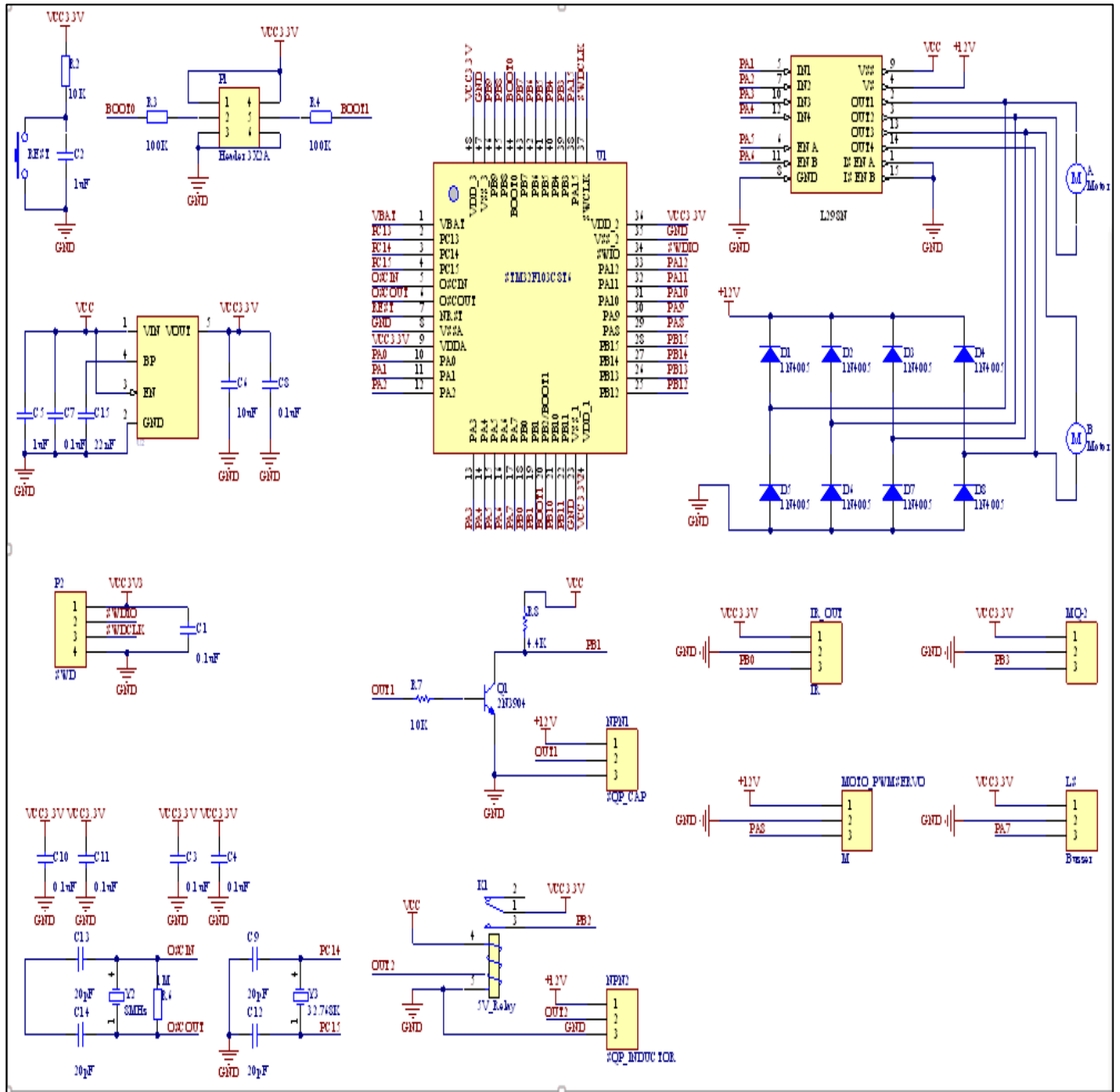


Fig. 5 Schematic diagram of the control circuit of intelligent trash can

IV DESIGN OF SYSTEM SOFTWARE

A Flow Chart in Program

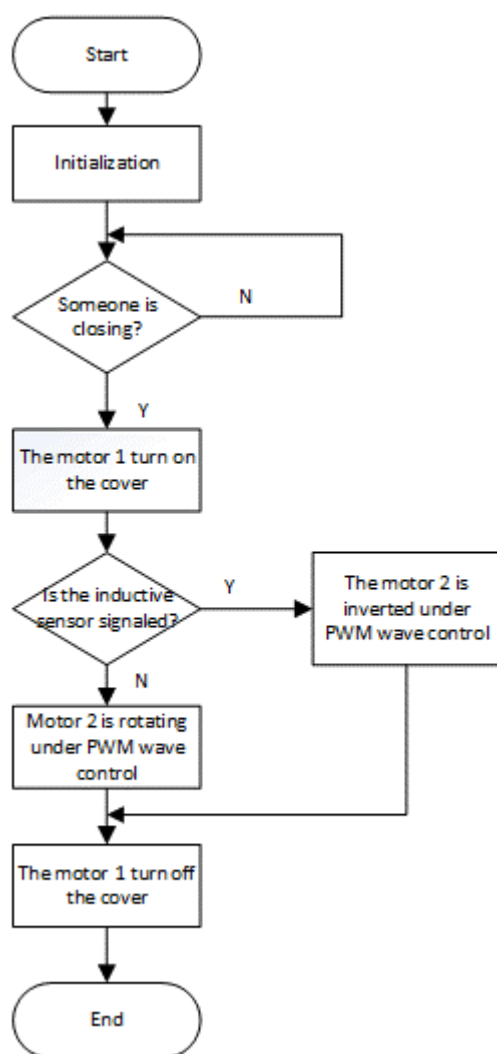


Fig. 6 System program flow chart

B Analysis of Flow Chart

First of all, the system into the initialization phase, when the detection of human close, the micro-controller through the control motor drive module control stepper motor rotation to complete the opening operation. When the inductance sensor detects the metal, the single-chip control steering gear reverse rotation, when the garbage moved to the corresponding sub-box, the rotating plate to restore the original position; the other hand, control the steering gear forward. When the steering gear to restore the original position, and when people leave the cover.

V TEST RESULT

Through the completion of the processing of the sample test, connected to the power, when people through the trash of the infrared sensor area, the trash automatically open the lid, thrown into the garbage, if thrown into cans, bars and other metal products, Its move to the metal sub-box; if the paper, plastic bottles and other non-metallic products, automatically into the non-metallic sub-box body. When the person leaves the

infrared sensing area, the lid is automatically closed.

VI CONCLUSION

The degree of this design's automation is relatively high, not only can automatically determine the person's proximity, but also can automatically complete the garbage sorting. Although the current can only distinguish between metal and non-metallic, but relative to other materials in terms of metal recycling value is greater, therefore, the design is able to achieve the task of garbage sorting. At the same time, when people leave, the trash is closed, for the spread of bacteria in the trash have a certain isolation. Therefore, the design of the trash can have a high practical value, due to lower production's cost, it can be used in general environment which has a high degree of universality.

References

- [1] Liao Rujun, Huang Jianzhong, Yang Danrong. Status Quo and Countermeasures of Classified of Municipal Solid Waste in China [J]. Occupational Health and Injury. 2012 (01)
- [2] LEI Ming, WANG Chenjing. Green automatic intelligent classification trash can [J]. Technology Information, 2017,15 (16): 124 + 126.
- [3] Duan Qiuming, Peng Xiumao, Yang Kaiqi, Lin Jie. Design of Intelligent Multi-function Safe Water Dispenser Based on Single Chip Microcomputer [J] Journal of Jilin University (Information Science Edition), 2014,32 (05): 516-520.
- [4] Zhou Hui-jun, XU Jin-biao. Design Scheme of New Intelligent Trash Can [J]. Journal of Guangdong University of Technology, 2006, (03): 85-88 + 94.
- [5] He Kan, Tian Yaqing, Li Qiang, Hu Zhurong, Zhang Jing. Design of Intelligent Trash Can Based on LD3320 Speech Recognition [J] Foreign Electronic Measurement Technology, 2015,34 (06): 85-88.
- [6] Xiong Jianqiao, Lu Wei, Ji Xiaohan, Wan Jinxiao, Zhang Zhigang, Fu Jie. Design of a smart sorting trash system [J]. Mechanical and electrical product development and innovation, 2016,29
- [7] Chen Weizhen. Design of Environmentally Friendly Automatic Trash Can [J / OL]. Light Industry Technology, 2013,29 (04): 71-72.

- [8] Zhou Qiang, Guan Feng, Lin Lin, Zhang Fei, Lu Sheng, Tang Gaoyang. Design of a self-locking, multi-functional intelligent trash can [J]. Machinery, 2016,43 (05): 51-54.
- [9] WANG Li, LI Yu-jie, YE Ti-ran, LIANG Li-pei. Design of Intelligent Trash Remote Real-time Monitoring System Based on 32-bit Microcontroller [J]. Mechanical Design and Manufacturing Engineering, 2017,46 (06): 45-48.
- [10] Fan Li Nan, Bai Zhiqiang. Design of Intelligent Trash System Based on Single Chip Microcomputer [J]. Instrumentation Users, 2008, (06): 16-17.
- [11] Gao Tonghui, Guo Rui. ARM-based home intelligent trash can design [J]. Electronic Technology, 2012,25 (11): 55-58

Soft switch plasma loudspeaker based on PWM pulse-width modulation

WU Zi-Bo; WANG Yu-Ge; TIAN Hao; YU Sheng-Bao

(*jilin university instrument science and engineering institute, changchun, 130021*)

Abstract—For the purpose of reducing power and improving production capacity of plasma loudspeaker. Firstly, this paper summarizes the methods of the existing plasma loudspeaker switch and analyzes the characteristics and principles of the two typical methods, namely, ZVS (Zero Voltage Switch), PWM (Pulse - Width Modulation); Then, based on the theoretical analysis, combining the advantages of two schemes, a soft switch control method based on PWM pulse width modulation is proposed. Finally, by comparing the effects of each scheme with the actual test, the paper focuses on the comparison and analysis of power, efficiency, stability, security and distortion. The results show that the proposed scheme has better practical application and production capacity.

Key words—Plasma loudspeaker ZVS PWM small power soft switch

I INTRODUCTION

THE magnitude of the current in the arc when the arc is discharged changes the diameter (thickness) of the cross section of the arc [1]. The degree of thickness is the difference in the degree of air expansion. The plasma loudspeaker vibrates the air by changing the magnitude of the current in the arc. The main feature of the radiator is that there is no mechanical distortion in the sound, it is not easy to have a variety of acoustic resonance, therefore, with other types of speakers can not reach the intermediate-frequency and high-frequency sound reproduction quality [2]. This can be attributed to the ion speaker without cone and other vibration systems, there is only the plasma area of the air volume vibration. Due to no resonance, resonance and other interference, and has a good transient and high-frequency characteristics, so with a more natural and realistic sound effects. At this stage plasma speakers are used in many high-end audio speakers, in the home and concert hall also has a good application prospects. In 1899, the British Phizik William Duddell invented the first plasma speaker, this plasma speaker using LC resonant circuit modulation arc, arc will produce some sound quality changes, but can not produce music. In 2007, Acapella used a high-voltage oscillatory amplitude modulation to generate corona discharge [3], but this approach would produce high-power radiation interference, and affect

the electrode and tube life. Not long ago, the Russian Viger-audio product passed the test and began production, the product can be used under different conditions of use, and showed a high reliability. At present, the main method of switching modulation in China is to use ZVS [4-6] method and pulse width modulation method [7-8]. This paper takes into account the performance of each company and the principle of corresponding products. PWM pulse width modulation of the low-power circuit, you can more effectively adjust the arc pulse, reduce power consumption, improve the life of the electrode and tube at the same time also get a better sound quality; through experimental verification, the design has good performance Advantages and product advantages.

II INTRODUCTION OF DESIGN PRINCIPLE

2.1 PWM control mode

Pulse width modulation technology is through the inverter circuit on-off control to achieve the control of the analog circuit. Pulse width modulation technology output waveform is a series of equal pulse, used to replace the required waveform to sine wave, for example, that is, the series of pulses equivalent voltage sine wave, and the output pulse as smooth as possible With less low harmonics. According to different needs, the width of each pulse can be adjusted accordingly to change the output voltage or output frequency equivalent, and then to control the analog circuit. The

principle is as follows:

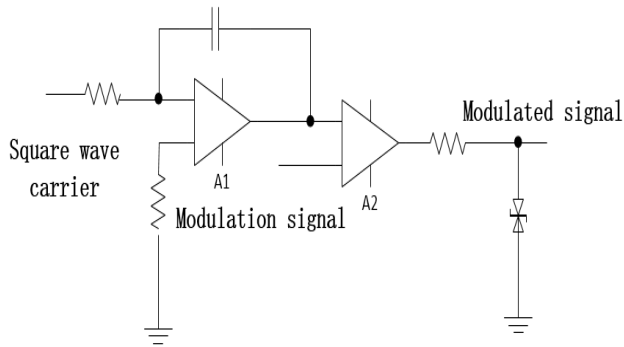


Fig.1 PWM pulse width modulation schematic diagram

Compared with the use of single-chip output PWM wave as the switch control signal [9], the current mainstream plasma speaker using TL494 chip, as a PWM wave generator, the control method is more simple, more current output current, the control circuit as shown below :

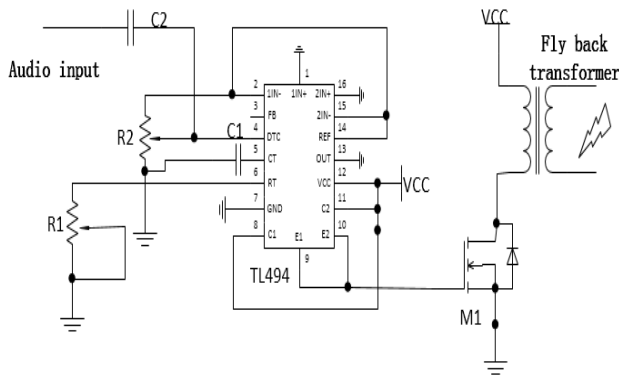


Fig.2 PWM control circuit

Where the potentiometer R1 and the capacitor C1 determine the frequency of the output PWM wave

$$f = \frac{1.1}{R1 \times C1}, \quad R2 \text{ adjusts the duty cycle of the PWM}$$

before the audio signal is not connected. After the audio signal is connected, the TL494 deadband voltage is affected by the amplitude of the audio signal, so that the duty cycle of the output PWM wave changes, that is, the high and low level The change occurs while the M1 transistor gate voltage is met

$$V_{GS} > V_{TN}$$

Which represents the M1 tube gate and the potential difference between the source, representing the M1 tube opening voltage. Because the source of M1 tube is grounded, so it can meet

$$V_G > V_{TN}$$

That is, the gate voltage difference is greater than

the opening voltage, M1 tube will turn on, otherwise the M1 tube in the cut-off state. Visible PWM wave duty cycle will directly affect the switch M1 conduction and cut-off time, further control the arc effect, so that the diameter of the arc changes, resulting in the surrounding air vibration sound.

The power supply provided by the PWM pulse width modulation scheme is small and the safety is high, but its low power will affect the volume of the final speaker output. In this program can use FET instead of IGBT, not only reduce costs, but also reduce the thermal effect of the switch; because of its principle using a hard switch, switching loss, power efficiency is low, the switch tube heat will be more serious, At the same time TL494 as a modulation chip will introduce additional noise, and directly with the TL494 output PWM wave drive switch, the drive capacity close to saturation, easy to make PWM wave distortion, thus affecting the final sound quality.

2.2 ZVS soft switch mode

The PWM switching power supply operates in hard switch mode (voltage drop / rise in the on / off process overlap with the current rise / fall waveform), resulting in large switching losses. High frequency can reduce the volume weight, but the switching loss is even greater. To this end, we must study the switching voltage / current waveform does not overlap the technology, the so-called zero voltage switch (ZVS) / zero current switch (ZCS) technology, or soft switching technology, low power soft switching power supply efficiency can be increased to 80% To 85%.

Because of its high power efficiency, in the production of plasma speakers on this program is very popular with senior enthusiasts, especially in the production of high-power plasma speakers to take this program, so that MOS tube to soft switch mode of work [10], More efficient, able to produce more thick and longer arc, great visual impact. The schematic is as follows:

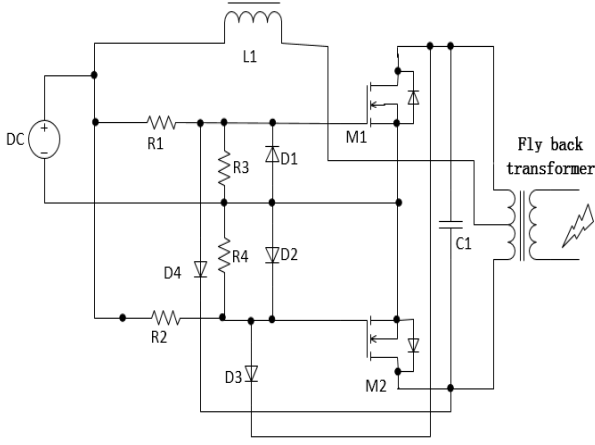


Fig.3 ZVS control circuit

The supply voltage through the current limiting resistor directly applied to the two N-channel MOS tube on the gate, due to the small difference between the two resistors and the two tube junction capacitance of the small differences, there is a tube conducted, assuming that the first tube is conducted. There is

$$V_{GS1} > V_{TN1}$$

Which represents the M1 tube gate and the source of the potential difference, representing the M1 tube opening voltage. At this time the current through the inductor through the tube grounding, due to the on-resistance (switch is not ideal conductor, there is a certain resistance) is very small, so the drain voltage is almost 0, that is, this time, the bottom of the fast recovery diode (Fast diode) negative electrode is connected to the top of the drain, the drain voltage is similar to 0V, so the diode is biased conduction, the negative junction, is the next tube of the gate, the next tube gate junction capacitance current To the ground, the gate voltage quickly dropped to 0V, when the M2 tube gate and the source of the potential difference is less than the opening voltage, the M2 tube from the beginning of the semi-open to cut off. There is

$$V_{GS2} < V_{TN2}$$

Where V_{GS2} represents the potential difference between the gate and the source of the M2 tube, and V_{TN2} represents the opening voltage of the M2 tube.

And the primary coil in parallel with the capacitor from the resonant action, the circuit just when it is charged on the charge, the tube drain voltage down to 0V, the capacitor discharge (in fact, began to discharge

when the voltage began to discharge), the charge charge The primary winding, here can be equivalent to the inductance), due to the role of the inductor freewheeling, the other end of the capacitor charge the other side of the capacitor and the other end of the discharge, the original oscillation should continue, but the other end of the capacitor completely discharged After the original tube voltage is 0V, but now it has been inducted charge, so the original down tube gate also restored power supply, the next tube conduction, and vice versa under the drain, the voltage dropped to approximately 0V, the other Fast recovery diode conduction, the original conduction of the top of the gate voltage to pull low, the tube cut off. This completes the oscillation cycle.

The oscillation frequency of the ZVS will be determined by the primary inductance of the transformer and the capacitance across the primary ends. Can be calculated using the following formula:

$$f = \frac{1}{2\pi \cdot \sqrt{LC}}$$

f is the frequency, the unit Hz; L is the primary inductance, the unit H; C is the capacity of the resonant capacitor, the unit F.

ZVS (zero voltage switch) is a kind of soft switch, this way switch loss is small, is conducive to improving the circuit efficiency; the entire circuit does not use active devices, which does not introduce temperature drift, time drift and other interference; but its current, ; High power lead to serious IGBT fever, if you want to make the circuit a long time stable work, you need to add additional cooling device, not only increase the volume of the entire product, but also improve the cost of the product; high current lead to high breakdown air arc , The radiation power is stronger, the surrounding electronic products have a serious impact; from a security point of view, because the ZVS circuit input power is high, so the use of the security is poor.

III SOFT SWITCH DESIGN BASED ON PWM PULSE WIDTH MODULATION

In this paper, from the power, security, efficiency point of view, in the PWM pulse width modulation program to make innovations and improvements, the

schematic is as follows:

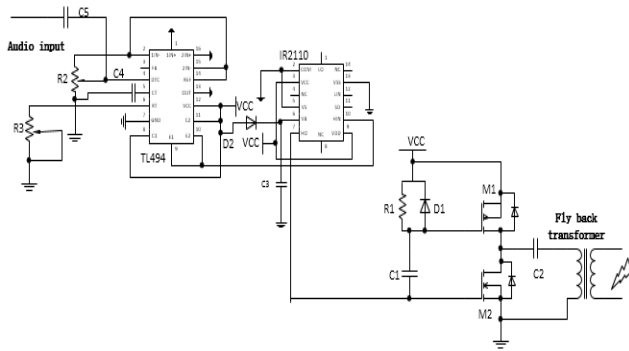


Fig.4 Proposed design circuit

Mainly from the drive circuit and switch circuit to make innovation and improvement:

A good MOS tube drive circuit has the following requirements:

(1)When the switch is turned on, the drive circuit should be able to provide a sufficiently large charge current to quickly raise the voltage across the MOSFET gate to the desired value to ensure that the switch can be quickly turned on and there is no high frequency oscillation on the rising edge.

(2)During switching, the drive circuit ensures that the voltage across the MOSFET gate remains stable and reliably on.

(3)Turn off the momentary drive circuit to provide a low impedance path as possible for the MOSFET gate source capacitor voltage between the rapid discharge to ensure that the switch can quickly turn off.

(4)Drive circuit structure is simple and reliable, small loss.

(5)Apply isolation according to the actual situation.

Considering the above points, the actual selection of IR2110 chip to build MOS tube drive circuit.

IR Company IR2110 drive produced by IR. It has the advantages of high optocoupler isolation (small size) and electromagnetic isolation (fast speed); high operating frequency, up to 500kHz; open, turn-off delay is small, respectively 120ns and 94ns; its wide supply voltage range, 3.3V to 20V power supply can be, do not need to do for its additional level conversion; totem pole output peak current of 2A.

The totem pole drive circuit is actually a current amplifier circuit consisting of an N-channel transistor and a P-channel transistor. The driving circuit acts to boost the output current capability and quickly complete the charging process for the gate input capacitor charge. This topology increases the time

required for conduction, but reduces the turn-off time, the switch can quickly turn on and avoid rising edge of the high-frequency oscillation. At the same time the structure of the external circuit is very simple, is conducive to reducing wear and reduce product size.

The half-bridge circuit, which is composed of N-channel MOS tube (M2) and P-channel MOS tube (M1), increases the power efficiency and reduces the thermal effect of the switch tube, which enhances the stability of the circuit, in which the diode D1 and resistor R1 to accelerate the discharge process, so as to avoid resonance, capacitance C1 and C2 is to play the role of anti-interference, and enhance the anti-jamming ability of the circuit. The circuit works as follows:

When the IR2110 output PWM wave is low, the M2 tube in the cut-off state, that is

$$V_{GS1} < V_{TN1}$$

And M1 tube gate voltage and its source voltage is the same, are the power supply voltage, so there is

$$V_{GS2} < V_{TN2}$$

And M1 tube is a P-channel enhanced MOS tube, so when the M1 tube in the conduction state, the primary coil at both ends of the pressure difference, the secondary coil at both ends of the high pressure to produce air to break the arc.

When the output of the PWM wave is high, the M2 tube gate voltage is high, the source voltage is low, so there is

$$V_{GS1} > V_{TN1}$$

M1 tube in the conduction state, M1 tube conduction, the equivalent of both ends of the primary coil shorted, the potential difference is almost 0, so the secondary coil voltage is small, can not produce arc. This is a half-bridge work of a cycle.

In this paper, the program based on the PWM pulse width modulation soft-switching control, compared to the PWM single-tube push-pull program to improve the circuit to soft-switching control, reducing the switching losses, improve power efficiency and enhance the stability of the circuit. And anti-interference ability, but also reduces the arc after the output PWM wave distortion, improve the sound quality.

Compared to ZVS zero-voltage switching scheme,

the power is reduced, the safety of the circuit is improved, the circuit volume is reduced and the required cost is reduced. The thermal effect of the switch is greatly reduced, and the stability and resistance of the circuit are improved. Interference ability.

In summary, compared with the above two schemes, the proposed half-bridge push-pull control based on PWM pulse width modulation is more advantageous from the aspects of power, efficiency, distortion and sound performance, and from the point of view of product , The proposed control method is low cost, simple structure, high security, better stability, so it has great potential for development.

IV RESULTS ANALYSIS OF ACTUAL TEST

4.1 Circuit power and efficiency testing

Table I Actual test data table

Program	Source Voltage	Source Current	Switch Tube Surface Temperature	Length of The Arc
ZVS	20V	3A	86℃	1.5cm, But its cross-sectional area increased significantly
PWM single-tube	12V	3A	78℃	1.5cm
PWM half-bridge	12V	1A	58℃、50℃	1.5cm

(In ZVS program, the switch tube is IRF260. In PWM single-tube program, the switch tube is IRF540. In PWM half-bridge program, the switch tubes are IRF540 and IRF9540. In the actual test, the surface temperature of IRF540 is 58℃, that of IRF9540 is 50℃.)

From the test results can be seen, according to the power calculation formula:

$$P = I \bullet U$$

It is very difficult to detect the actual power [11], so the actual power is measured with the power provided by the power supply. In the ZVS zero voltage switching scheme, the power supply to the power of up to 60W, the switch tube surface temperature is high, which is not conducive to the safety and stability of the circuit, the need for external cooling or cooling device, which will greatly increase the cost; From the PWM single-tube scheme and the PWM half-bridge scheme

proposed in this paper, it can be seen that the PWM half-bridge scheme proposed in this paper has only 12W of power under the same arc length, which is much smaller than that of the PWM single-tube scheme. Reducing the switching loss, improve the circuit efficiency, the switch tube surface temperature is also greatly reduced, the circuit stability and security, higher security, we can see this article half-bridge circuit proposed PWM soft switch control greatly improved the circuit Of the performance indicators.

4.2 Distortion test

ZVS program:

When the circuit is working normally, the waveforms that drive the switch off are as follows. As a result, there is a very significant distortion in the normal PWM wave, especially in this case, since the rising and falling edges of the waveform are not steep, The deadline has changed.

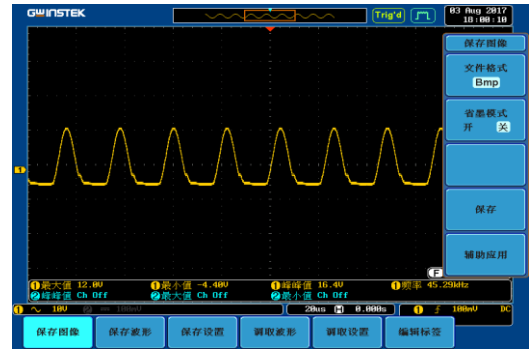


Fig.5 ZVS measured waveform diagram

PWM half-bridge program:

The waveform of the PWM wave of the control switch is as follows (the frequency has been adjusted to the resonant frequency) when the circuit is in the normal operation (the circuit before the high pressure packet is not connected.)

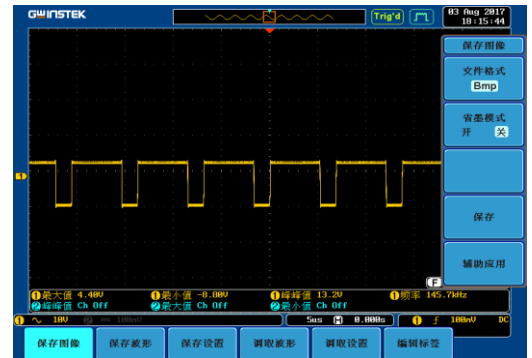


Fig.6 PWM measured waveform diagram

The waveform of the PWM wave that drives the switch after the arc is connected to the high-voltage

circuit is as follows. It can be seen that the waveform is distorted after the high voltage is connected and there is a significant spike at its rising edge, which causes the sound produced by loudspeaker will be mixed with some sharp noise, but the good thing is that the rising and falling edge of the waveform is still steep, even if the high level of some fluctuations will not affect the switch-on and turn-off time.



Fig.7 Proposed design measured waveform diagram

Attached: The test results used in the instrument model is as follows:

Oscilloscope: GDS-2202A ;

Power Source: GPS-3303C ;

Digital Multimeter: GDM-8261A .

V CONCLUSION

In this paper, by understanding the advantages and disadvantages of various plasma speaker production schemes, a design of soft-switched plasma speakers based on PWM pulse width modulation is proposed for the problem that the traditional plasma speaker power is too high and the heat is serious. The design adopts PWM Pulse width modulation, combined with ZVS zero voltage switching technology, in the switch circuit at the use of half-bridge push-pull structure, the traditional hard switching mode improved to soft-switching mode, reducing power and improve efficiency, but also to solve the switch overheating The use of IR2110 as a driver chip to solve the pulse width modulation encountered in the drive capacity of the problem, reducing the control switch off the waveform distortion, and indirectly improve the overall stability of the circuit and improve the stability of the circuit Which is based on the actual waveform detection and the comparison of the power and efficiency under the three schemes, which verifies the advantages and characteristics of the design in terms of the product. At

the same time, the design can further study and improve the elimination of the quantization noise Interference to further improve the sound quality.

References

- [1] Lin Chunfang. High frequency electronic circuit [M]. Beijing Electronic Industry Press, 2010.
- [2] Yu Jinyuan. Today's Ion Speakers [J]. Electroacoustic technology, 2017,41 (3): 22-26.
- [3] Yu Jinyuan. Lonophoe for today[J]. Audio Engineering, 2017,41(3):22-26. Acapella ONTW 1s(Ionic Tweeter0)[EB/O]. http://www.Acapella.de/en/horn-speaker-s/ionic_tweeter.php, 2017-01-16.
- [4] Hack S, Kim , Small. highly efficient current-source type base drive circuit using ZVS converters[J], International Journal of Electronics, 1994(5).
- [5] An Xiang, Ruitao Chen. Small Signal Analysis of a Novel Type of ZVS DC-DC Converter for Fuel Cell .In:4th IEEE International Conference on Information Science and Technology, ShenZhen, China, 2014.
- [6] Hao Zhang, Yinhui Que. A novel ZVS step-down chopper circuit. In: 2017 Asia-Pacific Computer Science and Application Conference , ShangHai, China, 2017:17-21
- [7] M. A. R. Ghonaimy, G.M. Aly. A phase-plane method for the analysis of pulse-width-modulated control systems[J]. International Journal of Control, 1972(4).
- [8] Shi-cheng Zheng, Study on Pwm Control Strategy of Photovoltaic Grid-connected Generation System, In: CES/IEEE 5th International Power Electronics and Motion Control Conference , ShangHai, China, 2006: 190-194.
- [9] Zhang Xinbao, Wang Haixuan, Zhou Shengli, Li Baohua. Methods of MCU-51 Rectangular Single Pulse Pulse Width Accuracy Based on Serial Port. Journal of Jilin University (Information Science Edition), 2016, vol.34 (4): 496-500
- [10] Kasper, Matthias; Burkart, Ralph, M, 1; Deboy,

Gerald2;Kolar, Johann, W, 1(1, Department, of, Electrical,
Engineering, Power, Electronic, Systems, Laboratory,
ETH, Zurich, Zurich, Switzerland, 2, Infineon,
Technologies, AG, Villach, Austria) . ZVS of Power
MOSFETs Revisited.[M]. IEEE Transactions on Power
Electronics: 2016 Vol.31 No.12 P8063-8067

- [11] Chen Geheng, Xie Zeliang. Study on AC power detection
circuit based on M0516 [J]. Journal of Jilin University
(Information Science Edition), 2016,34 (6): 742-746.

Time - Frequency Characteristic Analysis for Electromagnetic Detection of Motion Noise

Pang Yidi; Zhang Xiaoshuang; Qian Zeli; Zhu Kaiguang
(Jilin University College of Instrumentation and Electrical Engineering)

Abstract—The motion noise is introduced by the change of the attitude angle, which affects the consistency of the observed data, due to the influence of the flight attitude, velocity and temperature conditions of the aeronautical electromagnetic detection system. Based on Faraday Law of Electromagnetic Induction, the spectrum of the motion noise caused by the attitude angle is simulated. It is analyzed that the correlation between the attitude angle and the motion noise in the time domain and the frequency domain. The time-frequency analysis method of Gabor transform is used to study the influence of motion noise generated by attitude angle on electromagnetic response. The relationship between the attitude angle and the motion noise is analyzed from the amplitude. Comparing the correlation of different frequencies can obtain that in the case of this analysis the derivative effect is more serious than the attitude angle itself. This time - frequency characteristic analysis method provides a feasible idea for noise reduction of motion noise.

Key words—information science airborne-electromagnetic method time-frequency analysis coil motion noise attitude angle

I INTRODUCTION

AERONAUTICAL electromagnetic method is one of the commonly used methods of aeronautical geophysical exploration. The method uses the theory of electromagnetic field and combines the hardware design and software data processing method of airborne coil [1], which has the advantages of large coverage area, fast flight speed and high working efficiency, The application of low cost, good complex terrain and other geophysical methods can not be replaced by the unique advantages, especially in the harsh environment, human difficult to reach the area of great value [2-3]. The research of this paper is based on the helicopter aviation electromagnetic system, which has high resolution and suitable for shallow geological exploration.

It is necessary to collect and read the effective electromagnetic field information of the ground structure and underground material feedback, which is the necessary link of aeronautical electromagnetic exploration. Therefore, it is important to extract the effective signal and make a reasonable explanation in the aeronautical electromagnetic method. However, due to the limitations of measurement methods, environmental interference and aircraft flight attitude

and so on, the observed data quality and imaging data accuracy will be reduced by noise interference. The coil motion noise is one of the main noise sources, causing the change of the magnetic flux in the receiving coil to produce the induced electromotive force.

Predecessors have put forward many theoretical methods in the analysis and removal of motion noise. Macnae [4] analyzed the characteristics of aeronautical electromagnetic data and various noise sources, including motion noise; Lane et al [5] analyzed the characteristics of motion noise from the perspective of time domain; Buselli et al [6] analyzed the motion from the frequency domain Noise characteristics and the main energy of the motion noise concentrated in the low frequency domain; Munkholm [7] using the sum of the three-component magnetic field in the home direction of the projection and motion noise coupling between the minimum principle to suppress motion noise; Davis et al [8] The influence of the geometrical parameters of the system caused by the coil motion; KASS et al. [9] used the principal component to suppress the noise in the inversion operation.

In this paper, we study the correlation between motion noise and attitude angle in amplitude and frequency range in time domain and frequency domain.

In the time-frequency domain, the Gabor transform method is used to study the relationship between attitude angle and motion noise at time of the amplitude characteristics.

II GABOR TRANSFORM TIME - FREQUENCY METHOD AND PRINCIPLE

To a window with a short time width and to slide it, the short-time Fourier transform of the signal $x(t)$ is

$$STFT(\tau, \omega) = \int_{-\infty}^{+\infty} x(t)w(t-\tau)e^{-j\omega t} dt \quad (1)$$

When the variable τ changes in the window function, the function window moves along the time axis, and the frequency characteristics of each time period are analyzed one by one. When the window function in the short-time Fourier transform selects the Gaussian window, the transform is called the Gabor transform. The expression for the window function is

$$w(x) = \pi^{-\frac{1}{4}} e^{-\frac{x^2}{2}} \quad (2)$$

The Gabor transform of the signal $f(t)$ is

$$T^{Gabor} f(\tau, \omega) = \pi^{-\frac{1}{4}} \int_{-\infty}^{+\infty} f(t) e^{\frac{(t-\tau)^2}{2}} e^{-j\omega t} dt \quad (3)$$

Since the Fourier transform of the Gaussian function is still a Gaussian function, it is equivalent to adding the Gaussian function window to the time-frequency domain so that both the time domain and the frequency domain are localized, thus providing the change signal in any local time range Frequency information.

The resolution of the Gabor transform is uniform, and according to the Heisenberg uncertainty principle, the product of the time and frequency resolution is limited and can not be improved at the same time. However, the Gaussian windowing method has reached the lower limit of the Heisenberg principle, so the time-frequency analysis method using Gabor transform has reached the optimal degree of STFT transform.

III ANALYSIS OF ATTITUDE ANGLE AND MOTION NOISE

A Calculation of motion noise and time domain analysis

The calculation principle of motion noise is to establish the Cartesian Cartesian Cartesian coordinate system based on the ground. The transformation of the

coil vector is used to represent the rotation attitude of the coil plane, and the size of the motion noise is calculated by calculating the induced electromotive force. To pitch pitch rotation as an example, the diagram shown in Figure 1. A is the normal vector of the coil plane in the motion state, and the rotation matrix of the transformation process is T , then $A' = T \cdot A$ [10], where

$$T = \begin{pmatrix} \cos \beta \cos \gamma & \cos \gamma \sin \alpha \sin \beta - \cos \alpha \sin \gamma & \sin \alpha \sin \gamma + \cos \alpha \cos \gamma \sin \beta \\ \cos \beta \sin \gamma & \cos \alpha \cos \gamma + \sin \alpha \sin \beta \sin \gamma & \cos \alpha \sin \beta \sin \gamma - \sin \alpha \cos \gamma \\ -\sin \beta & \cos \beta \sin \alpha & \cos \alpha \cos \beta \end{pmatrix} \quad (4)$$

Where α , β , γ are the roll angle roll, pitch angle pitch, yaw angle yaw three attitude angle corresponding to the angle value. If the magnetic flux is the geomagnetic field, the effective area of the coil, where S is the coil area, the magnitude of the induced electromotive force generated by the motion noise is

$$\varepsilon = -\frac{d\Phi}{dt} = -B \frac{dS}{dt} = -B \frac{dA'}{dt} S = -B \frac{dT}{dt} AS \quad (5)$$

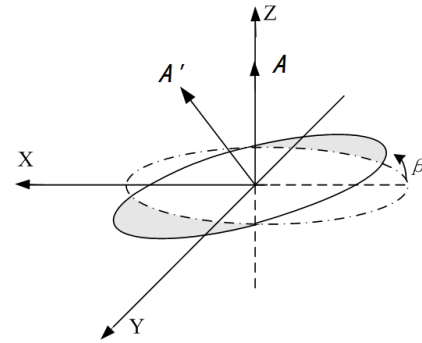


Fig.1 Normal vector change of pitch angle rotation

With the help of the key laboratory data of the Ministry of Education of the Ministry of Education of Jilin University, Jilin University, Jilin University, China, the geophysical and remote sensing center of China Land and Resources and Jilin University jointly developed the CHTEM of the helicopter electromagnetic survey system, The trapezoidal wave with a fundamental frequency of 25 Hz is transmitted, the receiving coil radius is 0.3 m, and the number of turns of the receiving coil is 28 turns. The sampling angle is 1 Hz, the sampling time is 1800 s, including pitch angle pitch, yaw angle yaw, and the pitch angle of the yaw, Roll angle roll three posture.

According to the measured angle, it can be seen that the range of pitch angle is large, and its influence is more important. Therefore, this paper mainly explains the change of pitch attitude. The time domain image of

the pitch angle and its first derivative spectrum are shown in Fig. As the attitude angle has the same influence on each component coil, this paper takes Z coil component as an example to illustrate its time-frequency characteristics. The motion noise produced by the Z-coil component under the influence of the pitch angle is shown in Fig.

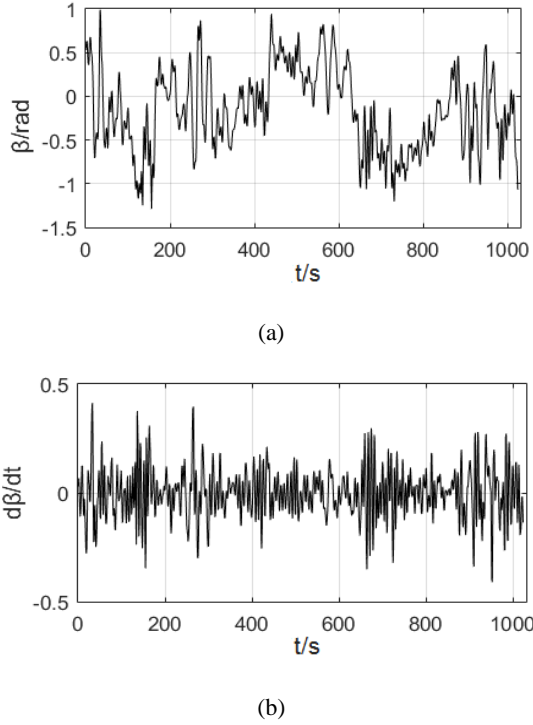


Fig.2 Pitch angle and its first derivative time domain spectrum

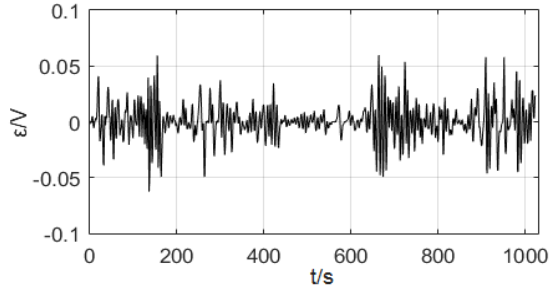


Fig.3 Z component coil motion noise time domain spectrum

According to the amplitude characteristics of the data, compared with the first-order derivative spectrum and the Z-coil component motion noise time-domain map, it can be seen more intuitively that the magnitude of the motion noise and the variation range of the frequency concentration are related to the first derivative S_{β} . The cross correlation coefficient between the Z component motion noise and the pitch orientation angle first derivative data is $-0.9451; \pm 0.80 \pm 1.00$ is the height correlation according to the statistical correlation coefficient, and the original attitude The correlation coefficient between the angle

and the motion noise is only $+0.1070$, so the first order derivative data in the time domain can directly affect the motion noise of the coil component according to the spectrum information. According to the algorithm, it can be proved that when the yaw and roll attitude angles are not introduced, the α and γ angles in the rotation matrix (4) are 0, and the corresponding rotation matrix

$$T_{\text{pitch}} = \begin{pmatrix} \cos \beta & 0 & \sin \beta \\ 0 & 1 & 0 \\ -\sin \beta & 0 & \cos \beta \end{pmatrix}$$

Where the geomagnetic field B is decomposed into a coordinate system $B = (B_x \ B_y \ B_z)$, for the Z

component $A = \begin{pmatrix} 0 \\ 0 \\ 1 \end{pmatrix}$. So the Z component caused by

the size of the induced electromotive force, according

to $\varepsilon = -B \frac{dT}{dt} AS$ it can get

$$\varepsilon_z = S \sqrt{B_x^2 + B_z^2} \sin(\beta - \arctan \frac{B_x}{B_z}) \frac{d\beta}{dt} \quad (6)$$

It can be seen from the formula that the size of the motion noise is proportional to the relationship between $\frac{d\beta}{dt}$ and the linear relationship, and the sine

relationship with $\beta - \arctan \frac{B_x}{B_z}$ is theoretically verifying the correctness of the correlation between the two graphs.

B Frequency Domain Analysis of Motion Noise

The frequency domain spectrum of the data and the frequency domain spectrum of the first derivative are shown in Fig. 4. It can be seen from the spectrum (a) that the pitch angle of the coil is the largest in the low frequency range near DC, With the increase of frequency, the attitude angle of the overall trend of a downward trend, but in 0.030 Hz-0.045 Hz and 0.135 Hz-0.1507 Hz when the angle of the maximum value, and 0.030 Hz-0.045 Hz amplitude is roughly 0.135 Hz- 0.1507 Hz amplitude of 2 times.

Z-component coil motion noise frequency spectrum as shown in Figure 5. Figure (b) is similar to Figure 5, the spectrum is normal and the frequency resolution is the same under the correlation coefficient of $+0.9593$,

so the frequency range of motion noise components and the first derivative still meet the correlation, Leaf transformation is consistent only with the same energy expression theory for different domains. Z-component coil motion noise frequency spectrum as shown in Figure 5. Figure (b) is similar to Figure 5, the spectrum is normal and the frequency resolution is the same under the correlation coefficient of +0.9593, so the frequency range of motion noise components and the first derivative still meet the correlation, Leaf transformation is consistent only with the same energy expression theory for different domains. The above analysis is the same as the rate of change in formula $\varepsilon = -B \frac{dT}{dt} AS$, that is, the higher the frequency, the larger the induced electromotive force is consistent. Similarly, in the vicinity of the DC range, despite the large angle of attitude, but because of the low rate of change, resulting in movement noise is not obvious. And the peak at 0.271 Hz to 0.281 Hz is the second harmonic at 0.136 Hz to 0.156 Hz.

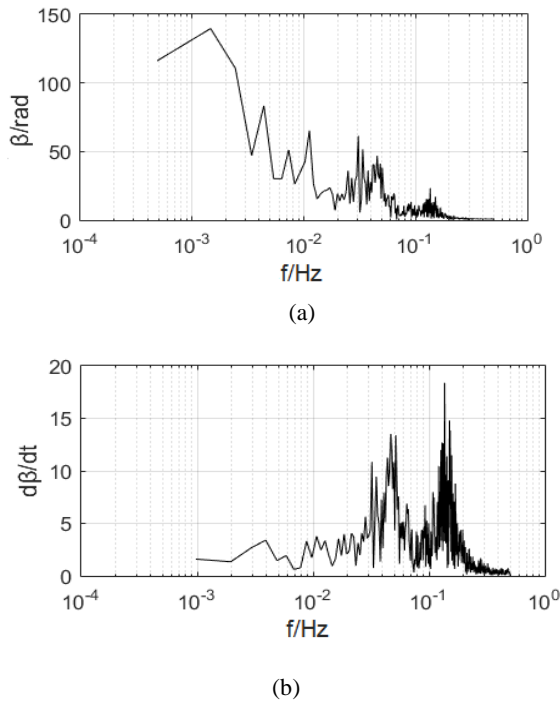


Fig.4 Pitch angle and its first derivative frequency domain spectrum

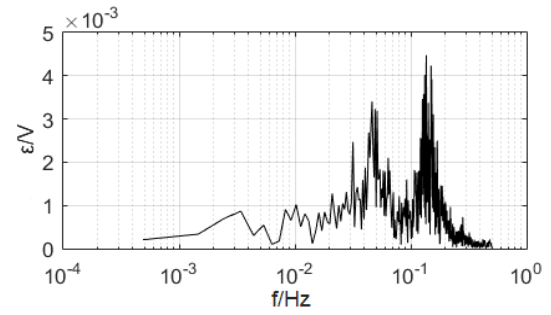


Fig.5 Z component coil motion noise frequency domain spectrum

C Time-frequency analysis of motion noise

Pitch attitude angle and its first derivative Gabor transform spectrum shown in Figure 6. It can be seen from (a) that the points with large amplitude are mainly concentrated in the low frequency domain close to the DC, and there is a slightly stronger attitude angle vibration in the vicinity of 0.15 Hz with respect to 0.10 Hz-0.15 Hz. The vibrations around 0.4 Hz on the time axis basically penetrate the entire time domain, and the posture vibration near 0.15 Hz is intermittent and weak. In terms of vertical, different frequencies at different time points still have the same or lower amplitude. In (b), it can be seen that the amplitude near 0.15 Hz is enhanced compared to the original pose spectrum, and there is a significant continuity in the time domain, whether near 0.4 Hz or near 0.15 Hz. The continuity of the low frequency amplitude of the attitude angle and the superposition of the high frequency effect. Compared with the motion noise spectrum of the Z-component coil, it can be seen that the frequency of motion noise is mainly concentrated in two frequency ranges, one is around 0.046 Hz and the other is near 0.150 Hz. Almost simultaneously at the same time in the domain, at the time point 450 s-600 s time period, the two movements of the noise amplitude of the frequency of almost disappear at the same time. This is related to the pitch amplitude spectrum of the 450 s-600 s period with only a large amplitude near the DC, without a large high frequency amplitude.

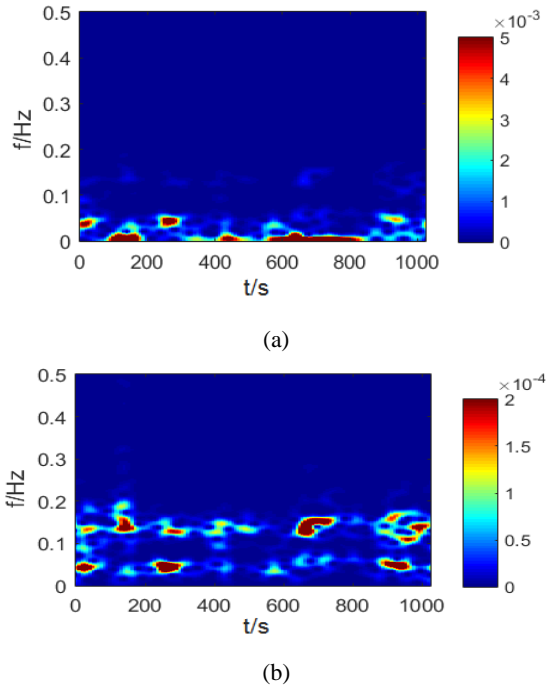


Fig.6 Pitch angle and its first derivative time - frequency spectrum

According to the characteristics of the spectrum, the correlation coefficient and frequency curve of the Gabor transform are shown in Fig. 8, and the correlation characteristic of the different frequency points can be seen. In addition to the accidental error of the measured data, the correlation between the two is relatively high in the region of 0.2 Hz, because the change rate is low at this time, the effect on the induced electromotive force is not obvious, and with the increase of the motion frequency High, $\frac{d\beta}{dt}$ in the frequency domain because of the relationship between the more rapid growth, and thus appear more than 0.2 Hz part of the correlation curve. As can be seen from the overall trend, in the case of error tolerance, the first and second derivative of the motion noise and attitude angle are highly correlated over the entire frequency range.

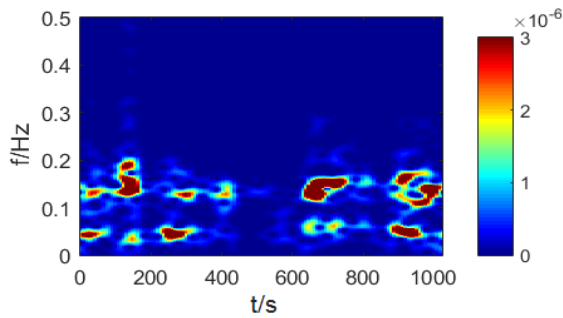


Fig.7 Z component coil motion noise time - frequency spectrum

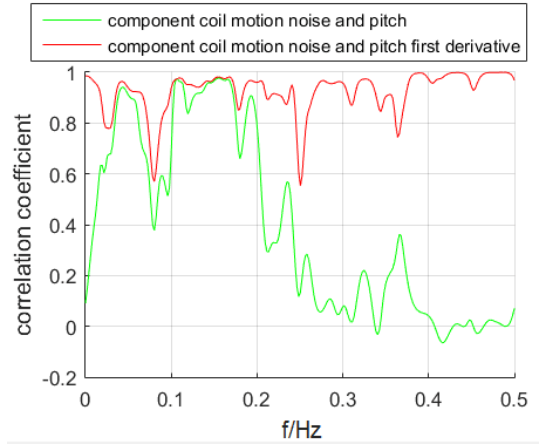


Fig.8 The Correlation and Frequency Curve of Gabor Transform

IV CONCLUSION

In this paper, the time - frequency characteristic analysis method is used to reveal the characteristic relationship between the change of attitude angle caused by coil vibration and the motion noise generated in time, frequency and amplitude. According to the characteristics of the spectrum, with the rotation matrix algorithm to be explained, the following conclusions:

In the time domain, the first-order derivative of the attitude angle is highly correlated with the motion noise generated by the measured angle, and the correlation between the attitude angle itself and the motion noise is not strong, which is consistent with the theoretical value calculated by the rotation algorithm Consistent.

In the frequency domain, the low frequency range introduces a large attitude angle due to the small swing speed, but the magnitude of the rate of change plays a decisive role in the electromagnetic response. The amplitude of the motion noise is not prominent, so the relative high frequency attitude Corner effects are more severe and introduce significant motor noise.

In the time-frequency domain, the localized information can be obtained by estimating the instantaneous frequency of the time point, so as to determine the relative magnitude of the noise amplitude and the time-sharing range. According to the time-spectrum diagram, we can study the different frequency points or different time According to the relevant characteristics of this paper, it can be concluded that the influence of the first derivative of

the attitude angle on the motion noise is more direct and serious than the attitude angle. The frequency of the aeronautical electromagnetic system is 25 Hz, and the motion noise is mainly concentrated in the low frequency range below 0.2 Hz, and the noise amplitude decreases rapidly with the frequency increase, so we can consider the corresponding filtering method. According to the motion noise time-frequency characteristic analysis method in this paper, we can determine the distribution characteristics and relative size of motion noise, so as to provide a basis and method for the suppression and removal of motion noise.

References

- [1] Li Nan. Research on Airborne Time-domain Electromagnetic Data Preprocessing[D]. Jilin University: College of Instrumentation and Electrical Engineering, 2016.
- [2] Yin Dawei, Lin Jun, Zhu Kaiguang, et al. Simulation Research on Coil Motion Noise Removal for Time Domain Airborne Electromagnetic Data[J]. Journal of Jilin University(Earth Science Edition), 2013, 43(5): 1639-1645.
- [3] Wu Yong. Noise Analysis and Simulation Test Research for Pod Vibration of Helicopter-borne TEM System[D]. Jilin University: College of Instrumentation and Electrical Engineering, 2014.
- [4] Macnae J C, Lamontagne Y, West G. Noise processing techniques for time-domain EM systems[J]. Geophysics, 1984, 49(7): 934-948.
- [5] Lane R, Green A, Golding C, et al. An Example of 3D Conductivity Mapping Using the TEMPEST Airborne Electromagnetic System[J]. Exploration Geophysics, 2000, 31: 162-172.
- [6] Buselli G, Hwang H S. AEM Noise Reduction with Remote Referencing[J]. Exploration Geophysics, 1998, 29: 71-76.
- [7] Munkholm M S. Motion-Induced Noise from Vibration of a Moving TEM Detector Coil: Characterization and Suppression[J]. Journal of Applied Geophysics, 1997, 36: 21-29.
- [8] Danvis A C, Macnae J, Robb T. Pendulum Motion in Airborne HEM System[J]. Exploration Geophysics, 2006, 37: 355-362.
- [9] Kass M A, Li Y, Krahenbuhl R, et al. Enhancement of TEM Data and Noise Characterization by Principal Component Analysis[R]. Douglas Oldenburg: Department of Geophysics Colorado School of Mines, 2010.
- [10] Wang Qi, Lin Jun, Yu Shengbao, et al. Study on Influence and Correction of Coil Attitude and Bird Swing for the Fixed-wing Time-domain Electromagnetic system[J]. Chinese J. Geophys. (in Chinese), 2013, 56(11): 3741-3750.

Design of Three Dimensional Magnetic Compensation System Based on PID Algorithm

Jiao Bin; Suo Peng; Wang Zhaoxun

(College of Instrumentation and Electrical Engineering, Jilin University, Changchun 130026, China)

Abstract—When the atomic magnetometer is at 0.05 mT, the Zeeman effect will affect the sensitivity of the magnetometer; while fluxgate tensor probe has the defects of poor stability and nonlinear error in the Earth's magnetic field environment. In order to obtain the reliable measured data, it is necessary to ensure fluxgate and atomic magnetometer work at near zero magnetic field. In this paper, we propose a three dimensional magnetic compensation device, which is based on the PID algorithm. In this paper, a three-dimensional geomagnetic field canceling device based on PID (proportional integral derivative) algorithm is designed to create a near-zero magnetic environment locally. The experimental results show that the system can attenuate 40dB when the interference signal is 40000nT and the frequency is 10Hz, which improves the application of atomic magnetometer and fluxgate in geophysical exploration.

Keywords—magnetic compensation Three-dimensional Helmholtz coil PID

I INTRODUCTION

THE basic characteristic of a magnetic field measurement sensor is that it is possible to sense a change in the magnetic field and to convert the change into a corresponding electrical signal without distortion. With the sensor production materials and processing technology changes, weak magnetic measurement sensor development also occurred with the ever-changing[1-4]. Due to the presence of geomagnetic field, the characteristics of the weak magnetic field measurement sensor are affected by the local magnetic field during the measurement and use. Therefore, it is necessary to provide a reliable near-zero magnetic environment for the development and use of weak magnetic field measurement sensors [5].

The existing methods of eliminating geomagnetic field are mainly divided into two aspects of shielding and offsetting. In the case of field environment or small experiment, the shielding method is costly and it is difficult to build the required precision with shorter time Shielding device. In contrast, in this case the way of offset is more targeted and practical, in the field of magnetic field measurement has a greater room for development[6]. However, the existing equipment used in the way of offset does not have a high versatility, and more problems encountered in the design and

manufacture of related equipment. In this paper, the adjustment of the relevant parameters in the PID algorithm makes the bandwidth of the system to meet the needs of atomic magnetometer, fluxgate and so on [7-8].

II SYSTEM DESIGN

In this paper, the design of the three-dimensional magnetic compensation device block diagram shown in Figure 1. Magnetoresistive sensor and analog-digital conversion circuit constitute the magnetic compensation of the input module to achieve the magnetic signal acquisition and pretreatment; STMicroelectronics STM32F103ZET6 as a microprocessor to achieve the compensation signal analysis and calculation; digital-analog conversion circuit And the power amplifier circuit constitutes the magnetic compensation of the output module to achieve the compensation signal conversion and amplification; three-dimensional Helmholtz coil as a magnetic compensation cancellation device to achieve a direct offset of the magnetic signal; data acquisition card and the computer constitutes a magnetic compensation Test device, to achieve the compensation signal accuracy and frequency band analysis.

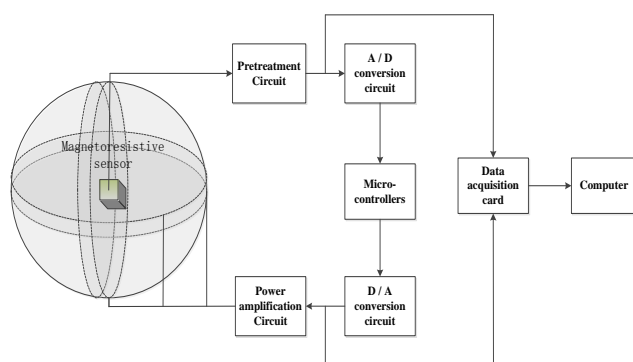


Fig.1 The overall system diagram

A Magnetoresistive Sensor HMC5843

The HMC5843 triaxial magnetoresistive sensor used in this system uses Honeywell's anisotropic magnetoresistive (AMR) technology. The sensor circuit is a triple sensor and a special auxiliary circuit is used to measure the magnetic field. By applying a power supply, the sensor can convert any incident magnetic field in the direction of the measuring axis into a differential voltage output. The magnetoresistive sensor is placed on a silicon wafer by a nickel-iron (permalloy) film and forms a belt-type resistance element. In the presence of a magnetic field, a change in the bridge resistance element will cause a corresponding change in the output voltage across the bridge. The main features of this sensor are axial high sensitivity and linearity, solid structure, vertical axis between the low sensitivity, can be used to measure the direction of the Earth's magnetic field and magnetic force. Because Honeywell's magnetic sensor is located in the industry's highest sensitivity and reliability of the best low-intensity magnetic field sensor, the system compares its several major three-axis magnetoresistive sensor, and ultimately determine the selection of HMC5843 as the core of the system chip.

B Microcontrollers

The design of the microcontroller is STM32F103ZET6 STMicroelectronics is a 32-bit RISC core based on the Cortex-M3, its performance up to 1.25DMIPS / MHZ, with low power consumption, short interrupt time, cost Lower and so on. In addition STM32 has a strong ability to expand, easy to transplant, peripheral unit rich in resources, to achieve the system requirements of the accuracy and scope.

C D/A Conversion And Power Amplification

D / A conversion and power amplifier part of the main realization of the STM32 microcontroller output signal processing, making the final output of the signal

can be directly loaded on the three-dimensional Helmholtz coil, the task of completing the magnetic compensation. The D / A conversion part of the use of 16-bit external DA chip LT1650, by using the subtractor bias voltage, you can make the output side of the bipolar signal on the power amplifier part. The power amplifier part of the use of OCL B complementary amplifier circuit, the theoretical output efficiency of up to 78.5%, heat a small, measured in the process to meet the needs of the system.

D Three-dimensional Helmholtz Coil

The three-dimensional Helmholtz coil unit consists of three pairs of Helmholtz coils. Helmholtz coil is composed of two radii with the same radius and number of turns. The internal magnetic field has a wide uniform area, and there is a good linear relationship with the supply current, which is suitable for constructing three-dimensional Space combined magnetic field, based on the above characteristics, three-dimensional Helmholtz coil can produce a corresponding magnetic field to achieve better offset compensation. In this design, the offset magnetic field space is located in the three-dimensional Helmholtz coil center of the cube, the magnetoresistive sensor is located in the space, real-time measurement of the magnetic field strength within the space, through the three-dimensional Helmholtz coil The magnetic field is superimposed with the geomagnetic field, making the space approximately zero magnetic environment.

III SOFTWARE DESIGN

A Overall Program Flow

In order to facilitate the use and maintenance of the system, the system procedures are used modular design ideas, the program is mainly composed of initialization and program control components. The initialization part of which mainly includes the microcontroller initialization, sensor initialization and LCD display initialization. The program control part mainly through the use of PID algorithm, the magnetoresistive sensor HMC5843 collected data processing. The overall system flow chart shown in Figure 2.

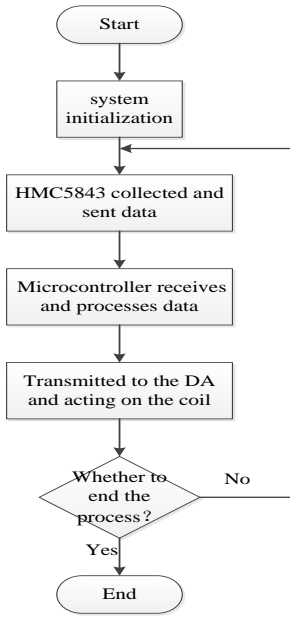


Fig.2 System flow chart

B PID control

According to the specific situation of the system, we can establish the corresponding mathematical model, as shown in Figure 3, by adjusting the parameters of the model can be completed on the system optimization.

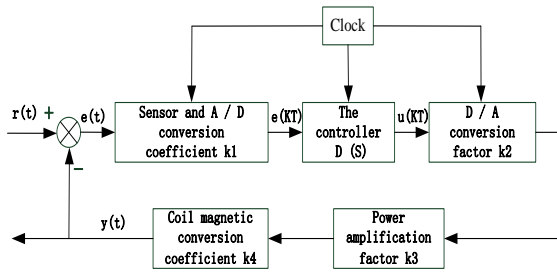


Fig.3 System mathematical model

$$r(t) = B_1 \cos I \cos D + B_1 \cos I \sin D + B_1 \sin I + a_x B_2 + a_y B_2 + a_z B_2 \quad (1)$$

Where B_1 represents the geomagnetic field, the geomagnetic element takes the X axis to the geographic north, the Y axis points to the geographic east, and the Z axis is directed downwards. B in the XOY plane of the component H , H for the magnetic north, H and B between the angle recorded as I , and the north direction of the angle recorded as D . B_2 is a magnetic field other than the geomagnetic field, and a_x , a_y and a_z represent the modes of the components in the three directions of X, Y, and Z, respectively.

Here is:

$$\begin{aligned} r_x(t) &= B_1 \cos I \cos D + a_x B_2 t \\ r_y(t) &= B_1 \cos I \sin D + a_y B_2 t \\ r_z(t) &= B_1 \sin I + a_z B_2 t \end{aligned} \quad (2)$$

The geomagnetic field B_1 can be approximated as a constant value, and B_2 is the environment where the magnetic field interference is considered to be the velocity signal.

Introduce PID control in the controller. The control amount $u(t)$ has:

$$u(t) = K_p [e(t) + \frac{1}{T_i} \int e(t) dt + T_d \frac{de(t)}{dt}] \quad (3)$$

In the S domain with a transfer function that is obtained:

$$D(s) = \frac{U(s)}{E(s)} = K_p [1 + \frac{1}{T_i s} + T_d s] \quad (4)$$

When the frequency field of the input magnetic field signal is within the available bandwidth, the output of the system can effectively track and compensate the corresponding input magnetic field signal. Closed-loop transfer functions are available from mathematical models

$$G_{B(s)} = \frac{T_i s}{k_1 k_2 k_3 k_4 K_p [1 + T_i s + T_d T_i s^2] + T_i s} \quad (5)$$

Get the system steady-state error:

$$e_{ss} = k_1 k_2 k_3 k_4 K_p B_2 (a_x + a_y + a_z) \quad (6)$$

K_p and e_{ss} have a linear relationship with the expression of steady-state error. With the increase of K_p value, the system steady-state error increases, and the step response corresponding to the different K_p values in Table 1 yields the K_p value Small will make the system to increase the time to adjust the above factors to choose $K_p = 0.1$ as the system application value.

Table 1 The response table corresponding to different K_p values

K_p	0.001	0.01	0.1	1	10
Transition time /s	0.253	0.018	0.091	0.147	0.152

IV TEST RESULTS

In order to verify the effect of the system on the interference signal, the test results in a magnetic field with a peak-to-peak value of about 40000nT as a source of interference using a coil with a turn of 50 turns and a radius of 10 cm. The test results are shown in Table 2.

Table 2 Different frequency magnetic compensation effect

Frequency /Hz	0.1	0.5	1	2	5	10
After compensation n /nT	177	175	179	207	273	395
Attenuation factor /dB	47.1	47.2	47.0	45.7	43.3	40.1

From the data in Table 2 can be obtained when the interference signal frequency is less than 2Hz, the system's offset effect is basically stable, can make the interference signal attenuation of 45dB or more. And when the interference signal frequency within 10Hz can ensure that the attenuation rate of 40dB or more, to meet the design requirements. In summary, the system bandwidth of up to 10Hz, the original offset device can significantly improve the bandwidth. At the same time the scope of the basic coverage of the fluxgate probe disturbance, test the environment to bring the scope of the interference signal, with the application value.

V IN CONCLUSION

The system uses STM32 as the processor to complete the real-time acquisition and processing of the measured signal of the magnetoresistive sensor. By adjusting the corresponding parameters in the PID algorithm during the measurement process, the bandwidth of the system is extended to about 10Hz, which is the atomic magnetometer, The application of the fluxgate provides a suitable external environment. But the system still has the sampling rate is insufficient, the resolution is not high and so on, these problems and sensor indicators and other factors have a direct relationship, follow the system needs to select the appropriate accuracy of the sensor can be.

References

- [1] WU Hong-bin, YI Xue-qin. Three-dimensional time-domain detection of low-frequency magnetic field based on HMC1053 [J]. China Ship Research, 2007, (03): 72-77.
- [2] Cao Wen. Geomagnetic signal detection based on magnetoresistive sensor [D]. Huazhong University of Science and Technology, 2007.
- [3] Jose M.G. Merayo, P. Brauer, F. Primdahl. Triaxial fluxgate gradiometer of high stability and linearity. Sensors and Actuators A 120 (2005) 71–77
- [4] Wang Guoyu, Zhang Xin, Jing Liang. Application of new magnetoresistive sensor in geomagnetic field measurement [J]. Sensor Technology, 2002, (10): 43-45.
- [5] Li Shuguang. Study on atomic magnetometer [D]. Zhejiang University, 2009.
- [6] LI Li-yi, SUN Zhi-yin, PAN Dong-hua, LIU Jia-xi, LIU Tian-hao. Study on the Present Situation of Near-Zero Magnetic Environment Device [J]. Journal of Electrical Engineering, 2015, (15): 136-140.
- [7] LIU Hong-hua. Study on active magnetic field calibration system based on triaxial square Helmholtz coil [D]. Beijing University of Technology, 2013.

A design of non-contact ECG machine based on capacitive coupling

LING Zhen-bao; FAN Tian-jiao; ZHOU yu-cheng; YU Si-jia

(The College of instrumentation and Electrical Engineering, Jilin University, Changchun 130021, China)

Abstract—Targeting on avoiding the secondary damage which traditional ECG machines bring to those extensively burnt or cutaneously infected, our group has designed a capacitive coupling-based ECG machine. The design is consisted of composite electrode plates, differential amplification circuits, filter circuits, master controller, RAM, ROM and LCD screen. Clear ECG signals can be displayed on the screen in real time, and the stored ECG datas can be uploaded to the PC for analysis. The actual operation also shows obvious R wave, the error is less than 30%, and the S wave is not obvious. After the data processing, the calculation error is less than 50%.

Keywords—ECG capacitive coupling electrode non-contact probing

I INTRODUCTION

THE ECG signal measuring has significance for the research in primary heart function and heart pathology[1]. The traditional ECG measuring is mostly implemented by wet method using Ag/Cl complex electrode[2] and electrode jelly or dry method using electrode lead. These years some institutes also came up with designs of non-contact ECG measuring. For instance, Kim[3] develops a non-contact ECG measuring chair using large size electrode as reference electrode. Ueno A.'s team[4] implants measuring electrode into a mattress and analyses the results of different coupling conditions[5]. Specializing in extensive burnt patients and specific people, this essay presents a device which is totally non-contact and doesn't cause any pressure or infection.

II MEASUREMENT PRINCIPLE AND SYSTEM MODEL

As shown in Figure 1, the measuring instrument consists of a composite electrode plate, a differential amplifying circuit, a filter circuit, a device amplifier, a master controller, a data storage and display module. The probe consists of two signal collecting electrodes and one reference electrode, to differentiated from Vc and Vi1 with Vc and Vi2. The differential amplifier uses INA103 amplifier, which has the characteristics of low noise and low offset voltage. After amplifying 1000 times of the signal which output by the voltage follower circuit, the signal with higher signal-to-noise ratio is obtained by high pass filtering, 50Hz notch and low-pass filtering, the preamplifier and filter losses are further compensated by the instrumentation amplifier,

then it is stored in the data memory after the AD conversion. The display module is used to display the waveform of the ECG signal in real time.

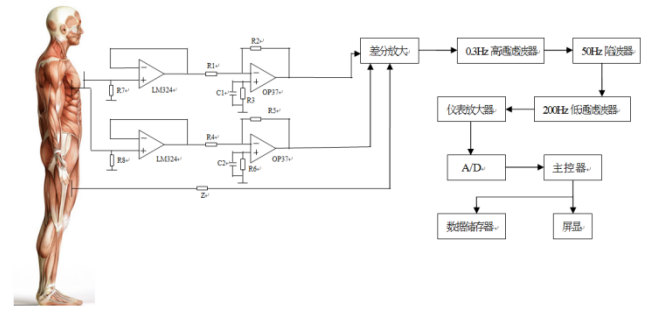


Fig. 1 system diagram

II THE DESIGN OF FRONT-END SIGNAL PROBING

A the layers of complex electrode

The whole complex electrode can be divided into four layers: insulating layer, electrode, PCB and shielding layer[6]. According to the diastole and systolic of heart atrium, the size of complex electrode is 6cm*8cm. The expression of coupling capacitance is:

$$C_{e1} = \frac{\epsilon S}{d}$$

S: the effective area between coupling electrodes

d: the distance between two coupling electrodes

ϵ : air dielectric constant

if the electrode is 5mm to skin, it is simple to figure out that the coupling capacitance is

$$C = 8.85 \times 10^{-12} \times 48 \times 10^{-4} \div 5 \times 10^{-3} = 8.5 pF$$

The variation of output signal is resulted by distance of coupling electrode and dielectric. The output signal amplitude decreases with coupling distance increases. If inserted a shielding layer in the dielectric[7], the coupling capacity would increase its capacitance. Then the output amplitude rises.

The front-end coupling electrode and bias resistance compose a HP filtering circuit. The bias resistance is not supposed to be low, because the range of ECG signal frequency is 0.05Hz—40Hz. The expression of cut-off frequency is:

$$f_c = \frac{1}{2\pi R_{Bias} C_{E1}}$$

If the $f=0.05\text{Hz}$, it is inferred that $R=375\text{M}\Omega$.

The time constant expression is $t=RC$. According to the expression, the theoretical time is 0.06-1.5s. After examination, $t=1.3\text{s}$.

PCB is made up with printed plate. And there is a copper foil shielding layer inserted between PCB and shielding layer aiming at avoiding the electromagnetic field noise generated by electrode and electrified circuit. Meanwhile, it blocks out the electromagnetic wave in the air, which raises the SNR.

B differential amplifying circuit

This circuit is designed to amplify ECG signal using a differential amplifier. The amplifier causes ultra low noise and extra low voltage imbalance. The input noise is $2\text{nV}/\sqrt{\text{Hz}}$ under the circumstance that input signal frequency is 10Hz and $1.2\text{nV}/\sqrt{\text{Hz}}$ under the circumstance that input signal frequency is 100Hz. And the common mode rejection ratio is greater than 100dB. The gain is determined by external resistance. Besides that, it contains two implanted resistance which determine the gain to be 1 and 100. The expression of gain is $G=1+$.

In this unit, we use the implanted resistance to implement precise gain. This can avoid the deviation caused by external resistance and the gain is proper for the input signal amplitude.

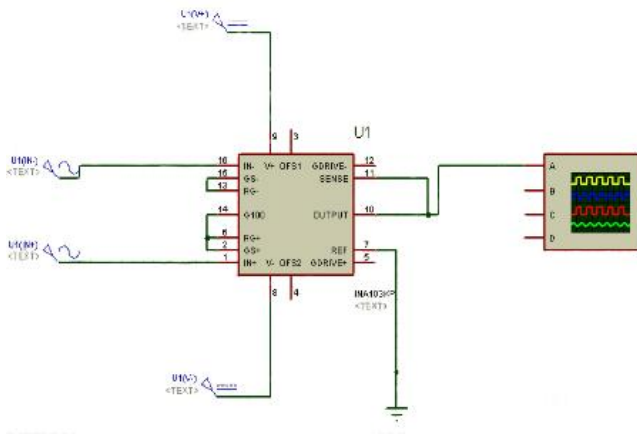


Fig.2 differential amplification circuit

C filtering circuit

The 50Hz frequency is not a composition of ECG signal, therefore, the problem of power frequency interference would be more serious if amplified. To avoid the power frequency interference, a BP filtering circuit is inevitable. This circuit implements the function with a dual T network active filter[8].

If

$$R_1 = R_2 = R_3 = R_4 = R$$

$$C_1 = C_2 = C_3 = C_4 = C$$

the upper half of is R_5 , the lower half is R_b , so

Transfer function is

$$F(S) = \frac{1 + R^2 C^2 S^2}{1 + 4\left(1 - \frac{R_a}{R_b}\right) + R^2 C^2 S^2}$$

Center frequency is :

$$f = \frac{1}{2\pi RC}$$

When the quality factor is 0.707, the transfer function

is $F(s) = \frac{10000 + S^2}{17070 + S^2}$, the center frequency is

48.4Hz. the amplitude-frequency characteristic is :

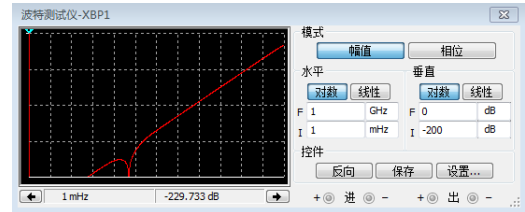


Fig. 3 amplitude frequency characteristic of trap

To filter the low frequency noise caused by differential amplifying circuit and eliminate the voltage error ranging on human body[9], a two order Butterworth active high pass filter is applied to this circuit and the cut-off frequency is 0.1Hz. The transfer function is:

$$A(S) = \frac{10459s^2}{1000s^2 + 6468s + 1000}$$

To filter the myoelectricity noise in the differential amplifying circuit and electromagnetic noise[10], a two order Butterworth active low pass filter is applied to this circuit and the cut-off frequency is 100Hz. The transfer function is:

$$A(S) = \frac{20000}{1 + 7960s + 6336s^2}$$

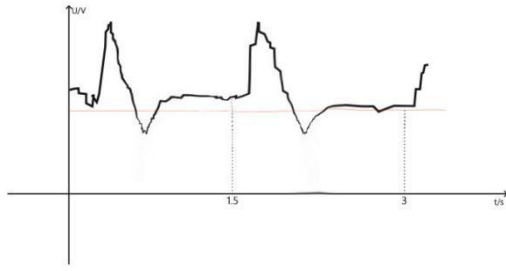


Fig. 4 the measured ECG signal

III EXPERIMENTAL TEST AND RESULT ANALYSIS

The test is made of silver chloride as metal electrode, chemical composite oxide as dielectric, and connected with subsequent shield and printed PCB circuit as probe. The actual ECG signal is shown in figure 4. The amplifier is amplified 1000 times by internal amplifier, and the maximum output amplitude is 1.26V.

The experimental results show that the first amplifier theoretically amplifies 100 times and the loss is 6dB. The theory of two stage amplifier is magnified 10 times, and its attenuation rate is 14dB. Based on the standard ECG, the amplitude of the R wave should be 1V, and the actual 1.26V is measured. Using δ to express the error of the amplitude of the R wave

$$\delta = (1.26 - 1) \div 1 = 26\%$$

The P wave, T wave and Q wave are not captured in the test results, but the S wave is captured. The amplitude value of S should be 0.2V, and its amplitude is about 0.28V by oscilloscope. Using ζ to express the error of the amplitude of the S wave:

$$\zeta = (0.28 - 0.2) \div 0.2 = 40\%$$

The error is large, so the real S wave is not analyzed. After simulation and data searching, it can determine the voltage drop caused by the internal circuit adjustment or the error when the software is processed. By Figure 4 can be obtained, the time interval is about 1.3s, calculated:

$$N = 60 \div 1.3 = 46$$

A normal adult has about 70 to 80 beats per minute, with a normal range of 60 to 100 heartbeats. If you set the number of times 75 times. Using η to express the error of the amplitude of number of heartbeats:

$$\eta = (75 - 46) \div 75 = 38.7\%$$

The error of capturing ECG signals is about 38.7%. Analysis of the reasons, on the one hand for capacitive measurement of ECG, capacitor charging and discharging period will have an impact on the ECG signal. On the other hand, when the human body

breathes, the displacement of the chest cavity will change the distance between the human body electrode and the compound electrode, so that some captured signals are similar to the clutter, and are processed by subsequent software.

IV CONCLUSION

This electric measuring instrument to achieve a different contact measurement method, the interval of cloth, or special materials to measure ECG, but by air and insulating materials as the dielectric, calculate the equivalent composite dielectric materials to achieve complete non surveying contact ECG, is a new method of ECG measurement, there are certain practical application value in the treatment of special populations.

Reference

- [1] ZHU L Y, WU B M, WANG ZH G, et al. A real-time QRS complex detection algorithm for mobile ECG telemonitoring system [J]. Instrument Technique and Sensor, 2005, 26(6): 603-607
- [2] Sear A, Kirkup L. A Direct Comparison of Wet, Dry and Insulating Bioelectric Recording Electrodes [J]. Physiological Measurement, 2000, 21(2): 271
- [3] Baek H J, Chung G S, Kim K K, et al. A Smart Health Monitoring Chair for Noninvasive Measurement of Biological Signals [J]. IEEE Transactions on Information Technology in Biomedicine, 2012, 16(1): 150-158.
- [4] LI H Q, CUI D Y, YUAN D Y, et al. Research on the Detection and De-Noising Algorithm of Wearable ECG Signal Based on Capacitive Coupling Electrode [J]. Chinese Journal of Sensors and Actuators, 2017, 1: 8-15
- [5] UENO A, AKABANE Y, KATO T, et al. Capacitive sensing of electrocardiographic potential through cloth from the dorsal surface of the body in a supine position: A preliminary study [J]. Biomedical Engineering, IEEE Transactions on, 2007, 54(4): 759-766.
- [6] LUO F R. Understand and measure the ECG by oneself [J]. Old Friend, 2017, 1: 56
- [7] QU B L, WANG L F. Numerical simulation for effective permittivity of two-phase [J]. Journal of Functional Materials, 2016, 1: 1172-1176
- [8] Zhou Ping, Feng Wang, Liu Mengxing. Study on noise restraint in non-contact electrocardiographic measurement

[J].Chinese Journal of Scientific Instrument,2013(10) .

- [9] GAO shan,LI Yongqin,WEI liang.Technical Research of Non-contact Electrocardiogram Based on Capacitive Coupling[J]. Journal of Biomedical Engineering,2015(3)
- [10] Jiang wenwen. Research on Portable ECG Detection System[D]. Harbin: Harbin University of Science and Technology, 2016:1-53.

Research on Sign Language Translation System Based on Kinect

Liu HuaiBin; Xia Tao; Shao JingYa

(College of Instrumentation & Electrical Engineering, Jilin University, Changchun 130000, China)

Abstract—In order to realize the design of Chinese sign language translation system based on Kinect, this paper proposes a dynamic language recognition method using finite state machine and dynamic time regularization scheme. Using the Kinect technique to obtain the hand depth image and skeleton feature information, the HOG feature operator with high recognition rate is selected. On this basis, the finite state machine and the dynamic time planning algorithm are used to realize the Chinese dynamic sign language translation. The sign language translation system finally realizes 50 sign language words and sign language sentences, and the accuracy rate can be up to 90%.

Key words—Dynamic sign language recognition Chinese sign language translation Kinect Algorithm of Histogram of Oriented Gradient bones features information

0 INTRODUCTION

Sign language as the most primitive way of communication, is widely used in the field of virtual environments and human-computer interaction, it can make the hearing disabilities get useful information, and transmit or receive orders in the special work environment silent or aseptic control platform[1]. Studies have been done at home and abroad for the automatic identification of sign language, and the team, such as Hyeon-kyu Lee, used a self-created PowerGesture system to show the slide through the hand gestures[2];Foxconn lab, matching the commonly used gestures, using the traditional camera to collect color image and to process, but due to technical parameter of camera itself is susceptible to environmental impact, can only implement simple sign language recognition[3]; In 2010,Microsoft developed Kinect technology, which has the technical advantages of identifying human skeletal images and obtaining 3D dynamic tracks, making it a new leap in the field of automatic sign recognition[4-5]. In 2012, the Chinese university of Hong Kong designed a kind of gesture translation system based on the SVM method, its use was carried out on the characteristics of the joint coordinates classification of learning way, better finished for sign language word recognition[6]; 2013 X.chai et al. used Kinect to perform the three-dimensional reconstruction of the gesture trajectory to complete the daily sign language identification. Through the comparison of the various algorithms and the analysis of the experimental results, the DTW (dynamic time warping) algorithm is

improved on the basis of the highest accuracy of the HOG algorithm, and a dynamic sign language Chinese translation system based on Kinect is designed[7].

I EXTRACTION OF HAND FEATURE DATA

1.1 Acquisition of Kinect multi sensor image data

Kinect in the middle of the RGB camera and the two sides of the depth sensor through the spatial modeling, bone information tracking technology can get RGB color image, depth image, body image, as shown in Figure 1[8]. Using the three kinds of images obtained by Kinect, the hand segmentation algorithm is introduced to obtain the accurate ROI region of the hand, and the sign language recognition algorithm is used to process the hand characteristic information, thus completes the establishment of the sign language translation system.

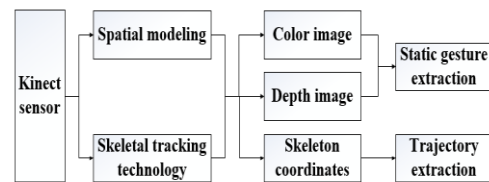


Fig.1 Diagram of hand information collection system

1.2 The extraction of hand shape information and motion trajectory

There are two kinds of dynamic sign language, one is the 3D trajectory of dynamic sign language, and the other is its iconic static sign form data[9]. By using the skeleton recognition and the depth image to obtain the depth threshold of the hand, the palm shape is captured, and then the hand shape information is obtained through the skin color recognition, edge detection

algorithm and so on. The movement of the hand can be extracted by spherical coordinate transformation of bone coordinates[10].

The extracted hand region is easily affected by the background noise of the environment, which can be used to extract the human skin color by RGB images to achieve accurate hand shape extraction. Experiment results commonly used six kinds of skin color recognition shown in Figure 2.

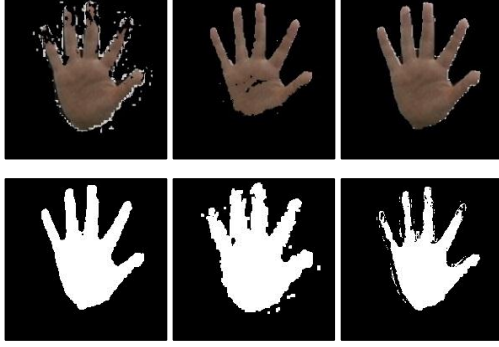


Fig.2 Comparison of six skin color recognition schemes

The experimental results show that the detection results of skin color threshold segmentation based on RGB image parameters and chromaticity parameters Cr and Cb are better than those of the remaining five schemes. In order to make the algorithm transplantable into the embedded system, the system program is optimized, and the skin color recognition based on the RGB image is selected to complete the system skin color recognition.

II THE REALIZATION OF CHINESE SIGN LANGUAGE TRANSLATION

The system selects two scenarios for testing: one is a dynamic gesture that contains a static hand type. The second is the dynamic gesture which is determined by the hand movement trace completely.

Image features can be divided into geometric feature, texture feature, gray level characteristics, etc. And the image feature information is extracted by four common static gesture recognition algorithms, as shown in figure 3. By comparing the results of the four methods, the results of the optimal dynamic gesture recognition were obtained.

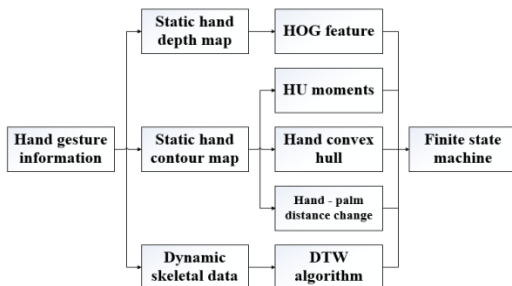


Fig.3 Sign language translation flow chart

2.1 HU moment

In the image processing, the gray scale density distribution feature of the image is obtained by the moment method, and the feature extraction of the image is completed. As the preferred feature extraction method, the moment feature is defined as the image function in the discrete image with pixels as the unit, the order geometry moment and the center distance are respectively[11]:

$$m_{pq} = \sum_{y=1}^N \sum_{x=1}^M x^p y^q f(x, y) \quad p, q = 0, 1, 2, \dots$$

$$\mu_{pq} = \sum_{y=1}^N \sum_{x=1}^M (x - \bar{x})^p (y - \bar{y})^q f(x, y) \quad p, q = 0, 1, 2, \dots$$

Where $\bar{x} = \frac{m_{10}}{m_{00}}$ and $\bar{y} = \frac{m_{01}}{m_{00}}$ represent the center of gravity of the image, N and M represent the height and width of the image. The normalized center distance is defined as:

$$\eta_{pq} = \frac{\mu_{pq}}{\mu_{00}^{\frac{p+q}{2}}}$$

Using the second and third order normalized distance of the center, Hu deduced that the seven features of rotation, zooming and shifting invariant, the constant moment M1-M7.

Figure 4 shows that the number 3 of M5 and M6 are negative and different from the other digital templates, indicating that there are some fluctuations in the Hu moment between the different samples, and each template still has a unique data characteristics.

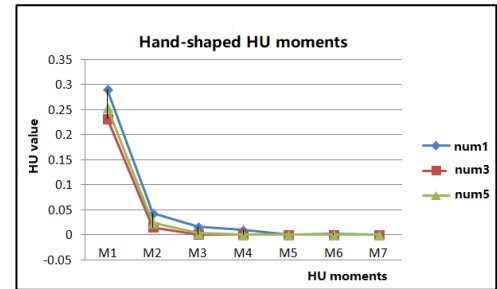


Fig.4 Hu moment of gesture number 1,3,5 hand sample

Hu moments as features for gesture recognition has a faster speed. However, due to the fact that the moment invariants in the Hu feature of the hand contour are generally small and the opponent type is sensitive, it is not conducive to the expansion of the template and the recognition of the multi user gesture.

2.2 Hand convex hull

The finger morphological information can be extracted by using the hand convex and convex defect, which provide the hand template that can find the area of convex hull and the angle of convex defect. The fingertip information is selected from the candidate

fingertip by calculating whether the feature angle between the vector sum is less than the threshold of the finger angle. In the case of sign language "good morning", a convex hull experiment is carried out to extract the tip information of the image, as shown in figure5.



Fig.5 "good morning" hand convex hull extraction

2.3 Contour and palm distance characteristics

The contour of the hand selects the distance from the contour to the center of the image to represent. The edge of the gesture is sampled at 500 pixels, and the distance from the edge to the center of each image is subtracted from the minimum edge of the edge of the image to the palm distance. At the lowest end of the image, the Freeman chain code is introduced, and the Euclidean distance from each edge point to the palm is obtained along a certain direction, as shown in figure6.

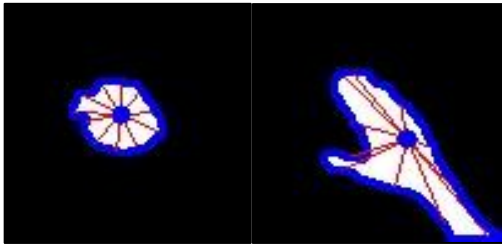


Fig.6 "morning" hand-palm distance diagram

2.4 HOG feature vector

The HOG algorithm divides the image to a small connected region, the cell unit which is connected to the large block interval, and then completes the normalized processing of the cell gradient[12]. All the information in the Block is combined into an image feature vector for subsequent template matching.

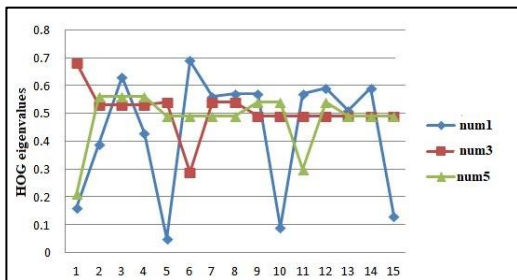


Fig.7 Number 1,3,5 HOG characteristic value

As shown in figure 7, most HOG eigenvectors are 0.49 or 0.54, each of which has its own feature level. The obtained eigenvectors are provided to the machine classification algorithm, and the accuracy rate is approximately 90%.

III ALGORITHM IMPLEMENTATION OF HAND TRANSLATION SYSTEM

It is the main way of dynamic hand gesture recognition using statistics, templates and grammar. The template-based approach has dynamic programming, DTW, etc., which are based on the size of the norm of the measured event and the stored template event[13]. The system uses the finite state machine as the main way to identify the dynamic gestures that contains a symbol for static gestures. The dynamic gestures that represent the meaning of sign language by hand gestures are selected by dynamic time warping to complete the sign language translation.

3.1 Finite state machine

In order to complete the "good morning" this dynamic gesture recognition, it is necessary to satisfy the static hand shape that is contained in the measured which it appears in order. Figure 8 is a two-group 'good morning' gesture, with different hands in the process of hand gestures, but the hand characteristics of the beginning and the end are similar.

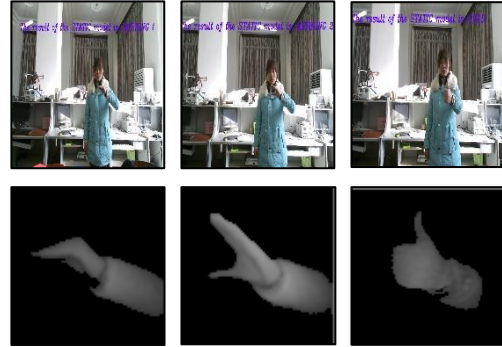


Fig.8 Two-group 'good morning' gesture

3.2 Dynamic time warping

The dynamic gestures, which are determined by the trajectory of the hand, are mainly based on the comparison of the spherical coordinates data of the normalized feature joint and the template gesture characteristic joint data[14].

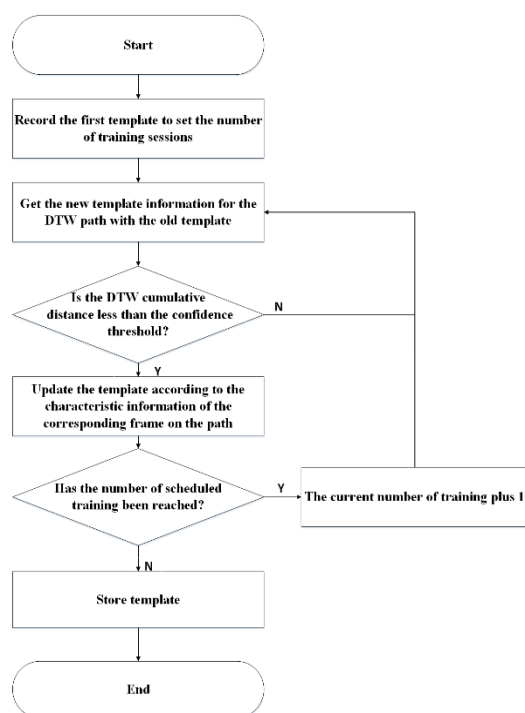


Fig.9 Flow chart of DTW algorithm

The theory of DTW is based on dynamic programming, comparing the two sequences of the different lengths but the similar content, extracting the users' joint features multiple times. The DTW algorithm diagram is shown in figure 9[15-16]. Through the regular path, if the cumulative distance is less than the threshold, the two templates match, and the updated skeletal coordinate values are obtained by the cumulative average of the joint images on the regular path.

3.3 Design of sign language standard library

Sign language standard library is divided into static feature hand and dynamic hand trajectory. The static feature hand-standard library stores the depth images which are obtained by static manual standardization. Taking into account the individual differences and the diversity of the Kinect perspective, the multi-user information was built and the multi-angle static hand model was tested in the standard library.

The experiment concluded that a well-performing classifier model was obtained when the sample image of the static manual characteristic library was about 10 times the number of images.

IV TEST RESULTS AND ANALYSIS

The system can be tested comprehensively from two aspects: the correct rate of sign language recognition and the effective area of the gesture. Figure 10 is the user interface of the sign language translation system:



Fig.10 the user interface of the sign language translation system

4.1 Test the accuracy of sign language recognition

The accuracy of sign language recognition is the most important index to evaluate the sign language translation system. Therefore, this situation is chosen as the standard of gesture recognition, that the distance between the user and the sensor 1.3m and the angle of the cross section is 0 degrees, and four kinds of static gestures are used to complete the gesture recognition.

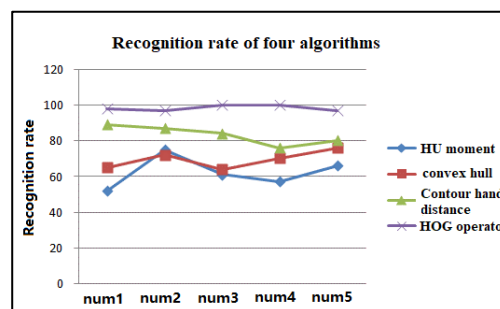


Fig.11 The relationship between four kinds of characteristic operators and recognition rate

As shown in Figure 11, in the static handgesture recognition of digital and sign hand gestures, the picking accuracy of HOG is better than that of the first three classes, so HOG is selected as recognition method of the "first class" hand gesture.

As shown in figure 12, the recognition rate of accuracy can reach above 90%, when the finite state machine is added to complete the handwritten sentence translation after dynamic gesture recognition of "first class".

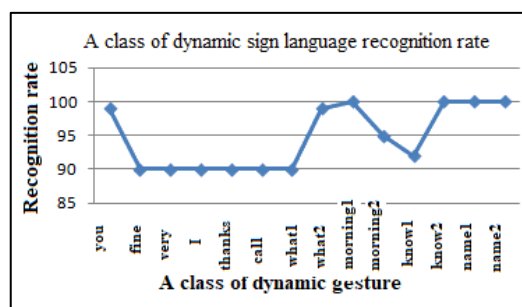


Fig.12 Recognition accuracy of the "first class" dynamic sign language

As shown in figure 13, the "second class" dynamic sign language recognition uses the DTW algorithm, and the accuracy rate can reach 90%.

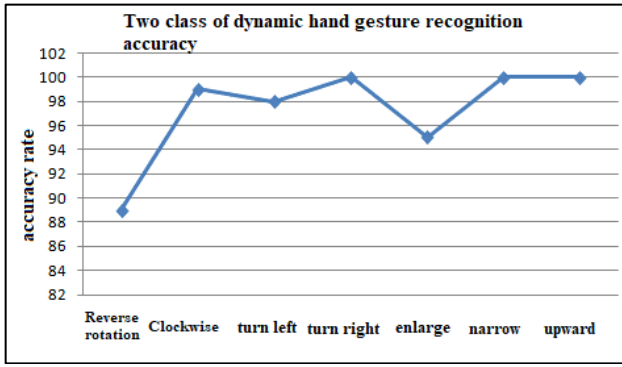


Fig.13 Recognition accuracy of the "second class" dynamic sign language

4.2 Test the effective area of gesture recognition

The effective area of gesture recognition is an index that directly relates to the scope of application of the algorithm, which includes the depth distance between the user and the sensor and the angle between the user section and the sensor cross section. As shown in figure 14 and 15. After the standardization of static images, the "first class" dynamic gesture is less affected by distance parameters, and the factors, from the angle of cross section, inhibit the accuracy of the gesture, can be eliminated by training the static sign which means machine learning.

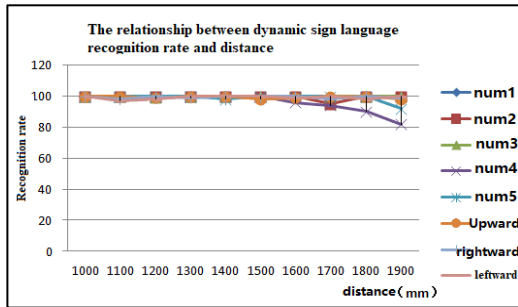


Fig.14 Relationship between accuracy and distance of dynamic gesture recognition

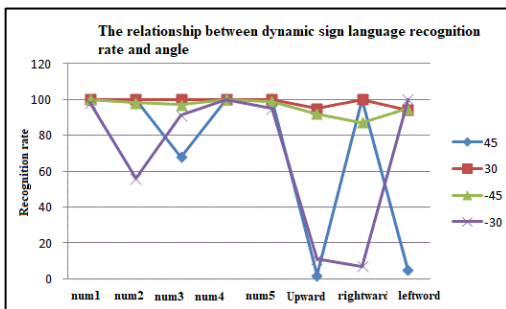


Fig.15 Relationship between accuracy and angle of dynamic gesture recognition

The "second class" dynamic gesture uses human skeletal joint to normalize skeletal coordinates. When the main joint of the human body is in the range of Kinect's data acquisition, the accuracy of the gesture recognition is largely unaffected by the distance parameters. However, the "second class" gestures are greatly affected by the rotation angle of the cross section, with the increase of the angle, the correct rate

of gesture recognition dropped significantly. Therefore, the standardized algorithm of skeletal characteristic parameters of the "second class" dynamic gesture still needs to be improved.

V CONCLUSION

From the above experiments, the HOG feature operator has higher recognition accuracy rate compared with other feature algorithms for static image feature extraction. The effective identification distance of the system is 0.9 to 2 meters, the angle of the cross section is angle plus or minus 45 degrees, and the detection time is less than 1s. In the "first class" dynamic sign language recognition, the use of finite state machine to implement Chinese sentence translation can make the accuracy of the recognition up to 90%, and in the "second class" dynamic sign language recognition, adding the DTW algorithm, the recognition accuracy is also over 90%.

References

- [1] Stokoe, W.: Sign Language Structure, University of Buffalo Press.
- [2] Kendon, A.: Current Issues in the Study of Gesture The Biological Foundation of Gestures: Motor and Semiotic Aspects, pp. 2347, Lawrence Erlbaum Associates, Hillsdale.
- [3] Takahashi T, Shino F K. Hand gesture coding based on experiments using a hand gesture interface device [J]. Sigchi Bulletin.
- [4] Wu Caifang, Xie Jun, Yu Lu, Zhou Dian. Static gesture recognition with continuous hidden Markov algorithm [J]. computer system applications, 2016, (08): 115-119.
- [5] Zhang Yi, Zhang Shuo, Luo Yuan, Xu Xiaodong. Recognition and application of hand gesture track based on Kinect depth image information [J]. computer application research, 2012, (09): 3547-3550.
- [6] Zhang Xuan, Li Minghan. Research on sign language recognition based on improved DTW algorithm [J]. electronic production, 2015, (16): 11-12.
- [7] Zhu Mingming. Research on the application of sign language recognition technology based on Kinect in deaf mute teaching [D]. Southwest Jiao Tong University, 2014.
- [8] Wang Songlin. Research on gesture recognition and robot control technology based on [D]. Kinect Beijing Jiaotong University, 2014.

- [9] Zhang Hao. Gesture recognition based on Kinect and its application [D]. Dalian University of Technology, 2014.
- [10] Bi Xueqin and friends'. The face skin color segmentation and AdaBoost algorithm to detect [J]. foreign electronic measurement technology, based on the 2015 (12): 82-86.
- [11] Zhang Jianfei, Qi Chun. Wave motion analysis of low resolution geometric moment scale invariants [J]. computer engineering and applications, 2015, (21): 150-154+204.
- [12] Shi Wen, Zhu Xuefang, Zhu Guang. Adaptive edge detection algorithm of MRI images based on morphology [J]. Journal of instrumentation, 2013, (02): 408-414.
- [13] Tan Chang, Xiao industrial. Static gesture recognition [J]. computer engineering and application, improved RCE and RBF neural network based on 2011 (07): 172-176.
- [14] Wang Peipei. Research on video based human motion recognition [D]. Nanjing University of Posts and Telecommunications, 2013.
- [15] Chen Jianbin. Research and implementation of image feature extraction and similarity [D]. Xi'an Electronic and Science University, 2012.
- [16] Yang Jie, Corelle. Research on dynamic time warping DTW algorithm [J]. science and technology, 2016, (04): 11-12.

Study on High Power LED Electrical Parameter Model

WANG Zhao-feng; CAO Jia-rui; LI Gang; HE Zong-ze

(College of Instrumentation & Electrical Engineering, Jilin University Changchun 130012)

Abstract— With the increasing application of high power LED lamps, the requirements of the analysis of its electrical parameters are gradually increasing. The ordinary PN junction equations can not accurately describe the volt-ampere characteristics of high-power LEDs. Therefore, the classical Shockley equation is combined with the LED physical model to deduce the theory, the Taylor equation is developed and the model is segmented to construct the electrical parameter model of high power LED. The volt - ampere characteristic curve of the high - power LED is verified to be closer to the actual volt - ampere characteristic curve than the classical PN junction model, which is more consistent with the measured curve and more practical value.

Key words—high power LED; Taylor expansion; segment processing; electrical parameter model ; Volt-ampere characteristic

I INTRODUCTION

HIGH-POWER LED is a semiconductor light source , which is a light-emitting diode with large operating current , whose core is PN junction, so it has a general PN junction I-V characteristics[1], which is forward conduction, reverse cut off and the breakdown characteristics. In addition, under certain conditions, it also has a light-emitting characteristics. At the forward voltage, the electrons are injected into the P region from the N region. The holes are injected into the N region from the P region, and the minority carriers into the other region recombine with the majority of the carriers and glow. Compared with the traditional electric light source, it has the following significant features: First, high luminous efficiency, in general, incandescent, halogen light effect is $21 \sim 24 \text{ lm / W}$, but high-power LED luminous efficiency can reach $25 \sim 200 \text{ lm / W}$, which has narrow spectrum, good monochrome, and no need to filter, directly issued monochromatic light[2]. Second, it is energy-saving and environmentally friendly, and a high-power LED light source's light energy is equal to a $35 \sim 150$ watts of incandescent light's light energy. When they have the same lighting effect, the high-power LED lighting can save energy than traditional light source 80% to

90%. The third is high security: the high power LED light source can stable light, and can accurately control the light type, glare small, less heat. And because it is cold light ,it can be safe to touch. It does not contain mercury elements,so it is more environmentally friendly. Four is long life .High-power LED single tube life is 100,000 hours[3], whose light source life can reach 20,000 hours or more. It can be expected that in the near future, high-power LED is about to add a new energy-saving, environmental protection, longevity, safe common light source to human's life[4].

As a light-emitting special PN junction device[5], high-power LED's working principle is similar to common PN junction, but the unique place is that the current includes the radiation current and no radiation current, and the voltage includes junction Voltage and equivalent series resistance voltage drop. The working principle is related to the diffusion of the internal carriers, the elegant, the complex and the photon release. Therefore, it is not accurate to describe the high-power volt-ampere characteristic with the traditional PN junction characteristic model[6]. Moreover, the electrical parameters of the model directly affect the performance of LED performance [7].

From the traditional P-N knot shockley equation(8),therefore, this paper presents a sub-mathematic model for high-power LEDs[9],

which can accurately describe the high-power LED voltage and current relationship, combined with the ideal physical model and the measured data. It is a solution to the original equation in the application of high power LED's inappropriate, large-error method [10].

In the near future, I believe that this scientific model can be applied to make reasonable adjustments to the drive source of the high-power LED and to accommodate commissioning in different working conditions, as well as to provide LED its own manufacturing process, life study and testing reasonable theoretical guidance, improving high-power LED performance from process benchmarks [11].

II MODEL

2.1 Simplification of the Shawley equation

Since the linear model can not accurately describe the volt-ampere characteristics of the LED, the traditional Shockley equation can only describe the voltage and current of the P-N junction, and can not describe the V-I relationship of high-power LEDs. In order to describe the characteristics of LEDs more accurately, we modify the Shockley equation[12].

We know that the traditional P-N knots of the Shockley equation is [13]:

$$I_F = I_{SAT} \cdot (e^{\frac{qV_F}{nKT}} - 1) \quad (1)$$

Since $\frac{qV_F}{nKT}$ is much larger than 1 in the actual calculation, we can simplify the Shockley equation as:

$$I_F = I_{SAT} \cdot e^{\frac{qV_F}{nKT}} \quad (2)$$

We will be high-power LED circuit equivalent to the model shown in Figure 1, that is, by an ideal diode, diode equivalent resistance, and the equivalent voltage composition, the equivalent voltage from the figure to show:

$$V_F = V_{LED} - RI_F \quad (3)$$

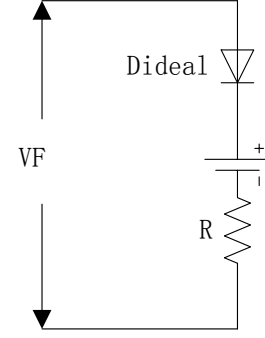


Figure 1 Diode physical model

Where V_F is the forward conduction voltage, I_F is the forward conduction current, n is the ideal factor, K is the wavezmann constant, whose value is $1.38 \cdot 10^{-23}$, T is the absolute temperature:

$$V_T = \frac{KT}{q} \quad (4)$$

According to the formula (2) - (4) we conclude that:

$$I_F = I_{SAT} \cdot e^{\frac{V_{LED} - RI_F}{nV_T}} \quad (5)$$

2.2 Determination of parameters

We check the reverse saturation current of the diode:

$$I_{SAT} = \frac{I_K}{e^{\frac{V_K - RI_K}{nV_T}}} \quad (6)$$

I_K is the turn-on-current, U_K is the turn-on-voltage, R is the diode equivalent resistance, we see it as the data slope of the operating point, so that the resistance is more equivalent to the current working state.

In order to make the calculation process more simple and accurate, we used (5) to have Taylor expansion[14], then to study its volt-ampere characteristics. Its Taylor expansion is:

$$I_F = I_{SAT} \sum_{j=0}^{\infty} \frac{\left(\frac{V_{LED} - RI_F}{nV_T}\right)^j}{j!}$$

According to the situation of Figure 2, when the number of unfolds is 37, the degree of fitting is good,

so we choose j for 37.

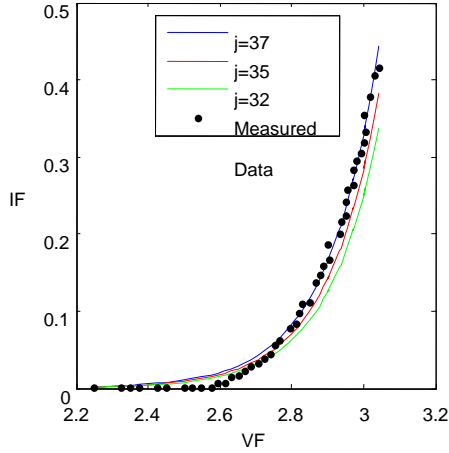


Figure 2 Fitting curve with different k values

2.3 Model correction

According to Figure 3, we can see that since the current is too small to be zero before the voltage V_K is turned on, we will be equivalent to 0. To simplify the model, we approximate the place between the open voltage and the inflection point as a straight line, whose corresponding mathematical model is:

$$I = \frac{I_r - I_K}{V_r - V_K} V + \frac{I_r V_K - I_K V_r}{V_r - V_K}$$

After the inflection point the voltage that is as (7) said. The final model effect is shown in Figure 4.

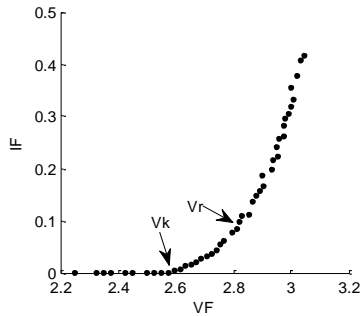


Figure 3 Data source

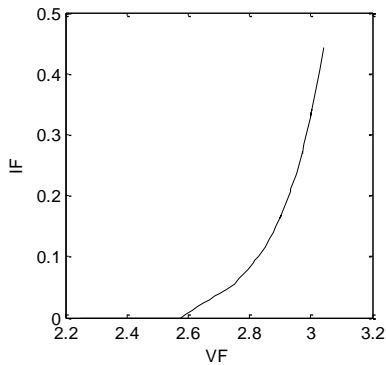


Figure 4 Equivalent model of high power LED electrical parameters

As the different manufacturers of LED production of different parameters, it is necessary according to the relevant parameters of the LED and the measured data to modify the curve several times to achieve a better fit effect.

III EXPERIMENT AND ANALYSIS

For the purpose of model validation, we have selected three different lamp beads, which are OSRAM-W5AP-AW lamp beads, ball package (amber) LED-1W lamp beads, CREE lamp beads (5000K cool white) -1W conduct experiment.

First, through the data test, we got the voltage and current data of multiple groups of OSRAM, preliminary finished the experimental data, removed the unreasonable points which deviated curve manually, finally got Figure 5's scatter plot.

According to the data in Table 2, Substituting the formula (6), (7), (8), we can make the optimization model fitting chart, and compare with the previous scatter plot, as shown in Fig. 5

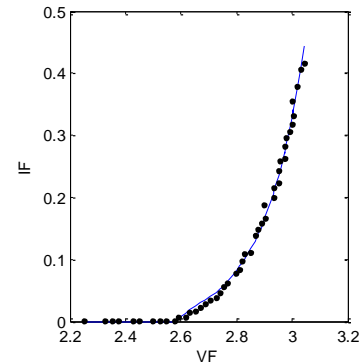


Figure 5 OSRAM-LED (W5AP) experimental fit chart

From the figure we can see that the effect of fitting is relatively good, the standard deviation is shown in Table 1, whose error is less than 1%, which is within the allowable range. So the model of the fit is better, in line with the operation of high-power LED.

Similarly, we have made the ball casting lamp beads^[15] and CREE lamp beads model, and compare them as shown in Figure 6 and Figure 7, which verify the accuracy and applicability of our method more.

IV CONCLUSION

In this paper, based on the Shockley equation, we first propose a high power LED electrical parameter

model and have Taylor expansion combining with the LED physical model. According to the actual situation, the segmentation optimization is carried out to construct a high-power LED Electrical parameter model and the error control is in less than 1%. This model can effectively describe the volt-ampere characteristics of high-power LEDs during operation.

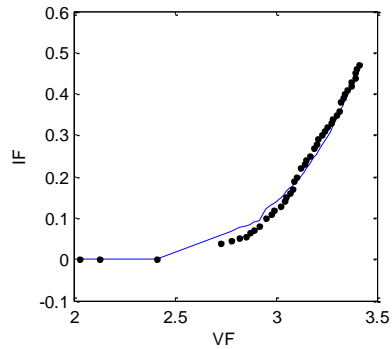


Figure 6 ball package LED lamp beads fit chart

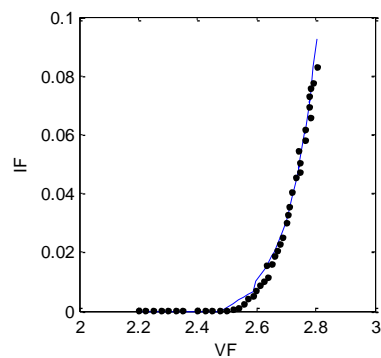


Figure 7 CREE-LED (XBD2525) lamp beads fit chart

Table 1 Error Analysis Table

Raw data I_F/A	Fit value	Error (standard deviation)
0.006043	0.005365	0.000479
0.007817	0.012486	0.003301
0.01392	0.017782	0.002731
0.017416	0.024177	0.004781
0.022357	0.029964	0.005379
0.029384	0.034871	0.00388
0.033477	0.041014	0.005329
0.045378	0.051736	0.004495
0.055388	0.055386	1E-06
0.062839	0.064836	0.001413
0.078152	0.079593	0.001019
0.084482	0.089281	0.003393
0.097853	0.093798	0.002867
0.109786	0.09987	0.007011
0.112027	0.116372	0.003073
0.137778	0.129431	0.005903
0.147862	0.140421	0.005262
0.158451	0.151395	0.004989
0.166126	0.167711	0.001121
0.199814	0.206454	0.004695
0.216247	0.210804	0.003849
0.22409	0.233159	0.006412
0.242765	0.233159	0.006792
0.263306	0.272631	0.006593

Table II

	V _k /(V)	V _r /(V)
Ball package	2.41	2.95
CREE-XBD252 5	2.474	2.596
OSRAM-W5AP	2.575	2.751

References

- [1] XU Sheng,XU Yu-zhen,CHEN En-guo,etal. Study on the new models of high powerLED current-voltage characteristics[J]. Journal of Optoelectronics Laser, 2015, 26(11):2077-2082.
- [2] Lee Y C ,HWU F S, YANG M C ,et al.Exprtimental and numerical analysis of p-electrode patterns on the lateral GaN-based LEDs[J].Journal of light wave technology,

- 2014,32(15):2643-2648.
- [3] Xiang Lei, Huai Zheng, Xing Guo,etal. Reduction of Die-Bonding Interface Thermal Resistance for High-Power LEDs Through Embedding Packaging Structure[J]. IEEE Transactions on Power Electronics,2017,32(7):5520-5526.
- [4] Junhui Li, Xiaorui Zhang, Can Zhou.etal. New Applications of an Automated System for High-Power LEDs[J]. New Applications of an Automated System for High-Power LEDs,2016,21(2):1035-1042.
- [5] Pai-Yang Tsai, Hou-Kuei Huang, Chien-Min Sung, etal. High-Power LED Chip-on-Board Packages With Diamond-Like Carbon Heat-Spreading Layers[J]. Journal of Display Technology,2016,12(4):357-361.
- [6] Wei Lai, Xianming Liu,Weimin Chen,etal. Thermal Characteristics Analysis of Die Attach Layer Based on Time-Constant Spectrum for High-Power LED[J]. IEEE Transactions on Electron Devices, 2015, 62(11): 3715-3721
- [7] Ray-Lee Lin,Jhong-Yan Tsai,Jos é Marcos Alonso,etal. Four-Parameter Taylor Series-Based Light-Emitting-Diode Model[J]. IEEE Journal of Emerging and Selected Topics in Power Electronics,2015,3(3):581-588.
- [8] J. Marcos Alonso, Marina S. Perdigão, Guirguis Zaki Abdelmessih,etal. SPICE Modeling of Variable Inductors and Its Application to Single Inductor LED Driver Design[J]. IEEE Transactions on Industrial Electronics,2017,64(7):5894-5903.
- [9] Julio Molina, Juan Jose Mesas, Nadhir Mesbahi,etal. LED lamp modelling for harmonic studies in distribution systems[J]. IET Generation, Transmission & Distribution,2017,11(4):1063-1071.
- [10] Shang-Ping Ying, Han-Kuei Fu, Hsin-Hsin Hsieh,etal. The Modeling of Two Phosphors in Conversion White-Light LED[J]. IEEE Transactions on Electron Devices,2017,64(3):1088-1093
- [11] XU Jinghua,SHANG Nan.Optimization Design of Power LED Light Based on Finite Element Analysis[J]. Journal of Jilin University(Information Science Edition),2015,33(05):550-558.
- [12] Philipp Wittmuess, Cristina Tarin, Alexander Keck,etal. Parametric Model Order Reduction via Balanced Truncation with Taylor Series Representation[J]. IEEE Transactions on Automatic Control, 2016 , 61(11): 3438-3451.
- [13] Ray-Lee Lin, Shun-Yao Liu, Chia-Chun Lee, Yi-Chun Chang. Taylor-Series-Expression-Based Equivalent CircuitModels of LED for Analysis of LED Driver System[J]. IEEE Transactions on Industry Applications,2013,49(4): 1854 – 1862.
- [14] WU Yanling.A Node Localization Algorithm Based on Local Information Least Square Method[J].Journal of Jilin University(Science Edition),2017,55(04):952-956.
- [15] Jing Wang,Xin-Jie Zhao,Yi-Xi Cai,etal. Thermal Model Design and Analysis of High-Power LED Headlamp Cooling Device Based on the Thermoelectric Effect[J]. IEEE Transactions on Components, Packaging and Manufacturing Technology,2015,5(5):641-649.

Design of Bluetooth Car Lock Based on Fingerprint Recognition

Fang Zizheng; Liu Shuai; Zhang Zhichao

(*jilin university instrument science and engineering institute, changchun, 130021*)

Abstract—In view of the fact that the fingerprint lock on the market is less and is fixed in the car itself and there is no problem that the fingerprint recognition system can be used for remote control, a Bluetooth lock system based on fingerprint recognition is proposed in this paper. This system combines Bluetooth module and fingerprint identification module through single chip microcomputer, so that fingerprint identification system can be carried around and used remotely, which improves the convenience of the system. In addition, the system uses a fingerprint unlock mode, compared to the traditional way of unlocking more reliable, but also to ensure that the keys lost or stolen after the car locks will not be opened by others, security performance greatly enhanced. Through experimental tests, the Bluetooth based vehicle lock system designed by this paper can open the door for remote fingerprint identification, and the correct rate of unlocking in 5m is as high as 97%.

keywords—Fingerprint identification Bluetooth communication safety car lock

I INTRODUCTION

WITH the rapid development of China's economy, people's lives to achieve well-off, the car as a means of transport has been gradually widely used. With the increasing number of cars in society, car safety problems become more serious and car theft cases often occur. Car door locks as the first barrier to prevent car theft, can be said to be the most important vehicle safety. In order to solve the safety of car locks, some models used car fingerprint recognition technology to improve the safety factor of the car door. However, the current car fingerprint identification system is loaded on the car door, that means the driver must reach out to touch the fingerprint identification system on the door to unlock. This is not easy in comparison with the existing remote unlocking, and now the fingerprint identification systems are mostly equipped only on advanced models, with few ordinary cars, which means most car safety locks still have not been resolved^[1-6]. Today, including smart phones, including many electronic products have been identified fingerprints as a major selling point. Therefore, the combination of high safety factor fingerprint recognition technology and Bluetooth technology capable of transmitting data at appropriate distance has become an inevitable trend in the development of automobile lock system.

In order to solve the problem of car door lock safety, this paper introduces a Bluetooth lock system based on fingerprint recognition. It combines the Bluetooth module and the fingerprint recognition module through

the single chip computer, causes the fingerprint recognition system to be carried and to be used at a long distance, enhances the system convenience. In addition, the system uses a fingerprint to unlock, which is more reliable compared to the traditional way to unlock. At the same time, you can also ensure that the car lock will not be opened by others when the key is lost or stolen, so the security is significantly enhanced. In addition, the system can be extended in a number of areas to adapt to the characteristics of different environments, to provide specialized application requirements. The scope of application is more extensive. After experimental testing, the design of Bluetooth lock fingerprint recognition system based on fingerprint identification can remotely open the door, and its accuracy of unlocking within 5m is up to 97%.

II SYSTEM OVERALL DESIGN

The fingerprint-based Bluetooth car lock circuit system proposed in this paper includes a key having a function of fingerprint unlocking and transmitting signals and a lock having a function of receiving a signal to determine whether or not to unlock. The key part includes a single chip system, a HC-05 Bluetooth module, a fm-608 type fingerprint module, a liquid crystal display 12864, a 24C02 reservoir, a keyboard and a power supply part, etc. The HC-05 lock part includes a Bluetooth module, a single chip system, an electromagnetic relay, an LED indicator, an electromagnetic lock power supply, etc. The system block diagram is as shown in Figure 1.

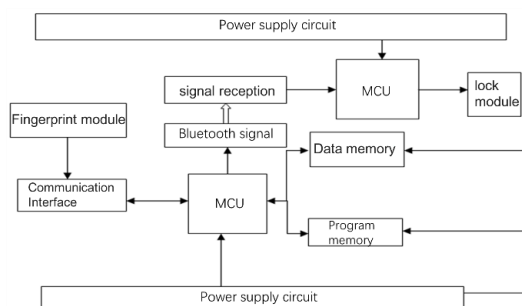


Fig 1 System Block Diagram.

The system is divided into two main functions, as the fingerprint signal acquisition and processing and the verification code transmission and comparison. First of all, the key part of the system collects and compares the user's fingerprint through the fingerprint identification module. Then, it sends different signals according to the results of the comparison to the microcontroller system. The microcontroller according to the received signal for the next step of the action, if allowed to unlock the signal, then start the serial communication, the use of Bluetooth module will store the check code sent to the car lock part; if not allowed to unlock the signal, the serial port does not work, and does not send checksum. At the same time, the key part of the combination of alarm system will alarm, means fingerprint error, could not unlock. If the checksum transmission and reception is successful, the lock portion of the received check code stored in its internal check code will start to compare. If they are equal, the part of the LED will light, and the system will start the electromagnetic relay connection, Electromagnetic lock power on to open, to achieve unlock function. After a period of time delay after the relay power, the electromagnetic lock power off. If the two check code is different or the system do not receive the check code, the car lock part of the microcontroller system on the peripheral equipment will do nothing, and electromagnetic will not act, always waiting for the arrival of the next signal.

At the same time, in order to prevent injury due to fingers, fingers dirty or due to other factors that fingerprint identification are temporarily unable to use, the text independently added the password unlock function, which uses the keyboard to enter the password. Similar to the fingerprint lock, if the input password and the key password which has been stored is same, then send the checksum. If they are not same, the key port will not send anything, and the combination of alarm system will sound the alarm.

III SYSTEM HARDWARE DESIGN

The whole system is combined by the key part section and the car lock part section [7-9]. The key

portion is composed by a FM-608-type optical fingerprint module, a 24C02 memory chip, a HC-05 Bluetooth module, a 12864 character LCD, a buzzer, and a red 5MM LED and a microcomputer system. The physical system is as shown in Figure 2. We choose the STC89C52 microcontroller, with the advantages of production capacity, technology is mature, low-cost, etc. For the 52 MCU only has one full-duplex serial communication, we use the micro switch to separate the use of a serial set of fingerprint identification module and a Bluetooth module. The system physical is shown in Fig2.

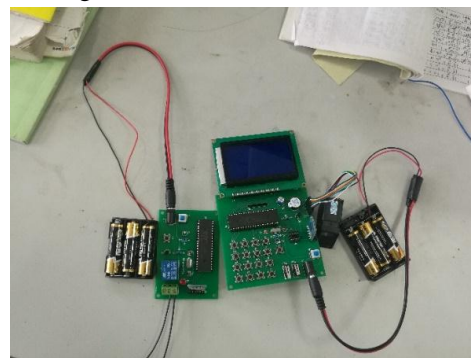


Fig 2 System physical diagram

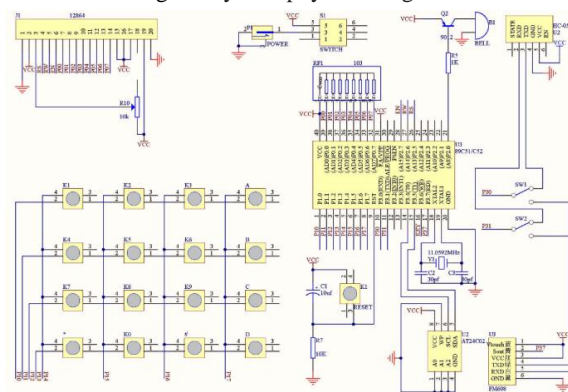


Fig 3 Key circuit external wiring diagram

The car lock portion comprises a HC-05 Bluetooth module, a STC89C52 microcontroller, a 5MM red LED, an electromagnetic relay and an electromagnetic lock portion. As the car lock only need to communicate with the Bluetooth module serial port, the lock on the microcontroller serial port no longer need to use micro-switch, only need to directly connect with the Bluetooth module. Fig lock external wiring circuit, is as shown in Fig3.

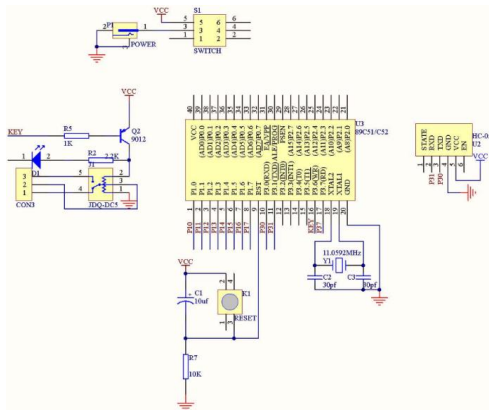


Fig 4 Lock circuit external connection diagram

A Fingerprint Identification module

System uses a FM-608 series of optical fingerprint module. This kind of Fingerprint recognition module section has a high-performance DSP processor core, an optical fingerprint sensor and a Flash chip. It has the following superior advantages : (1) algorithm, comply with the current highest fingerprint industry standards; (2) strong fingerprints responsive adaptation; (3) self-learning function adapted to be customized to automatically adjust the parameters according to the user's habits, such as climate change to match better; (4) a particular highlight green LED light source, with excellent anti-aging properties.

When the user presses the fingerprint identification module, the module sends an inductive signal to the microcontroller. After receiving the signal, the microcontroller system sends the instruction to the fingerprint identification module to start collecting the user's fingerprint. Then performs image processing to extract the fingerprint feature information according to the DSP algorithm to compare the fingerprint with the stored information, and then transmitting different signals to the microcontroller system in accordance with the results of comparison. The microcontroller system selects the next step based on the received different signal selection. Fingerprint recognition module also carries the function of entering users' fingerprint and deleting users' fingerprint.

B Combination Of Light And Sound Alarm System

When the fingerprint identification module found that the fingerprint is not correct after query and comparison, the system determines the fingerprint error, and the combination of alarm system on the key starts to work. At this point, the LED does not work, the buzzer starts to work, screeches, which represents the fingerprint error. This user has no right to unlock, and we need to press the reset button to restore to the initial state of the system. If the fingerprint is correct, the combination of the alarm system does not start, the LED lights, the buzzer does not start. After a short

delay, the key portion sends a code to the key lock to unlock the lock after verification is correct. When the finger is injured so we can not use a fingerprint to unlock and require the use of a password unlock, The combination alarm system boot, LED grow lights off, the buzzer starts to work if the password is wrong. When the password is correct, the combination of the alarm system does not start, LED lights up, the buzzer does not start. Its work is the same of the use of fingerprints.

C Bluetooth Wireless Transmission System

HC-05 Bluetooth type module is the most widely used, technology mature, and inexpensive Bluetooth module. Through the following settings, you can achieve a specific signal transmission and encryption between the two Bluetooth module: When using the host computer to initialize the Bluetooth module, first we need to set the two Bluetooth modules' master and slave roles; and then we need to bind the address of the two Bluetooth modules so that they can only communicate with the other side and do not communicate with other Bluetooth modules; Finally we need to set the connection passwords and query access codes to achieve the transmission signal encryption. The use of Bluetooth module for wireless data transmission and data encryption is not only a simple method, but also with a high reliability.

IV SYSTEM SOFTWARE DESIGN

The system software includes a key lock procedure and a car lock procedure [10-15]. The key part of the process flow chart is as shown in Fig 5.

After the key part starting, it starts to initialize the operation and determine whether the key is connected with the car lock. If not successful, it continues to return to create a connection; If successful, then it determines whether there is a fingerprint. If the fingerprint inputs, it starts the fingerprint matching. When the fingerprint match is successful, it sends an unlock signal; If the match is not successful, then it continues to collect fingerprints. When the number of fingerprint input reaches the upper limit, the power out.

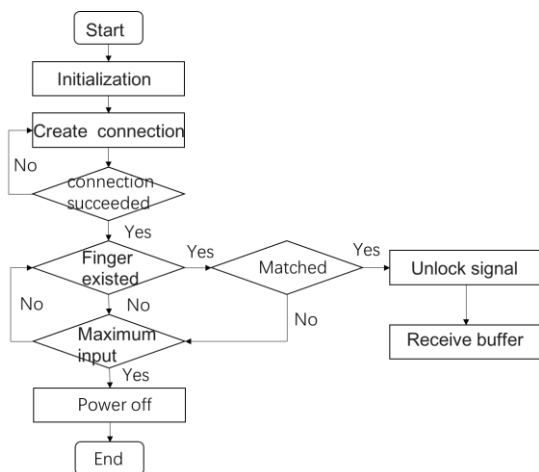


Fig 5 Key part of the program flow chart

The lock part program flow chart is as shown in Fig 6. The system starts to initialize the operation, and it determines whether the car lock is connected with the key. If the connection is successful, it start to match the check code received with the checksum stored inside the lock system. If the match is successful, then unlock; if the match is not successful, then continue to receive the checksum.

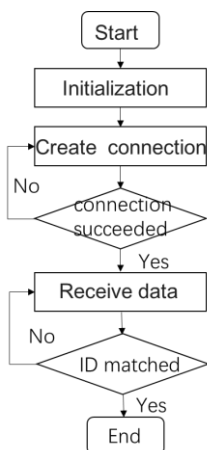


Fig 6 Lock part of the program flow chart

V EXPERIMENTAL TEST

We tested the whole system at a temperature 25 °C conditions without obstacle of the lock system. The key part's initialization interface is as shown in Fig 7 and the unlock statue is as shown in Fig 8. According to the test results, the system basically reached the required functional requirements. In the actual test, the key part of the fingerprint recognition module and the communication between the microcontroller and the Bluetooth module is stable. We can achieve fingerprints' input, deletion, contrast and match in the key part. Table 1 and Table 2 show the performance of fingerprint and password unlock in the distance of 5m. It could be seen from the table that the fingerprints' unlock success rate in 5m away is of 97.3%,

and the password's success rate is of 99%; Table 3 and Table 4 show the performance of fingerprint and password unlock in the distance of 10m. It could be seen from the table that the fingerprints' unlock success rate in 10m away is of 72%, and the password's success rate is of 69.7%. Therefore, it is recommended that the key and car lock is used in a short distance, so as to avoid excessive signal losses.



Fig 7 Key-side initialization interface

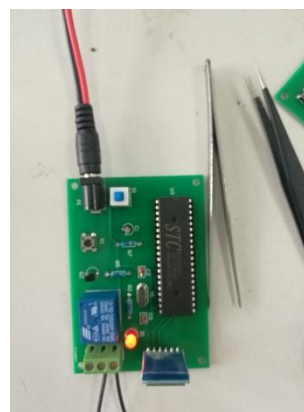


Fig 8 Successfully unlocked interface

Table 1 Test fingerprint unlock system performance over a distance of 5m (test 300)

Times of error identities	Times of successful deletions	Times of correctly add	Times of successful unlocks	Times of signal lost
3	300	293	292	5

Table 2 Test unlock password system performance over a distance of 5m (test 300)

Times of error identities	Times of correctly change	Times of successful unlocks	Times of signal lost
0	300	297	3

Table 3 Test fingerprint unlock system performance over a distance of 10m (test 300)

Times of error identities	Times of successful deletions	Times of correctly add	Times of successful unlocks	Times of signal lost
4	300	291	216	80

Table 4 Test unlock password system performance over a distance of 10m (test 300)

Times of error identities	Times of correctly change	Times of successful unlocks	Times of signal lost
0	300	209	91

VI CONCLUSION

At present, with the increase in the number of cars in society, the car safety problems have become increasingly significant. Fingerprint recognition as a body recognition technology, can extend the car doors' anti-theft ability in some way. However, the number of cars with fingerprint recognition lock on market is very little, and they are all fixed in the car itself. There is no remote fingerprints Identify control car lock system can used in the market. To solve the problem, this paper combines the Bluetooth module with the fingerprint recognition module through the single chip computer, designs the fingerprint lock system based on the fingerprint recognition system, which makes the fingerprint recognition system could carried and used remotely to improve the convenience of the system. In addition, the system uses a fingerprint to unlock the car lock. Compared to the traditional way to unlock ,it is not only reliable, but also ensures that the lock will not be opened by others after the key is lost or stolen. The security is significantly enhanced. Seen by many experiments, the design of Bluetooth car lock based on Fingerprint Recognition's Fingerprint recognition unlock accuracy within 5m is up to 97%. This car lock system is of low cost, high safety factor and using easily. It has automatic alarm function and other advantages. So it is a small security equipment which could bring more convenience to people who use the car now or in the future.

References

- [1] Zhao Zhe, Ma Xiaojun, Network Vehicle Anti-Theft System Design Based on Fingerprint Identification[J]. Computer Measurement & Control, 2013, 21(12) : 3356-3358.
- [2] Pan Jianjun, Zhang Haoyang, Wang Yong, Design of embedded automatic finger print identification system[J]. Journal of Beijing Information Science & Technology University, 2010, 25(1):62-65.
- [3] He Han, Design of Embedded Automatic Fingerprint Identification System[J]. Information & Communications, 2014(7):55.
- [4] Zhao Haifeng, Embedded Automatic Fingerprint Identification System Designation Based on Linux [J]. Information Security and Technology, 2013(10):25-26.
- [5] Yang Jifeng, Yang yong, Design of Auto-guard System Based on Fingerprint Identification[J]. Modern Electronics Technique, 2011, 34(15):197-199.
- [6] Chen Qixin, Luo Weidong, Zhangli, Automobile anti-theft system based on mobile phone-electronic key fingerprint identification technology[J]. Guizhou Science, 2016, 34(4): 91-96.
- [7] Zhang Qin, Design of Anti - theft Control System Based on Fingerprint Identification[D], Wuhan, 2011
- [8] Ling Bin, Suo Jianwen, Xu Jingtao, Design of Automotive Door System Based on Fingerprint Identification and Lin Bus[J]. Computer Measurement & Control, 2016, 24(3): 193-195
- [9] Sheng Gang, Research and Design of Automobile Anti - theft Fingerprint Identification System Based on DSP[D], Hangzhou, 2014
- [10] Xin Libin, Zhang Zhenguo, Wang Shunping, Optimization and Improvement of the Algorithm of Automatic Fingerprint Identification System[J]. Electronic Science and Technology, 2016, 29(6):41-43.
- [11] Tian Miao, Feng Jinliang, Wen Qin, A study on fingerprint entrance guard system based on Linux system[J]. Electronic Design Engineering, 2014, 22(2):134-136.
- [12] Wang Wei, Li Chunming, Design of the fingerprint identification system based on ARM-Linux [J]. Electronic Design Engineering, 2012, 20(15):180-183.
- [13] Hu Rong, Design and Implementation of ARM Cortex - M3 Fingerprint Identification Door Lock Control System[D]. Nanchang, 2014
- [14] Shen Zhengnan, Jiang Haobin, Ma shidian, Research of the Vehicle Antitheft System Based on Fingerprint Identification Technology[J]. Automobile Parts, 2014(11):20-22.
- [15] Zhang Yanhong, Wang Lixue, Tong Chenke, Design of Fingerprint Identification Password Lock Based on SCM [J]. Industrial Control Computer, 2016, 29(12):128-129.

The study of light intensity traceable photovoltaic power generation lighting system

Xia Tiancheng; Yang Yuanyuan; Huang Sibao

(Jilin university instrument science and electrical engineering institute, changchun, 130021)

Abstract—In view of the most present domestic photovoltaic power generation systems adopt fixed Angle bracket mounting method, low generation efficiency, we present a design scheme for a light intensity traceable photovoltaic power generation lighting system. Based on the STC89C52RC MCU, we use light sensor to collect light intensity, judge in the MCU to control the stepping motor to achieve the purpose of tracking light intensity. The wireless sensor network is adopted to realize the real-time monitoring of system storage power. When the lighting system stores low power, it can automatically switch to the city power grid to power the system. The system has simple structure and low cost, which can ensure the efficiency of power generation and overcome the negative effects of objective factors.

Keywords—traceable, photovoltaic power generation, MCU control, electric power detection, power supply mode switching

I INTRODUCTION

SOLAR energy is one of the most promising renewable energy sources in today's world, for this reason, the world has done a lot of in-depth research on it. The most popular solar energy products are solar street lamps. Most of the solar streets lamps in China adopts fixed Angle of installation, in which way, there is a problem of low solar utilization and difficulty in working in bad weather, such as rainy weather. Based on the above problems, this paper designed a kind of light intensity traceable photovoltaic power generation lighting system which is based on STC89C52RC MCU. The system is based on the light intensity of sensor collection, which can realize the automatic tracking function by comparing the light power, and can effectively improve the utilization of solar energy.

II GENERAL DESIGN OF SYSTEM

STC89C52RC is a low-power-consumption and high-performance CMOS 8-bit microcontroller produced by STC, with 8K byte system programmable Flash memory. STC89C52 uses the classic MCS-51 kernel, but has done a lot to improve the ability of the chip compared with traditional 51 MCU. With a smart

8-bit CPU and programmable Flash in the system, STC89C52 provides a highly flexible and super-efficient solution for many embedded control applications. Using STC89C52RC as the control center of the whole system can meet the complex control requirements^[1]. The tracking control is realized mainly according to the light intensity in each direction of the location of the system. By the four light sensors installed on the solar panel, the system automatically determines whether to conduct a horizontal and pitching freedom movement. The measured values of each illumination sensor can be displayed by LCD in order to monitor the lighting intensity in real time. The electricity generated by the solar panels is stored in the battery, which is supplied by the battery to the street lamp when the light intensity is small at night. When the bad weather, such as rain a lot, causes the battery power to be insufficient to continue the power supply, the system automatically switches to the city power grid to power the system., until the battery is recharged to a certain amount of power. When the system is actually running, the upper computer can monitor the residual power of the battery in real time and can switch the power supply manually. The general design of system is shown in figure 1.

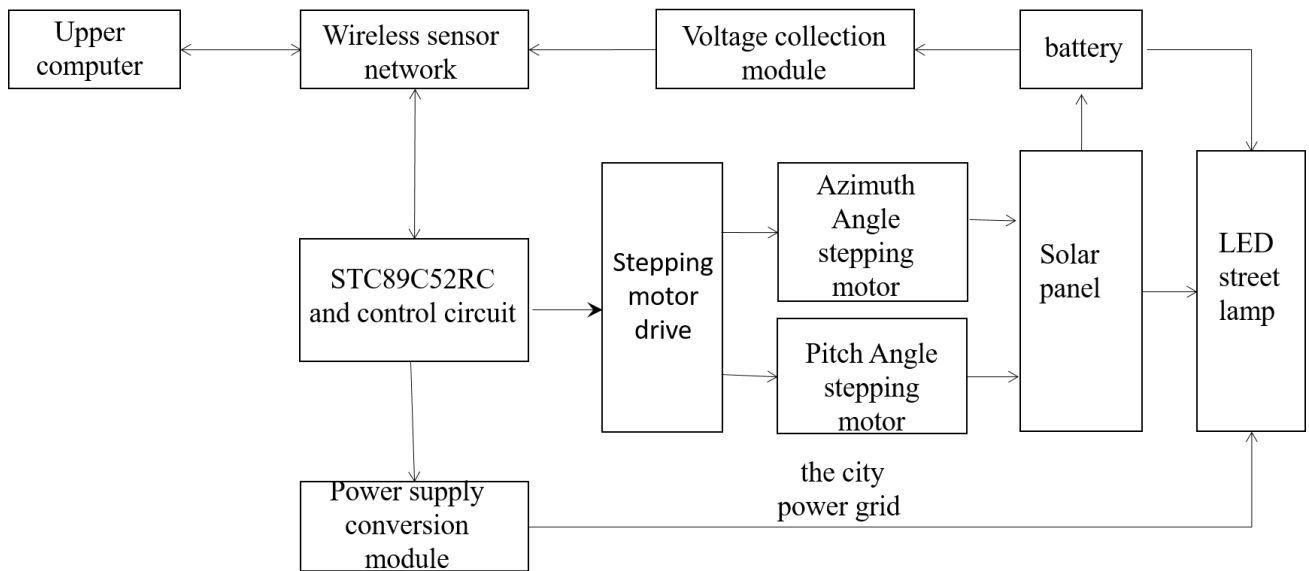


Fig 1 Structure diagram of the light intensity traceable photovoltaic power generation lighting system

III THE HARDWARE DESIGN

A Light intensity sensor module

In order to enable the system to track the maximum light intensity in real time and to improve the efficiency of power generation, the light-intensity sensor on the solar panel was collected and monitored by the GY-30 light sensor. The sensor does not distinguish the ambient light source, it can be used to determine the high accuracy of 1lx for a wide range of brightness. The light sensor is mounted on the midpoint of the four edges of the solar panel, which can be read and passed to the MCU directly[3], as shown in figure 2.

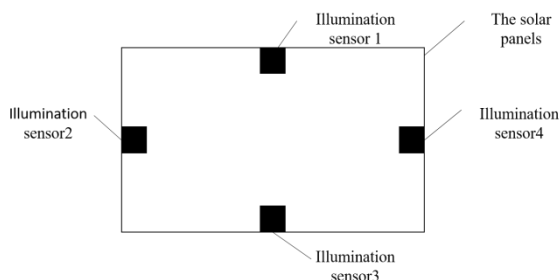


Fig 2 Light sensing module

B Stepper motor drive module

The system adopts the dual-axis tracking design, [4] we use two stepper motors to control the azimuth and pitch Angle respectively. If the light intensity of 1 and 3 is not equal, the system will determine which light intensity is large and control the pitch Angle stepper motor, and adjust the pitch Angle until 1 and 3 are equal. In the same way, if the light intensity of 2 and 4

is not equal, the azimuth Angle stepper motor will adjust the azimuth until they are equal. If the four sensors have a light intensity of less than the specified value (when the environment is dark enough), light the lamp, as shown in figure 3[2].

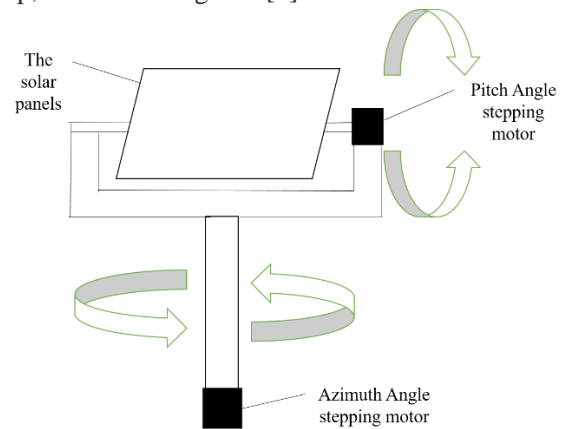


Fig 3. Stepping motor drive module

C Voltage collection module

The voltage collection module collects the voltage of the battery and passes the voltage value to the upper computer and the MCU through the wireless sensor network. The upper computer can monitor the battery voltage of each street lamp in real time, improve the battery utilization, prevent the battery from overcharging and discharging, and prolong the battery life. When the battery is less than 45% of the charge, according to current voltage, the charging current is required to stop charging when it reaches or exceeds 70% of the charge.

D Conversions of the supply mode module

The power supply of the system is dominated by solar panel power, with 220V ac power supply mode.

In this mode, the battery capacity can be small. The electricity generated by the solar panels during the day is stored in the battery, and the electric lighting in the battery is used at night. In this way, the electricity generated during the day is just enough for nighttime use. When the battery voltage is low, the system automatically switches the power supply mode, from the power supply of the battery to the city power grid. In most parts of our country, there are more than two-thirds of the clear weather in the whole year, so that the system can light up the street lamps for more than two-thirds of the year. In the rest of the time, the system uses city electricity to replenish energy, which can both reduce the one-time investment of solar photovoltaic lighting system and have significant energy saving and emission reduction effect. It is an effective method for the promotion and popularization of solar LED street lighting in the current stage.

IV THE SYSTEM SOFTWARE DESIGN

After completing the self-check and initializing procedure, the system begins to read various setting parameters such as battery status and working mode. Then, by comparing the values of light intensity and the setting value, judge whether the system works during the day or at night (or the rainy weather with less light intensity). When the system works during the day, the light sensor collects the data every minute. If the intensity of light measured by a pair of illumination sensors is not equal, then the MCU controls the stepper motor to adjust the Angle until the measured value is equal. If the light intensity measured by the light sensor is lower than the setting value, the system starts the night work mode. When the system works at night or when the light intensity is low, the light sensor collects the data every 30 minutes and lights up the street lamps. If the light intensity reaches the setting value, the system starts the day work mode [5]. The system flow diagram is shown in figure 4.

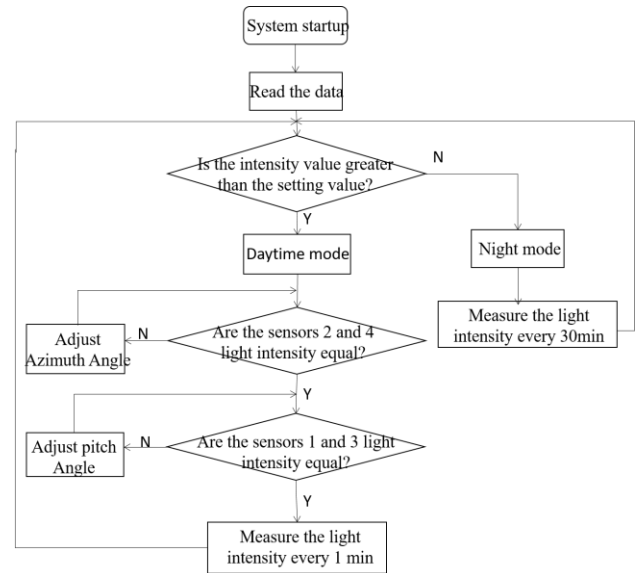


Fig 4 System flow diagram

V EXPERIMENT TESTING

Select two solar panels with the same performance parameters, one is installed in the best Angle of local illumination and the other is installed on the system [6]. Put them outside and collect the mean data of the seven days of light intensity as the experimental data. The experimental results are shown in figure 5 and data is shown in table 1.

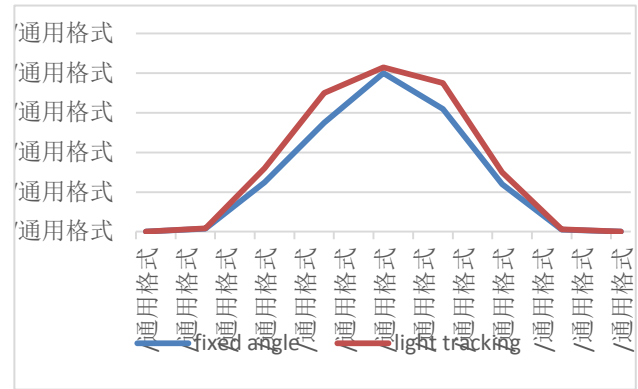


Fig 5 light intensity contrast diagram in two ways

Table 1 Light intensity contrast in two ways

Time	0	3	6	9	12
Fixed angle	0	154	2521	5539	8004
Light tracking	0	160	3254	7023	8371
Time	15	18	21	24	
Fixed angle	6260	2418	133	0	
Light tracking	7597	3011	120	0	

VI CONCLUSION

In the clear weather, the efficiency of solar panels used in this system is much higher than that of fixed Angle installation. Even in the rainy weather, the efficiency of solar panels used in the system is obviously higher than that of fixed Angle installation. Therefore, the generation efficiency of the system is superior to the system of fixed Angle installation in different environments.

References

- [1] Wang wanle,Song jian,Xie yunxing,Lu xiangfeng,Gong maofa.Design of High Precision and All-weather Solar Auto-tracking System[J].Instrument Technique and Sensor.2017,(07):76-78+83.
- [2] Liu qingqing,Yuqiang,Zhao maomao,Wang jingxiong. Design of STM32-Based Photoelectric Solar Tracking System[J].Instrument Technique and Sensor.2017, (01): 123-125+129.
- [3] Wang rui,Tan tu,Wang lei,Wang guishi,Zhu gongdong,Cao yanan,Gao xiaoming.Development of High-Precision Solar Tracking System Based on 51 Microcontroller[J]. JOURNAL OF ATMOSPHERIC AND ENVIRONMENTAL OPTICS. 2016,11(06):466-473.
- [4] Zhao jianhua,Zhang tingting.Research and design of sun-tracking control system[J].ELECTRONIC MEASUREMENT TECHNOLOGY.2016,39(03):1-3+28.
- [5] Li renhao,Gong simin,Yang fan,Liu song,Li xiaobing. Design of Solar Energy Automatic Tracking System Based on Single-chip Microcomputer Control[J].Instrument Technique and Sensor,2015,(04):51-53+60.
- [6] Takahashi, Akiko; Yamagata, Akihiro; Imai, Jun. Decomposition of Fluctuating Photovoltaic Generation Power in Frequency Bands and Analysis of Chaotic Properties.[J].ELECTRICAL ENGINEERING IN JAPAN.2017.(12);26-33

Research of brain-computer interface based on multi-feature integration and BP neural network

Liu Guangda; Wang Can; Li Mingjia; Sun Ruichen; Cai Jing; Gong Xiaoyu
(College of Instrumentation&Electrical Engineering, Jilin University, Changchun Jilin 130061)

Abstract—This research is carried out to re-design a brain-computer interface(BCI) system based on motor imagery recognition through extracting features of Alpha wave in electroencephalography(EEG) signal during motor imagery process, using multi-feature classification method in order to increase the accuracy of classification . Aiming at the shortcomings such as low accuracy and time-consuming when only one feature is adopted in the classification process, methods including autoregressive model (AR), statistical features extraction and frequency domain analysis,etc. are taken to extract various features of Alpha wave. BP neural network is used to classify features. The system is designed to identify motor imagery and through experimental verification, it has achieved expected effect with high classification accuracy. The research proves the feasibility of brain-computer interface system combining multi-feature integration with BP neural network.

Key words—Multi-feature BP neural network Brain-computer interface (BCI) Motor imagery Alpha wave

I INTRODUCTION

ELECTROENCEPHALOGRAPHY (EEG) signal consists of complex components, which can be divided into different waves according to different frequency ranges[1].

The Alpha wave in EEG signals is pronounced in the frontal lobe and more rhythmical than other EEG signals, which appears mostly when people are conscious with eyes closed. When humans think about problems with eyes open or are simulated by the outside, the Alpha wave disappears, and when eyes are closed again, it reappears, which is called Alpha-blocking phenomenon[2]. It has been shown in the research that Alpha wave is related with memory, movement and sensory activity[3]. The relationship is of great importance in judging the brain's movement intention.

Using brain-computer interface(BCI) system to collect, preprocess, extract features and classify patterns of EEG signals is the focus of recent research to realize motor imagery recognition.

In recent years, methods used to extract features of EEG signals include AR model[4], statistical features extraction[5] and frequency domain analysis[6,7]. And methods used to classify patterns include linear discriminant classification method and BP neural network[8].

In the process of extracting features, classifying patterns with single feature can lead to large amount of training data, being time-consuming and even low classification accuracy. Therefore, in this research,

features of the Alpha wave are extracted and patterns classified based on multi-feature integration method and BP neural network, which has the advantage of high accuracy. Human's movement consciousness can be judged through extracting features and classifying patterns of motor imagery EEG signal. Combined with BCI, there are great prospects for rehabilitation of physically handicapped people, control assistance and entertainment[9].

II FEATURE-EXTRACTED METHOD AND TEST

A AR model

It is convenient to calculate AR model. A single channel EEG signal is provided, consisting of sampling points ranging from x_0 to x_{n-1} . Suppose

a_i is AR model coefficient, p is AR model order

and e_k is residual white noise. According to AR

model, the value of x_k can be calculated as shown in

formula (1),

$$x_k = \sum_{i=1}^p a_i x_{k-i} + e_k \quad (1)$$

Parameters of AR model are estimated through methods including autocorrelation, covariance adjusted approach and Burg algorithm, etc. Calculation of Burg algorithm is easy and the spectrum it produces is of high quality. Therefore, Burg algorithm is adopted to estimate parameters of AR model. Through

experimental verification, p equals 3.

B Statistical features extraction

1) Integral value of EEG signal

Suppose that the value of EEG signal data is x_i and the length N . The integral value, which represents the concentration degree of the signal, is calculated as shown in formula (2),

$$P = \frac{1}{N} \sum_{i=0}^{N-1} |x(i)| \quad (2)$$

2) Root mean square value of EEG signal

Root mean square(RMS) is calculated as shown in formula (3), which reflects dispersion of the signal.

$$Q = \sqrt{\frac{1}{N} \sum_{i=0}^{N-1} x(i)^2} \quad (3)$$

C Frequency domain analysis

In the research, power spectrum, mean power frequency(MPF) and power spectral density are chosen as characteristic values.

Assumptions are made that EEG signal is random signal $x(n)$ with limited energy and the number of sample values is N . And Fourier transformation of $x(n)$ is $X_N(e^{j\omega})$ [10]. The calculation of power spectrum is shown in formula (4),

$$P(e^{j\omega}) = \frac{1}{N} |X_N(\omega)|^2 \quad (4)$$

From the power spectrum of EEG, the peak value can be observed and both sides' amplitude of the peak value decreases. The power spectral density ratio [10] can be obtained by using power in some frequency range divided by the power in the whole spectrum, as shown in equation (5),

$$K = \frac{\int_{f_{\max}-n}^{f_{\max}+n} P(f) df}{\int_{-\infty}^{+\infty} P(f) df} \quad (5)$$

f_{\max} in the equation represents the frequency where peak value appears and n means the range of integration.

MPF quantitatively describes the feature of EEG frequency spectrum, which can be obtained through equation (6).

$$L = \frac{\int_0^{+\infty} fP(f) df}{\int_0^{+\infty} P(f) df} \quad (6)$$

D Features test

In order to improve the accuracy of classification, the K-W test is used to test extracted characteristic values, as shown in equation 7,

$$H = \frac{12}{N(N+1)} \sum_{i=1}^m N_i \left(\bar{R}_i - \frac{N+1}{2} \right)^2 \quad (7)$$

In the equation above, N refers to the number of sample, m refers to types and \bar{R} refers to the average of each sample's number. The greater value of H , the stronger the classification ability of the feature.

The test result of 600 pieces of characteristic values in front, back, left and right, four directions is shown in table 1.

TABLE I K-W TEST

Feature	H	Feature	H
Integral value	126.262 5	Power spectrum	7.241 5
RMS	125.291 3	Power spectral density ratio	3.643 2
AR model	100.850 3	MPF	5.263 7
	108.082 1		

It can be seen from table 1 that H of integral value, RMS and AR model is higher than the others. Therefore, these three features are selected to classify patterns in the following procedure.

III CLASSIFICATION METHOD

After extracting features of EEG, BCI system chooses BP neural network to carry on classification.

BP neural network in the research, as shown in figure 1, consists of four input layers, which represent four characteristic values, seven hidden layers and four output layers, which represent four classification categories.

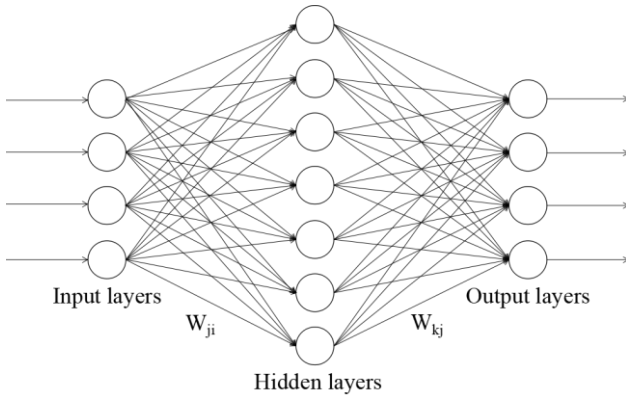


Fig. 1 BP neural network structure

The three-layer network can complete the required mapping in the case of limited neurons. The learning process of BP neural network consists of forward and backward propagation. The input signal x_i passes through the intermediate node acting on the output node, and then the output signal y_i is finally produced through nonlinear transformation. The network training samples contain the input vector and the expected output. The deviation is the actual output of the neural network. Through adjusting the connection weight W_{ji} between input nodes and hidden nodes, the connection weight W_{kj} between hidden nodes and output nodes and threshold, error of the deviation can be reduced. After repeated training, the weights and thresholds of the corresponding neural network are determined when approaching the minimum error. At this point, the training is finished[12].

IV EXPERIMENT AND RESULT ANALYSIS

A Design of Experimental System

The structure of EEG collecting system is shown in figure 2. The electrode collects the EEG signal. The weak signal is firstly amplified through the amplifier, then the interface is filtered. After filtering, A/D modulation converts it into digital signal. Finally, digital signal is sent to the host computer for further processing via bluetooth.

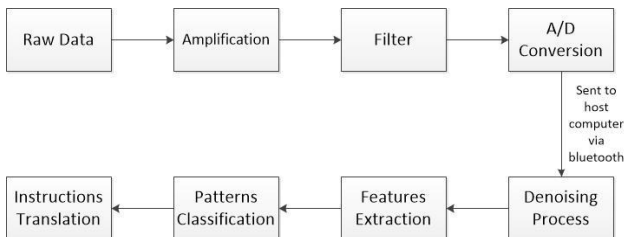


Fig. 2 EEG signal collecting system

B Experimental conditions and methods

The electrode position is arranged in accordance with the Montreol method and the international standard lead 10-20 system, as shown in figure 3. The electrode is positioned to the frontal lobe of the subject to collect Alpha wave, where the arrow in the figure points. The ear clamps used as the reference electrodes are attached to the left and right lobes.

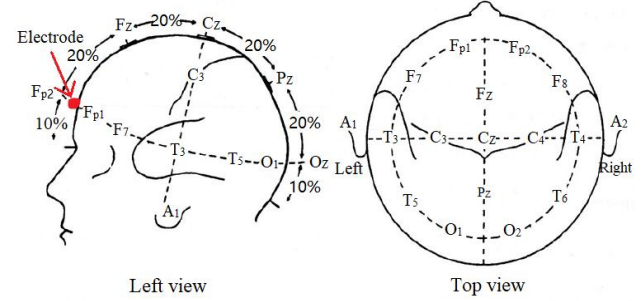


Fig. 3 Electrode position

In order to ensure the accuracy of the acquired data, the subject's attention received a large number of training with Schulte grid^[14] before the experiment.

C Experimental process

The subject is a male, healthy and right-handed youth who has corrected-to-normal vision. The environment in the laboratory is quiet with a normal room temperature. Dry electrodes are used to collect EEG.

Before collecting experimental EEG data, Alpha-blocking experiment needs to be carried out to verify the correctness of the acquired EEG signals. The result is shown in the figure 4.

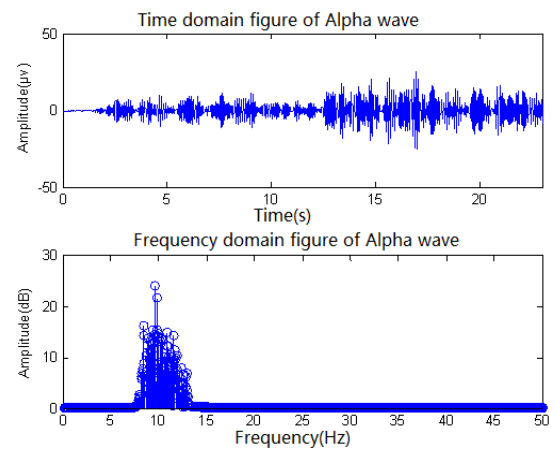


Fig. 4 Alpha-blocking experiment

In the experiment, the subject carries out the motor imagery task according to the example experiment as shown in the figure 5.

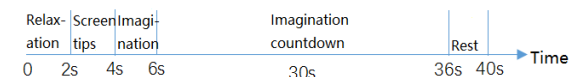


Fig. 5 Example experiment

Half an hour before the start of the experiment, the

subject left actual movement feeling in the brain through actual movements of left and right hands and left and right legs. In the experiment, the subject sits on a comfortable chair with body relaxing and imagines the movement of right and left hands and right and left legs according to the screen tips.

D Data process

Every piece of data of motor imagery lasts 30 seconds and the sampling rate is 512 Hz. Figure of raw data is shown below,

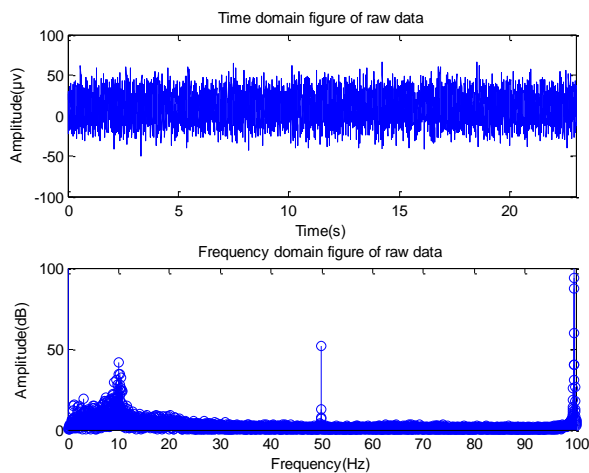


Fig. 6 Figure of raw data

First, the raw data enters into the band-pass filter to filter out the Alpha wave. Then the 50 Hz notch filter is used to clear the power frequency interface. Finally, the wavelet packet denoising is used to make the data better process. Figures of raw data after a series of filters are shown below,

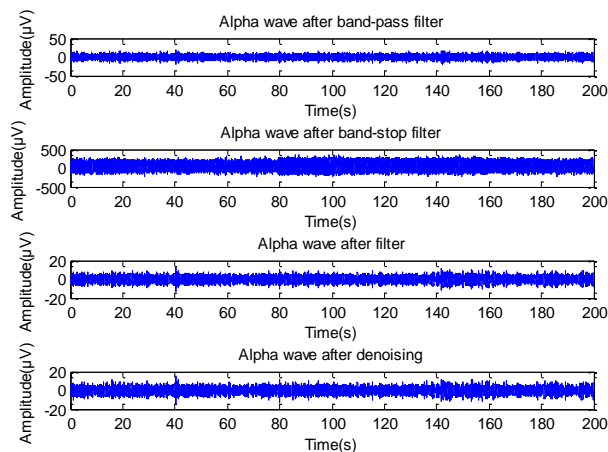


Fig. 7 Figures of alpha signal after process

Raw data can be used to extract characteristic values and carry on classification training after process like filter.

E Analysis of results

Classification accuracy in each direction of motor imagery is shown in the table 2, in which LH represents left hand, RH right hand, LL left leg and RL right leg.

TABLE II CLASSIFICATION ACCURACY IN EACH DIRECTION

	Average accuracy	Highest accuracy
LH	82.71%	88%
RH	85.41%	92%
LL	82.61%	89.29%
RL	83.33%	85.19%

V CONCLUSION

Various features combined with BP neural network in an innovational way are used to analyze EEG signals in the research. After extracting proper statistics, the final classification accuracy is higher than methods like single feature and linear classifier, which proves the feasibility of the method of multi-feature with BP neural network in processing EEG signals. And it shows an effective way for EEG signal process.

References

- [1] Zhang Ledi, Wang Junsheng, Chang Xu et al. Research and design of a portable EEG collector[J]. Application of Electronic Technique 2014(02):27~29.
- [2] Arroyo S, Lesser RP, Gordon B et al, Functional significance of the mu rhythm of human cortex: an electrophysiologic study with subdural electrodes[J], Electroenceph clin Neurophysiol 1993, 87:76~87.
- [3] Chen Jian. Design and Experiment Research of TV Remote Control System Based Brain-computer Interface System[D]. Tianjin University, 2005.
- [4] K. Inoue, S. Matsuoka. Pattern recognition of EEG signals during right and left hand motor imagery based on AR-model[J], Clinical Neurophysiology, 2007, 118(10):209-209.
- [5] Matthias K, Peter M, Ulf G. BCI competition 2003-Data Set II b:support vector machines for the P300 speller paradigm[J]. IEEE Transactions on Biomedical Engineering, 2004, 516 (6) :1073-1076.
- [6] Ronager. Power Spectrum Analysis of EMG Pattern in Normal and Diseased Muscles[J]. J Neurol Sci, 1989, 94(1-3):283-294.

Research on gesture recognition based on Probabilistic Neural Network

Wei Qingli; Xiao-Wei; Liang Weiqiang; Sun Zhenchao; Zhang-Li

(College of Instrumentation and Electrical Engineering, Jilin University, Changchun 130061, China)

Abstract—In order to achieve the goal of gesture recognition, the AgCl patch electrode is used as the signal sensing end. By collecting the forearm surface EMG signal, the signal is amplified, filtered, and then the active segment detection, noise reduction and other signal processing, the root mean square values and the integral EMG values of the four kinds of gesture that stretched forefinger, fist, wrist extension and wrist flexion were used as the eigenvector to be trained into the Probabilistic Neural Network to realize the identification of gestures. The experimental results show that Probabilistic Neural Network can achieve 97.625% correctness for pattern recognition of forearm EMG signals, and it is feasible to apply Probabilistic Neural Network to gesture recognition system.

Key words—Probabilistic Neural Network; surface electromyography signal(SEMG); gesture recognition; pattern recognition

0 PREFACE

SURFACE electromyography signal(SEMG) picked up from the surface of the human skin through the surface of the patch electrode can reflect the neuromuscular system-related activities of the weak bioelectric signal[1]. The untreated SEMG is very weak, usually in the tens of microvolts to several millivolts[2]. SEMG because of its advantages of collection process of noninvasive, easy to detect the the same time with the detection technology and signal processing technology by the rapid development of more and more researchers of all ages, domestic and foreign scholars on the use of neural networks to deal with SEMG also has a more in-depth study. Mahdi Khezri, an overseas scholar, used an adaptive neuro-fuzzy inference system to identify hand action commands and got an action recognition rate of 92%[3]; Zhang Yi and other domestic scientists use wavelet transform and AR model SEMG analysis and processing using RBF neural network on the SEMG signal pattern recognition, correctly identified the gesture action[4]; YANG Shan-xiao Using the maximum and minimum values of multi-scale decomposition coefficients of wavelet transform as the feature quantity, the eigenvector was input to the improved BP neural network based on L-M algorithm, and the ideal recognition effect was achieved[5]. With the rapid development of computer algorithm technology, the development space of neural network will be very broad.

Based on the characteristics of SEMG, this paper takes the signal acquisition and processing as the basis, extracts and selects the more effective eigenvalues,

constructs the neural network input vector and uses it to train the PNN neural network, analyzes the pattern recognition results, and analyzes the follow- Research provides theoretical basis.

I PROBABILISTIC NEURAL NETWORK

Probabilistic Neural Network(PNN) is a kind of feedforward type network, using Parzen window function density estimation method to estimate the condition probability, the classification pattern recognition[6]. Generally divided into input layer, pattern layer, sum layer and output layer. The input layer is responsible for inputting the eigenvector into the network; the pattern layer connects with the input layer through the connection weight to compute the degree of matching between the input feature vector and the various patterns in the training set; the summation layer is responsible for connecting the model class elements of each class. The degree of matching of the class is summed and averaged to get the category of the input sample. The basic structure of the Probabilistic Neural Network[7] is shown in Figure 1.

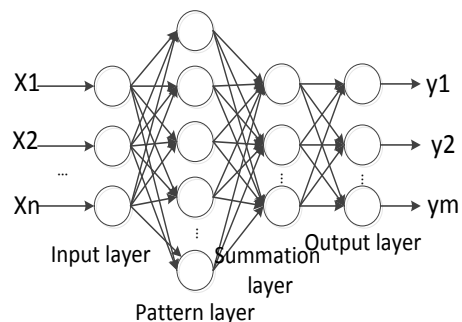


Fig 1 PNN network basic structure

II GESTURE RECOGNITION SYSTEM

Identification system is mainly made of the acquisition module, signal processing module, A / D conversion module, wireless communication module, the host computer display interface and other components. First, use the non-invasive AgCl chip electrode to collect forearm SEMG, through the EMG sensor for amplification, filtering and other processing, after processing the signal through A / D conversion and Bluetooth wireless communication, transmission to the host computer for signal processing and display. And finally through the visual information such as feedback to confirm the recognition results. The overall block diagram of the identification system is shown in Figure 2. The signal processing is shown in Figure 3.

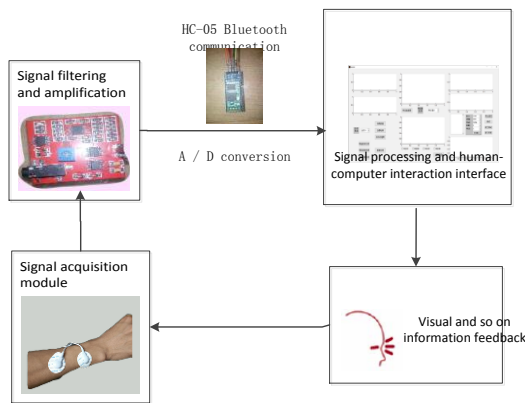


Fig 2 system block diagram

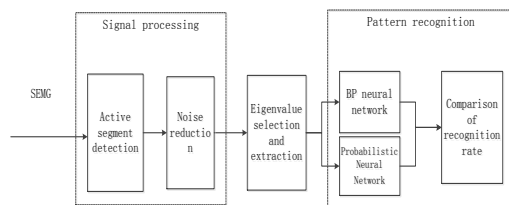


Fig 3 signal processing flow chart

III EXPERIMENTAL RESULTS AND ANALYSIS

The collected SEMG still need to be further processed to achieve the purpose of gesture recognition. Including the signal processing, eigenvalue selection and extraction, pattern recognition and other experimental process.

3.1 Signal Processing

Signal processing is divided into SEMG active segment detection and SEMG noise reduction.

Due to the intermittent and randomness of the SEMG, it is necessary to carry out the active section detection. In this paper, the edge detection method is used to detect and extract the active segment, that is the gradient operator of each pixel is approximated by

small area template convolution to obtain the edge intensity in X and Y directions[8]. To grasp the boxing action, for example, the action signal and the activities of the test results shown in Figure 4.

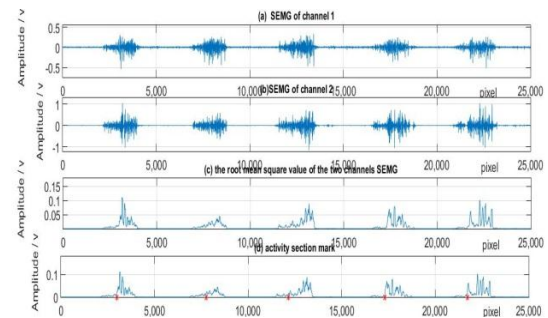


Fig 4 time domain map of active segment detection

Design Butterworth band-pass filter and band-stop filter to remove the baseline drift and power frequency interference. Comparison of filtering before and after frequency domain is shown in Figure 5.

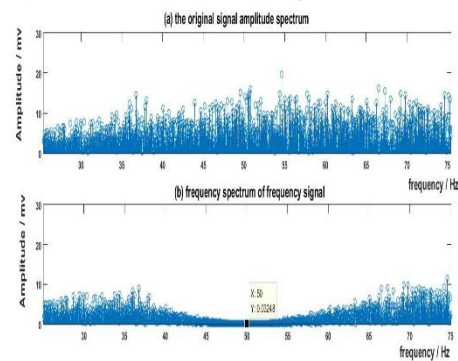


Fig 5 Comparison of filtering before and after frequency domain

As can be seen from Figure 5, 50Hz frequency interference is filtered.

3.2 Selection And Extract Of Eigenvalues

The SEMG after noise reduction processing needs to extract the eigenvalues to perform pattern recognition. This article focuses on the extension of the index finger, stretching wrist, wrist and fist action generated surface EMG signal, the action diagram is shown in Figure 6

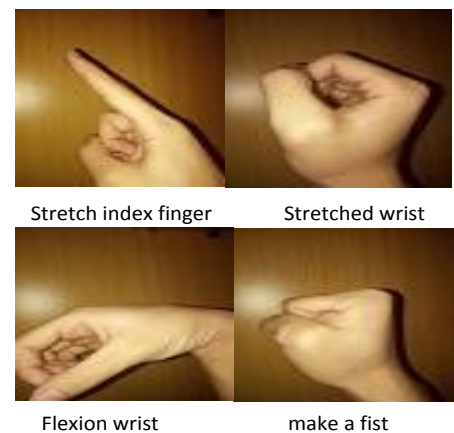


Fig 6 Schematic diagram of the action

The eigenvalues to be selected have time-domain analysis of the integral electromyography (IEMG) and

root mean square (RMS), the frequency domain analysis of the average power frequency (MPF) power spectral density(PSD) and median frequency(MF).

Integral electromyography is the mean value of the signal after the average, which is calculated as

$$IEMG = \frac{1}{N} \sum_{i=0}^{N-1} |x(i)|$$

The root mean square value can be used to describe the average degree of the signal, which is calculated as

$$RMS = \sqrt{\frac{1}{N} \sum_{i=0}^{N-1} x(i)^2}$$

The average power frequency in the frequency domain can also reflect the SEMG characteristic to a certain extent, and its formula is

$$MPF = \frac{\int_0^{\infty} fp(f)df}{\int_0^{\infty} p(f)df}$$

Where $p(f)$ represents the SEMG power spectral density function.

After a large number of experiments, it is found that the extension of the index finger, stretching wrist, wrist and fist four kinds of movements of the average root value and integral electromyography eigenvalue distinction is more obvious. The distinguishing degree is checked by using the eigenvalues as punctuation coordinates, and the mark results are shown in Figure 7

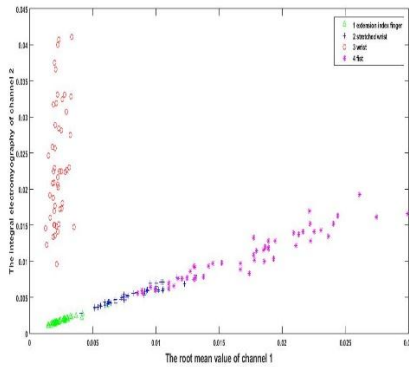


Fig 7 Eigenvalue extraction results

Set the extension finger to 1, marked with 'Δ', mark the wrist as 2 and use '+' to identify it, identify the wrist as 3 and 'o', mark the fist action as 4, with '*' logo. It can be seen from the figure that the overlapping area of the distribution of different actions is less, further confirming the selection of eigenvalues

3.3 Pattern Recognition

A total of 200 sets of eigenvectors were selected for each action. A total of 120 sets of data were selected for each group of 30 sets of data. The remaining 20 groups of 80 data for each operation were used as the test.

Probabilistic Neural Network, set the radial basis

function of the expansion factor spread = 0.0006, training network after the forecast recognition. A recognition result is shown in Figure8

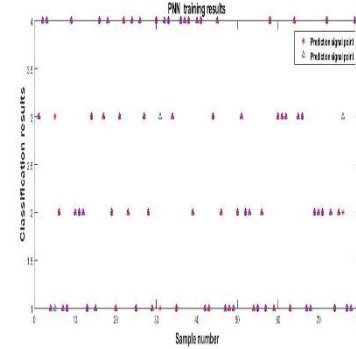


Fig 8 PNN pattern recognition results

In order to verify the PNN network recognition effect, use the common BP neural network as a contrast. Set the number of input nodes $n = 12$, the number of hidden layer nodes $l = 13$, the number of output layer nodes $m = 4$, the initial value of less than 1 random number. One of the identification results shown in Figure 9

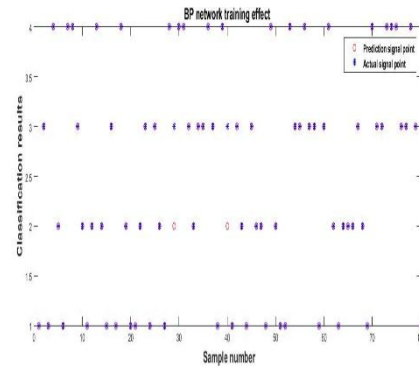


Fig 9 BP neural network pattern recognition results

Through a large number of repeated tests, randomly selected 10 groups of two networks under the four action recognition rate results and recorded in Table 1 and Table 2 respectively

Tab 1 BP neural network recognition rate results (%)

Serial number	BP network recognition rate				average
	action 1	action 2	action 3	action 4	
1	96.43	100.00	100.00	100.00	98.75
2	95.83	77.78	100.00	100.00	93.75
3	100.00	57.14	95.83	100.00	87.50
4	100.00	95.45	27.78	100.00	82.50
5	100.00	70.00	100.00	95.65	91.25
6	100.00	88.46	92.86	100.00	95.00
7	92.31	78.26	100.00	100.00	92.50
8	95.45	81.25	89.47	100.00	92.50
9	95.24	82.61	81.25	100.00	90.00
10	100.00	100.00	60.00	100.00	87.50

Tab 2 PNN recognition rate results (%)

Serial number	PNN network recognition rate				
	action	action	action	action	average
	1	2	3	4	
1	94.44	68.18	100.00	100.00	90.00
2	100.00	100.00	100.00	100.00	100.00
3	100.00	95.00	100.00	100.00	98.75
4	93.75	100.00	100.00	100.00	100.00
5	100.00	95.45	100.00	100.00	98.75
6	100.00	94.74	100.00	100.00	98.75
7	95.24	100.00	100.00	100.00	98.75
8	95.00	100.00	95.45	100.00	97.50
9	100.00	100.00	85.71	100.00	96.25
10	100.00	89.47	100.00	100.00	97.50

Through a large number of experiments and analysis, the average correct rate of pattern recognition of PNN network is 97.625%, while the average correct rate of BP neural network is 91.125%, and the recognition result of PNN network is more ideal

IV CONCLUDING REMARKS

In this paper, based on the SEMG pretreatment, the Battworth bandpass filter and the Butterworth bandstop filter are used to filter the baseline drift and the power frequency interference in the original signal respectively. By extracting the integral myoelectric value in the time domain, the root surface value and the power spectral density in the frequency domain. The eigenvalue samples are constructed by analyzing the eigenvalues, and then a large number of samples are trained by BP neural network and PNN network respectively. The experimental results show that PNN neural network has a high accuracy in pattern recognition of surface EMG signals and can meet the needs of pattern recognition. Which can be used for gesture recognition research, can provide a theoretical basis for subsequent gesture action recognition system

References

- [1] HONG Jie, WANG Lu, WANG Chao, et al. SEMM identification of hand motion based on artificial fish swarm algorithm optimization SVM[J]. Sensors and Microsystems. 2016,35(02):23-25
- [2] MAO Dong-jie et al. Low-power compression filtering algorithm for surface electromyography based on wavelet transform[J]. Chinese Journal of Sensors and Actuators. 2016,29(05):648-653.
- [3] MAHDI KHEZRI, MEHRAH JAHED. A Neuro-Fuzzy Inference System for SEMG-Based Identification of Hand Motion Commands[J]. IEEE TRANSACTIONS ON INDUSTRIAL ELECTRONICS, 2011, 58(5): 1952-1960.
- [4] ZHANG Yi, LIAN Youqi, LUO Yuan. Study on EMG Pattern Recognition Based on Wavelet Transform and AR Model[J]. Journal of Electronic Measurement & Instrumentation. 2011, 25(09): 770-774
- [5] Wang Hongqi et al. Characterization of Surface EMG Signal Based on Linear Discriminant Analysis[J]. Journal of Henan Polytechnic University: Natural Science Edition. 2015, 34 (06): 832-835.
- [6] Application of Probabilistic Neural Network in Handwritten Chinese Character Recognition[J]. Electronic design engineering, 2016, 24(02): 32-34.
- [7] Shi Feng, Wang Xiaochuan. Matlab neural network analysis of 30 cases[M]. Beijing: Beijing University of Aeronautics and Astronautics Press, 2010: 1
- [8] Li Haihua, Fan Juan. An Improved Edge Detection Algorithm Based on Gradient[J]. Science & Technology and Engineering, 2013, 13(01): 90-93.

Design of small-sized full tensor magnetic gradiometer

ZHANG WEN-YE; WEN YAN-LING; ZHU WEN-HAO

(Jilin university instrument science and engineering institute, changchun, 130021)

Abstract—Magnetic field positioning is a passive location technique, with the advantages of good concealment, strong adaptability, and uneasy interference. At present, it is gradually applied to a wide range of respects, such as underwater target location and navigation, metal geophysical prospecting, water exploration, urban engineering, geophysical prospecting, archeology and military geophysical prospecting, etc. The ordinary magnetic exploration judge the distribution range and position of the magnetic subject by observing and analyzing the magnetic difference of the object and the magnetic field characteristics, but it needs repeated detection in different sections, and it can only determine the general direction and range of magnetic objects, so it is difficult to achieve the precise positioning of magnetic targets. The measuring object of the magnetic gradient tensor measurement system is the gradient of the magnetic induction vector, in spite of the limitation of field measurement. The measurement information can reflect the magnetic moment information, with a slight effects from the dip angle and deflection angle of the geomagnetic field. The magnetic source can be well presented through this way and the magnetic gradient tensor inversion can well describe the field source direction of magnetization and geometry, such as orientation, direction, and field source boundary, improving the resolution of magnetic bodies.

Keywords—Total tensor magnetic measurement small-sized Magnetic measuring device

I INTRODUCTION

TOTAL tensor magnetic gradient detection is one of the most advanced technologies and has become a hot topic in the field of magnetic measurement. Flux gate or full tensor magnetic gradient detection device those aiming at the superconducting has large volume and high power consumption, which cannot solve the prominent problem of local detection. The miniaturization of full tensor magnetic gradient measurement device can be applied to the exploration and testing, biological detection and other fields.

The main target of the full tensor magnetic gradient is the magnetic field of the earth. The plane and ship is used as the instrument platform to carry out the aeromagnetic gradient survey and the magnetic gradient measurement of the ocean. High sensitivity sensors are used: superconducting magnetic gradiometer, fluxgate and so on. At present, the magnetic field full tensor magnetic gradient measurement device only Germany Yarra aviation superconducting system is put into application. led by Institute of Microsystem of the CAS in Shanghai, our school join in the development of superconducting magnetic air full tensor gradient measuring device in the laboratory of Jilin University, and successfully developed the fluxgate magnetic gradient tensor system. These platforms and measuring devices are large installations. The full tensor magnetic gradient

devices for exploratory wells, industrial flaw detection and biological exploration have not been reported at home and abroad. For these areas, it is true that smaller devices are needed to use for measurement, and the device we designed is designed to meet these requirements.

By using this micro total tensor magnetic gradient measurement device, the full tensor magnetic gradient can be applied in many fields. For example, it can confirm the safety situation of mine exploration, borehole and ore; it can protect object in the process of damage detection. The universal significance of this system is to promote the science and technology of magnetic detection to multiple across the field.

II SYSTEM DESIGN

Magneto resistive sensor as input module, achieve acquisition and preprocessing of the magnetic signal; the STMicroelectronics production STM32 F103ZET6 as microprocessor, realize the analysis of the collected data and calculation; acrylic plate customized as the core support structure and probe module; 3.5 inch MCU display as display output module; the system use analog I2C communication technology to collect the four sensor data at the same time; based on the Cartesian coordinate system, the permanent magnet is fixed by COMSOL permanent magnet magnetic field simulation, and the permanent magnet is set to the

coordinate (0,0,0) probe, comparing the actual measurement results.

2.1 GMR sensor HMC5843

The Honeywell HMC5843 is a surface mount multi-chip module designed for low field magnetic sensing with a digital interface for applications such as low cost compassing and magnetometry. The HMC5843 includes our state of the art 1043 series magneto-resistive sensors plus Honeywell developed ASIC containing amplification, strap drivers, offset cancellation, 12-bit ADC and an I2C serial bus interface. The HMC5843 is in a 4.0 by 4.0 by 1.3mm surface mount leadless chip carrier (LCC). Applications for the HMC5843 include Consumer Electronics, Auto Navigation Systems, Personal Navigation Devices, and Magnetometers. The HMC5843 utilizes Honeywell's Anisotropic Magneto Resistive (AMR) technology that provides advantages over other magnetic sensor technologies. The sensors feature precision in-axis sensitivity and linearity, solid-state construction with very low cross-axis sensitivity designed to measure both direction and magnitude of Earth's magnetic field. Honeywell's Magnetic Sensors are among the most sensitive and reliable low-field sensors in the industry. After the comparison of several main three axis magneto resistive sensors, we chose HMC5843 as the core chip.

2.2 Micro controller

The micro controller used the STMicroelectronics STM32F103ZET6. It is based on a 32 bit RISC kernel Cortex-M3, and its performance can reach 1.25DMIPS/MHZ, with advantages of low power consumption, interrupt latency short time and low cost. In addition, STM32 has a strong expansion ability, easy to transplant, peripherals rich in resources, and can achieve the accuracy and range required by the system.

2.3 Theoretical analysis of magnetic survey

A magnetic dipole is a physical model established by analogy with an electric dipole. A system consisting of two magnetic charges with an equivalent number is called a magnetic dipole. But since there is no magnetic monopole, the physical model of the magnetic dipole is not two monopole but a closed loop current. The magnetic dipole model can well describe the magnetic field distribution produced by small scale closed circuit elements. We model a circular loop with an electric current as a magnetic dipole.

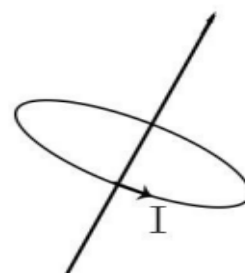


Fig. 1 Simulation Model of magnetic dipole

Formula is represented as: $\vec{\mu} = I \vec{S}$

(1)

I is loop current, and S is loop area vector, the direction is decided by current direction, and satisfies right hand rule.[1]

The simulation of magnetic dipole using COMSOL is based on the finite element physical field analysis. To solve problems with simpler problems instead of complex ones, finite element analysis will solve the field as many as interconnection of small subdomain finite element. For each unit assume an appropriate (simpler) approximate solution, then solve the domain satisfying conditions (such as structural equilibrium conditions), so as to get the solution of the problem. This solution is not an exact solution, but an approximate solution, since the actual problem is replaced by a simpler one. [2] Because most practical problems are difficult to obtain accurate solutions, the finite element method not only has high computational accuracy, but also can adapt to a variety of complex shapes, and it has become an effective means of engineering analysis.

COMSOL simulation achieve Multi-slices, magnetic data obtained by exporting, and the data is too large to show. The multi-slice figure, color represent magnetic energy, reducing energy from red to blue. Streamline represent magnetic field lines, magnetic field lines is closed inside and outside the coil.

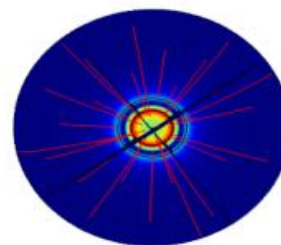


Fig. 2 multi slice of magnetic dipole COMSOL simulation

III SOFTWARE DESIGN

3.1 Overall program flow

In order to facilitate the use and maintenance of the system, the system designed in modular design thinking, the program is mainly composed of

initialization and program control. The initialization part mainly includes initialization of MCU, sensor, button, analog I2C communication MCU display. The program control section mainly deals with the data acquired by the HMC5843, by using data storage and full tensor algorithm. The overall flow chart of the system is shown in figure 3.

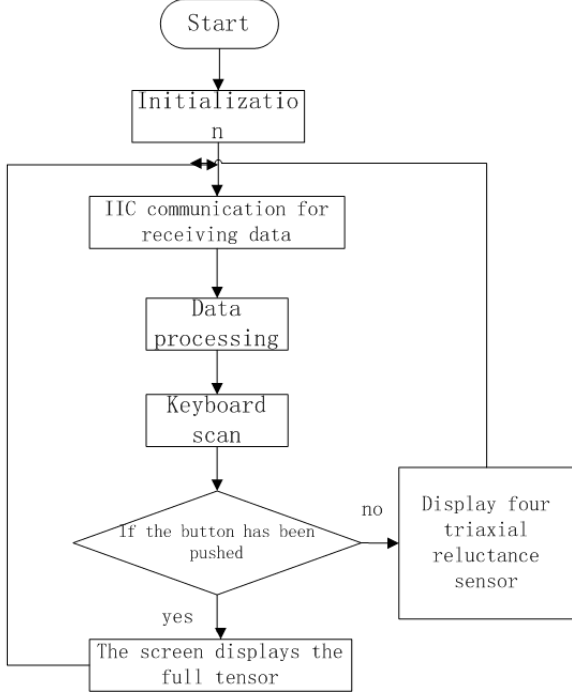


Fig. 3 flow chart of the system

3.2 magnetic field gradient tensor Calculation

When the distance between magnetic object and the reference point more than a certain, the magnetic object can be regarded as a magnetic dipole model, and the magnetic induction intensity is:

$$\mathbf{B} = \frac{\mu_0}{4\pi} \left[\frac{3(\mathbf{m} \cdot \mathbf{r})\mathbf{r}}{r^5} - \frac{\mathbf{m}}{r^3} \right] \quad (2)$$

Among them, μ_0 is dielectric permeability, $\mathbf{m}(\mathbf{m}_x, \mathbf{m}_y, \mathbf{m}_z)$ is the magnetic moment of magnetic objects, and $\mathbf{r} = x\mathbf{i} + y\mathbf{j} + z\mathbf{k}$ is the position vector, $r = |\mathbf{r}|$.

The gradient tensor of magnetic induction intensity \mathbf{B} is

$$G_{ij} = \frac{\mu_0}{4\pi} \left[\frac{15(\mathbf{m} \cdot \mathbf{r})r_i r_j}{r^7} + \frac{3m_i r_j}{r^5} + \frac{3m_j r_i}{r^5} + \frac{3(\mathbf{m} \cdot \mathbf{r})\delta_{ij}}{r^5} \right] \quad (3)$$

$$\delta_{ij} = \begin{cases} 1 & i = j \\ 0 & i \neq j \end{cases} \quad (4)$$

When the change rate is expressed in terms of three directions (x, y, z), the magnetic field gradient tensor consists of nine elements:

$$\mathbf{G} = \begin{bmatrix} \frac{\partial B_x}{\partial x} & \frac{\partial B_x}{\partial y} & \frac{\partial B_x}{\partial z} \\ \frac{\partial B_y}{\partial x} & \frac{\partial B_y}{\partial y} & \frac{\partial B_y}{\partial z} \\ \frac{\partial B_z}{\partial x} & \frac{\partial B_z}{\partial y} & \frac{\partial B_z}{\partial z} \end{bmatrix} = \begin{bmatrix} B_{xx} & B_{xy} & B_{xz} \\ B_{yx} & B_{yy} & B_{yz} \\ B_{zx} & B_{zy} & B_{zz} \end{bmatrix} \quad (5)$$

Practically, the magnetic field is usually measured by a plurality of magnetic sensors. Thus indirectly obtain magnetic field intensity, and next through contraction obtain the amount of a magnetic gradient tensor modulus. The location of the space is shown in figure 4.[3]

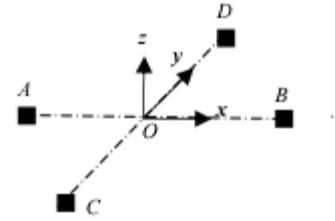


Fig. 4 layout of magnetic sensor

Magnetic field gradient produced by Magnetic objects in the 'O' points is as follows:

$$B_{xx} \approx \frac{B_{xA} - B_{xB}}{L} \quad (6)$$

$$B_{yy} \approx \frac{B_{yC} - B_{yD}}{L} \quad (7)$$

$$B_{zz} \approx -B_{xx} - B_{yy}$$

$$B_{yz} = B_{zy} \approx \frac{B_{zC} - B_{zD}}{L} \quad (8)$$

$$B_{xz} = B_{zx} \approx \frac{B_{zA} - B_{zB}}{L} \quad (9)$$

$$B_{xy} = B_{yx} \approx \frac{B_{xC} - B_{xD} + B_{yA} - B_{yB}}{2L} \quad (10)$$

$$(11)$$

Among them, B_{xi} , B_{yi} , B_{zi} ($i=A, \dots, D$) is the magnetic induction intensity of each magnetic sensor, and the L is the baseline distance between the probes.[4] In this paper, the baseline distance is 0.175m.

IV TEST RESULT

After several tests, the instrument can successfully measure the magnetic field vector and calculate the full tensor. By comparison with data obtained from COMSOL software simulation, the results are consistent. The measurement level of the device is basically stable. It can obtain the full tensor accurately and the precision is in the expected rang. To sum up, this device can meet the requirements of full tensor magnetic gradient measurement, and conforms to the small-sized requirements in practical applications. The accuracy is within a certain range and has practical value.

V CONCLUSION

This system adopts the STM32 as the processor, achieve real-time acquisition and processing of GMR sensor signal, and the four three axis magnetic sensor is fixed on the bracket structure model. According to full tensor algorithm calculate the full tensor, in order to achieve the application of exploration and injury measurement. But the device is still subject to external influence, errors caused by display. There is a direct relationship between these problem do a lot with lack of the angle sensor. According to the follow-up requirements of the system, corresponding compensation sensor can be increased.

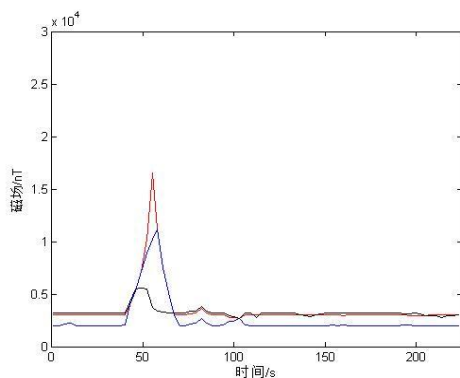


Fig.5 measurement of sing HMC5843

References

- [1] Zhao Jing. Research on Key Technologies of high temperature superconducting magnetic gradiometer .Jilin University, 2011
- [2] Zhang Changda, Dong Haobin. Gravity and magnetic prospecting have entered a new era. Journal of Engineering Geophysics, 2010.
- [3] Guan Zhining, Hao Tianyao, Yao Changli. Prospects for gravity and magnetic exploration in twenty-first Century: geophysical advances, 2002.
- [4] Zhao Yu, Zhang Jin, Deng Ruihui. RS-HC3 Ocean total tensor magnetic gradient system and its applications. Marine mapping, 2014.